MULTISPECTRAL IMAGING FOR INTRAOPERATIVE TUMOUR DETECTION IN BREAST CANCER SURGERY

Dhurka Shanthakumar

Imperial College London
Department of Surgery & Cancer

This dissertation is submitted for the degree of Doctor of Philosophy

January 2025

Declaration of Originality

I hereby declare that this thesis is my own work, except for where indicated (in the “Acknowledgements” section or throughout the text of this thesis), and has not been submitted in any form for another degree or diploma elsewhere. Information derived from the published and unpublished work of others has been recognised appropriately via citations as found in the bibliography.

Copyright Declaration

The copyright of this thesis rests with the author. Unless otherwise indicated, its contents are licensed under a Creative Commons Attribution-Non-commercial 4.0 International Licence (CC BY-NC).

Under this licence, you may copy and redistribute the material in any medium or format. You may also create and distribute modified versions of the work. This is on the condition that: you credit the author and do not use it, or any derivative works, for a commercial purpose. When reusing or sharing this work, ensure you make the licence terms clear to others by naming the licence and linking to the licence text. Where a work has been adapted, you should indicate that the work has been changed and describe those changes. Please seek permission from the copyright holder for uses of this work that are not included in this licence or permitted under UK Copyright Law.

Abstract

On average 19% of patients undergoing breast conserving surgery (BCS) require re-excision due to positive margins. Augmenting a surgeon's intraoperative visualization of margin disease could improve precision. Multispectral imaging (MSI) utilizes spectral differences between normal and tumour tissues to characterise pathology in real-time. The diagnostic accuracy of a custom-built MSI camera was assessed.

BCS patients were recruited to a single centre, prospective study (REC= 08/H0719/37). Multispectral images were acquired from each resection surface of freshly excised BCS specimens. Image pre-processing included data normalization and dimensionality reduction. Intraoperative radiography and gold standard histological analysis were used to extract ground truth. Four machine learning classifiers were used for data analysis.

46 patients were recruited. MSI images provide information about tissues up to depths of 3mm, therefore image analysis was conducted on resection surfaces where tumour was noted within this depth. 6 specimens were excluded due to gross contamination with blue dye or poor image quality. Therefore, 38 surface images from 23 specimens were included for final analysis. Logistic regression resulted in an area under the curve of 89% (SD ± 7), sensitivity 86% (SD ± 12), and specificity 80% (SD ± 8).

MSI can distinguish between normal and malignant breast cancer tissues. Unlike existing systems, MSI provides immediate visualisation and evaluates the entire resection surface. Future work will focus on adapting MSI to overcome spectral artifacts and improving image analysis using varying machine learning classifiers, as speed and accuracy will optimize surgical workflow.

Acknowledgements

This thesis would not have been possible without the guidance, support, and encouragement of many individuals within Imperial College, but friends and family outside too. I would like to start by thanking Professor Ara Darzi for allowing me to enrol into this degree during the pandemic, at a time of uncertainty and significant change. You have opened my eyes to the world of academia and to the innovative work of this University.

I wish to express my deepest gratitude to my main supervisors Mr Daniel Leff and Professor Daniel Elson, for whom without this PhD would not have been possible. I am eternally grateful for their invaluable guidance, time spent reviewing my work, and insightful feedback throughout. Firstly, to Mr Leff, you have shown me that no mountain is too high to climb! Your ethos of hard work is exemplary and have pushed me to improve so many skills which will be useful in the academic and clinical environment. I thank you for always being honest with your critique, making me think outside the box, and opening doors to the world of breast surgery. Next, and by no means second, many thanks to Prof Elson. I thank you for your continued patience throughout this whole process, as you have always helped me navigate the challenges of this translational work. Your eye to detail is superb and has taught me how to think like a scientist. You have also always been understanding of the demands of clinical work and enabled me to balance this with academia. You both have impacted this work so positively due to your diverse backgrounds and immense knowledge.

My heartfelt thanks to Dr Vadzim Chalau and Dr Maria Leiloglou. Vad, you have my saviour on so many experimental days in the lab and in theatre! Thanks for always explaining complex scientific ideas in layman's terms and always coming to help at a moment's notice. I will miss our coffee catch ups and conversations on non-PhD related topics whilst we waited for tissue specimens. Thank you for teaching me the importance of protocol in science and being patient with me. Maria, you have done an amazing job with data analysis for this work, and I am so thankful for the number of hours you've dedicated in explaining image processing to me as well as analysing images. Your willingness to learn about things which are unknown to you is so admirable, and you are the epitome of true dedication and passion in science. A

special thanks also to Martha Kedryzycki who has paved the way for clinical fellows in exploring margin assessment, and for all your guidance in being a research fellow.

I thank all the breast consultants and registrars at Charing Cross Hospital for allowing me to be in theatre with them during data collection. A special thanks to Dr Anna Silvanto for reviewing all histopathology for this project and accommodating this work in a very busy department. I am also grateful to the lab technicians for processing samples in a timely fashion. To Sanjay Mistry, who also helped with patient identification for recruitment to chapter six.

Lastly, to my friends and family who have supported me throughout the past few years, what a journey it has been! To all my friends who have understood the trials and tribulations of research and encouraged me to plough on. To my parents who have always encouraged me to strive for the best and supported in me in every way possible. I am always grateful for the multiple early morning drop offs, hot food and listening to my dilemmas. Finally, thanks to my husband who has been patient throughout this journey and solved my many technical crises at all times of the day! I appreciate you have had to make sacrifices for me to finish this work, and I am eternally grateful.

Research Outputs

The work from this thesis has resulted in the following presentations and publications.

Presentations & Published Abstracts

June 2024 **Machine learning in combined multiseperation diffuse reflectance and intrinsic fluorescence spectroscopy diagnostics of breast tumours**

V Chalau, D Shanthakumar, I Gkouzionis, Y Shi, M Leiloglou, A Silvanto, D Leff, D Elson

Oral presentation (Dr V Chalau presented)

Proceedings of SPIE PC13009, Clinical Biophotonics III, PC130090J.

May 2024 **Multispectral Imaging for Intraoperative Margin Assessment in Breast Conserving Surgery**

D Shanthakumar, M Leiloglou, V Chalau, A Darzi, DS Elson, DR Leff

Oral presentation

Association of Breast Surgeons Conference, Bournemouth, UK, 13-14th May.

European Journal of Surgical Oncology, Volume 50, Supplement 1, 108074.

A systematic review and meta-analysis based on margin width and patient outcomes following breast conserving surgery for early invasive disease

D Shanthakumar*, A Ezzat*, N Laskar, R.I. Cutress, DJ Hadjiminas, M Boland, M Joshi, R Patel, Y Grant, R Naik, Nur A Che Bakr, S Hajev, H Elghazaly, J Holt, A Darzi, H Ashrafian, DR Leff (* = joint 1st author)

Prize Winning Oral presentation (Presented by A Ezzat)

Association of Breast Surgeons Conference, Bournemouth, UK, 13-14th May.

European Journal of Surgical Oncology, Volume 50, Supplement 1, 108074.

The Influence of Margin Width on Risk of Local Recurrence following Breast Conserving Surgery for Ductal Carcinoma In-Situ: a Systematic review and Meta-analysis

D Shanthakumar, A Ezzat, N Laskar, R.I. Cutress, DJ Hadjiminas, M Boland, M Joshi, R Patel, Y Grant, R Naik, Nur A Che Bakri, S Hajev, H Elghazaly, J Holt, A Darzi, H Ashrafian, DR Leff

Poster presentation

Association of Breast Surgeons Conference, Bournemouth, UK, 13-14th May. European Journal of Surgical Oncology, Volume 50, Supplement 1, 108074.

Combined multi-separation diffuse reflectance and intrinsic fluorescence spectroscopy: a tool for rapid diagnostics and intraoperative margin assessment in breast surgery

D Shanthakumar; V Chaulau; Y Shi; I Gkouzionis; A Silvanto; M Leiloglou; A Darzi; DR Leff; DS Elson

Poster presentation

Association of Breast Surgeons Conference, Bournemouth, UK, 13-14th May. European Journal of Surgical Oncology, Volume 50, Supplement 1, 108074.

April 2024 **Impact of Margin Width on Risk of Local Recurrence following Breast Conserving Surgery for pure Ductal Carcinoma In-Situ : a Systematic review and Meta-analysis**

D Shanthakumar, A Ezzat, N Laskar, R Cutress, D Hadjiminas, M Boland, M Joshi, R Patel, Y Grant, R Naik. Nur A Chek Bakri, S Hajev, H Elghazaly, J Holt, A Darzi, H Ashrafian, D Leff

Poster presentation

The American Society of Breast Surgeons, Annual Meeting, April 10-14th, Orlando, Florida.

The American Society of Breast Surgeons Official Proceedings, Volume XXV 2024 Annual Meeting Scientific Session Abstracts. *Ann Surg Oncol* 31 (Suppl 2), 295–703 (2024).

Multispectral Imaging: A Precision Tool in Margin Assessment in Breast Conserving Surgery

D Shanthakumar, M Leiloglou, V Chaulau, P Thiruchelvam, A Darzi, D Elson, D Leff

Poster presentation

The American Society of Breast Surgeons, Annual Meeting, April 10-14th, Orlando, Florida.

The American Society of Breast Surgeons Official Proceedings, Volume XXV 2024 Annual Meeting Scientific Session Abstracts. *Ann Surg Oncol* 31 (Suppl 2), 295–703 (2024).

Relationship between Margin Width and Local Recurrence following Breast Conserving Surgery for Invasive Breast Cancer – a Meta-Analysis
A Ezzat, D Shanthakumar, N Laskar, R Cutress, D Hadjiminas, M Boland, M Joshi, R Patel, Y Grant, R Naik. Nur A Chek Bakri, S Hajev, H Elghazaly, J Holt, A Darzi, H Ashrafian, D Leff
Poster presentation
The American Society of Breast Surgeons, Annual Meeting, April 10-14th, Orlando, Florida.
The American Society of Breast Surgeons Official Proceedings, Volume XXV 2024 Annual Meeting Scientific Session Abstracts. *Ann Surg Oncol* 31 (Suppl 2), 295–703 (2024).

June 2023 **Investigation of multispectral imaging classification routines for intraoperative margin assessment in breast conserving surgery**
M Leiloglou, D Shanthakumar, I Gzouzionis, V Chaulau, D Leff, D Elson
Oral presentation (by Dr M Leiloglou)
European Conferences in Biomedical Optics, Munich, Germany
Conference Paper 12627-48

May 2023 **Intraoperative Multispectral Imaging for Precision In Breast Conserving Surgery**
D Shanthakumar; M Leiloglou; V Chalau; A Darzi; D Elson; D Leff
Oral presentation in Prize Session
Association of Breast Surgeons (ABS), Belfast, UK, 15 – 16th May
European Journal of Surgical Oncology, Vol 49, Issue 5, E218

Tissue Optics for Margin Assessment in Breast Conserving Surgery: Systematic Review & Meta-Analysis
D Shanthakumar, M Leiloglou, C Kelliher, A Darzi, D Elson, D Leff
Oral presentation in Prize Session
Association of Breast Surgeons (ABS), Belfast, UK, 15 – 16th May
European Journal of Surgical Oncology, Vol 49, Issue 5, E218

5-ALA induced fluorescence imaging for margin status identification during breast conserving surgery

M Leiloglou, M Kedrzycki, V Chalau, D Shanthakumar, D Elson, D Leff

Oral presentation (presented by Dr M Leiloglou),

Association of Breast Surgeons (ABS), Belfast, UK, 15 – 16th May

European Journal of Surgical Oncology, Vol 49, Issue 5, E218

Intraoperative hyperspectral imaging in breast conserving surgery: Systematic Review

D Shanthakumar, M Mohammed, M Leiloglou, A Darzi, D Leff

Poster presentation

Association of Breast Surgeons, Belfast, UK, 15 – 16th May

European Journal of Surgical Oncology, Vol 49, Issue 5, E218

Fluorescence and Multispectral Imaging use for tumour identification in breast conserving surgery

Poster presentation

M Leiloglou, M Kedrzycki, D Shanthakumar, V Chalau, D Elson, D Leff

Association of Breast Surgeons (ABS), Belfast, UK, 15 – 16th May

European Journal of Surgical Oncology, Vol 49, Issue 5, E218

April 2023 **Fluorescence and Multispectral Imaging in Breast Conserving Surgery – Proof of Concept Trial**

M Kedrzycki, M Leiloglou, D Shanthakumar, V Chalau, P Thiruchelvam, D Leff, D Elson

Poster presentation

The American Society of Breast Surgeons, Annual Meeting, April 26 - 30th, Boston, USA.

The American Society of Breast Surgeons Official Proceedings, Volume XXIV 2023 Annual Meeting Scientific Session Abstracts. *Ann Surg Oncol* 30 (Suppl 2), 295–664 (2023).

5-ALA induced fluorescence for tumor visualization in breast conserving surgery – Part 2 of the "GLOW "study

M Kedrzycki, M Leiloglou, D Shanthakumar, V Chalau, P Thiruchelvam, D Elson, Daniel Leff

Poster presentation

The American Society of Breast Surgeons, Annual Meeting, April 26 - 30th, Boston, USA.
The American Society of Breast Surgeons Official Proceedings, Volume XXIV 2023 Annual Meeting Scientific Session Abstracts. *Ann Surg Oncol* 30 (Suppl 2), 295–664 (2023).

May 2022 **Preliminary findings of Raman spectroscopy and Confocal Laser Microendoscopy in breast cancer diagnostics**
Oral presentation (Presented on behalf of Dr A Ezzat)
Association of Breast Surgeons (ABS), Liverpool, UK, 15 – 16th May

Multiexcitational laser induced fluorescence spectroscopy for breast cancer diagnostics
D Shanthakumar, V Chalau, A Darzi, D Elson, Daniel Leff
Poster presentation
Association of Breast Surgeons (ABS), Liverpool, UK, 15 – 16th May
European Journal of Surgical Oncology, Volume 58, Issue 5, E241

April 2022 **Tissue Optical Imaging as an emerging technique for intraoperative margin assessment in breast-conserving surgery**
D Shanthakumar, D Elson, A Darzi, D Leff
Poster presentation
The American Society of Breast Surgeons, Annual Meeting, April 6-10th, Las Vegas, USA.
The American Society of Breast Surgeons Official Proceedings, Volume XXV 2024 Annual Meeting Scientific Session Abstracts. *Ann Surg Oncol* 29 (Suppl 2), 1-330 (2022).

Publications

A Comparison of Spectroscopy and Imaging Techniques Utilizing Spectrally Resolved Diffusely Reflected Light for Intraoperative Margin Assessment in Breast-Conserving Surgery: A Systematic Review and Meta-Analysis
D Shanthakumar, M Leiloglou, C Kelliher, A Darzi, D Elson, D Leff
Cancers (Basel) 2023 May 23;15(11):2884.
doi: 10.3390/cancers15112884

Impact of resection margin width on local recurrence following breast-conserving surgery and whole breast radiotherapy for pure ductal carcinoma in situ: a systematic review and meta-analysis

Shanthakumar D, Ezzat A, Laska N, Cutress RI, Hadjiminas D, Boland M, Joshi M, Patel R, Grant Y, Naik R, Bakri NAC, Hajev S, Elghazaly H, Holt J, Roddan A, Cleator S, Darzi A, Ashrafian H, Leff DR

BMJ Oncol. 2025 Mar 6;4 (1):e000633.

doi: 10.1136/bmjonc-2024-000633

Contents

CHAPTER 1: BACKGROUND TO BREAST CANCER AND CURRENT CLINICAL PROBLEM 24

1.1 Breast Cancer Incidence 24
1.2 Evolution of Breast Cancer Management 24
1.3 Margins in Breast Cancer 26
1.3.1 Margin width practice 27
1.3.2 Factors influencing positive margins 27
1.4 Re-excision Surgery 30
1.4.1 GIRFT Report – How to Tackle The Problem of Re-excision Surgery 31
1.4.2 Harmful Impact of Re-excision Surgery 32
1.4.2.1 Impact on adjuvant therapy 33
1.4.2.2 Cosmetic outcome 33
1.4.2.3 Psychosocial and emotional impact 34
1.4.2.4 Higher cost and healthcare utilization 34
1.4.2.5 Risk of mastectomy 35
1.4.2.6 Environmental impact 36
1.5 Techniques to Reduce Reoperation Rates 37
1.5.1 Non-Surgical Approaches 37
1.5.2 Surgical approaches 37
1.5.2.1 Increase Volume of Tissue Excised 37
1.5.2.2 Selective or Routine Cavity Shave Margin Excision 38
1.6 Intraoperative Margin Assessment Techniques 39
1.6.1 Traditional 39
1.6.1.1 Specimen Radiography 39
1.6.1.2 Frozen Section Analysis 41
1.6.1.3 Imprint Cytology 43
1.6.2 Emerging Technologies 43
1.6.2.1 Technologies Using Imaging 44
1.6.2.1.1 Micro-computed Tomography 44
1.6.2.1.2 Magnetic Resonance Imaging 45
1.6.2.2 Technologies using optical imaging 46
1.6.2.2.1 Photoacoustic tomography 46
1.6.2.2.2 Raman Spectroscopy 47
1.6.2.3 Technologies Based on Differences in Electrical Properties of Tissue 48
1.6.2.3.1 MarginProbe 48
1.6.2.3.2 Clear Edge 49
1.6.2.4 Technologies Based on Biochemical Differences in Tissue 49
1.6.3 Future IMA Tool Characteristics 50
1.7 Thesis summary 52

1.7.1 Hypothesis *52*
1.7.2 Summary *52*

CHAPTER 2: LIGHT – TISSUE INTERACTIONS 54

2.1 Tissue Optics Background 54
2.1.1 Reflection and refraction *55*
2.1.2 Scattering *55*
2.1.3 Absorption *56*
2.1.4 Intrinsic Fluorescence *56*
2.2 Systematic Review and Meta-Analysis 57
2.2.1 Diffuse Reflectance Spectroscopy *57*
2.2.2 Multispectral/Hyperspectral Imaging *60*
2.2.3 Spatial Frequency Domain Imaging *62*
2.3 Methodology 63
2.3.1 Literature Search Methodology *63*
2.3.1.1 Study selection 63
2.3.1.2 Data Collection 64
2.4 Meta-Analysis 65
2.5 Results 66
2.5.1 Categorization of Selected Studies *66*
2.5.1.1 Tissue Optic Modality Type 66
2.5.1.2 Probe-Based Systems vs. Imaging Based Systems 68
2.5.1.3 Patient and tissue heterogeneity amongst studies 71
2.5.1.4 Diagnostic ability of different tissue optic techniques 75
2.6 Meta-Analysis 76
2.6.1 Heterogeneity Results *76*
2.6.2 Pooled sensitivity/specificity results *77*
2.7 Discussion 80
2.7.1 Meta-Analysis on Probe Based vs Image Based Approaches *80*
2.7.2 Meta-analysis on modality sub-divisions *82*
2.8 Future Work 83
2.9 Conclusions 85

CHAPTER 3: SPATIAL RESOLUTION OF OPTICAL MARGIN ASSESSMENT TOOLS 86

3.1 Relevance of Margins to this Thesis 86
3.2 Impact of Margin Width on Oncological Outcome 87
3.3 Global Variability in Margin Guidance 89
3.3.1 Invasive Breast Cancer Margin Guidance Currently *89*
3.3.2 Current Ductal Carcinoma In Situ Margin Guidance *90*

3.4 Systematic Review and Meta-Analysis 90
3.4.1 Indication for Revised Systematic Review and Meta-Analysis *90*
3.4.2 Methodology *92*
3.4.2.1 Search Strategy and Selection Criteria 92
3.4.2.2 Meta-Analysis 94
3.5 Results 94
3.5.1 Studies selected and demographic data *94*
3.5.1.1 Invasive Cancer 94
3.5.1.2 Ductal carcinoma in-situ (DCIS) 97
3.5.2 Overall pooled results of performance metrics *100*
3.5.2.1 Invasive Breast Cancer 100
3.5.2.2 Ductal Carcinoma In-Situ (DCIS) 104
3.6 Discussion 107
3.6.1 Justification of Optical Imaging Penetration Depth *107*
3.6.2 Invasive Ductal Carcinoma *107*
3.6.3 Ductal Carcinoma In Situ (DCIS) *109*
3.6.4 Limitations *111*
3.6.5 Future Work *112*

CHAPTER 4: SPECTROSCOPY USE ON FRESHLY FROZEN BREAST TISSUE SAMPLES 113

4.1 Introduction 113
4.2 History of Optical Spectroscopy 113
4.3 Optical Spectroscopy 114
4.3.1 Components of Optical Spectroscopy *114*
4.3.1.1 Spectrometer 114
4.3.1.2 Light source 115
4.3.1.3 Slit 115
4.3.1.4 Diffraction Grating 115
4.3.1.5 Detector 116
4.3.1.6 Fibre 116
4.3.1.7 Diffuse reflectance probes 117
4.3.1.8 Fluorescence spectroscopy probes 118
4.4 Methodology 119
4.4.1 Study Setting *119*
4.4.2 Spectroscopy Instrumentation *119*
4.4.3 Data Acquisition Protocol *121*
4.4.4 Histopathology Correlation *122*
4.4.5 Data Processing Techniques *123*
4.4.5.1 Pre-Processing 123
4.4.5.1.1 DRS Calibration and Pre-Processing 124

4.4.5.1.2 Fluorescence Spectroscopy Calibration and Pre-Processing 125
4.4.5.2 Outlier Detection 126
4.4.5.3 Feature Extraction 126
4.4.5.3.1 Fixed Window Features 126
4.4.5.3.2 Peak Valley Features 127
4.4.5.3.3 Peak Valley Slopes 128
4.4.5.4 Feature Selection 128
4.4.6 Quality Assessment of Samples 129
4.4.7 Spectra Classification 130
4.4.7.1 Binary Classification on Individual channels 130
4.4.7.2 Combining Channels 131
4.4.8 Classifiers 131
4.4.8.1 Evaluation of Performance of Classification Algorithms 132
4.5 Results 134
4.5.1 Spectral Data Quantity & Spectral graphs 134
4.5.2 Demographics 134
4.5.3 Performance Metrics 134
4.5.3.1 Healthy Breast Tissue versus Malignant Breast Tissue 135
4.5.3.2 Healthy Tissue versus Different Histological Subtype Results 137
4.5.3.3 Comparison of performance metrics with intertumour heterogeneity 139
4.5.4 Spectral Graphs 141
4.5.5 Confusion Matrices 143
4.6 Discussion 144
4.6.1 Assessment of Performance Metrics (Healthy versus Malignant) 144
4.6.2 Assessment of Performance Metrics (Malignant versus Malignant) 145
4.6.3 Critical Analysis of Methodology 147
4.6.4 Further Clinical Applications 149
4.6.5 Limitations 150

CHAPTER 5: MULTISPECTRAL IMAGING SYSTEM – USE IN THE *EX-VIVO* AND *IN-VIVO* SETTING 152

5.1 History of Multispectral Imaging 152
5.2 Multispectral Instrumentation 154
5.2.1 Hardware Components of the Multispectral Imaging System 155
5.2.1.1 Multispectral Camera Components 157
5.2.1.2 Colour Camera Component 157
5.2.1.3 Light Source 158
5.2.1.4 Beamsplitter 159
5.2.1.5 Relay Lens 159
5.2.1.6 Software Interface 160

5.3 Methodology 161
5.3.1 Laboratory (ex-vivo) Study *161*
5.3.2 Intraoperative (in-vivo) Study *162*
5.3.2.1 Inclusion Criteria 162
5.4 Data Acquisition Protocol 163
5.4.1 Multispectral Imaging of Freshly Frozen Tissue Samples *163*
5.4.2 Multispectral Imaging of Breast Conserving Surgery Specimens Intraoperatively (in-vivo) *166*
5.4.3 Image Processing *168*
5.4.3.1 Histopathology Correlation 168
5.4.3.1.1 Freshly Frozen Tissue Samples 168
5.4.3.1.2 Intraoperative Freshly Excised Specimens 169
5.4.3.2 Ground Truth Extraction 169
5.4.3.2.1 Tissue Samples 169
5.4.3.2.2 Freshly excised wide local excision specimens 170
5.4.3.2.3 Pre-Processing of the MSI Images 171
5.4.3.2.4 Noise Reduction 171
5.4.3.2.5 Spectral Correction 172
5.4.3.2.6 Normalization Techniques 172
5.4.3.2.7 Spectral Calibration 174
5.5 Tissue Sample Classification 174
5.5.1 Logistic Regression *174*
5.5.2 Support Vector Machines *175*
5.5.3 Multilayer Perceptron *176*
5.5.4 Extreme Gradient Boosting *177*
5.6 MSI Classification Overlays 177
5.7 Results 178
5.6.1 Freshly Frozen Tissue Samples *178*
5.6.1.1 Demographics 178
5.6.1.2 Validation Metrics 180
5.6.2 In-vivo Freshly Excised Breast Specimens *181*
5.6.2.1 Demographics 181
5.6.3 Validation Metrics *184*
5.7 Discussion 186
5.7.1 Spectral Data Quantity *186*
5.7.2 Ability to Distinguish Between Normal Versus Malignant Tissue *186*
5.7.3 Comparison of MSI on Frozen Tissue Versus Fresh Tissue *187*
5.7.4 Translational Ability To Intraoperative Use *188*
5.8 Limitations 189

5.8.1 Patient Recruitment *189*
5.8.2 Drop Out Rate of Specimens *189*
5.8.3 Heterogeneity of Tissue Samples/Patients *190*
5.8.4 Ground Truth Marking *191*
5.8.5 Machine Learning *192*
5.9 Conclusion 193

CHAPTER 6: COMPARISON OF MULTISPECTRAL IMAGING *VERSUS* FLUORESCENCE GUIDED IMAGING 194

6.1 Fluorescence Imaging 194
6.2 Fluorophores 195
6.3 Current Use of Fluorophores in Medicine 196
6.3.1 Indocyanine as a Fluorophore *197*
6.3.2 ALA as a Fluorophore *197*
6.4 Challenges of Fluorescent Guided Surgery 199
6.5 Methodology 199
6.5.1 Patient Recruitment *200*
6.5.1.1 Inclusion Criteria 200
6.5.1.2 Exclusion Criteria 201
6.5.2 Fluorescence Camera Set Up *201*
6.5.3 Multispectral Camera Set Up *202*
6.5.4 Data Acquisition Protocol *202*
6.5.4.1 ALA administration 202
6.5.4.2 ICG adminitration 202
6.5.4.3 Image Acquisition 203
6.5.5 Image Processing *203*
6.5.5.1 Multispectral Image Processing 205
6.5.5.2 Fluorescent Image Processing 205
6.5.6 Comparison of MSI versus different fluorophores *205*
6.6 Results 206
6.6.1 Demographics *206*
6.6.2 Comparison of Precision Metrics of MSI versus FGS *207*
6.7 Discussion 210
6.8 Conclusion 211

CHAPTER 7: CONCLUSIONS AND FUTURE WORK 213

7.1 Conclusions 213
7.1.1 Clinical problem in breast conserving surgery and methods to tackle this *213*
7.1.2 Light-Tissue Interactions *213*

7.1.3 Influence of Margin Width on Local Recurrence *214*
7.1.4 Spectroscopy use on Freshly Frozen Breast Tissue Samples *215*
7.1.5 Multispectral Camera Use in the ex-vivo and in-vivo Setting *216*
7.1.6 Multispectral Imaging Versus Fluorescence Guided Surgery *217*
7.1.7 Concluding Remarks *218*
7.2 FUTURE WORK 218
7.2.1 Growth of ex-vivo and in-vivo Database *218*
7.2.2 Improvements to Data Analysis Methods *219*
7.2.3 Overcoming Challenges with Image Marking and Processing *220*
7.2.4 Multimodal Approach for an IMA Tool *220*
7.2.5 Adaptation of Hardware *221*
CHAPTER 8: REFERENCES 222
CHAPTER 9: APPENDICES 248

List of Tables

Table 2.1 Summary of modality and wavelength range for the technology being assessed in the selected 19 studies. 67

Table 2.2 Characteristics of probe-based systems of studies included in this review. Parameters evaluated include probe geometry; acquisition time; area covered and probe depth. Not all papers documented such parameters..... 69

Table 2.3 Parameters extracted from imaging studies included spatial resolution; area of field-of-view (FOV) imaging system can capture; time taken to image and depth penetration. Not all studies discussed these parameters. 71

Table 2.4 Highlighting patient ages and tissue types utilized in studies involved in this review. 15 studies characterized tissue samples into malignant and non-malignant types. Only 10 studies subdivided tissue types into various histological subtypes. (FA – fibroadenoma; IDC – invasive ductal carcinoma; ILD – invasive lobular carcinoma; DCIS – ductal carcinoma in-situ). Only 3 studies neither mentioned patient ages nor tissue types[163, 167, 170]. 74

Table 2.5 Summary table of the number of breast tissue samples interrogated by probe based or imaging-based technologies from each study (in relation to the number of patients recruited and lumpectomy specimens). The number of spectral measurements were recorded where possible. Sensitivity and specificity of the ability to distinguish between normal and invasive malignant tissue is tabulated. Of note, some studies also noted sensitivity/specificity of the ability to identify DCIS however these figures were not used in pooled statistics. 75

Table 2.6 Heterogeneity based on probe-based studies versus image based studies. The posterior probability for heterogeneity has been calculated for a prior probability for heterogeneity of Pr(Het)=0.5..... 76

Table 2.7 Heterogeneity based on modality subdivisions. The posterior probability for heterogeneity has been calculated for a prior probability for heterogenety of Pr(Het)=0.5. 77

Table 2.8 Pooled sensitivity/specificity results for probe based vs image based approaches – fixed (random). 77

Table 2.9 Methodology used for ground truth extraction for probe and image-based studies..... 82

Table 3.1 Demographic data and tumour characteristics of patients with invasive breast cancer. 95

Table 3.2 Demographic data and tumour characteristics of patients with DCIS included in this study. 98

Table 3.3 Pooled risk scores for ipsilateral locally recurrent invasive breast cancer based on varying threshold of resection margin width. (I2 = sample heterogeneity score, p = probability significance <0·05). ND = unable to compute..... 102

Table 3.4 Pooled risk scores for ipsilateral locally recurrent disease in patients with DCIS based on varying threshold of resection margin width. (I2 = sample heterogeneity score, p = probability significance <0·05). ND = unable to compute. 105

Table 4.1 Tissue samples categorised into histopathological subtype; tumour grade and receptor status. (IDC- invasive ductal carcinoma; ILC-invasive lobular carcinoma; DCIS-ductal carcinoma in situ; pCR-pathological complete response to neoadjuvant chemotherapy. 135

Table 4.2 Overall performance metrics of both GB and XGB classifiers on either selected tissue samples (i.e. the best quality score samples) and all tissue samples. 136

Table 4.3 Table depicting performance metrics for both classifiers when comparing healthy tissue with invasive lobular cancer. 137

Table 4.4 Table depicting performance metrics for both classifiers when comparing healthy tissue with invasive ductal cancer. 138

Table 4.5 Table depicting performance metrics for both classifiers when comparing healthy tissue with ductal carcinoma in-situ. 138

Table 4.6 Table depicting performance metrics for both classifiers when comparing healthy tissue with tissue taken from patients who received NACT and achieved a pathological complete response. 139

Table 5.1 Specifications of the 8 optical filters installed on the SpectroCam™ filter wheel. 157

Table 5.2 Nine normalization techniques were utilised in pre-processing of spectral data acquired from the MSI images. $\boldsymbol{xi, j, \lambda, new}$ is the new normalised pixel value at the spatial image location I,J of the band Λ, while the $\boldsymbol{xi, j, \lambda, old}$ is the old non-normalised value of the same pixel. $imagemin/imagemax$ is the minimum or maximum, respectively, pixel value in the whole spatial image. $bandmin/\ bandmax$ is the minimum or maximum, respectively, pixel value in each pixel spectrum. $\lambda = 470nm\lambda = 775nmxi, j, \lambda, old$ is the sum of all pixel values at the different 8 bands for each pixel, λ is the total number of bands, $i = 1i = 1044j = 1j = 1408xi, j, \lambda, old$ is the sum of all pixel values in a single image (band) and $i * j$ is the total number of image pixels. $pixel\ value\ rank$: $\{1,2,3,4,5,6,7,8,\}$ means replacing a pixel value with its rank when compared to the other values across the nine bands of the same pixel. 173

Table 5.3 Patient demographic data and tumour characteristics of all freshly frozen breast tissue samples utilized in final data analysis. (pCR – pathological complete response; DCIS – ductal carcinoma in situ; IDC – invasive ductal carcinoma; ILC – invasive lobular carcinoma; ER+ - oestrogen receptor positive; ER - - oetrogen receptor negative; PR- - progesterone receptor negative; PR+ - progesterone receptor positive; Her2+ - Herceptin receptor positive; Her2- Herceptin receptor negative); NACT – neoadjuvant chemotherapy). 178

Table 5.4 Table to show results for each classification model (Logistic regression; SVM; MLP and XGB for each normalization approach. (AUC – area under curve). 180

Table 5.5 Outcome metrics for the Multilayer Perceptron and Extreme gradient boosting. Grey shaded boxes are the best performance results for each classifier. 181

Table 5.6 Patient demographic data and tumour characteristics of all freshly excised breast specimens from 23 patients included in analysis. 182

Table 5.7 Overall validation metrics for each classifier and each normalization technique. 184

Table 5.8 Classification results for different combinations of normalisation and classification methodologies in the freshly excised specimens data-set. 185
Table 6.1 Table showing examples of fluorophores that have been investigated for passive and active targeting. For each fluorophore, the wavelength of light they have been associated with is noted with their mechanism of action (if known) and the solid tumours the have been investigated with. Finally, it is documented if the fluorophore has been approved for clinical use. 196
Table 6.2 Demographic data and tumour characteristics of all participants of this study. 206

List of Figures

Figure 1.1 Diagram to illustrate the difference between negative, close and positive margins. The black arrow in the 'negative' and 'close' images depicts how a pathologist measures the margin width from the outer aspect of cancer cells to the outer edge of the healthy tissue excised by a surgeon. A 'negative' margin contains no cancer cells at the outer edge of the inked specimen. A 'positive' margin has cancer cells that extend to the edge of the specimen, but a 'close' margin is any distance between negative or positive margins. 26

Figure 1.2 Table highlighting clinicopathological features with contribute to positive margins. 30

Figure 1.3 Schematic identifying how re-excision surgery impacts the patient and the healthcare system. Re-excision surgery can delay radiotherapy or chemotherapy; affect the cosmetic appearance of the breast; lead to anxiety, stress and affect quality of life; have financial implications to the patient due to delayed return to work but also puts a financial burden onto the healthcare system; there is a risk of mastectomy if positive margins persist; there is an environmental impact due to emission of greenhouse gases from further surgery..... 32

Figure 1.4 Illustration of the equipment for two dimensional (2D) specimen radiography and associated 2D radiographs produced (a-b); and set up of the three dimensional (3D) digital tomosynthesis machine and associated 3D image produced. (A) A 2D radiograph where a Magseed® localisation technique has been used to find the epicentre of the cancer. The dotted blue line highlights the Magseed® location and associated cancer. It is difficult to establish the boundaries of the cancer. (B) A 2D radiograph from a patient who received neoadjuvant chemotherapy and to help identify the lesion post treatment, a SAVISCOUT was inserted. The dotted blue circle shows the location of the localizer and a previous biopsy clip. The orange arrows highlight two wires used to "bracket" where disease on preoperative imaging was seen. (C) A 3D image construct from a lesion which was localized with a Magseed.® This image gives more detail about the lesion extent. 41

Figure 1.5 Illustration to depict how frozen section and imprint cytology are performed, and following a pathologist inspecting slides under a microscope the histopathological findings from the same specimen where a patient has invasive ductal carcinoma. (A) A freshly excised specimen is orientated as a clockface and small tissue samples are in this case taken circumferentially and prepared into slides following H&E staining (B) Under a microscope the histopathological findings following frozen section from one small area (C) One side of an excised specimen is pressed against a slide and then prepared to be read by a pathologist (D) A cytological slide following imprint cytology. (This illustration has been created from modified images from the following sources: Tamanuki *et al.*, Osaka *et al.*, and Pallialil *et al.* [[48, 112-114] with permission from publishers granted)..... 42

Figure 1.6 Emerging IMA tools categorized into four groups; imaging (e.g. X-ray; MicroCT, Bruker Inc); Optical (e.g. fluorescence imaging, SPY Elite, Stryker); Bioimpedance (e.g. Margin Probe); Mass Spectrometry (e.g.iKnife, Waters)..... 44

Figure 1.7 Representation of the mobile units of a micro-CT and MRI system used for intraoperative assessment of an excised specimen, and the corresponding images acquired. (A) Micro-CT tomography system used to image a specimen with invasive ductal cancer, with the red arrow highlighting disease at the posterior margin. (B) Micro-CT image of a specimen containing ductal carcinoma in-situ, with evidence of calcifications at the edge of the specimen highlighted by the red arrow. (C) A freshly excised specimen inked with pathology ink and the white squares depict the areas scanned by the MRI system. (D) Following image processing the MRI system highlights which areas have disease (purple squares) and those with normal breast tissue (blue/black squares).....45

Figure 1.8 Representation of handheld devices used for photoacoustic imaging and Raman spectroscopy and the corresponding images produced from these devices. (A) The ultrasonic transducer once placed onto breast tissue produces a image which here shows a hypoechoic mass with irregular edges which relates to a tumour. (B) A corresponding photoacoustic image of the same area highlights as red which represents vessels feeding the tumour. (C) A Raman spectroscopy probe produces raw Raman spectra to help distinguish between normal (purple) and malignant (green) breast tissue. Each peak relates to a specific molecular vibrational bond. 47

Figure 1.9 Representation of MarginProbe and mass spectrometry devices as would be used in the intraoperative setting, and the corresponding images produced to help guide a surgeon about margin pathology. (A) The MarginProbe device identifies cellular changes associated with cancer and this is reflected in electrical properties. These signals are captured and compared to known tissue signatures to help distinguish between healthy or malignant breast tissue and produces red (cancer) or blue (healthy tissue) bars on a chart. (B) Following electrosurgical cautery during dissection of breast tissue, the aerosol produced represents release of cellular content to a gas phase. This gas is transferred via plastic tubing to a mass spectrometry machine which performs mass spectrometric chemical analysis, and machine learning helps to differentiate the chemical differences between tissue types. The graph represents mean spectral intensities of metabolites. Molecules are assessed by measuring the mass-to-charge ratio (m/z) of molecular ions within the aerosol.....49

Figure 1.10 Schematic to highlight key characteristics of any future intraoperative margin assessment tool (IMA) for breast conserving surgery. Features that should be exhibited include speed of use to fit into surgical workflow; the ability to scan a whole resection surface of an excised specimen; a tool that can visualise beyond the surface of the specimen; breast tissue and patients are heterogeneous, an ideal IMA tool must account for this; the surgeon should be able to use the tool by themselves and not rely on other trained staff; the best IMA tool must be accurate in discriminating between normal and malignant breast tissue; the IMA tool should have ease of function and not occupy too much room in the operating theatre.....51

Figure 2.1 Schematic showing the different processes light undergoes when it interacts with breast tissue. (1) Specular reflection is when light reflects at an equal but opposite angle to the incident light ray. (2) Scattering is a phenomenon that occurs when incident light interacts with the ultrastructures of tissue and is caused by variations in the refractive index. (3) In breast tissue light is absorbed by

molecules called chromophores, namely water and β-carotene. (4) Light is also absorbed by haemoglobin (both oxygenated and deoxygenated forms) which are found in blood vessels. (5) Diffuse reflection is defined by how an incident light ray is reflected at many different angles from the tissue surface. (6) Fluorescence is where incident light is absorbed by molecules called 'fluorophores' and re-emitted at a different wavelength. Relevant fluorophores in breast are nicotinamide adenine dinucleotide and hydrogen, flavin adenine dinucleotide, collagen, elastin and tryptophan and lipo-pigments. (Image created using Biorender.com software).....54

Figure 2.2 Diagram illustrating the way in which the direction of light changes with reflection and refraction when an incident light ray hits breast tissue. With reflection the light hits the breast tissue surface and is reflected into the air in a different direction. Comparatively, with refraction the incident light ray passes through breast tissue and changes speed and direction. 55

Figure 2.3 Schematic of the three imaging categories; (a) diffuse reflectance spectroscopy, (b) multispectral/hyperspectral imaging; (c) spatial frequency domain imaging. (A) With diffuse reflectance spectroscopy a probe is applied to a tissue sample. The probe delivers light to tissue in one fibre, and in different fibres collects diffusely reflected light which is measured by a spectrometer. (B) Multispectral or hyperspectral imaging systems capture light reflected from a tissue sample via a lens, which has been illuminated with light from an external source. The spectral filtering component selectively disperses light according to its wavelength onto a charged couple device (CCD), which breaks the two-dimensional image elements into pixels. Each pixel (depicted by a red square) represents a spectral band of the electromagnetic spectrum. A three-dimensional data cube is generated which has spatial and spectral coordinates. (C) With spatial frequency domain imaging systems, a projector illuminates the target tissue area with a two-dimensional light pattern composed of various frequency modulations of a sinusoidal wave. The reflectance pattern of this sinusoidal patten is captured by the camera lens. The CCD component picks up the emitted diffuse light, which then undergoes demodulation by a computer to extract diffuse reflectance. Demodulation is a process that calculates amplitude modulation for every pixel of the image. Optical properties per pixel are extracted using light propagation models. 59

Figure 2.4 Illustration of a 'hypercube' produced from a spectral imaging data set. Each two dimensional small square (x,y) represents a pixel. Each three dimensional small square represents a spectral image (x,y,λ). A hypercube can be interpreted as an image (x,y) at each wavelength (λ), or as a spectrum at every pixel (x,y). (Modified from Garini *et al*.[148]).....62

Figure 2.5 Inclusion and exclusion criteria used to screen abstracts.....64

Figure 2.6 Studies were divided into probe-based (point based) or imaging-based studies (whole field-of-view). Within these groups further subdivisions occurred. Probe-based studies were divided dependent on the type of modality described in studies: diffuse reflectance spectroscopy (DRS) or DRS combined with intrinsic fluorescence spectroscopy, that is the probe system relies on the inherent fluorescent properties of breast tissue rather than when exogenous agents are given.

Imaging based studies where subcategorized depending on the type of hardware components used: multi/hyperspectral imaging or spatial frequency domain imaging. 65

Figure 2.7 PRISMA flowchart highlighting the study selection process. Following electronic searches on Medline, Embase and Scopus 3614 studies were identified. 2850 abstracts were screened using the inclusion and exclusion criteria, from which 54 studies were then read in full text. 19 studies were utilized for final meta-analysis. 67

Figure 2.8 Schematic to show the patient related factors and tumour related factors that influence breast cancer heterogeneity. 72

Figure 2.9 (a) Forest plot of the probe-based studies category where a fixed-model analysis provided a pooled sensitivity of 0.84, lower limit at 0.78 and upper limit at 0.89. b) Forest plot of the probe-based studies category where a fixed-model analysis provided a pooled specificity of 0.85, lower limit at 0.79 and upper limit at 0.91. (c) Forest plot of the image-based studies category where a fixed-model analysis provided a pooled sensitivity of 0.90, lower limit at 0.76 and upper limit at 1.03. (d) Forest plot of the image-based studies category where a fixed-model analysis provided a pooled specificity of 0.92, lower limit at 0.78 and upper limit at 1.06. 79

Figure 2.10 Conventional or traditional intraoperative margin assessment techniques are compared to emerging techniques in terms of sensitivity and specificity. 81

Figure 3.1 Schematic to show orientation of a wide local excision specimen following breast conserving surgery from the left breast of a patient, where the anterior and lateral aspects of the tumour are close to the surface of the specimen. The brown area represents healthy tissue, and yellow represents cancer cells. (A) If an intraoperative margin assessment tool utilising tissue optics is applied to the anterior surface of the specimen it should be able to discriminate between the healthy and tumour border, spatial resolution. A 1 – 2mm spatial resolution is possible between different tissue types. (B) Visible light of the electromagnetic spectrum covers a range of wavelengths from 380 to 750 nm. Incident light separated into different wavelengths represents different colours represented by the vertical arrows. Here if a IMA tool is applied to the lateral surface of the excised specimen, light should be able to penetrate deep enough to identify cancer cells. Any real-time feedback to the surgeon in theatre would be useful to help guide them to know where to take further tissue to prevent re-excision surgery. 87

Figure 3.2 PRISMA diagram depicting how final studies for review were selected. Following the described search strategy on Medline and Embase, 2644 studies were identified and a further 45 were found from cross-referencing. Following removal of duplicates, 1846 study abstracts were screened by myself and Ahmed Ezzat. 69 full articles were reviewed, and data demographic data and outcome measures (OR, RR and HR) was extracted from 43 studies. 95

Figure 3.3 PRISMA diagram depicting how final studies for review were selected. Following the described search strategy on Medline and Embase, 2644 studies were identified and a further 12 were found from cross-referencing. Following screening of 1801 of abstracts, 36 studies underwent full text

review and five of these were excluded to leave 31 studies where data was extracted for outcome measures (OR, RR and HR) and demographic data. 98

Figure 3.4 Forest Plot showing pooled results for different performance metrics of local recurrence of different margin comparisons for invasive breast cancer (A) Forest plot for pooled odds ratio (B) Forest plot for pooled odds ratio where sensitivity analysis performed (C) Forest plot for pooled relative risk (D) Forest plot for pooled relative risk where sensitivity analysis performed (E) Forest plot for pooled hazards ratio. 103

Figure 3.5 Forest Plot showing pooled results for different performance metrics of local recurrence of different margin comparisons in patients who had DCIS. (A) Forest plot for pooled odds ratio (B) Forest plot for pooled relative risk (C & D) Forest plot for pooled relative risk where adjustment has been made for boost radiotherapy (E) Forest plot for pooled hazards ratio. 106

Figure 4.1 Schematic showing principal components of a spectrometer. A light source (commonly a tungsten halogen, laser emitting diode or xenon arc) emits light which passes through a slit, and the size of the slit determines the amount of light the spectrometer measures and influences optical resolution. Once the light hits a collimating mirror. The collimated light rays fall onto a diffraction grating which disperses light into its constituent wavelengths. Light spectra are captured by a detector which measures the intensity of light as a function of wavelength, and the information is digitized into spectral graphs. 116

Figure 4.2 DRS-IFS experimental setup: a) Schematic of the components of the custom-built probe system illustrating two lamps (Lamp 1 (L1) and Lamp 2 (L2)) which deliver light in the wavelength range 360 – 2400nm; two laser diodes delivering light at wavelengths 375nm and 405nm for fluorescence excitation; two spectrometers detecting spectra in the wavelength range 400 – 1100nm. (b) Photographic illustration of myself in the laboratory with the spectroscopy probe set up with all components in situ. (c) Diagram of fibre configuration, where L1 and L2 are the fibres connected to the broadband DRS light sources, D1 and D2 are the fibres connected to laser diodes 405 nm and 375 nm, Sp1 and Sp2 are the fibres connected to spectrometer 1 (DRS and IFS) and spectrometer 2 (DRS) (d) DRS-IFS multifiber probe distal tip, inset –photograph of the fibre configuration (e) Sample holder and fibre optic probe with tissue sample. 120

Figure 4.3 Acquisition of DRS and LIFS spectra: a) Lamp 1 is on and SDR spectra with source-detector separations 0.5 mm and 2.8 mm are registered; b) Lamp 2 is on and SDR spectra with source-detector separations 0.8 mm and 1.8 mm are detected; laser diode with wavelength c) 375 nm or d) 405 nm is on and IFS spectrum is recorded. 121

Figure 4.4 (a) Macroscopic photograph of breast tissue sample interrogated with our DRS-IFS system. (b) Corresponding histopathology slide image following review by an experienced consultant pathologist identified invasive lobular cancer. (c) Macroscopic photograph of a further breast tissue sample with normal breast tissue appearances. (d) Corresponding histopathology slide identifying healthy breast tissue. 123

Figure 4.5 Schematic to summarise the processing of spectral data. This was conducted in two phases – pre-processing followed by classification. 1) Pre-processing of spectral data is performed to account for inter-sample, background light, and signal quality variability. DRS spectra integration time was normalised. A Savitzky-Golay filter was used to smooth the data and remove noise. Similar technique was done for fluorescent spectra, but to account for variability in laser power the fluorescent spectrum of normal and malignant tissues was scaled by multiplying the scale ratio. Three types of features were extracted from the raw spectra namely Fixed Window Features, Peak Valley Features and Peak Valley Slope Features. Feature selection using Boruta was performed on DRS and fluorescent spectra to reduce dimensionality of data and improve accuracy. 2) The spectral data was subdivided into six different subsets for binary classification from each of the six channels as follows: healthy vs. invasive ductal cancer (IDC); healthy vs. invasive lobular cancer (ILC); healthy vs. ductal carcinoma in-situ (DCIS); healthy vs. pathological complete response (PCR); healthy vs. invasive cancer (IDC and ILC); healthy vs. all cancer (IDC and ILC and DCIS). Binary classification was carried out on multiple channel combinations. Utilising DRS08, DRS28 and fl405 channels were deemed to produce the best overall results and the channel combinations presented in the results section. 124

Figure 4.6 Graph depicting "peaks" and "valleys" acquired from spectral data, which represent the intensity of light at different wavelengths. This graph is an example of one diffuse reflectance channel only. A "peak" represents a point where the intensity of reflectance or fluorescence light is at its highest for a particular wavelength. A "valley" depicts a point where the intensity of reflectance of fluorescence is at its lowest between two adjacent peaks. The different colours represent the different tissue types interrogated in this experimental work (blue = healthy breast tissue, red = invasive ductal carcinoma, green = invasive lobular cancer, yellow = ductal carcinoma in-situ, purple = pathological complete response). 127

Figure 4.7 Confusion matrix schematic where each row represents the actual class of the tissue histological subtypes in relevance to this thesis, and each column represents the predicted tissue histological subtype [325]. 133

Figure 4.8 Bar chart comparing performance metrics (accuracy, sensitivity, specificity and AUC) for all healthy tissue samples when compared to all malignant tissue samples (IDC & ILC & DCIS). For each performance metric comparison results are represented for GB classifier and XGB classifier with the vertical error bars representing standard deviations. 136

Figure 4.9 Bar chart comparing performance metrics (accuracy, sensitivity, specificity and AUC) for quality three healthy tissue samples when compared to quality three malignant tissue samples (IDC & ILC & DCIS). For each performance metric comparison results are represented for GB classifier and XGB classifier with the vertical error bars representing standard deviations..... 137

Figure 4.10 Bar chart depicting performance metrics for intertumour comparisons for all tissue samples (quality 1 to 3) when gradient boost classifier was applied. The vertical bars represent standard deviations. 140

Figure 4.11 Bar chart depicting performance metrics for intertumour comparisons for all tissue samples (quality 1 to 3) when extreme gradient boost classifier was applied. The vertical bars represent standard deviations. 140

Figure 4.12 Spectral graph for mean spectra of DRS08 channel. With DRS08 channel, the three main peaks identified were at 525, 560 and 625nm respectively. The troughs were identified at 540 and 580nm. (norm - normal breast tissue; IDC – invasive ductal cancer; ILC – invasive lobular cancer; DCIS – ductal carcinoma in situ; PCR – pathological complete response). 141

Figure 4.13 Spectral graph for mean spectra of DRS28 channel. With DRS28, the main peak was identified at 560nm and the main trough at 575nm. (norm - normal breast tissue; IDC – invasive ductal cancer; ILC – invasive lobular cancer; DCIS – ductal carcinoma in situ; PCR – pathological complete response). 142

Figure 4.14 Spectral graph for mean spectra of fl405nm channel. The main peak occurred at 475 nm. Mean spectra for the different tissue classes in the three different channels used for analysis a) Diffuse reflectance 08 b) Diffuse reflectance 28 c) Fluorescence at excitation wavelength 405 nm. (norm - normal breast tissue; IDC – invasive ductal cancer; ILC – invasive lobular cancer; DCIS – ductal carcinoma in situ; PCR – pathological complete response). 142

Figure 4.15 Confusion matrix comparing gradient boost classifier and extreme gradient boost classifier on healthy tissue samples versus all tumour samples (IDC & ILC & DCIS) on quality three samples. 143

Figure 4.16 Confusion matrix comparing gradient boost classifier and extreme gradient boost classifier on healthy tissue samples versus all tumour samples (IDC & ILC & DCIS) on all tissue samples irrespective of quality score. 143

Figure 5.1 Schematic of the MSI imaging principles highlighting how when biological tissue is illuminated by light, the diffusely reflected light is received by the camera system and is converted into an electronic signal for computational analysis. (A) Upon tissue illumination the incident light (i) can be reflected from the surface yielding the specular reflection (ii), or refracted inside the tissue, where it can undergo scattering (iii) from scatterers or absorption (iv) from chromophores and re-emerge from the surface as diffusely reflected light (v) to be captured by the MSI system. (B) Lens has a specific field of view and spectral filtering decomposes the captured light into its spectral components (colours). (C) There are two camera systems (CMOS) and RGB (D) 3D-multicube encompassing spatial and spectral information. The illustration demonstrates the capability of MSI to capture a spectral signature (values at different colour bands) for each pixel in the MSI image. 154

Figure 5.2 Experimental setup for the acquisition of multispectral and colour images. (A) schematic diagram, (B) image acquisition in the operation theatre, (C) MSI camera consists of (1) zoom lens, (2) beamsplitter, (3) relay lens, (4) multispectral camera with spinning filter wheel, (5) colour camera. (D) Screenshot of software interface with monochromatic image at 600 nm band (1), colour image for visualisation and focus control (2) and 7 monochrome images at the rest of the spectral bands (3). 156

Figure 5.3 (A) Absorption spectra of the typical breast light absorbers: fat [373], oxygenated haemoglobin [374], deoxygenated haemoglobin [374]. Tabulated data were obtained from the Oregon Medical Laser Centre site. (B) Emission spectrum of the Asahi Spectra Max-303 Xe lamp (our data) and installed in the bandpass filters (Salvo Coatings, USA [375]). In the legend for each filter, the central wavelength is presented with the "Full width half maximum" (FWHM). 159

Figure 5.4 Original software interface produced for data collection by the MSI camera. The left hand section (red box) is where information is selected to ensure data is stored in the correct folders. The right upper section (blue box) shows the 8 different MSI images collected for each data acquisition. The bottom right box (green box) was the colour (RGB) image acquired during data acquisition. This was not "user friendly" as all images were not on one page, and the user has to repeatedly scroll down to see the RGB image and adjust acquisition time. 160

Figure 5.5 Final software interface utilised for data acquisition. All relevant areas that need to be identified or adjusted by the user now all present on the same page without requirement for scrolling down the page. The left-hand section (red box) shows all necessary icons to ensure the correct folders for storage of images are selected. The central section (blue box) shows the eight images captured on image acquisition – the multispectral images. The right-hand section (green box) illustrates the colour (RGB) image captured simultaneously. 161

Figure 5.6 (A) Photograph of the experimental set up of the MSI camera in the laboratory imaging the anterior surface of a thawed breast tissue sample. 1-light ring of MSI camera 15 cm away from sample holder; 2-black sample holder; 3-tissue laid onto black cloth to absorb fluid as excess fluid causes increased reflectance; 4-tissue sample reference number (B) A cylindrical cover was place over the sample to allow the MSI light source to illuminate the sample but to prevent ambient room light affecting the images. The distance from light ring to sample holder was 15 cm. 164

Figure 5.7 Example of the images acquired from data acquisition from the anterior aspect of one freshly frozen tissue sample previously stored in Imperial College London Tissue Bank. The anterior surface imaged here has a separate MSI image from each filter (F1-8) which represents a particular wavelength of light from the visible and NIR spectrum. In the "F1" image in the bottom left hand corned there is a scale which represents 1 cm. 165

Figure 5.8 For each tissue sample that is imaged, each experiment involved the acquisition of the following further four images (clockwise) colour (red-green-blue) image of the freshly frozen tissue sample with a scale bar shown in the top left hand corner representing 1 cm (here the anterior surface of the same tissue sample from figure 5.7); a white reference image; a black reference image – the light source turned off; and an image of a crosshair target. 165

Figure 5.9 (A) Photograph of equipment used for image acquisition of a freshly excised wide local excision in the operating theatre. 1- wide local excision specimen marked with orientation sutures by the surgeon placed onto a black cassette, 2- cylindrical device to block ambient light placed over specimen at time of data acquisition to block out ambient light, 3- crosshair target and 'white' reference tool used for scale and 'white' reference image. (B) Photographic illustration depicting

data acquisition in the operating theatre with a working distance of 30 cm from light ring to specimen holder. 167
Figure 5.10 Colour RGB) images of each resection surface of a wide local excision specimen excised from the right breast of a cancer patient. This specimen is marked with a short superior suture with one staple, a long lateral suture with two staples, and one looped suture emphasising the anterior aspect of the specimen. Each resection surface has been imaged in this specimen. 167
Figure 5.11 Photograph of a sliced wide local excision specimen following being inked on each resection surface with a different colour. The specimen was then "breadloafed" into individual slices. Here a tumour is noted as a white coloured mass within the slices. 169
Figure 5.12 Illustration of the ground truth extraction process based on the H&E staining. (A) A scanned H&E slide was marked with the regions of interest (the blue segmentation is adipose tissue, and the pink segmentation is lobular cancer) using GIMP software (B) the corresponding multispectral image was marked for the regions of interest after scaling and alignment with the marked H&E image for mask extraction. 170
Figure 5.13 Schematic to illustrate how a multispectral was marked to show areas of healthy tissue and regions of interest (i.e., tumour) to create masks for spectral analysis. This example shows a case where the tumour is less than 1 mm from the anterior surface. (A) X-ray image of a BCS specimen from a patient. The specimen has been orientated by the surgeon intraoperatively, one clip to represent superior aspect of the specimen, two clips to represent lateral aspect of the specimen. (B) MSI image marked for the tumour (green) and healthy margins (orange). (C) RGB image of the specimen for reference. 171
Figure 5.14 Schematic highlighting the sequential steps involved in pre-processing of multispectral images. 171
Figure 5.15 Graph showing a 2D representation of several separation hyperplanes that separate the input data set well. There are many potential hyperplanes that could separate the data. (Modified from Cervantes *et al*. 2020 [391]). 176
Figure 5.16 Examples of colourmaps produced from two different multispectral images. Colourmaps are classification overlays that depict the probability of tumour within 3mm of the resection surface. As seen in the far right images, the colour gradient represents likelihood of tumour and normal tissue (blue). The corresponding marked multispectral image for ground truth marking is also presented (the area within the centrally marked area depicts known tumour, and area outside the most peripherally marked area represents healthy breast tissue). 178
Figure 6.1 Illustration of metabolic pathways of 5-aminolevulinic acid (5-ALA) and mechanism of protoporphyrin IX (PpIX) accumulation in a cancer cell, which relies on multiple enzymatic reactions. Production of PpIX increases with increased activity of the following enzymes as represented by the green arrows: ATP-binding cassette subfamily B member (ALAD) , hydroxymethylbilane synthase (HMBS) and uroporphyrinogen decarboxylase (UROD). Decreased activity of ferrochelatase (FECH) and ATP-binding cassette subfamily G member 2 (ABCG2) as represented by the red arrows, causes PpIX

to accumulate by limiting conversion to haem. This image was reproduced and modified with permission of the author [418]. 198

Figure 6.2 GLOW camera (fluorescence imaging camera) set up. (A) Lens system which collects visible and fluorescence (B) A beamsplitter which splits light into two beams. (C) Fluorescence is transmitted through a bandpass filter to (D) monochrome camera and (E) colour images are captured in a RBG camera. Reproduced with permission from Dr M Kedzycki [429]..... 202

Figure 6.3 Series of images highlighting what the fluorescence guided camera produces for the posterior aspect of the same specimen, and how images are marked. (A) Colour image produced by FGS (B) Laser produces two points, distance between these two points measures a fixed distance of 3.2cm. With GIMP, the distance between these two points is measured in pixels and divided by 3.2cm and is correlated with margins distances given on the histology report (C) The monochrome camera of the FGS system produces an image. (D) The green circle represents the final marked image highlighting disease. 204

Figure 6.4 Box and whisker plots depicting comparative sensitivity (p = 0.049) results for ALA (filter 8) vs MSI vs ICG (angiography cohort) vs ICG (EPR cohort) vs ALA (filter 7). 208

Figure 6.5 Box and whisker plots depicting comparative specificity (p = 0.0278) results for ALA (filter 8) vs MSI vs ICG (angiography cohort) vs ICG (EPR cohort) vs ALA (filter 7). 209

Figure 6.6 Box and whisker plots depicting comparative accuracy (p = 0.0014) results for ALA (filter 8) vs MSI vs ICG (angiography cohort) vs ICG (EPR cohort) vs ALA (filter 7). 209

List of Abbreviations

5-ALA	5-aminolevuinic acid
ABS	Association of Breast Surgery
AIDEP	Atypical intraductal epithelial proliferation
AJCC	American Joint Committee on Cancer
ASTRO	American Society of Radiation Oncology
AUC	Area under the curve
BCS	Breast conserving surgery
BMI	Body mass index
CCD	Charged couple device
CI	Confidence Interval
CMS	Cavity margin shave
CT	Computed tomography
CV	Cross-validation
DCIS	Ductal carcinoma in-situ
DRS	Diffuse reflectance spectroscopy
DRS-IFS	Diffuse reflectance spectroscopy combined with intrinsic fluorescence spectroscopy
EPR	Enhanced permeability and retention
ER	Oestrogen receptor
FAD	Flavin adenine dinucleotide
FEA	Flat epithelial atypia
FGS	Fluorescence guided surgery
GB	Gradient boosting
GIRFT	Getting It Right First Time
H&E	Haematoxylin and eosin
HER2	Human epidermal growth factor receptor 2
HR	Hazard ratio
HSI	Hyperspectral imaging
ICG	Indocyanine green
IDC	Invasive ductal cancer
IHC	Immunohistochemistry
ILC	Invasive lobular carcinoma
IMA	Intraoperative margin assessment

IR	Infrared
LDA	Linear discriminant analysis
LED	Light emitting diode
LR	Local recurrence
MDT	Multidisciplinary Team
MeSH	Medical subject headings
MFP	Mean free path
Micro-CT	Miro-computed tomography
MLP	Multilayer Perceptron
MRI	Magnetic Resonance Imaging
MSI	Multispectral imaging
NACT	Neoadjuvant chemotherapy
NADH	Nicotinamide adenine dinucleotide and hydrogen
NHS	National Health Service
NIRF	Near infrared range
NOS	No special type/Not otherwsie specified
OR	Odds ratio
pCR	pathological complete response
PpIX	Protoporphyrin IX
PR	Progesterone receptor
PRISMA	Preferred Reporting Items for Systematic Reviews and Meta-analyses
REIMS	Rapid evaporative ionization mass spectrometry
RGB	Red-green-blue
ROC	Receiver operating characteristics
RR	Relative risk
SFDI	Spatial frequency domain imaging
SLNB	Sentinel lymph node biopsy
SR	Specimen radiography
SSO	Surgical Society of Oncology
SVM	Support vector machines
TNM	Tumour, Node, Metastasis
UICC	Union for International Cancer Control
UV-VIS	Ultraviolet and visible wavelength

VAB	Vacuum-assisted biopsy
XGB	Extreme gradient classifier

Chapter 1: Background to Breast Cancer and Current Clinical Problem

1.1 Breast Cancer Incidence

Breast cancer represents a significant global health challenge, being the most prevalent cancer worldwide. In 2020, 2.26 million women were diagnosed with breast cancer [1] and 685,000 deaths were associated globally [2]. Breast cancer transcends socio-economic status and is seen in every country globally. In the United Kingdom, approximately 56,000 invasive cancer [3] and 8,000 cases of in-situ, non-invasive breast cancer are diagnosed each year [4]. In 2020, in England, 40,000 new breast cancer cases diagnoses were made, which accounts for 28% of all new cancer diagnoses [5].

1.2 Evolution of Breast Cancer Management

Historically, the earliest documentation of breast cancer dates back three thousand years in the Egyptian papyrus [6]. However, it was not until the second century AD that the term ‘mastectomy’ was coined [7]. Mastectomy is defined as the surgical removal of all, or part of the breast. Until the nineteenth century, mastectomy procedures were aggressive and brutal in nature, occurring in a period before the advent of anaesthesia and antisepsis [7].

In 1894, William Halsted published a paper detailing his concept of the ‘radical mastectomy’, in which the whole breast, underlying pectoralis muscle and ipsilateral axillary contents were removed [8]. This paper impacted surgical practice worldwide from here on. Radical mastectomy became the standard of care for patients with breast cancer for decades. However, with time the radical mastectomy was met with criticism due to significant intraoperative blood loss and deformity leading to poor cosmesis [9]. In the early 1930s, D.H Patey introduced the ‘modified radical

mastectomy', where he spared the pectoralis muscle as this was believed not to add further survival benefit [10].

Over the past three decades there has been a transition in the surgical approach to breast cancer, from radical mastectomy to breast conserving surgery (BCS). BCS is defined as an oncological procedure with three primary aims. Firstly, to achieve oncological control, by removing all cancer with adequate margins; secondly, to preserve the breast aesthetic; and lastly, to enable survival to be equivalent to that of the traditional mastectomy. This transition has occurred via a systematic and evidence-based de-escalation process through landmark trials [11-16]. These trials have established that there is no difference in overall and disease free-survival between BCS and mastectomy [11-16]. The trials identified that the use of adjuvant radiotherapy after BCS is crucial with respect to control and survival rates. More recently, a large prospective cohort study suggests that BCS and radiotherapy may yield better survival than mastectomy alone [17].

Breast cancer management has evolved to become multifaceted, rather than surgical intervention alone. Apart from surgery with or without radiotherapy, breast cancer patients can also be treated with chemotherapy, endocrine treatment, immunotherapy or targeted therapies [18, 19]. A more recent focus on survivorship allows for a transition of care from disease management to the maintenance of the health and well-being of patients [19]. Particular therapies, namely chemotherapy, endocrine treatment and targeted therapy, can be given either in the neoadjuvant setting (pre-operatively) or adjuvant setting (post-operatively) [20]. Neoadjuvant systemic therapies not only serve the purpose of allowing reduction in breast cancer size to facilitate BCS, but also facilitate precision medicine by assessing the response to neoadjuvant therapy to predict outcomes and select the optimal adjuvant therapy [21]. Adjuvant systemic therapies aim to improve disease free survival and overall survival by treating latent micrometastases [21]. This transformation has been achievable with better knowledge of molecular and genetic pathways driving breast cancer [22]. This knowledge has facilitated precision medicine, including a more targeted approach in the neoadjuvant and adjuvant setting, with assessment tools for prognosis and prediction of treatment benefit also now available [23].

1.3 Margins in Breast Cancer

The issue of margins is critical for oncological control in BCS. During BCS, the surgeon aims to remove the cancer with a rim or border of normal healthy breast tissue surrounding it. This border zone around the tumour is defined as the surgical “margin”. A pathologist evaluates this specimen to determine the distance between the edge of disease to the resection margin, this distance is referred to as the margin width (Figure 1.1). Margin width is established by the pathologist measuring the distance from the outer edge of cancer cells to the edge of normal tissue that was excised. Based on the resection margin width, the adequacy of the resection is categorised as either “negative” (clear); “close” or “positive” (involved). Negative margins contain no cancer cells at the outer inked edge of the tissue. A positive margin is defined by cancer cells or tumour that extends to the edge of the sample (Figure 1.1). A close margin is where there are cancer cells close to, but do not touch, the rim of healthy tissue that is free of cancer.

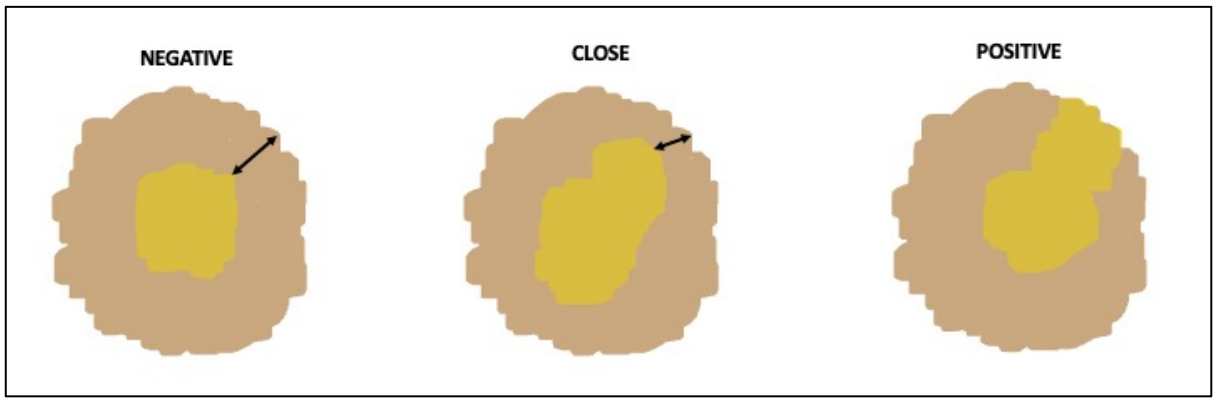


Figure 1.1 Diagram to illustrate the difference between negative, close and positive margins. The black arrow in the ‘negative’ and ‘close’ images depicts how a pathologist measures the margin width from the outer aspect of cancer cells to the outer edge of the healthy tissue excised by a surgeon. A ‘negative’ margin contains no cancer cells at the outer edge of the inked specimen. A ‘positive’ margin has cancer cells that extend to the edge of the specimen, but a ‘close’ margin is any distance between negative or positive margins.

1.3.1 Margin width practice

Margin width dimensions in breast surgical practice in the United Kingdom vary between non-invasive breast cancer and invasive breast cancer. For non-invasive disease, namely ductal carcinoma in situ (DCIS), the negative margin width recommended by the National Institute of Clinical Excellence (NICE NG101) is two millimetres [24]. However, with invasive breast cancer, NICE advise to achieve a negative margin width of one millimetre. Chapter three of this thesis will discuss in more detail the international variation in margin width guidance, and how variation in negative, close or positive margins can affect local recurrence rates.

1.3.2 Factors influencing positive margins

There are several known predictors of positive margins in BCS which can be categorised into either clinical or pathological factors, as depicted in Figure 1.2. Clinical factors which lead to risk of a positive margin include larger tumour size, multifocality of disease, increased breast density, presence of mammographic microcalcifications and pre-operative localisation of impalpable tumours. In a large population-based cohort study, in which 25,311 patients who underwent BCS were assessed it was identified that larger tumours, described as over 5cm had a higher risk of a positive margin (odds ratio (OR) 6.31, 95% confidence interval (CI) 4.54 – 8.77) compared to those between 2 to 5cm (OR 1.78, 95% CI 1.65 – 1.92) [25]. Multifocal tumours are described as tumours located within the same breast quadrant, which have resulted from a single cell tumour cell clone spreading within the ductal or lobular complexes. Multifocality has been shown to have a threefold increase in the risk of positive margins (OR 3.25; 95% CI 2.68 – 3.95) [25]. Breast density refers to the mammographic density of the breast correlating to the amount of radiodense fibroglandular tissue that exists, and can increase the risk of breast cancer four-fold [26]. Breast density is also a predictor of a positive margin, with those with the most dense breasts having an increased odds for re-excision surgery (OR 3.2, 95% CI 1.2 – 11) [27]. Calcifications, which present on mammograms as white opaque markings in a variety of distributions and morphologic patterns, and represent calcium deposits

also increase risk of positive margins. Specifically, the detection of calcifications increases the odds for re-excision surgery approximately two-fold (OR 2.14, 95% CI 1.22 – 3.77) [28].

Pre-operative localization of impalpable breast tumours involves radiological insertion of a tumour guidance system, which is performed by a radiologist [29], and post-insertion imaging is then performed to confirm accurate placement. The surgeon then assesses tumour size and localization on imaging prior to surgery, and once they locate the tumour epicentre during surgery, they aim to remove a healthy rim of tissue around the lesion. The surgeon is predicting how wide this healthy rim should be, and therefore there is an element of imprecision here as the surgeon cannot directly visualise the healthy-cancer tissue interface. There are several categories of tumour localization systems to identify the epicentre of a tumour, wire guided localization or wire-free, with the latter further being divided into radioactive or non-radioactive techniques.

Wires are inserted via a needle under radiological guidance and are deployed with a hook within or near the lesion [30]. Wires can dislodge or migrate following insertion [31]. Radioactive wire free localization techniques are radioactive occult lesion (ROLL) or radioactive seed localisation (RSL). ROLL utilises a radioactive tracer which is injected into a lesion under radiological guidance, whereas RSL involves inserting a radioactive iodine seed into a cancer which emits low-energy gamma radiation, and a handheld gamma probe is used by the surgeon to detect emitted radiation from ROLL or RSL during surgery [32, 33]. Advantages of these radioactive techniques is that they do not cause discomfort to the patient and that they have less involved surgical margins than wire localizations [34]. Non-radioactive localization techniques are more popular, and include a ferromagnetic seed (Magseed®; Endomag, Cambridge, UK), or a reflector to electromagnetic radar signals (SAVI SCOUT®; Meritmedical, South Jordan, UT, USA) [31, 35, 36] which are also placed into the tumour under radiological guidance. *Shirazi et al.* performed a meta-analysis to compare the pooled re-excision rates following wire and non-wire localisation techniques, identifying ROLL was 12.6%, wire 20.8%, Magseed 13.4% and SAVISCOUT was 8.6%. Despite variety in localization techniques, there remains imprecision in identifying the tumour-healthy interface for surgeons leading to positive margins [30].

Pathological features that increase the risk of incurring a positive margin are DCIS, lobular histology, higher tumour grade, lymphovascular invasion, and extensive intraductal component. Breast tissue is composed of epithelial elements, namely lobules and ducts, but also stromal elements which surrounds these structures consisting of adipose and fibroconnective tissue with neurovascular components. DCIS is described as malignant cells within the ductal lumen, but have not invaded the basement membrane of the ductal lining [37]. DCIS is a strong predictor for re-excision surgery, whether it is present alone (OR 2.71, 95% CI 2.29 – 3.22), or present with invasive disease (relative risk (RR) 8.76; 95% CI 6.64 – 11.56) [25]. Lobular breast cancer is characterized microscopically by small discohesive tumour cells with scanty cytoplasm and monomorphic nuclei, found in single lines due to a lack of a cohesive cell-adhesion protein [38]. These features mean lobular cancer is detected less on mammograms, is more multifocal and is a risk factor for re-excision surgery (OR 2.79, 95% CI 2.38 – 3.28) [25, 38]. All breast cancers are graded from one to three using the Bloom-Richardson system, taking into account nuclear pleomorphism, mitotic count and the amount of tubule formation, and reflects how abnormal the cancer cells appear under the microscope in comparison to normal cells [39]. Grade two (OR 1.38, 95% CI 1.27 – 1.51) and three (OR 1.32, 95% CI 1.19 – 1.46) tumours are associated with a higher risk of a positive margin [25]. Lymphovascular invasion is defined as the presence of tumour cells within either lymphatic or vascular endothelial lined spaces, and is known to increase the risk of metastasis [40] and positive margins (OR 1.63, 95% CI 1.33 – 2.01) [25].

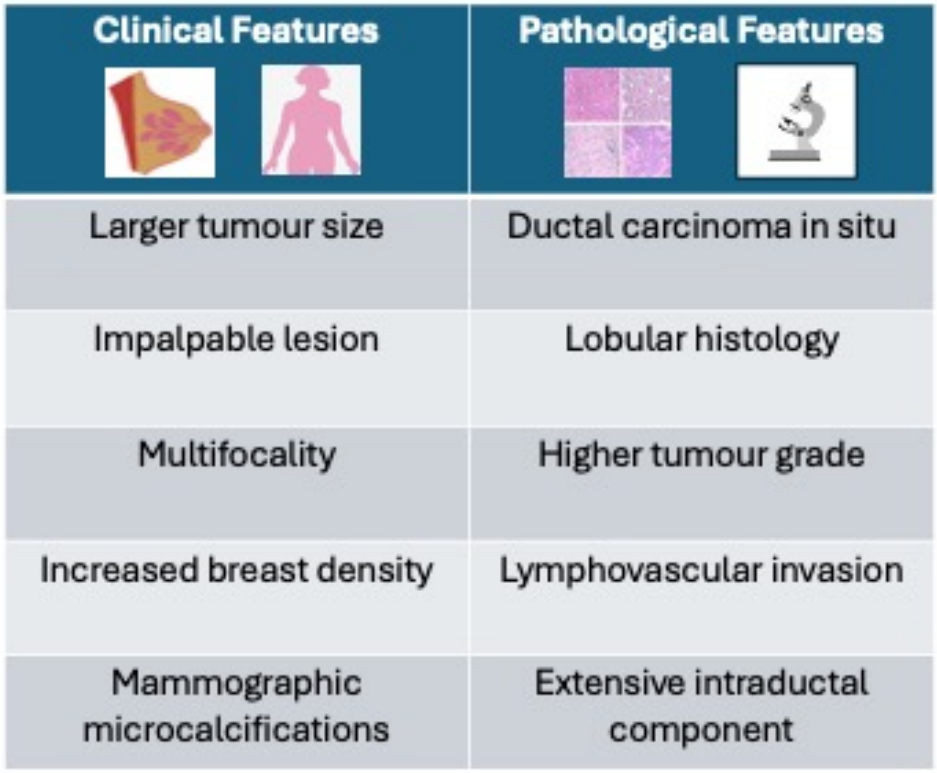


Figure 1.2 Table highlighting clinicopathological features which contribute to positive margins.

1.4 Re-excision Surgery

Where patients are found to have residual cancer cells in their excised specimen (i.e. positive or close margins) it has long been recommended that they undergo further surgery. This surgery is either re-excision of margins whereby the previous tumour cavity is identified, and a further rim of tissue is excised from the relevant margin, or completion mastectomy. It is known that residual disease increases the risk of local recurrence [41-43].

It is important to note that in patients with positive or close margins who undergo re-excision surgery, there is still an issue of disease persistence within the re-excised margin. Various studies have explored disease persistence at the newly excised margin, and rates of persistent disease ranged from 25.8% to 65%, with clinicopathological variables contributing [44-46]. This indicates there is a clinical need to have techniques that can improve the precision of disease detection within the tumour cavity intraoperatively or detect whether margins are clear at the time of surgery.

1.4.1 GIRFT Report – How to Tackle The Problem of Re-excision Surgery

The “Getting It Right First Time“ (GIRFT) is a national programme within the National Health Service (NHS) aiming to improve patient care and outcomes. GIRFT identifies national delivery of services and care, with the aim to minimize variation. In 2021, the GIRFT report for breast surgery data was accumulated from 130 hospital trusts across England, where in total over 100,000 breast procedures were carried out from 2015 to 2018 [47]. Data was gathered from the hospital episode statistics database.

The GIRFT report identified that between 2014 to 2017 the national average re-excision rate for patients undergoing BCS was 19% [47]. A relevant finding was that national re-excision rates ranged from 8 to 33% [47]. Following a wide local excision, re-excision surgery was a margin shave, and therefore these patients still achieved breast conservation. However, the second surgery where mastectomy was required due to inadequate margins, varied from 2.54% to 34.38% [47]. It is also important to note significant differences in practice amongst different hospital trusts, with 13 trusts having a re-excision rate of 25% but only eight trusts had re-excision rates less than the national average at 12.5% [47]. Therefore, GIRFT has highlighted significant national variation in breast surgery performance.

Interestingly, the data presented by GIRFT is from the past ten years of surgical practice, and if compared to data from prior to this there has been a minimal reduction in re-excision rates. Jeevan *et al.* assessed 55,297 patients who underwent BCS from 2005 to 2008, from 156 hospital trusts (data also from hospital episode statistics) [48]. They identified 20% of women needed at least one breast re-operation. In 29.5% of patients with DCIS, they required at least one further operation compared with 18% of patients with invasive breast cancer [48]. They also concluded practice varied amongst trusts ranging from re-excision rates of 12.2% to 30.2%, when adjusting for clinicopathological factors [48]. Therefore, in the past 12 years there has been almost no change in average re-excision rates.

It is evident that because of imprecision in breast conserving surgery, the burden of close/positive margins and re-excision surgery is an urgent healthcare problem to be addressed. GIRFT serves to reduce national variation in breast surgery,

and suggested several recommendations to help reduce re-excision rates [47]. These include better use of localising techniques; improved accuracy of MDT (multidisciplinary team meetings) to complete diagnostic work-up and preoperative assessment of disease extent and the use of primary systemic therapy. Relevant to this thesis, GIRFT suggests adopting the use of intraoperative margin assessment (IMA) techniques. Although GIRFT suggests use of IMA techniques, they stop short of recommending a specific technology, as they require robust evidence from clinical trials. To date, there is no single IMA technique validated in clinical trials.

1.4.2 Harmful Impact of Re-excision Surgery

Re-excision surgery can cause a harmful impact not only to the patient, but also to the healthcare system (Figure 1.3) as outlined below:



Figure 1.3 Schematic identifying how re-excision surgery impacts the patient and the healthcare system. Re-excision surgery can delay radiotherapy or chemotherapy; affect the cosmetic appearance of the breast; lead to anxiety, stress and affect quality of life; have financial implications to the patient due to delayed return to work but also puts a financial burden onto the healthcare system; there is a risk of mastectomy if positive margins persist; there is an environmental impact due to emission of greenhouse gases from further surgery.

1.4.2.1 Impact on adjuvant therapy

Breast cancer care is multifaceted, and the initiation of adjuvant therapy must be delayed until the patient has evidence of clear margins. It has been reported that completion of adjuvant therapy can take up to at least one year following surgery [49]. The optimal time to initiate adjuvant chemotherapy is unknown, however there is evidence that in particular types of breast cancer with a less favourable receptor status (triple negative or human epidermal growth factor receptor 2 positive status) who start chemotherapy more than 61 days after surgery compared to those who start one month after surgery had worse survival (hazard ratio (HR) 3.09; 95% CI, 1.49 to 6.39 and 1.54; 95% CI 1.09 to 2.18) [50]. Similarly, with radiotherapy the importance of the time interval between surgery and initiation of radiotherapy, has not been well studied. However again there is evidence to show that significant delays of more than three months can contribute to a higher risk of mortality (HR 3.84; 95% CI 3.01-4.91) [51]. Delayed adjuvant therapy can therefore affect overall oncological outcomes in terms of survival, but also delay a patient's road to recovery if there are treatment delays influencing their perceptions of cancer care and affects their quality-of-life related outcomes [52].

1.4.2.2 Cosmetic outcome

Reoperative intervention risks poor cosmesis, and may negatively influence patients' perceptions of aesthetic outcomes [53]. Patient reported outcome measures (PROMS) are a method to assess the quality of care delivered to patients from their perspective and are collected in short self-completed questionnaires. In a study where 564 women underwent re-excision BCS, it was evident that they had statistically significant lower breast satisfaction scores using BREAST-Q, a type of PROMS, than those who did not require re-excision surgery, particularly immediately post-operatively (73.6 ± 20.8 vs. 77.6 ± 20.2, p=0.009) [54]. Re-excision by definition, means a larger volumes of tissue will be excised, and Cochrane *et al.* have reported that patient satisfaction with cosmesis is 83.5% when low volume tissue is excised, compared with only 37% patient satisfaction when larger volumes (of more than 20% breast volume) was removed [55].

1.4.2.3 Psychosocial and emotional impact

Anxiety is defined as ‘a normal response to unpleasant stimuli’ leading a patient to adapt to these responses [56]. However, if there is an imbalance in coping mechanisms, a patient can be under undue stress, and hence why anxiety is one of the commonest psychological challenges a patient with breast cancer is expected to face. Several factors, which can be categorized, contribute to anxiety in breast cancer patients namely physical, psychosocial and environmental [56].

Physical factors which trouble patients include side effects of adjuvant therapy, hormonal changes, fertility issues, and increased fatigue [57]. Psychosocial adjustment is reported following BCS [58], including cognitive changes, mood disturbances and sexual well-being which can be protracted [59]. In a study where PROMS were assessed, patients who underwent re-excision BCS had lower sexual well-being scores two years postoperatively than women who underwent primary BCS (64.0 ± 22.7 vs. 70.2 ± 22.5, p=0.011) [54]. Patients who undergo BCS have altered perception of their body image. If anxiety is not addressed during treatment, there is a risk of development of clinical anxiety disorders such as post-traumatic stress disorder and even clinical depression [60].

Environmental factors contributing to anxiety include numerous hospital visits which impacts on day-to-day life, but can have financial implications if their work is affected or there are care-giving costs [61]. Re-operative intervention is likely to delay a patient’s return to work. Employment provides not only an income for a patient, but also health benefits [62]. Studies demonstrate that certain breast cancer patients do not return to work, with one study reporting up to 21% of patients do not return, and those who suffer significant psychological consequences are least likely to return [63]. Re-excision surgery can further compound on the factors described above and create further anxiety.

1.4.2.4 Higher cost and healthcare utilization

Re-excision surgery has financial implications not only for the patient, but also the healthcare system [63, 64]. One study computed that re-excision costs the NHS up to

£2136 per patient, equating to £118 million per annum additional cost to the healthcare system [65]. Histopathology departments are already stretched, and specimens from re-excision surgery creates a further workload. Only 3% of histopathology departments have enough staff to meet clinical demands [66].

Surgical site infection (SSI) is associated with revisional procedures, and a retrospective cohort study has shown that re-excision BCS carries a 2.44% risk SSI, and SSI remained significantly higher when accounting for multiple revisional procedures (odds ratio 1.34, 95% confidence interval, 1.07-1.67) [67]. Of note, if a patient with a positive margin required a mastectomy and reconstruction, there is a higher risk of SSI associated and therefore incurs a further cost to the healthcare system [68].

1.4.2.5 Risk of mastectomy

Multiple indications for mastectomy exist, however in the context of this thesis a mastectomy needs to be considered for a patient with BCS if they have persistently positive margins and there is a lack of breast volume to retain cosmesis [69]. The GIRFT report states that the number of women who require conversion to a mastectomy following an initial BCS procedure within the first year of surgery ranged from 2.54% to 34.48%.

Mastectomy has significant implications for patients and the healthcare system. As expected, patients who require a mastectomy experience a greater psychosocial distress [70]. However, it is well evidenced that having reconstruction with a mastectomy can lower this level of distress, For example, a meta-analysis by Chen *et al.* reported a decrease in the incidence of anxiety (RR=0.54, 95% CI 0.32-0.93,p=0.0006) and depression (RR=0.54, 95% CI 0.32-0.93,p=0.02) in patients receiving reconstruction [71]. Reconstruction could be an autologous free flap (vascularized tissue from the patient) or an implant/expander based form, with this being offered at the time of mastectomy or delayed following adjuvant treatment [72]. GIRFT estimates the average cost of a initial free flap reconstruction at £6548 compared to £3824 for an implant based operation. BCS is normally a day case procedure, but GIRFT reports only 19% of patients undergoing a simple mastectomy are discharged the same day, with mastectomy and implant based reconstruction

having an average length of stay of two days, with mastectomy and free flap reconstruction having an average length of stay of seven days [47]. The cost of the mastectomy and hospital stay is an implication following surgical re-excision. Complications related to mastectomy and reconstruction are extensive and include seroma, haematoma, capsular contracture and need for revisional surgery, which also have financial consequences to the healthcare system [73].

1.4.2.6 Environmental impact

Climate change is a global issue that is most associated with devastating environmental disasters, caused by the emission of the greenhouse gases (carbon dioxide, methane and nitrous oxide). The healthcare industry is a direct contributor to climate change responsible for 4.4% of greenhouse gas emissions globally, and the NHS in England is responsible for 25 mega tonnes of carbon dioxide equivalents [74, 75]. The main mechanism by which healthcare industries contribute to greenhouse gas emissions is from production from the operating room itself, with a single operation itself producing between six kilograms (kg) to 814kg of carbon dioxide alone, which is equivalent to an average petrol car travelling at 2273 miles [74]. Other contributors from healthcare industries are the anaesthetic gases used, consumable supply chain, sterilization of equipment and electricity required to power an operating room.

Breast cancer surgery is a significant contributor to greenhouse gas emissions due to the high volume of procedures and the shorter operating times compared to other surgical specialities [74]. Re-excision surgery for positive breast margins is therefore a cause for concern and strategies to reduce this should be sought. Some of the methods to mitigate greenhouse emissions in healthcare include patient selection and surgical decision making; altering delivery of anaesthesia to low flow rates and anaesthetic alternatives; recycling and prioritisation of reusable medical devices [76]. In the context of this thesis, there is a clear clinical requirement to adequately identify breast cancer intraoperatively at the time of primary BCS to reduce the need for re-excision surgery.

1.5 Techniques to Reduce Reoperation Rates

As outlined above (sections 1.4.2), there is a clear need to tackle imprecision in breast conserving surgery, as re-excision has a significant societal impact. Therefore, non-surgical and surgical approaches need to be discussed in attempt to find solutions to reduce re-excision surgery rates. This section will in turn discuss these different approaches and present the advantages and disadvantages of each.

1.5.1 Non-Surgical Approaches

There have been substantial developments in neoadjuvant and adjuvant therapies, allowing for improved survival [18], due to our understanding of breast cancer biology and genetics. It could be argued that the use of such therapies, including endocrine treatment, chemotherapy or radiotherapy could negate the effect of positive margins, and therefore avoid re-excision. Despite a paradigm shift in precision medicine neither chemotherapy, radiotherapy nor endocrine treatments can substitute for re-excision to achieve clear margins [77]. There are no prospective randomised trials and hence no evidence to support this. The risk of local recurrence exists even in low-risk tumours, and therefore accepting positive margins is presently unacceptable.

1.5.2 Surgical approaches

1.5.2.1 Increase Volume of Tissue Excised

Thus far I have discussed standard BCS. However, an alternative oncoplastic BCS also exists, which extends the principles of BCS by integrating plastic surgery techniques for immediate re-shaping of the breast after wide excision of the tumour [78]. Oncoplastic BCS can be classified into two levels, level I and II. A level I procedure is selected if less than 20% of the breast volume is being excised, and where no skin excision is required. A level II procedure is where 20 – 50% of the breast volume is excised requiring skin excision to restore breast shape [78].

By increasing the volume of tissue excised with oncoplastic BCS, the chances of a positive margin have been shown to be lower [79-81]. A systematic review by De La Cruz *et al.* identified 39 studies where oncoplastic BCS was performed, and re-excision rates ranged from 0% to 26.7%, with a weighted average re-excision rate of 6% and conversion to mastectomy rate of 6.2% [82]. Chen *et al.* report that re-excision rate was significantly lower in oncoplastic BCS compared to standard BCS (RR 0.06; p=0.001) [83]. In a meta-analysis of 18,103 patients where standard BCS was compared to oncoplastic BCS, oncoplastic BCS had a lower risk of re-operation (RR 0.64; 95% CI 0.46 – 0.89); p=0.01) but once publication bias was adjusted for differences in re-operation became insignificant (RR 0.86; 95% CI 0.56-1.31;p=0.44) [84]. Similarly publication bias was noted in a recent Cochrane study comparing oncoplastic BCS to standard BCS, where there oncoplastic BCS favoured lower re-operation rates (RR 0.76; 95% CI 0.69 – 0.85; p=0.003) [85].

Oncoplastic BCS has several disadvantages which counterbalances a lower positive margin rate and cannot be a generalised technique recommended to reduce re-excision rates. Firstly, it requires specific oncoplastic training. Secondly, not all patients are amenable for oncoplastic techniques, with relative contraindications of multifocal tumours, low volume breasts with a lack of ptosis, and medical co-morbidities [86]. Complications for oncoplastic BCS include liponecrosis, skin necrosis, seroma, infection, nipple necrosis and delayed wound healing, and are like that of standard BCS. However, *Tenofsky et al*. identified patients undergoing oncoplastic BCS compared to standard BCS had a higher rate of non-healing wounds (8.6% versus 1.2%; p=0.042), and a higher rate of fat necrosis (25.9% versus 9.5%; p=0.009) [87].

1.5.2.2 Selective or Routine Cavity Shave Margin Excision

Selective margin excision involves removing an extra area of tissue within the tumour cavity following tumour excision, where it is believed there is likely to be residual cancer, either due to the surgeon palpating the lesion at the edge of a BCS specimen or else if specimen radiographic imaging suggests close margins (see section 1.7.1.1). The SHAVE trial is level I evidence in support of immediate routine cavity margin shaves [88]. In the SHAVE trial, Chagpar *et al*. randomised patients undergoing partial

mastectomy (wide local excision) to undergo either selective shaves as described above or comprehensive cavity shaves of all radial margins [88]. Prior to randomization, there was no significant difference in rates of positive margins between the shave (36%) and no shave group (34%, P = 0.69) [88]. Cavity margin shaves involve circumferentially taking shaves of tissue from all aspects of the cavity and orientating these (normally via a suture) for histopathological validation. Retrospective [89-91] and prospective studies [88, 92-94] have identified that cavity margin shave excisions can reduce re-excision rates, with the SHAVE II trial achieving a positive margin rate of 9.7% in the “shave” group compared to 36% in the “no shave” group (p=0.001) [93].

There is variability in undertaking BCS with cavity shave, dependent on the surgeon and institution [95]. Although a cheap, technology free way to lower re-excision rates this solution lacks precision in identifying the healthy-tumour interface, and increases operative time compared to standard BCS (79 $\pm$ 4 minutes versus 67 $\pm$ 3 minutes, p=0.0002) [95]. BCS aims to preserve cosmesis, however cavity shaves can cause a larger volume of tissue to be excised. Chagpar *et al.* documented that the median total volume of cavity shaves equated to 36.3 cm^3 (range 2.1 – 440.2), and in comparison, to standard BCS this increases the volume of excision up to at least 50% more [88, 96].

1.6 Intraoperative Margin Assessment Techniques

1.6.1 Traditional

Currently established techniques for IMA include specimen radiography, frozen sections and imprint cytology. Each technique will be discussed to detail their accuracy rate and their advantages and disadvantages

1.6.1.1 Specimen Radiography

Specimen radiography (SR) has historically been used to assess if a non-palpable breast lesion has been adequately excised. Following excision of the cancer,

commonly a single two-dimensional (2D) radiograph is taken of the specimen. The surgeon will then identify if the lesion, and the localization method used to identify the tumour within the breast (i.e. magnetic seed, wire, or reflector) has been excised (Figure 1.4 A-B). If the lesion or any microcalcifications are close to any of the resection margins, then the surgeon may take a decision to excise further tissue from the resection cavity surface of concern. Conventionally, this is done by using a mobile radiography unit or taking the specimen to the radiology department, where the specimen is compressed between two mammography plates or a portable unit exists within the operating theatre and the surgeon places the specimen onto a plate already orientated, and images are taken [97]. It is well evidenced that SR has poor diagnostic accuracy, with a recent meta-analysis highlighting that SR has a pooled sensitivity of 53% (95% CI: 45 – 61%), and specificity of 84% (95% CI: 77 – 89%) [98].

A more advanced technology is digital specimen tomosynthesis, which takes multiple X-ray images of the specimen in 1mm slices to achieve a three-dimensional (3D) image construct [99]. Digital tomosynthesis provides a more detailed image for cancer detection particularly microcalcifications, as there is reduced anatomical noise from superimposed tissues [100], and avoids transportation so speeds up image acquisition time (Figure 1.4 C). Kaufman *et al*. described how conventional SR can take up to 20.7 minutes, whereas digital SR can take 1.1 minutes [101]. Compared to 2D radiography, digital tomosynthesis has been evidenced in a recent meta-analysis to have superior sensitivity for cancer detection (3D 76% versus 2D 67%) [102], with comparative clinical studies showing a range of sensitivity (66.67% to 91.67%) and specificity (74% to 91%) [99, 103].

The main limitation of specimen radiography is the inability to differentiate between cancer and fibroglandular tissue at the level of the edge of a specimen to guide a surgeon, hence why this method has a low sensitivity [104]. It has been demonstrated that following excision, breast specimens are flattened in height by up to 50%, and this can have implications in terms of margin assessment [105]. Digital tomosynthesis has improved accuracy however is very expensive to purchase and to maintain. Despite the ease of use of this technique, interpretation of images is subjective and to save time many surgeons interpret the image themselves. There remains imprecision in identifying residual disease at the specimen margin and specimen radiography is more useful if the person performing the localisation is present.

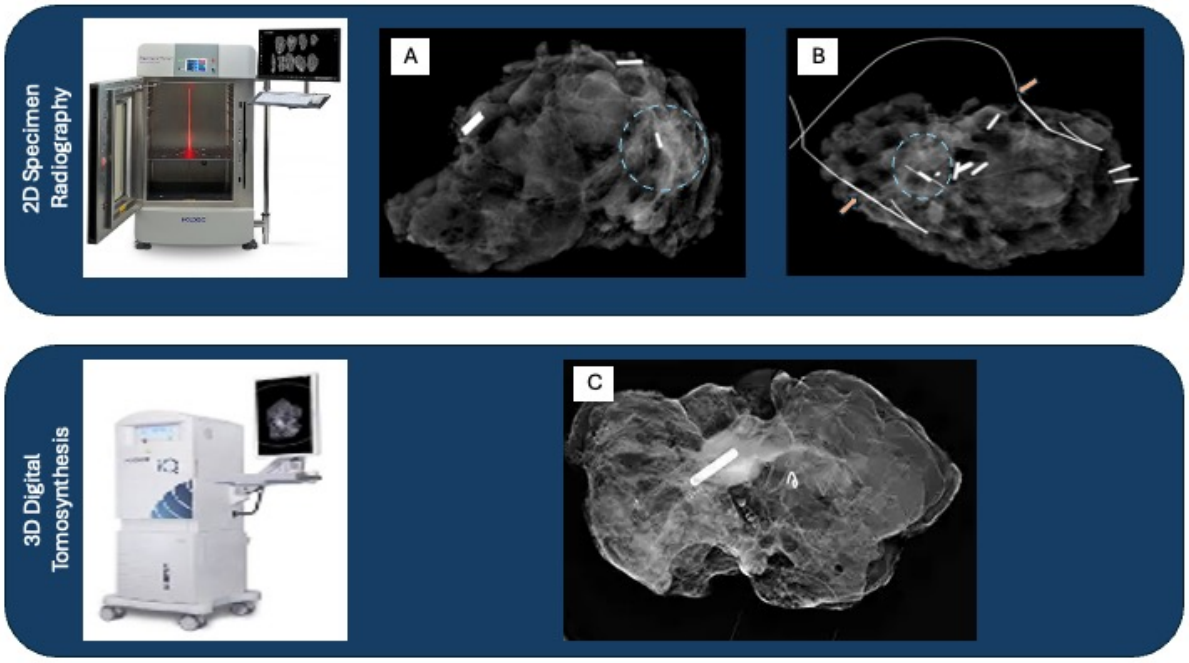


Figure 1.4 Illustration of the equipment for two dimensional (2D) specimen radiography and associated 2D radiographs produced (a-b); and set up of the three dimensional (3D) digital tomosynthesis machine and associated 3D image produced. (A) A 2D radiograph where a Magseed® localisation technique has been used to find the epicentre of the cancer. The dotted blue line highlights the Magseed® location and associated cancer. It is difficult to establish the boundaries of the cancer. (B) A 2D radiograph from a patient who received neoadjuvant chemotherapy and to help identify the lesion post treatment, a SAVISCOUT was inserted. The dotted blue circle shows the location of the localizer and a previous biopsy clip. The orange arrows highlight two wires used to "bracket" where disease on preoperative imaging was seen. (C) A 3D image construct from a lesion which was localized with a Magseed.® This image gives more detail about the lesion extent.

1.6.1.2 Frozen Section Analysis

Frozen section analysis involves sampling tissue from areas from an excised specimen where the surgeon has concerns about residual disease (Figure 1.5 A) from either the specimen radiograph or macroscopic features [106]. The small pieces of tissue from these regions are placed in special medium and frozen at -20^{o}C in a cryostat. The tissue is sliced into four micrometre slices and each tissue section is attached to glass slides and then stained with haematoxylin and eosin (H&E) [107, 108]. An experienced pathologist reads the slides to identify the presence of normal or malignant breast tissue (Figure 1.5 B). A recent systematic review and meta-analysis found that frozen section has a pooled sensitivity of 86% (95% CI: 78 – 91%) and pooled specificity of 96% (95% CI: 92 – 98%) [98], with evidence also to show

that this technique can reduce re-excision rates to 3.6% [109]. Other level one studies have found comparative accuracy rates [107, 110].

Despite good accuracy rates, frozen section analysis is disruptive to surgical workflow as processing time can range from 13 minutes to 53 minutes [110], and occurs whilst the patient remains under anaesthesia. It also requires a histopathologist to perform and interpret results, which can be a challenge particularly out-of-hours if an operating list is extensive and hence incurs a cost to the pathology department. Other weaknesses of this technique are that it is less effective at detecting DCIS; only the region of interest is examined and not the entire surface; and the freezing process can affect tissue for routine histological analysis [111]. Thus, the diagnostic ability of frozen section is outweighed by the logistical set up required and lack of surface scanning ability.

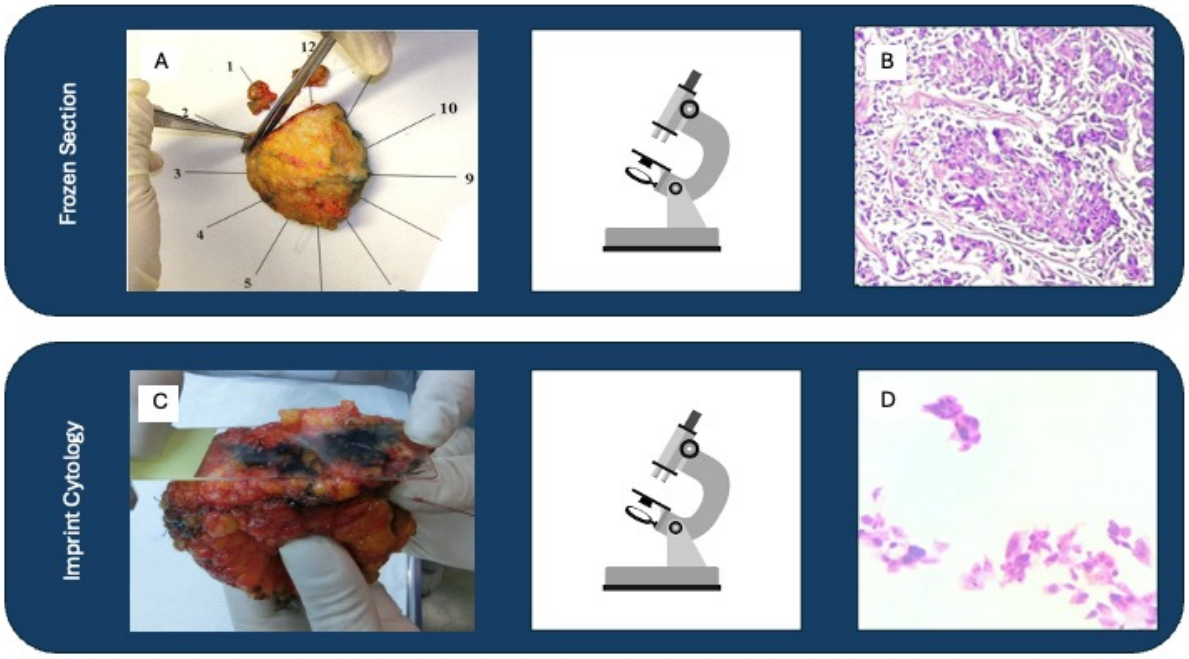


Figure 1.5 Illustration to depict how frozen section and imprint cytology are performed, and following a pathologist inspecting slides under a microscope the histopathological findings from the same specimen where a patient has invasive ductal carcinoma. (A) A freshly excised specimen is orientated as a clockface and small tissue samples are in this case taken circumferentially and prepared into slides following H&E staining (B) Under a microscope the histopathological findings following frozen section from one small area (C) One side of an excised specimen is pressed against a slide and then prepared to be read by a pathologist (D) A cytological slide following imprint cytology. (This illustration has been created from modified images from the following sources: Tamanuki *et al.*, Osaka *et al*., and Pallialil *et al.* [[48, 112-114] with permission from publishers granted).

1.6.1.3 Imprint Cytology

With imprint cytology each surface of a resected specimen is positioned and pressed onto a slide (Figure 1.5 C). The slide is then fixed and stained and read by an experienced pathologist (Figure 1.5 D). It is based on the premise malignant cells will adhere to the slide, unlike adipose cells [111]. In contrast to frozen section analysis therefore, imprint cytology offers the ability to examine the whole resection surface. A recent meta-analysis demonstrated that imprint cytology has a pooled sensitivity of 91% (95% CI: 71 – 97%) and pooled specificity of 95% (95% CI: 90 – 98%) [98].

Again, there is disruption to surgical workflow as here processing time has been reported to take up to 17 minutes [110], and an experienced pathologist is required to be available in theatre or at the time of surgery to interpret the slides. The effectiveness of interpretation of imprint cytology slides is impacted by several factors such as cauterization, dryness over the resection surface, and irregularity of the surface can alter results [111, 115]. There is also a limitation of measuring the distance of the tumour from the surgical margin [116]. Once again, the diagnostic accuracy of imprint cytology is offset by costs, availability of experienced staff and relies on specimen surfaces to be in optimal condition.

1.6.2 Emerging Technologies

Novel IMA technologies are currently being researched worldwide to improve precision in BCS. Based on their methodology, they can be broadly categorized into four groups. These technologies are imaging based (X-ray or magnetic resonance imaging (MRI)); optical imaging-based; detecting the electrical properties of tissue; and those technologies which exploit the biochemical differences in tissue (Figure 1.6) [117].

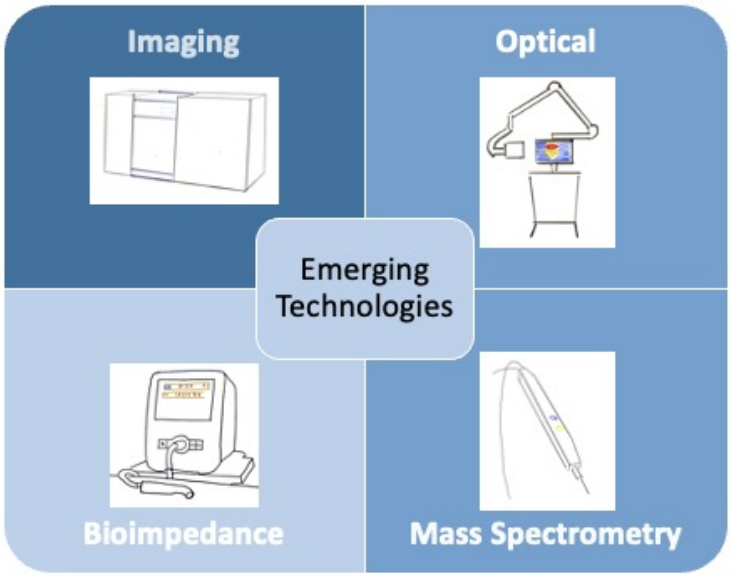


Figure 1.6 Emerging IMA tools categorized into four groups; imaging (e.g. X-ray; MicroCT, Bruker Inc); Optical (e.g. fluorescence imaging, SPY Elite, Stryker); Bioimpedance (e.g. Margin Probe); Mass Spectrometry (e.g.iKnife, Waters).

1.6.2.1 Technologies Using Imaging

Certain imaging modalities can provide a surgeon with multi-dimensional images to guide them during surgery. The use of X ray; computed tomography (CT) and magnetic resonance imaging (MRI) focus on capturing anatomical structures.

1.6.2.1.1 Micro-computed Tomography

Micro-computed tomography (micro-CT) produces a 3D volumetric image of a breast specimen using high resolution CT, via a compact scanner that sits within the operating room (Figure 1.7). They can image specimens in the tens of microns range (70 to 1000μm) and therefore have high spatial resolution [118]. A meta-analysis by Manhoobi *et al*. report a pooled sensitivity of 68% (95% CI: 34 – 90%) and pooled specificity of 69% (95% CI: 34 – 90%) [102]. Although commercial systems are available such as VSI-360™ (CLARIX Imaging), not many trials have been performed, but a recent observational study showed that out of 32 specimens imaged with micro-CT, 64% correctly matched with final histology, with a negative predictive value of 89% [119]. Microcalcifications are the main discriminator in micro-CT images to distinguish

between benign and malignant tissue (Figure 1.7 A & B). The limitation of this technology is that there is often an inability to distinguish between tumour and fibroglandular tissue, and it cannot identify isolated microcalcifications but more of clusters [111]. Another drawback is the technology is expensive to purchase and maintain, and some radiologic training will be required by the user as interpretation of images will be subjective as for specimen radiography.

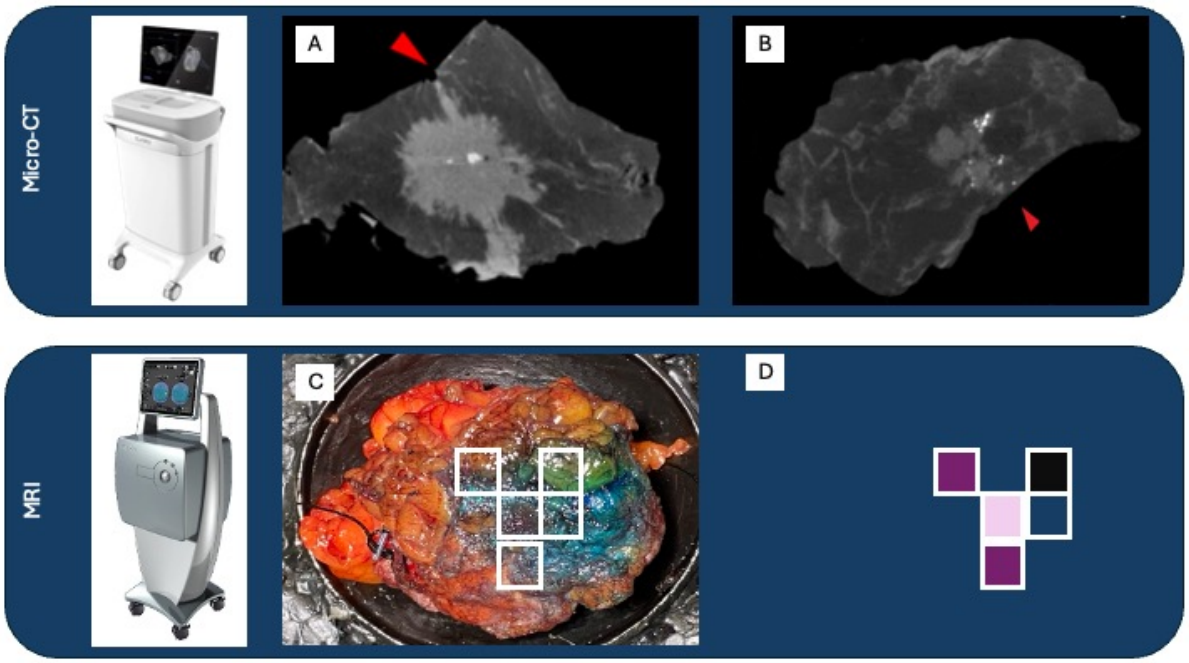


Figure 1.7 Representation of the mobile units of a micro-CT and MRI system used for intraoperative assessment of an excised specimen, and the corresponding images acquired. (A) Micro-CT tomography system used to image a specimen with invasive ductal cancer, with the red arrow highlighting disease at the posterior margin. (B) Micro-CT image of a specimen containing ductal carcinoma in-situ, with evidence of calcifications at the edge of the specimen highlighted by the red arrow. (C) A freshly excised specimen inked with pathology ink and the white squares depict the areas scanned by the MRI system. (D) Following image processing the MRI system highlights which areas have disease (purple squares) and those with normal breast tissue (blue/black squares).

1.6.2.1.2 Magnetic Resonance Imaging

MRI exploits the magnetic properties of certain nuclei within tissue cells [111]. By placing a breast specimen into a MRI machine, which can stand within the operating room (Figure 1.7), the nuclei align due to the magnetic field. By then applying a radiofrequency pulse, this creates signals that can be converted into detailed images (Figure 1.7 C & D). One study where 77 specimens were imaged with a ClearSight™ (Clear-Cut Medical Ltd., Rehovot, Israel) found that MRI achieved a sensitivity of 91%

and specificity of 93% [120]. Similarly to micro-CT, the main disadvantage of MRI is the cost of the device and scanning times [111], and the requirement for training to interpret images with evidence that there is interpersonal variability in reading MRI scans [121]. Another notable limitation is the lack in ability of MRI to accurately detect DCIS [121, 122].

1.6.2.2 Technologies using optical imaging

Tissue optical imaging technologies employ different wavelengths of light to illuminate tissue and then capture the interaction of light with tissue components via spatial and temporal data acquisition. Two of the hallmarks of cancer, increased vascularity and proliferation, are accessible to this technique. Optical techniques encompass an array of technologies including photoacoustic imaging, Raman spectroscopy, multimodal photon imaging, diffuse optical imaging and fluorescence imaging [123].

1.6.2.2.1 Photoacoustic tomography

Photoacoustic tomography combines the principles of photoacoustics and ultrasound to create images of tissue [123]. Here tissue is exposed to laser pulses, and absorbs the light energy and undergoes thermal expansion, generating ultrasonic waves. These waves are detected by an ultrasound transducer, in contact with the tissue, and converted to electrical signals (Figure 1.8 A). Vasculature is the main differentiating factor here between normal and cancerous tissue (Figure 1.8 B)[123]. In one study where 15 specimens were interrogated with this technology, the sensitivity was 100% and specificity was 96% [124].

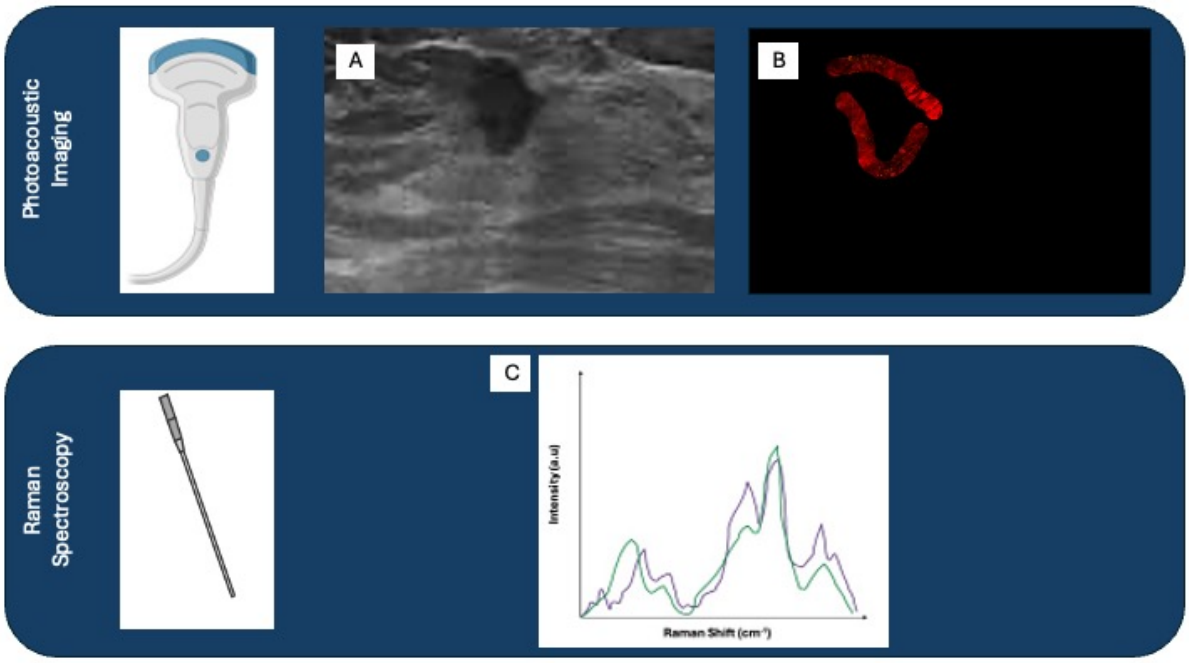


Figure 1.8 Representation of handheld devices used for photoacoustic imaging and Raman spectroscopy and the corresponding images produced from these devices. (A) The ultrasonic transducer once placed onto breast tissue produces a image which here shows a hypoechoic mass with irregular edges which relates to a tumour. (B) A corresponding photoacoustic image of the same area highlights as red which represents vessels feeding the tumour. (C) A Raman spectroscopy probe produces raw Raman spectra to help distinguish between normal (purple) and malignant (green) breast tissue. Each peak relates to a specific molecular vibrational bond.

1.6.2.2.2 Raman Spectroscopy

Raman spectroscopy, is a form of vibrational spectroscopy, that detects the interaction of monochromatic laser light with molecules by measuring the inelastic photon scattering [123]. The differences in energy between the incident and scattered photon relate to the biochemical composition of breast tissue and can be used in the form of a handheld probe for margin assessment (Figure 1.8 C). Majumder *et al.* found Raman spectroscopy could detect invasive breast cancer with a 99% accuracy, with data from 74 frozen-thawed tissue samples [125]. Although results appear promising, only small sample sizes have been used in studies and only small areas of breast tissue interrogated. Other limitations of this technique are weak signal intensity, a minimal field of view so lacks the ability to scan a whole resection surface, and has limited penetration depth [123] which do not preclude it being a suitable IMA tool [126].

1.6.2.3 Technologies Based on Differences in Electrical Properties of Tissue

Other handheld probe technologies exist, that can exploit the varying features of electrical properties of tissue, to determine positive margins. Malignant tissue has different electrical properties compared to benign tissue [117].

1.6.2.3.1 MarginProbe

MarginProbe® (Dune Medical Devices Ltd, Caesarea, Israel) is a commercialised device that measures local electrical properties in breast tissue within the radiofrequency range [127]. When tissues become malignant, physiologic changes occur which affect electrical properties. These changes are congruent with the hallmarks of cancer namely alterations in nuclear content, increased vascularity and changes in spatial cellular connectivity [128]. The MarginProbe® system applies an electrical field to breast tissue and analyses the reflection over a wide range of radiofrequency frequencies (Figure 1.9 A). Compared to other emerging technologies discussed in this chapter, there is evidence of prospective randomized trials investigating the efficacy of MarginProbe® , with one enrolling 596 patients and achieving a sensitivity of 75.2% but a specificity of 46.4% [127]. However, it was noted there was a high false positive rate, and larger volumes of tissue were excised. A recent randomised control trial performed in the UK of 457 patients showed that MarginProbe® did not impact re-excision rates [129], however a recent systematic review exploring the use of MarginProbe® in 2680 patients identified a 54.68% reduction in re-excision rates [130]. Despite the amount of work in this area this review has highlighted critical limitations to explain why MarginProbe® has not been widely adopted including: a lack of breast tissue heterogeneity in studies; too few randomized controlled trials; single-centre or single-surgeon users leading to bias; minimal patient heterogeneity (many studies had older patients with low density breast tissue and subsequent lower margin re-excision rates); poor definition of margin width in studies [130].

1.6.2.3.2 Clear Edge

In comparison, a different handheld device called Clear Edge™ utilises bioimpedance spectroscopy to assess intracellular and extracellular variations of tissue dielectric properties [131]. A study by Dixon *et al.* showed that this device had a sensitivity of 84.3% and specificity of 81.9% [131]. Although this was a two-phase cohort study trial, there has been no randomized controlled trials reporting clinical data outcomes.

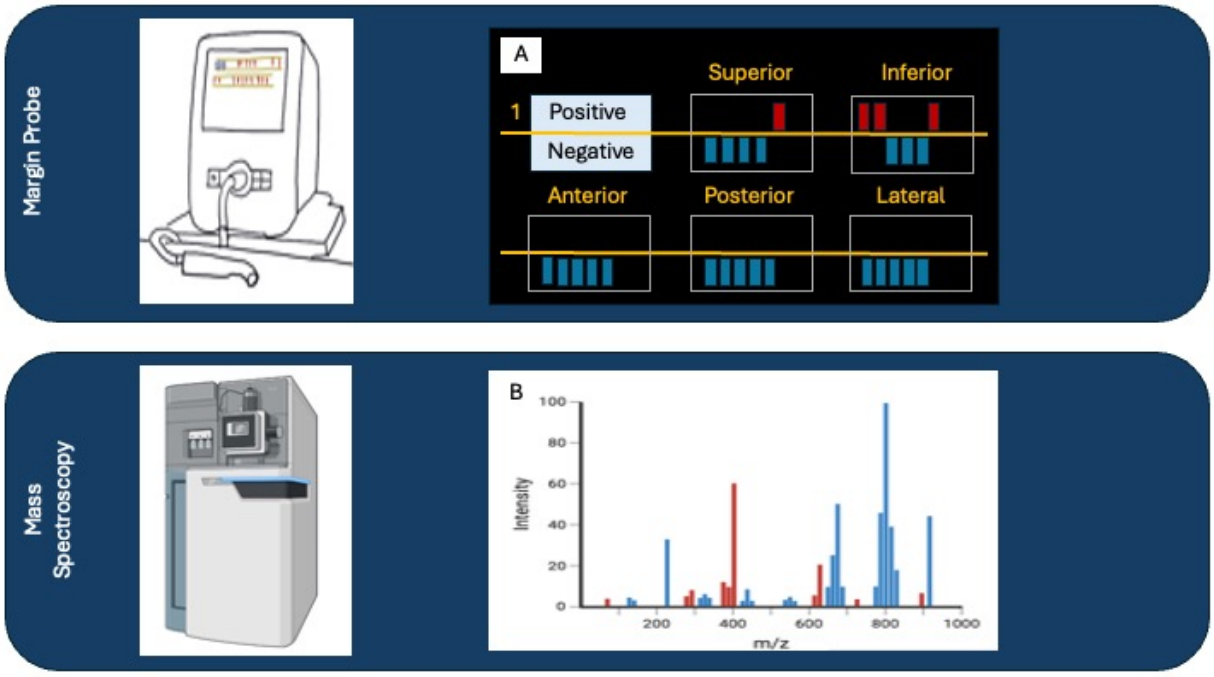


Figure 1.9 Representation of MarginProbe and mass spectrometry devices as would be used in the intraoperative setting, and the corresponding images produced to help guide a surgeon about margin pathology. (A) The MarginProbe device identifies cellular changes associated with cancer and this is reflected in electrical properties. These signals are captured and compared to known tissue signatures to help distinguish between healthy or malignant breast tissue and produces red (cancer) or blue (healthy tissue) bars on a chart. (B) Following electrosurgical cautery during dissection of breast tissue, the aerosol produced represents release of cellular content to a gas phase. This gas is transferred via plastic tubing to a mass spectrometry machine which performs mass spectrometric chemical analysis, and machine learning helps to differentiate the chemical differences between tissue types. The graph represents mean spectral intensities of metabolites. Molecules are assessed by measuring the mass-to-charge ratio (m/z) of molecular ions within the aerosol.

1.6.2.4 Technologies Based on Biochemical Differences in Tissue

Cellular metabolism differs between normal and malignant tissue. Electrosurgical dissection causes cellular lysis and release of cellular content into a gaseous phase [117]. Rapid evaporation ionization mass spectrometry (REIMS) can analyse the

smoke plume created from diathermy used in cutting breast tissue. REIMS quantifies the mass-to-charge ratio of aerolized particles and therefore reflects the chemical composition of recently evaporated tissues (Figure 1.9 B) [132]. St John *et al.* showed that REIMS could achieve a sensitivity of 90.9% and specificity of 98.8% [133], with a rapid turnover time. However, it has several disadvantages including the large footprint of existing machines impacting on theatre space and acoustic noise impinging on communication in theatre. REIMS is a destructive technique, hence accurate histopathological cross-reference to mass spectrometry signals may be challenging. [133].

1.6.3 Future IMA Tool Characteristics

This chapter has discussed the significant impact of re-excision surgery and the clinical issue of imprecision in BCS. Despite a fundamental change in breast cancer management in terms of delivery of adjuvant treatment, there is a lack of progression in methods to improve precision to guide tumour excision intraoperatively to prevent positive margins. Imprecision could potentially be overcome if an intraoperative tool was available to assess the excised specimen (and even the cavity), on a microscopic and macroscopic level. An IMA tool with the ability to give rapid and accurate information about the micro-morphology of tissue over a wide field-of-view, would be an asset to breast surgeons to avoid further surgical procedures. Characteristics of any future IMA tool are considered below:

- **Speed** - Surgeons require real time feedback to ensure surgical workflow is maintained. Ideally a device that relays information to the surgeon within minutes.
- **Scanning the entire surface of the specimen** - A useful tool should provide the surgeon with a whole field-of-view of the specimen, not only a region of concern. The total area of an excised specimen from breast conserving surgery can be variable, and the time needed to scan therefore can be time consuming.
- **Adequate depth penetration**- An ideal tool can penetrate to a depth of at least 2mm as current margin guidance states the risk of local recurrence is decreased if no cancer cells are present from the surface of an excised

specimen at this distance. Chapter three will discuss the international debate on the adequate margin width and how this relates to the technology being investigated in this thesis.

- **Ability to discriminate between benign and malignant tissue** - A successful tool must have the ability to detect histological changes at the margin, but consider the large inter-patient variation, as well as intra-patient variation of breast tissue with breast tissue heterogeneity as discussed in chapter two.
- **Utilisation and ideally interpretation by the surgeon alone** - An effective tool must require minimal personnel, and ultimately not require a pathologist. Artificial intelligence and deep learning algorithms provide a path to remove the need for expert interpretation.
- **Accuracy** - A high level of sensitivity and specificity to detect cancer will prevent further re-excision surgery.
- **Ergonomics** - For efficiency in the operating room, any IMA tool must have ease of function.
- **Cost** – A low-cost system is advantageous to any healthcare system, including costs attributed to maintenance of equipment.



Figure 1.10 Schematic to highlight key characteristics of any future intraoperative margin assessment tool (IMA) for breast conserving surgery. Features that should be exhibited include speed of use to fit into surgical workflow; the ability to scan a whole resection surface of an excised specimen; a tool that can visualise beyond the surface of the specimen; breast tissue and patients are heterogeneous, an ideal IMA tool must account for this; the surgeon should be able to use the tool by themselves and not

rely on other trained staff; the best IMA tool must be accurate in discriminating between normal and malignant breast tissue; the IMA tool should have ease of function and not occupy too much room in the operating theatre.

1.7 Thesis summary

1.7.1 Hypothesis

Breast cancer tissue exhibits distinct pathological and biochemical characteristics compared to normal breast tissue, and these differences can be detected and distinguished using multispectral imaging through their unique spectral signatures. Spectral databases can be built from spectral data derived from malignant and non-malignant breast tissue in the *ex-vivo* and *in-vivo* setting, and this can be used to classify new breast tissue according to tumour or normal tissue type. Multispectral imaging can be used in the intraoperative setting to identify positive breast cancer margins and has the potential to be an IMA tool for surgeons.

1.7.2 Summary

In subsequent chapters, this thesis will explore the interaction between light and breast tissue (Chapter two) to help construct technology to detect breast cancer in the intraoperative setting. By exploring previous research on this topic, we can build on previous discoveries to add novelty to this area. Two important characteristics of any IMA tool include the depth penetration of light and spatial resolution. Chapter three establishes what margin width guidelines that are used internationally currently to achieve oncological negative margins in BCS, which is relevant to technology development. This area is further scrutinized to establish if there is enough evidence to decide on an exact negative margin width to lower the risk of cancer recurrence but also justify the use of an IMA tool intraoperatively. Chapter four is the first experimental chapter within this thesis and explores the interaction of diffusely reflected light with freshly frozen breast tissue samples, using a custom-built spectroscopy probe. The aim of this chapter is to develop a spectral library, in the form of an *ex-vivo* database,

to help train future machine learning models in the development of an IMA tool to be used in the intraoperative breast surgical setting. Results of this chapter are compared to findings from chapter two and are unique to this thesis as freshly frozen samples are used unlike previous studies; tissue heterogeneity is explored; machine learning classifiers are applied for spectral data analysis; and lastly the potential use of spectroscopy in other aspects of breast diagnostics is discussed.

This thesis aims to explore the use of a custom-built multispectral camera for suitability in intraoperative breast cancer detection, as a potential IMA tool. Chapter five describes the background to multispectral imaging, and the hardware and software components of the multispectral camera utilized for subsequent experimental chapters. Multispectral imaging was used to interrogate both freshly frozen breast tissue samples in the *ex-vivo* setting in chapter five to establish a spectral database. Machine learning classifiers are used to assess the ability of multispectral imaging to distinguish between healthy and malignant breast tissue. Methodological challenges are discussed here, including the limitations of tissue samples used. Freshly surgically excised wide local specimens in the *in-vivo* setting are then imaged with the same multispectral system, and the performance metrics following data analysis are assessed. These results are compared to currently available IMA devices. In chapter six, to further assess the usefulness of multispectral imaging in the intraoperative setting, its ability to detect breast cancer is compared to a custom-built fluorescence imaging system. In this last experimental chapter, patients are given fluorescent agents which exploits another interaction of light and tissue, fluorescence. The ability of a fluorescent imaging system to distinguish between malignant and healthy breast tissue is compared to that of multispectral imaging.

Finally, chapter seven provides a comprehensive summary of the key findings presented throughout this thesis and discusses how the work has contributed to advancing the development and application of multispectral imaging within the intraoperative setting of breast surgery.

Chapter 2: Light – Tissue Interactions

2.1 Tissue Optics Background

The interaction between light and biological tissue is the basis of an optical IMA tool for precision breast surgery. Light delivered to biological tissues undergoes several processes, as illustrated in Figure 2.1 including reflection, refraction, scattering, absorption and intrinsic fluorescence occur [134].

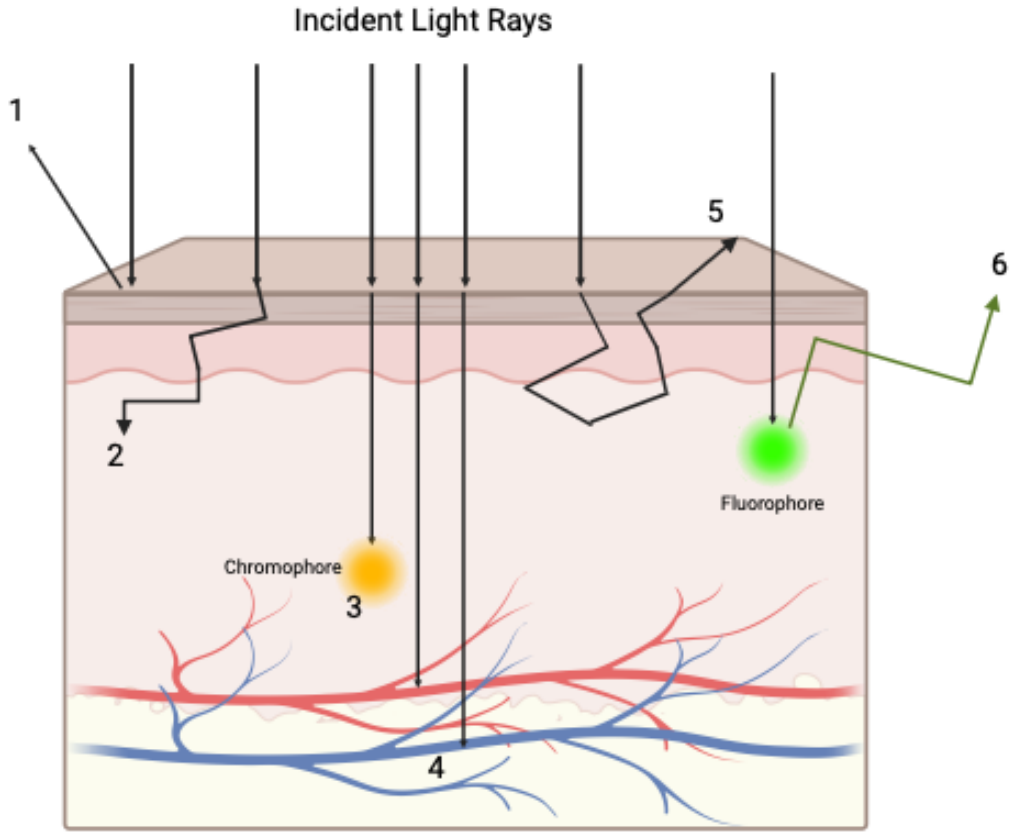


Figure 2.1 Schematic showing the different processes light undergoes when it interacts with breast tissue. (1) Specular reflection is when light reflects at an equal but opposite angle to the incident light ray. (2) Scattering is a phenomenon that occurs when incident light interacts with the ultrastructures of tissue and is caused by variations in the refractive index. (3) In breast tissue light is absorbed by molecules called chromophores, namely water and β-carotene. (4) Light is also absorbed by haemoglobin (both oxygenated and deoxygenated forms) which are found in blood vessels. (5) Diffuse reflection is defined by how an incident light ray is reflected at many different angles from the tissue surface. (6) Fluorescence is where incident light is absorbed by molecules called 'fluorophores' and re-emitted at a different wavelength. Relevant fluorophores in breast are nicotinamide adenine dinucleotide and hydrogen, flavin adenine dinucleotide, collagen, elastin and tryptophan and lipo-pigments. (Image created using Biorender.com software).

2.1.1 Reflection and refraction

Reflection and refraction of light within tissues, which are inhomogenous, is related to the change of direction and speed of light. When light rays reflect off a surface, they change direction. When light rays hit the uneven surface of biological tissue, they are reflected in many different directions, or “diffusely”. With reflection, light reflects into the same medium (Figure 2.2). Refraction is defined as the change of direction of a light ray when passing obliquely from one medium into another (Figure 2.2), in which the light speed (refractive index) differs [135].

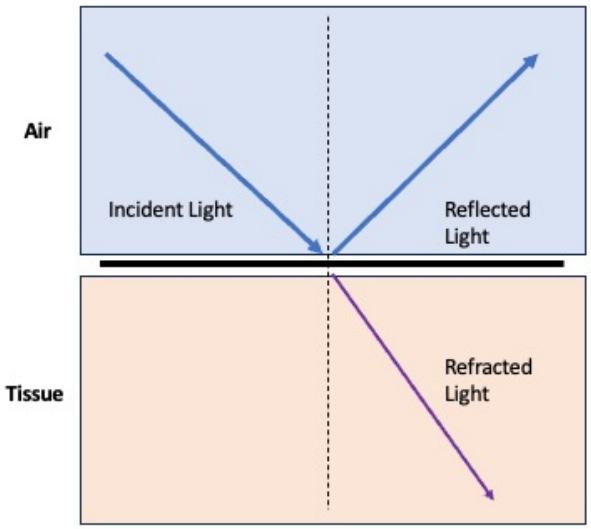


Figure 2.2 Diagram illustrating the way in which the direction of light changes with reflection and refraction when an incident light ray hits breast tissue. With reflection the light hits the breast tissue surface and is reflected into the air in a different direction. Comparatively, with refraction the incident light ray passes through breast tissue and changes speed and direction.

2.1.2 Scattering

Light scattering is the way light behaves when it interacts with a medium that contains particles, or the boundary between different mediums where structures or defects are present. In relation to breast tissue, this is cellular components or tissue structures, respectively. In breast tissue, scattering is sensitive to breast density (reflective of fibroglandular content) [136]. Collagen is another scatterer, which is involved in tumour progression through increased collagen deposition [137].

2.1.3 Absorption

Light may be absorbed by molecules called “chromophores”, which include water, lipid and haemoglobin [138]. The main absorbers of light in breast include β-carotene stored in adipocytes (reflective of fatty tissue) and haemoglobin found within red blood cells (reflective of vasculature). Absorption of these molecules occurs in the visible spectral range (450 – 600nm) of the electromagnetic spectrum [139]. When light is absorbed, molecules extract energy. Absorption peaks are related to transitions between two energy levels in a molecule at a specific wavelength, therefore provide information about molecules response to light [134, 139].

2.1.4 Intrinsic Fluorescence

Fluorescence is a further interaction of interest in tissue optics. Here, light energy is absorbed by fluorophores in the tissue (either endogenous or naturally occurring or else exogenous molecular probes) and then re-emitted at a longer ‘red-shifted’ wavelength [140]. Fluorescence in the visible and near infrared spectral ranges is typically a weaker interaction than scattering or absorption, although it becomes more significant for shorter wavelength (ultraviolet) illumination wavelengths. In breast tissue, inherent fluorescent molecules include nicotinamide adenine dinucleotide and hydrogen (NADH), flavin adenine dinucleotide (FAD), collagen, elastin and tryptophan and lipo-pigments [137].

NADH is a coenzyme integral for cellular metabolism [141] and NADH concentration changes during tumour progression [142]. Tumour growth causes a shift from oxidative phosphorylation to aerobic glycolysis [142]. NADH levels are expected to be higher in breast cancer tissue. Similarly, FAD is a coenzyme involved in cellular metabolism. FAD levels also change in breast cancer secondary to the metabolic requirements of tumour progression [143]. Normally NADH, acting as an electron donor, reduces FAD to FADH2. FADH2 is then oxidized to FAD following a few intermediate reactions [142, 143]. However, in tumour growth, there are more hypoxic conditions causing lower levels of FAD in breast cancer [143]. The NADH/FAD ratio is a more useful parameter in assessing the metabolic state of tissue [137].

2.2 Systematic Review and Meta-Analysis

Although there is an array of optical technologies being investigated worldwide, for the purposes of this thesis a systematic review was conducted focused on literature in which diffusely reflected light has been interrogated for breast cancer detection in the intra-operative setting. This focus on diffusely reflected light supports the basis of how instrumentation for experimental chapters in this thesis have been designed. Only papers that exploit endogenous breast tissue properties have been evaluated here, rather than studies relying on exogenous agents. To date, there has been no recent review appraising the effectiveness of technology which uses spectrally-resolved diffusely reflected light tested intraoperatively. This review enables the evaluation of the utilization of diffusely reflected light as a potential intraoperative margin assessment tool in breast conserving surgery and informs the work of this thesis with respect to the further research required to progress the field.

This review identified three optical imaging techniques capitalising on reflectance of light that may be sub-categorized into three related areas including a) diffuse reflectance spectroscopy (DRS) b) multi- or hyperspectral imaging (MSI/HSI) and finally c) spatial frequency domain imaging (SFDI). Figure 2.3 illustrates the hardware components and visual outcome of each technique.

2.2.1 Diffuse Reflectance Spectroscopy

Diffuse reflectance spectroscopy (DRS) measures the intensity of diffusely reflected light as a function of wavelength [144, 145]. To allow for DRS measurements a fibre optic probe is in contact with tissue. This probe contains several fibres, one of which is connected to a broadband light source and transmits light to the tissue being studied (Figure 2.3 A). Light is then diffusely reflected (sensitive to absorption and scattering) in tissue and collected by different fibres within the probe for measurement by a spectrometer. A spectrometer captures light through a narrow slit, which is then reflected onto a concave mirror. The collimating light beam that is produced, is directed onto a diffraction grating. The grating disperses the spectral components of light at

varying angles, which is then focused by a second concave mirror and imaged onto a detector. The detector measures the amount and intensity of light absorbed at each wavelength, and then digitalizes the signal as a proportional electrical signal which is displayed via a computer. Spectroscopy instrumentation is further discussed in chapter four (section 4.3). Important characteristics of the spectrum that is measured is the spectral resolution, which determines the closest wavelengths that can be determined and spectral range in which spectra are measured [146].

Tissue morphology determines the amount of absorption and scattering of light which can then be inferred from changes in the DRS spectrum [147]. Various methods allow the spectral analysis of diffuse reflectance, to enable the extraction of useful information about the optical properties of biological tissues. This is described as diffuse reflectance modelling. Most methods used to model diffuse reflectance from biological tissues involve approximations to the radiative transport equation (such as diffusion theory) which incorporate potential inaccuracies and deviations into the final model [148, 149]. Monte Carlo simulations is a commonly used method for spectral analysis [150]. This statistical method relies on calculating the propagation of many photons. Therefore, data processing requires long computational times [151]. To overcome this, machine learning methods may be utilized for data processing and these techniques are discussed in chapter four.

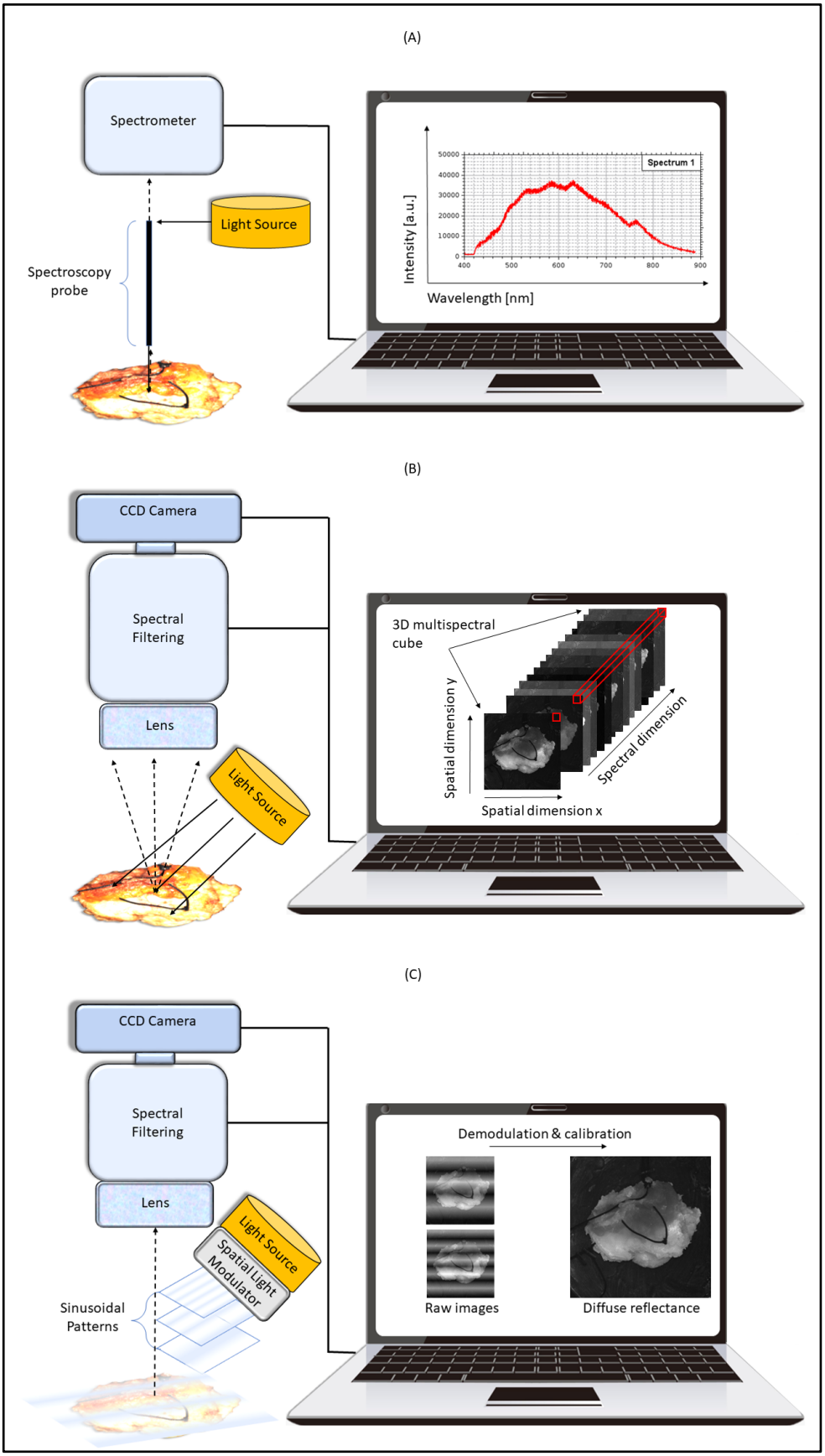


Figure 2.3 Schematic of the three imaging categories; (a) diffuse reflectance spectroscopy, (b) multispectral/hyperspectral imaging; (c) spatial frequency domain imaging. (A) With diffuse reflectance spectroscopy a probe is applied to a tissue sample. The probe delivers light to tissue in one fibre, and

in different fibres collects diffusely reflected light which is measured by a spectrometer. (B) Multispectral or hyperspectral imaging systems capture light reflected from a tissue sample via a lens, which has been illuminated with light from an external source. The spectral filtering component selectively disperses light according to its wavelength onto a charged couple device (CCD), which breaks the two-dimensional image elements into pixels. Each pixel (depicted by a red square) represents a spectral band of the electromagnetic spectrum. A three-dimensional data cube is generated which has spatial and spectral coordinates. (C) With spatial frequency domain imaging systems, a projector illuminates the target tissue area with a two-dimensional light pattern composed of various frequency modulations of a sinusoidal wave. The reflectance pattern of this sinusoidal patten is captured by the camera lens. The CCD component picks up the emitted diffuse light, which then undergoes demodulation by a computer to extract diffuse reflectance. Demodulation is a process that calculates amplitude modulation for every pixel of the image. Optical properties per pixel are extracted using light propagation models.

This review does not evaluate literature where exogenous agents have been given to enhance fluorescence. However, the use of fluorescence spectroscopy is evaluated 'intrinsic fluorescence spectroscopy (IFS)', as it is seen used with DRS in several studies. Here, the acquired fluorescence signal is leveraged to probe the presence of inherent fluorophores [152]. Fluorescence spectroscopy, as a separate entity, is not evaluated as it is outside the scope of this thesis. However, in chapter six the topic of fluorophores is discussed.

2.2.2 Multispectral/Hyperspectral Imaging

Spectral imaging is a technology that combines conventional imaging with spectroscopy (Figure 2.3 B), to obtain spatial and spectral information of an object [153]. Traditional optical imaging techniques such as red-green-blue (RGB) cameras only use three visible bands of light and have limited identification capability. Spectral imaging uses significantly more bands, helping to identify the alterations in tissue caused by tumour progression. Spectral imaging can be divided into either multispectral (MSI) or hyperspectral (HSI) categories, depending on the number of the acquired spectral bands, or else the spectral resolution [153]. Chapter five of this thesis elaborates on components of spectral imaging.

Multispectral or hyperspectral imaging systems contain a lens which captures light reflected from a tissue sample, which has been illuminated with light from an external source. Light enters the spectral filtering component, which selectively transmits light according to its wavelength. Like spectroscopy, this component disperses each wavelength of light to focus onto a charged couple device (CCD). A

CCD is a sensor that breaks the two-dimensional image elements into pixels. Each pixel represents a spectral band or part of the electromagnetic spectrum.

Image quality is paramount in spectral imaging to determine the amount of information about tissue being studied. Several parameters characterize the image captured including spatial resolution, lowest detectable signal, dynamic range, and field of view [146]. Spatial resolution determines the smallest discernible features amongst tissue being imaged, and depends on the signal quality, wavelength of light illuminating tissue, the aperture of the lens, magnification and pixel size of the CCD. Lowest detectable signal is reliant on the efficiency of the detector, noise level of the system and the numerical aperture of the optics. Dynamic range of the acquired data is defined by the ratio between the maximum and minimum measurable light intensities (white and black images essentially). Field of view (FOV) represents the maximum area that can be imaged [146].

The human eye only perceives light in the visible range (400 – 700 nm) which is a very small portion of the EM spectrum, but MSI/HSI systems frequently acquire bands from the ultraviolet through to the near infrared (NIR) spectral ranges. MSI/HSI creates a three-dimensional dataset called a ‘hypercube’ which has both spatial and spectral coordinates (Figure 2.3 B and 2.4) [154]. A three-dimensional hypercube is generated which is comprised of a set of two-dimensional images of a sample and records spectral information of each pixel in the image. Multispectral imaging provides discrete and discontinuous portions of the spectral range, whereas hyperspectral imaging uses a larger number of contiguous bands.

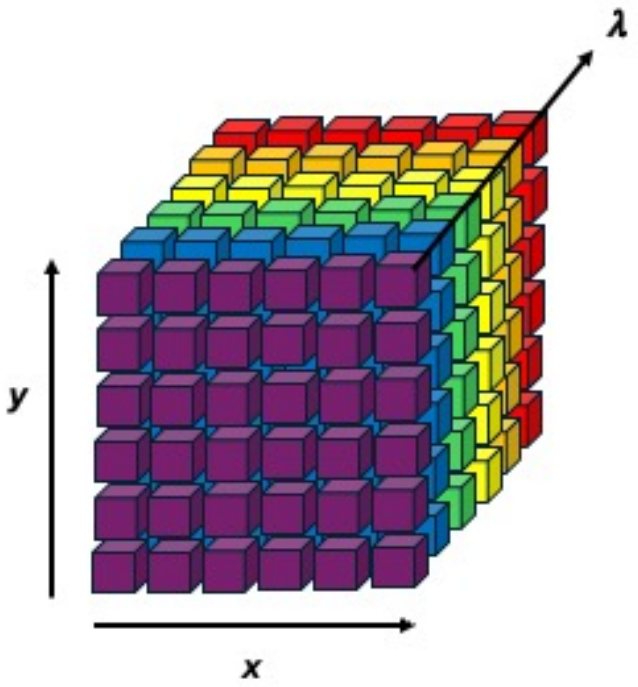


Figure 2.4 Illustration of a 'hypercube' produced from a spectral imaging data set. Each two dimensional small square (x,y) represents a pixel. Each three dimensional small square represents a spectral image (x,y,λ). A hypercube can be interpreted as an image (x,y) at each wavelength (λ), or as a spectrum at every pixel (x,y). (Modified from Garini *et al*.[148]).

The benefit of the NIR range is that it augments vision of the human eye and it has the ability to penetrate tissue from several millimetres (mm) to centimetres (cm) due to reduced scattering and absorption [155]. MSI/HSI allows for a greater surface area of tissue to be imaged in real time compared to probe-based DRS [156].

2.2.3 Spatial Frequency Domain Imaging

Spatial frequency domain imaging (SFDI) can separate the effects of the absorption and scattering of tissue. SFDI projects a two-dimensional light pattern onto a sample, which consists of sinusoidal stripes of varying spatial frequencies (i.e. stripes per mm) and a digital camera captures the reflectance image (Figure 2.3 C). Due to the absorption and scattering within the medium, the visibility of the projected pattern decreases, resulting in a measurable change in modulation depth. The demodulation is calculated for every pixel of an image for several spatial frequencies, from which a light propagation model can be used to extract the optical properties [157].

2.3 Methodology

2.3.1 Literature Search Methodology

Using the ‘Preferred Reporting Items for Systematic Reviews and Meta-analyses’ (PRISMA), a literature review was conducted. An electronic search of Medline, Embase and Scopus databases was conducted. Studies relevant to this review were identified from July 1985 to December 2021. Suitable search terms defining both ‘breast cancer’ and ‘breast surgery’; were identified. These were then combined using the Boolean operator ‘AND’ for search terms identifying the optical technologies being investigated in this review. The aim was to identify the use of the above three discussed modalities in the intraoperative setting, rather than the pathology setting. A combination of ‘Medical Subject Headings’ (MeSH) and free text words were identified to capture the various sections of the research question. Relevant papers were imported into Covidence software (Veritas Health Innovation, Melbourne, Australia) where duplicate papers were removed. The full search strategy is available in Appendix A. This review and meta-analysis were registered with PROSPERO (CRD 42022356216).

2.3.1.1 Study selection

Title and abstract screening were conducted according to pre-defined inclusion and exclusion criteria (Figure 2.4).

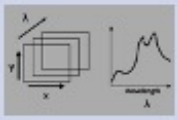
Inclusion Criteria	Exclusion Criteria
Only studies in the **English** language 	Studies using **contrast agents** 
Human subjects used 	Animal tissues 
Breast tissues evaluated using optical spectroscopy or MSI/HSI or SFDI (***in-vivo or ex-vivo***) 	Studies using **frozen samples** 
Diagnostic potential reported (i.e: **sensitivity/specificity**) 	Systems using a **single wavelength** 
Only conference abstracts where a substantial and **complete paper**, including clear methodology was available 	Papers which **did not record a multi/hyperspectral signal** (e.g modalities such as optical coherence tomography and confocal microscopy) 
Systems evaluating **surface pathology** in **a non-invasive manner** 	

Figure 2.5 Inclusion and exclusion criteria used to screen abstracts

2.3.1.2 Data Collection

Independent assessment of selected studies by two investigators (Dhurka Shanthakumar and Colm Kelliher (BSc student)) was conducted using Covidence software. Any conflicts were discussed and resolved with explanations of ‘yes’, ‘no’ or ‘uncertain’. All ‘uncertain’ cases underwent full text screening and were discussed with Dr Maria Leiloglou and Professor Dan Elson. A pre-defined Excel spreadsheet was used to collate the required information. Data extraction included sample size; wavelength of light; type of modality used and its type (i.e., probe geometry/imaging set-up); data acquisition time; tissue area sampled; tissue histological subtype under evaluation, and diagnostic accuracy to detect cancer.

2.4 Meta-Analysis

Before meta-analysis, studies were divided into two main sub-categories, namely either *probe-based* studies or *imaging-based* studies. Conclusions drawn from data analysis from these categories has informed designing experimental chapters four and six, and to ensure novelty within this thesis. Within these categories, further subdivisions occurred as depicted in Figure 2.5. Specifically, probe-based studies were divided into diffuse reflectance spectroscopy (DRS) or diffuse reflectance combined with intrinsic fluorescence spectroscopy (DRS-IFS). Imaging-based studies were divided into hyperspectral imaging (HSI) or spatial frequency domain imaging (SFDI).

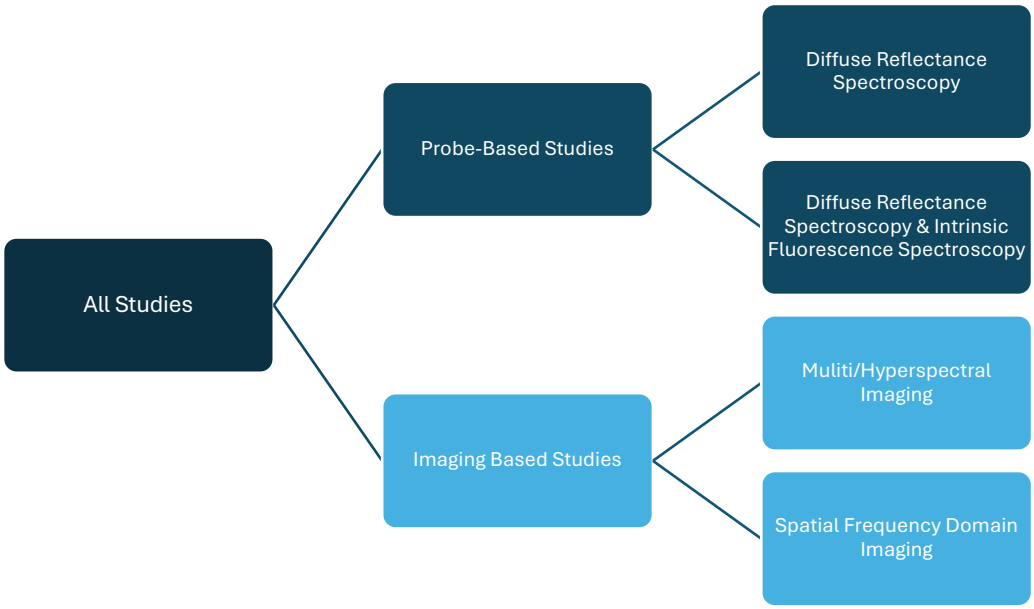


Figure 2.6 Studies were divided into probe-based (point based) or imaging-based studies (whole field-of-view). Within these groups further subdivisions occurred. Probe-based studies were divided dependent on the type of modality described in studies: diffuse reflectance spectroscopy (DRS) or DRS combined with intrinsic fluorescence spectroscopy, that is the probe system relies on the inherent fluorescent properties of breast tissue rather than when exogenous agents are given. Imaging based studies where subcategorized depending on the type of hardware components used: multi/hyperspectral imaging or spatial frequency domain imaging.

Heterogeneity between the studies for each main group, and subsequent group subdivisions was calculated using the Q statistic and was performed by Dr Maria Leiloglou. The null hypothesis was that the sensitivity (or the specificity) was the same in all the studies and that any in-between study variations in sensitivity (or specificity)

existed only due to sampling errors. After extraction of the Q statistic, the corresponding p-value was calculated with the use of the cumulative chi-squared distribution and with N-1 degrees of freedom, where N was the number of studies in each group. Alongside the p-value of the Q statistic, the posterior probability for heterogeneity Pr(Het|Q) was used as an in-between study heterogeneity indicator [158]. This probability was calculated according to Bayes theorem, taking into consideration the power of the Q test, the significance level used (a=0.05), and a prior probability for heterogeneity [159]. This prior probability reflected the observed in-between study heterogeneity including tissue samples and hardware equipment used, data acquisition / processing and ground truth extraction methods. In the cases where the null hypothesis could not be rejected, the posterior probability Pr(Het|Q) was close to the prior probability for heterogeneity for a Q test of low power or far from the prior probability for a Q test of high power. Both a fixed and a random effects model analysis were used to extract pooled sensitivity/specificity. Finally, the pooled sensitivity/specificity values for probe-based studies were compared with those of image-based studies with the help of the Q-statistic and chi-squared distribution. The same methodology was also used to compare the pooled results between the subdivisions (DRS; DRS-IFS; HSI; or SFDI) within the probe-based and image-based studies.

2.5 Results

The literature search identified 3614 studies, and nineteen of these studies met the inclusion criteria (Figure 2.6).

2.5.1 Categorization of Selected Studies

2.5.1.1 Tissue Optic Modality Type

Of the nineteen studies eligible for this study (Table 2.1), thirteen applied probe-based systems, and six studies used image-based modalities. Regarding image-based modalities, selected studies used the phrases ‘hyperspectral imaging’ and ‘spatial

frequency domain imaging'. Although the term 'multispectral imaging' was searched; no studies using this phrase were found for intraoperative application, although some of the hyperspectral studies may be termed multispectral depending on the preferred definitions.

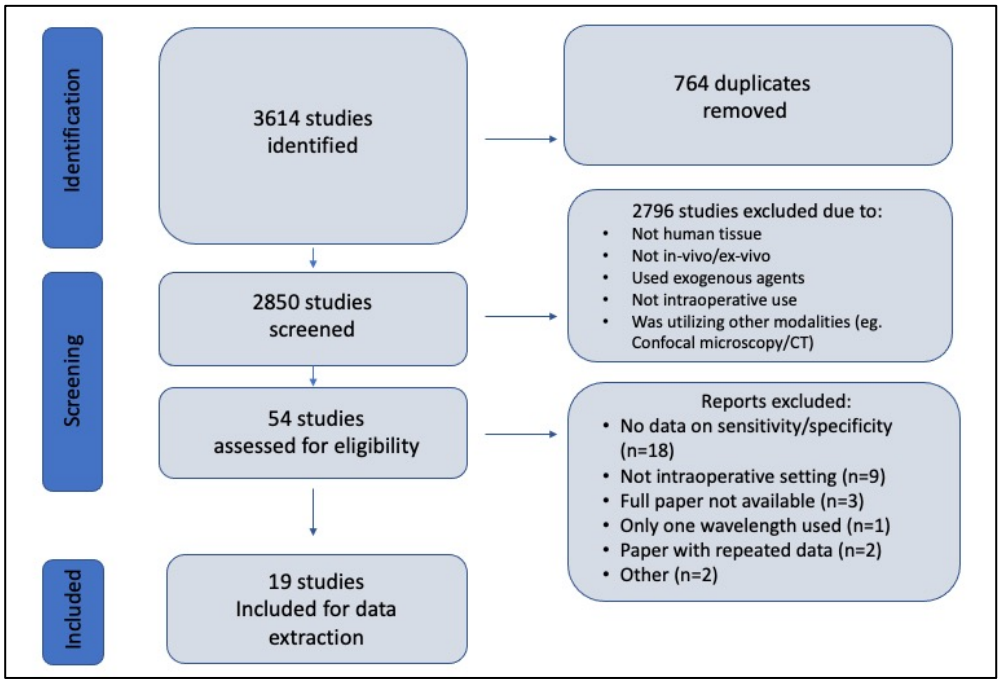


Figure 2.7 PRISMA flowchart highlighting the study selection process. Following electronic searches on Medline, Embase and Scopus 3614 studies were identified. 2850 abstracts were screened using the inclusion and exclusion criteria, from which 54 studies were then read in full text. 19 studies were utilized for final meta-analysis.

All studies used ex-vivo samples, and no in vivo work was identified. Most studies used the visible wavelength range [136, 147, 160-168], however six included the use of the near infrared range [169-175].

Table 2.1 Summary of modality and wavelength range for the technology being assessed in the selected 19 studies.

Author	Year	Modality type	Probe or imaging based	Wavelengths used(nm)
Nachabe[169]	2011	DRS	Probe	500-1600
de Boer[170]	2015	DRS	Probe	400-1600
Zhu[160]	2006	DRS	Probe	350-600
Brown[136]	2013	DRS	Probe	450-600
Evers[171]	2013	DRS	Probe	400-1700
Brown[161]	2010	DRS	Probe	381-630
Zhu[162]	2005	DRS-IFS	Probe	300-440
Volynskaya[147]	2008	DRS-IFS	Probe	300-800
Breslin[163]	2004	DRS-IFS	Probe	300-600

Keller[176]	2007	DRS-IFS	Probe	400-850
Palmer[164]	2003	DRS-IFS	Probe	300-600
Ramanujam[165]	2009	DRS-IFS	Probe	380-780
Keller[166]	2010	DRS-IFS	Probe	300-600
Pourezza-Shahri[167]	2013	HSI	Imaging	380-780
Kho[173]	2019	HSI	Imaging	953-1645
Aboughhaleb[168]	2020	HSI	Imaging	420-620
Kho[172]	2019	HSI	Imaging	450-1650
McClatchy[174]	2019	SFDI	Imaging	658,730,850
Laughney[175]	2013	SFDI	Imaging	658,730,850,970

2.5.1.2 Probe-Based Systems vs. Imaging Based Systems

An ideal IMA tool provides the surgeon with rapid visualisation of the region of interest. Of the nineteen studies, only six used whole field-of-view imaging modalities (Table 2.1). The rest all used probe-based technology to identify malignancy in breast tissue. The set-up of probe systems was variable (Table 2.2). Probe geometry varied in terms of being either single or multichannel; and inter-fibre distance varied.

Although the search term “Multispectral Imaging” was used, no papers were identified using precisely this term, hence imaging-based studies were divided into HSI and SFDI. The advantage of these technologies is that both a larger surface area of tissue can be examined with more rapidity. Certain studies quantified the maximum areas their technology can visualize (Table 2.3). The areas described (mean (StD)=x(y)) are significantly larger than that evaluated by any probe-based system.

Table 2.2 Characteristics of probe-based systems of studies included in this review. Parameters evaluated include probe geometry; acquisition time; area covered and probe depth. Not all papers documented such parameters.

Author	Probe Type	No. of fibres	Distance between fibres	Acquisition time	Sensing area	Probing depth
Nachabe[169]	Single (1.3 mm)	X3 200 um core diameter fibres; x1 connected to light source	2.48 mm	0.5 seconds	-	-
de Boer[170]	Single (1.75 mm)	-	1.5 mm	20 mins for 55 grid points (2.75 mins)	Probing volume = 1-3 mm^3	-
Zhu[160]	Single	Illumination core (19 fibres)	-	0.025 seconds/spectra	-	0.5 – 2 mm
Brown[136]	Multichannel (8 channels)	-	10 mm between each channel	10 mins per margin (8 spectra acquired per probe placement)	-	0.5 – 2.2 mm
Evers[171]	Single (1.3 mm)	X3 core fibres (x1 light; x1 NIRF and x1 visual spectrometer)	2.48 mm	0.2 seconds	5 mm^2	
Brown[161]	Multichannel (8 channels)	8 channel (19 illumination fibres; 4 collection fibres)	10 mm between each channel	40 seconds	1.5 cm x 5.5 cm	0.5 – 2.2 mm
Zhu[162]	Single	Illumination core (19 fibres); x3 collection rings (12 fibres)	3 illumination-collection separations 735/980/1225 um	1 minute (for 8 fluorescence spectra and 1 DRS spectra)	-	-
Volynskaya[147]	Single	1 delivery fibre; x6 collection fibres	-	1.5 seconds	-	100 um
Breslin[163]	Single	Central collection region; outer ring excitation fibres	-	-	-	-

Keller[176]	Single	x7 fibres – 300um, in a six-around-one configuration	-	100 milliseconds/spectra; 60 seconds per margin	25 mm x 25 mm	-
Palmer[164]	Single	31 fibres (central collection core diameter 1.52 mm; illumination ring outer diameter 1.5 2mm)	-	8 mins	-	1050 um
Ramanujam[165]	Multichannel (8 channels) with 19 illumination and 4 collection fibres in each	Illumination core (19 fibres – 200 um); x4 collection fibres (200 um)	-	-	-	-
Keller[166]	Single	Core (7 fibres – 300 um)	-	60-90 seconds per margin	-	-

Table 2.3 Parameters extracted from imaging studies included spatial resolution; area of field-of-view (FOV) imaging system can capture; time taken to image and depth penetration. Not all studies discussed these parameters.

Author	Modality	Type of HSI	Spatial Resolution	FOV	Time
Pourezza-Shahri[109]	HSI	Wavelength Filtering	150 Microns per Pixel	768 x 1024 pixels	1 minute
Kho[115]	HSI	Pushbroom	Each Pixel Equates to 0.5mm	200 lines scanned per patient (each line = 320 pixels)	4 seconds
Aboughaleb[110]	HSI	Pushbroom	Each pixel was 0.22 mm x 0.22mm	-	Capture time 5012 sec; Processing time 20 sec
Kho[114]	HSI	Pushbroom	0.16 and 0.5 nm/pixel	12.5 x 18 cm	20 sec for NIR; 40 sec for VIS
McClatchy[116]	SFDI	-	-	-	-
Laughney[117]	SFDI	-	30 spatial frequencies distributed between 0 and 0.33 mm-1	5.5 inch x 7.5 inch	10 mins, 360 images per specimen

2.5.1.3 Patient and tissue heterogeneity amongst studies

Patient and tumour related factors (Figure 2.8) can contribute to an increased risk of positive margins [25]. Patient related factors that must be taken into consideration include the patient's demographics such as age, body mass index, menopausal status, as well as breast density [28]. Pre-menopausal women have more fibroglandular tissue and denser breast tissue, and as referred to in chapter one breast density is a known positive predictor of a positive margin [26]. Very few of the evaluated studies provide a clear description of patient demographics.

Heterogeneity is a hallmark of cancer [177], with breast cancer being a highly heterogenous disease [178] with varying molecular and histological subtypes and immunophenotypes [178, 179]. Not only does breast cancer differ amongst patients (intertumour heterogeneity), but it also differs within each individual tumour (intratumour heterogeneity) [178]. This heterogeneity is a consequence of interplay due to intrinsic cancer cell traits and extrinsic microenvironmental factors [180]. Intrinsic cancer cell traits, including the ability to proliferate, migrate and invade, are due to the genetic profile of the cancer [180]. Extrinsic microenvironmental factors

include the degree of vascularization; tissue hypoxia and the interaction of cancer cells with surrounding tissue[180].

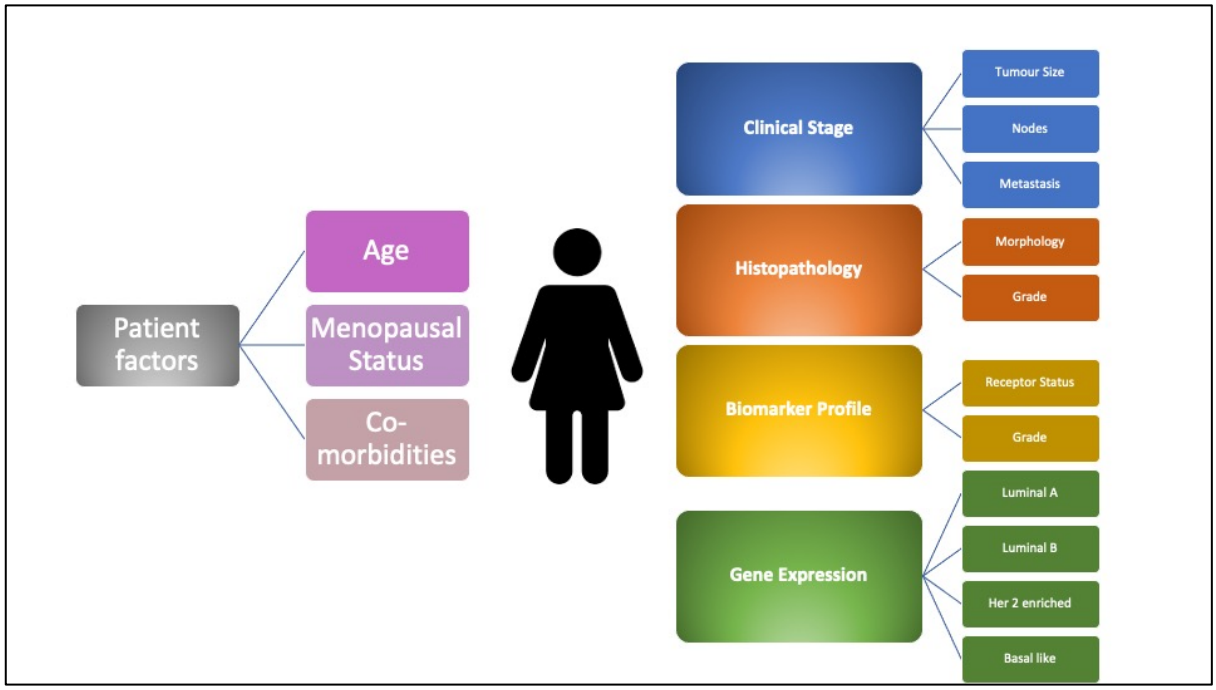


Figure 2.8 Schematic to show the patient related factors and tumour related factors that influence breast cancer heterogeneity.

An understanding of intertumour heterogeneity is crucial to plan breast cancer management. Histopathological classification of breast cancer is derived from tissue biopsy analysis and represents tumour heterogeneity. Tissue biopsy results provide information on tissue subtype, biomarker profiles and gene expression. The morphology of the breast cancer is identified by distinct features and then categorized into different types. Invasive ductal carcinoma (IDC) of no special type or not otherwise specified (NOS) is the commonest histologic subtype of invasive cancer, with up to 70% of patients having this morphological subtype [181]. Invasive lobular carcinoma (ILC) is the second commonest subtype with 5 to 15% of patients having this subtype [178]. Other less commoner subtypes include papillary carcinoma, tubular and mucinous. Ten of the reviewed studies here evaluated different histological subtypes (Table 2.4).

Biomarker expression is a leading factor in tumour heterogeneity. Biomarker profiles hold significant value in guiding patient treatment, and are an established prognostic factor in breast cancer [182]. The most important biomarkers relevant to

heterogeneity are hormone receptor status. These are assessed by immunohistochemistry (IHC). Oestrogen (ER) and progesterone receptors (PR) are sex steroid receptors found in the nuclei of luminal breast cells, and act as transcription factors [183]. In the UK up to 80% of invasive cancers are ER positive. Human epidermal growth factor receptor 2 (HER2) is another important receptor to be evaluated. This is a tyrosine kinase receptor, which when overexpressed, can drive tumour proliferation [184]. Up to 15% of early-stage breast cancers express HER2 [185]. Other biomarkers representing growth and proliferation (such as Ki67); and invasion and metastasis (such as p53) also have established prognostic relevance in breast cancer [178].

Gene expression analysis can identify one of four molecular subtypes breast cancer can fall into: luminal A, luminal B, HER2-enriched and basal-like [178]. From a clinical perspective, knowledge of a cancer's gene expression profile, can not only help predict survival but also guide which therapies are suitable [186]. Luminal A and B subtypes represent tumour heterogeneity within ER positive breast cancers. Although both express oestrogen receptors; luminal B have a higher expression of proliferation and cell cycle proteins. This contributes to the fact why luminal B has a poorer prognosis [186]. The HER2 enriched subtype encompasses tumours that express either ER-/PR-/HER2+ or ER+/PR+/HER2+. In comparison the basal-like subtype expresses neither hormone receptors nor HER2 and is regarded as 'triple negative'. The basal-like subtype is found more commonly in younger women and is more aggressive [186]. Receptor status such as oestrogen (ER), progesterone (PR) and HER2 dictate the modern medical management of breast cancer including neoadjuvant chemotherapy for triple negative, and ER-/HER2+ breast cancers. Only two studies included patients who had received neoadjuvant chemotherapy [166, 175].

As summarised in chapter one there are several well documented predictors for positive margins, namely the presence of ductal carcinoma in-situ (DCIS); lobular tumour type and a larger tumour size [25, 187, 188]. Therefore, any future IMA tool must be able to identify different histological subtypes. Table 2.4 illustrates that patients with lobular cancer were represented in only seven studies, and patients with DCIS only represented in nine studies.

Table 2.4 Highlighting patient ages and tissue types utilized in studies involved in this review. 15 studies characterized tissue samples into malignant and non-malignant types. Only 10 studies subdivided tissue types into various histological subtypes. (FA – fibroadenoma; IDC – invasive ductal carcinoma; ILD – invasive lobular carcinoma; DCIS – ductal carcinoma in-situ). Only 3 studies neither mentioned patient ages nor tissue types[163, 167, 170].

Author	Mean Age	Malignant Samples	Non- Malignant Samples	Adipose	Glandular	FA/Fibrous	IDC	ILC	DCIS
Nachabe[111]	-	9	73	43	23	7	21	0	8
De Boer[112]	-	25 (102 from tumour border)	42	-	-	-	-	-	-
Zhu[101]	-	35	50	39	1	10	28	1	2
Brown[86]	-	46	42	-	-	-	14	-	17
Evers[113]	52	59	148	79	37	32	30	5	24
Zhu[103]	-	13	34	20	2	12	7	4	2
Volynskaya[104]	-	9	95	31 samples were normal		64	9 samples were invasive		
Breslin[105]	48.4(51.5 for cancer)	20	36	21	15 samples were glandular/fibrous		16	2	1
Keller[118]	-	27	102	-	-	-	-	-	-
Palmer[106]	-	20	36	21	15 samples were glandular/fibrous		16	2	1
Keller[108]	-	34	145	-	-	-	-	-	-
Pourezza-Shahri[109]	-	14	33	-	-	-	-	-	-
Kho[115]	67+/-11	-	-	-	-	-	-	-	-
Kho[114]	57+/-11	13	18	13	5	-	10	-	3
McClatchy[116]	-	10	21	5	16 samples were fibroglandular		8	2	-
Laughney[117]	-	27	20	-	9	11	24	1	2

2.5.1.4 Diagnostic ability of different tissue optic techniques

Future intraoperative margin assessment tools using light-tissue interactions must have sufficient diagnostic accuracy to distinguish between normal and malignant tissue. In this review, I evaluated sensitivity/specificity of each optical imaging method. Table 2.5 summarises the number of tissue samples interrogated by either probe or imaging based studies (in relation to the number of patients and lumpectomy specimens), and the amount of spectral data acquired. Pooled sensitivity/specificity of each modality is represented in section 2.6. Diagnostic accuracy has been reported in five studies [163, 169, 171, 174, 175], however without the provision of true positive/negative rates for all studies I was unable to calculate pooled accuracy rates.

Table 2.5 Summary table of the number of breast tissue samples interrogated by probe based or imaging-based technologies from each study (in relation to the number of patients recruited and lumpectomy specimens). The number of spectral measurements were recorded where possible. Sensitivity and specificity of the ability to distinguish between normal and invasive malignant tissue is tabulated. Of note, some studies also noted sensitivity/specificity of the ability to identify DCIS however these figures were not used in pooled statistics.

Author	Modality Type	No.samples / locations	No. spectral measurements	No. lumpectomy	No. of patients	Sensitivity (%)	Specificity (%)
Nachabe[169]	DRS	102	980	-	52	91	95
de Boer[170]	DRS	169	169	16	-	100	100
Zhu[160]	DRS	85	-	-	45	83.9	88.6
Brown[136]	DRS	88	-	-	70	74	86
Evers[171]	DRS	207	1073	-	47	90	88
Brown[161]	DRS	56	-	-	48	79	66.7
Zhu[162]	DRS-IFS	47	-	-	18	61.54	82.35
Volynskaya[147]	DRS-IFS	104	202	-	17	100	96
Breslin[163]	DRS-IFS	56	-	-	32	70	71.1
Keller[176]	DRS-IFS	129	129	-	24	78	99
Palmer[164]	DRS-IFS	56	-	-	32	70	92
Ramanujam[165]	DRS-IFS	55	-	-	48	79	67
Keller[166]	DRS-IFS	-	179	-	40	85	96
Pourezza-Shahri[167]	HSI	47	-	19	-	99	98
Kho[173]	HSI	18	22000	6	18	93	84
Aboughhaleb[168]	HSI	10	-	10	-	95	96
Kho[172]	HSI	26	24539	-	42	98	99
McClatchy[174]	SFDI	31	50521	31	29	90	81
Laughney[175]	SFDI	59	265000	-	47	79	93

2.6 Meta-Analysis

2.6.1 Heterogeneity Results

The Q-statistic, interrogating the between study heterogeneity in sensitivity (or specificity) for each main group and subsequent group subdivisions are presented below in tables 2.6 and 2.7, respectively. In both tables, it is evident that p-values are greater than 0.05, and therefore the null hypothesis cannot be rejected. This suggests that a fixed effect model analysis would be appropriate to extract the pooled sensitivity/specificity. However, the pooled results from the random-effects model are also presented in the following section. This is because the power of the Q test is very low (3rd column), and the posterior probability for in-between study heterogeneity (4th column) strongly depends on the prior probability for heterogeneity.

Table 2.6 and 2.7 clearly demonstrate that in-between study variation in demographics, imaging equipment and geometry does exist. Therefore, a high prior probability for heterogeneity would be appropriate. However, here, we used a conservative prior probability of Pr(Het)=0.5 to demonstrate the strong dependence of the posterior (Pr(Het|Q)) on the prior probability (Pr(Het)).

Table 2.6 Heterogeneity based on probe-based studies versus image based studies. The posterior probability for heterogeneity has been calculated for a prior probability for heterogeneity of Pr(Het)=0.5.

Sensitivity Analysis				
	Q-Statistic	***P-Value***	***Q-Test Power***	***Pr(Het|Q)***
Probe Based Studies	17.48	0.09	~10-5	0.51
Image Based Studies	1.5	0.91	0.02	0.51
Specificity Analysis				
	Q-Statistic	***P-Value***	***Q-Test Power***	***Pr(Het|Q)***
Probe Based Studies	16.27	0.18	~10-5	0.51
Image Based Studies	0.92	0.97	0.02	0.51

Table 2.7 Heterogeneity based on modality subdivisions. The posterior probability for heterogeneity has been calculated for a prior probability for heterogenety of Pr(Het)=0.5.

Sensitivity Analysis				
	Q-statistic	***P-value***	***Q-Test Power***	***Pr(Het|Q)***
DRS	5.7	0.34	0.03	0.51
DRS with IFS	8.13	0.15	0.07	0.50
HSI	0.06	1	0.08	0.49
SFDI	0.29	0.59	0 (1 study)	0.51
Specificity Analysis				
	Q-Statistic	***P-value***	***Q-Test Power***	***Pr(Het|Q)***
DRS	7.2	0.21	0.05	0.50
DRS with IFS	8.29	0.14	0.67	0.26
HSI	0.35	0.95	0.08	0.49
SFDI	0.34	0.56	0 (1 study)	0.51

2.6.2 Pooled sensitivity/specificity results

Table 2.8 Pooled sensitivity/specificity results for probe based vs image based approaches – fixed (random).

Sensitivity Analysis			
	Pooled	Lower limit	Higher limit
Probe based studies	0.84 (0.83)	0.78 (0.76)	0.89 (0.90)
Image based studies	0.90 (0.91)	0.76 (0.82)	1.03 (1)
Specificity Analysis			
	Pooled		
Probe based studies	0.85 (0.85)	0.79 (0.78)	0.91 (0.92)
Image based studies	0.92 (0.92)*	0.78 (0.78)*	1.06 (1.06)*

Table 2.8 presents pooled sensitivity and specificity with the corresponding lower ($S_{\text{pooled}} - \text{S. E.}_{S_{\text{pooled}}}$) and higher ($S_{\text{pooled}} + \text{S. E.}_{S_{\text{pooled}}}$) limits for probe-based compared to image-based approaches. Similarly, pooled sensitivity/specificity has been calculated for modality subdivisions (presented in Table A4, Appendix A). The number outside the parenthesis represents the result from the fixed-effects model analysis, whereas the number in the parenthesis is the result from the random-effects model analysis. Results indicated with an asterisk (*) are categories where the Q-statistic was extremely small (Q<1). This means that the study heterogeneity within these categories was extremely small. The resulting tau-squared value (represents

the between-study variance) was negative and was set to zero. This resulted in: $w_i^* = w_i$ and the results of the random effects model match those of the fixed effects model.

The forest plots depicting pooled sensitivity/specificity are presented in Figure 2.9 for probe-based and imaging-based studies. The forest plots depicting pooled sensitivity/specificity for the occurred subdivisions within each modality can be found in Appendix A (Figure A1 - 2).

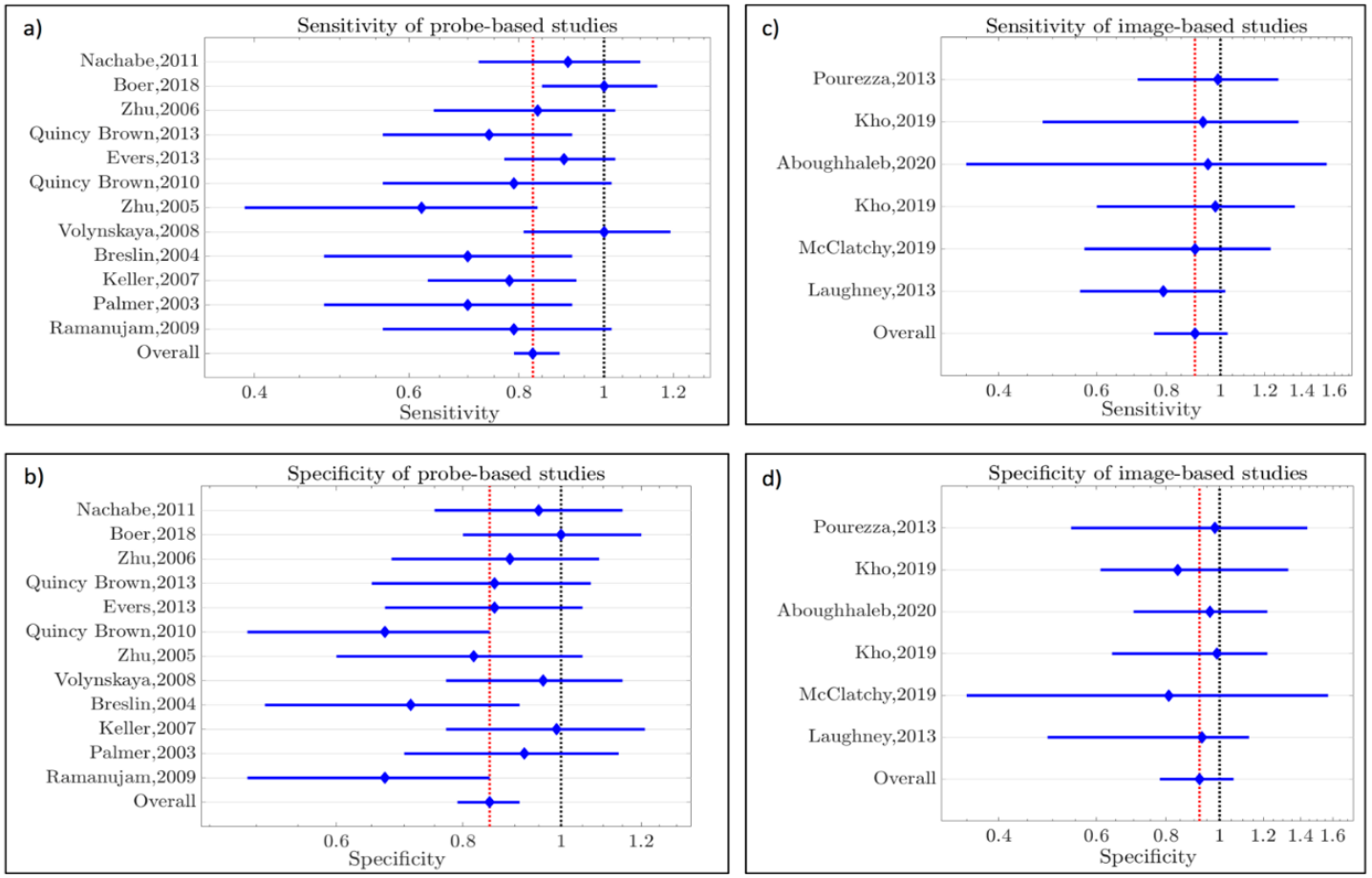


Figure 2.9 (a) Forest plot of the probe-based studies category where a fixed-model analysis provided a pooled sensitivity of 0.84, lower limit at 0.78 and upper limit at 0.89. b) Forest plot of the probe-based studies category where a fixed-model analysis provided a pooled specificity of 0.85, lower limit at 0.79 and upper limit at 0.91. (c) Forest plot of the image-based studies category where a fixed-model analysis provided a pooled sensitivity of 0.90, lower limit at 0.76 and upper limit at 1.03. (d) Forest plot of the image-based studies category where a fixed-model analysis provided a pooled specificity of 0.92, lower limit at 0.78 and upper limit at 1.06.

2.7 Discussion

2.7.1 Meta-Analysis on Probe Based vs Image Based Approaches

According to the results of the meta-analysis (presented in Table 2.8 and Figure 2.9), probe-based pooled sensitivity/specificity (0.84/0.85) was inferior to that of image-based results (0.90/0.92). However, when the Q-statistic was used to compare these pooled values, these differences were not statistically significant. There is insufficient evidence to support that probe-based modalities are inferior, however there are several reasons why this meta-analysis may have shown these findings. Firstly, superiority of imaging could be attributed to the recent/advanced image processing techniques used in these studies (e.g. U-Net, k-means clustering). Moreover, although the Q metric was extremely small for the image-based studies, it is unlikely that the in-between study variance was negligible as each of these studies employed different imaging instrumentation and image processing techniques. Table A5 in the appendix, highlights the variability in image processing techniques.

It is imperative to set into context the results with what available margin assessment methods are currently available, and Figure 2.10 depicts the sensitivity/specificity of traditional and emerging techniques from the published literature which have been discussed in chapter one (section 1.6). Probe-based techniques are comparable to the diagnostic potential of frozen section and ClearEdge™ and superior to micro-CT and MarginProbe®. Image-based modalities assessed in this review have much better sensitivity/specificity compared to traditional specimen radiography, and when compared to emerging imaging techniques such as Micro-CT are superior and equal to MRI.

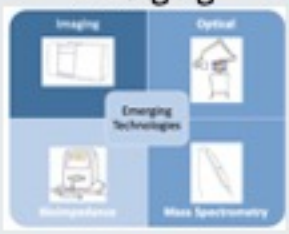
	Technique	Sensitivity (%)	Specificity (%)
Traditional 	Specimen radiography	53	84
	Frozen section	86	96
	Imprint Cytology	91	95
Emerging 	Micro-CT	68	69
	MRI	91	93
	MarginProbe	75.2	46.4
	ClearEdge	84.3	81.9
	REIMS	90.9	98.8

Figure 2.10 Conventional or traditional intraoperative margin assessment techniques are compared to emerging techniques in terms of sensitivity and specificity.

Another important consideration regarding comparisons between the diagnostic accuracy of probe-based and imaging systems, is statistical power. Although, sample size calculations were not reported in the investigated studies, the quantity of spectral data acquired from imaging approaches is greater than that of probe-based techniques. For example, Kho *et al.* gathered 224,861 spectra from 29 patients with his [169]. Similarly, SFDI produces large volumes of spectral data, with Laughney *et al.* gathering 265,000 pixels from 47 patients [39][189]. Comparatively, Keller *et al.* gathered 179 spectra from 40 patients.

A limitation of comparing probe-based to image-based approaches is that histological validation varied amongst the studies. Table 2.9 summarises the techniques used to correlate spectral readings to histological ground truth. The main difference noted is that with imaging techniques direct correlation with histology is more straightforward as pathologists were able to annotate regions of interest. Of note, with probe-based approaches, studies used a variety of methods to gain histological ground truth. Appreciating differences in methodology for ground truth extraction is crucial to help explain experimental data in experimental chapters four to six.

Table 2.9 Methodology used for ground truth extraction for probe and image-based studies

Author	Year	Modality type	How were spectra acquired?
Nachabe	2011	DRS	Pathologist identified macroscopically 5 different tissue classes on sliced mastectomy specimens
de Boer	2015	DRS	Pathologist identified macroscopically different tissue classes on sliced lumpectomy specimens
Zhu	2006	DRS	Probe placed on freshly excised specimen, and after that the location was inked and transverse sections sent for H&E
Brown	2013	DRS	Whole surface imaged; margin level analysis and site specific analysis
Evers	2013	DRS	Spectroscopy measurements taken from areas macroscopically identified by pathologist (x5 optical measurements per location); then biopsy from each area taken for histological comparison
Brown	2010	DRS	Optical research team place markers in region of interests which are scanned by DRS system. Pathologist is aware of these markers.
Zhu	2005	DRS-IFS	Probe placed on freshly excised specimen, and after that the location was inked and transverse sections sent for H&E
Volynskaya	2008	DRS-IFS	2 spectra per site acquired; sites chosen by pathologist from sliced tissue samples
Breslin	2004	DRS-IFS	Pathologist selected tumour or normal sites on mastectomy or lumpectomy specimens
Keller	2007	DRS-IFS	One point on each surface of lumpectomy specimen measured, trained pathologist available
Palmer	2003	DRS-IFS	Fresh samples cut (Minimum of 1cm x 3mm) and spectral measurements taken; a minimum of 1 cm had to be between normal and malignant areas
Ramanujam	2009	DRS-IFS	Margin level analysis with this multi-probe based system; 4 points each surface inked and correlation with final histology report
Keller	2010	DRS-IFS	One point on each surface of lumpectomy specimen measured trained pathologist available

2.7.2 Meta-analysis on modality sub-divisions

When comparing purely diffuse reflectance spectroscopy studies against DRS with intrinsic fluorescence spectroscopy studies, the sensitivity of the DRS approach (0.88 (95% CI: 0.82 to 0.95) – random model) was superior to the sensitivity of DRS combined with IFS (0.77 (95% CI: 0.67 to 0.87) – random model). The difference in sensitivities was not statistically significant using the Q-statistic (p=0.07). The difference was less prominent and not statistically significant (p=0.91) when

comparing specificity of the two approaches: 0.87 (95% CI: 0.78 to 0.95– random model) for DRS and 0.86 (95% CI: 0.75 to 0.96– random model) for DRS with IFS. Within the imaging studies, HSI was observed to have higher sensitivity|specificity (0.97 (95% CI: 0.78 to 1.16) | 0.95 (95% CI:0.76 to 1.14) compared to the SFDI studies sensitivity|specificity [0.82 (95% CI:0.64 to 1.01)|0.88(95% CI: 0.69 to 1.08)]. However, when using the Q-statistic, these trends were not statistically significant (p=0.28 for the sensitivity and p=0.63 for the specificity comparisons).

2.8 Future Work

In this review, I identified features that should be optimized in future optical IMA tools (Figure 1.10, section 1.6.3), previously summarized in chapter one, and will help drive experimental work in this thesis. In the visible wavelength range, blood is a principal absorber of light. Therefore, intraoperatively, blood on the surface being measured must be avoided, although we have not identified any studies in breast surgery which have explored this effect. De Boer *at al*. studied the use of an extended near infrared range (NIRF) range (1000 – 1600 nm) which reduces the effect of blood absorption of light [170]. Kho *et al.* found using the visible spectrum and NIRF could better identify areas of DCIS [172] and that in the NIRF range water and fat are the main absorbers of light [190]. Their HSI system could discriminate between benign and malignant tissues at a depth of 2 mm [190]. This spatial depth resolution could be deemed adequate as current clinical guidelines suggest clear margins of 1 mm can reduce the local recurrence rates [43, 191]. Comparatively, Aboughaleb *et al.* [168] have used only visible spectrum bands in their hyperspectral systems with good discrimination between normal and malignant tissue. Future work must explore what is the ideal wavelength in the in-vivo setting to achieve optimal spectral resolution. Algorithms trained on *ex-vivo* datasets may not be directly transferable to *in-vivo* applications due to physiological and structural changes in tissue post-excision. These changes include crystal formation, protein and enzyme denaturation, and disruption of cell membranes.

An ideal IMA tool gives the surgeon rapid visualization and tissue characterization of the region of interest. Only six studies used whole field-of-view imaging modalities (Table 2.3). The rest all used probe-based techniques, with variable experimental set-ups (Table 2.2). A limitation of probe-based techniques is that only a

limited surface area of tissue is sampled (around 1 mm^2), which means the region of interest may be missed. To survey a given resection margin of large surface area with reasonable resolution is difficult. Using a probe on multiple small areas of tissue can impose a time constraint in the surgical workflow. The use of a multi-channel device consisting of eight probes, was used in three papers included in this review [12,24,29]. A multichannel device can scan an area up to 4.5 x 9.5 cm (40 cm^2). This generates a spectral contour map. Brown *et al.* describe the strength of this multi-channel device as being able to focus on sensitivity of tissue discrimination, rather than spatial resolution [12].

Speed will be crucial to ensure any IMA tool used intraoperatively does not hinder surgical workflow. This review has identified the time taken to gather data from a margin edge or specimen can vary from seconds to minutes (Tables 2.2 and 2.3). Aboughaleb *at al.* reported a HSI image capture time from 5 to 12 seconds, with processing time of 20 seconds [168]. Similarly, Kho *et al.* developed a HSI system that takes 60 seconds to capture an image [172]. In comparison, SFDI systems take longer to image a specimen side, ranging from 5 to 10 minutes [192]. Evaluation methodologies of spectral readings is an important component of any optical system, and data processing techniques need to be optimized to allow for real-time feedback. Current spectroscopy-based classification procedures utilize signal processing methods such as k-nearest neighbours classification; principal component analysis, alone or combined with independent component analysis. The caveat to these algorithms is that they require a large database of cases with similar feature, to produce good reliability. This review contains studies of small sample size. Breast cancer is highly heterogenous, and any future work needs to include significant patient numbers to account for tumour and patient variability to train datasets accordingly.

Breast tissue is heterogenous, and when one takes into account if a patient is pre- or post-menopausal, further heterogeneity exists [193]. Pre-menopausal women have more fibroglandular tissue and denser breast tissue. Brown *et al.* wanted to take account of this interpatient variation. They discovered that patients with higher mammographic breast density were associated with higher baseline B-carotene concentrations and higher scattering coefficients [136]. Boer *et al.* identified that using the fat/water ratio is a good discriminator between benign and malignant tissue [170]. They recommend intraoperatively the surgeon should use the probe at benign spots to set a reference level [170]. Not all studies evaluated in this review have a clear

description of patient demographics, and future work should take this into consideration.

To ensure a tissue optics method is accurate in discriminating normal and malignant breast tissue, results must be correlated using histopathology. A weakness of the meta-analysis in this review is that studies used different methods to correlate optical spectral data with histopathology. A common challenge in this field is to develop robust classification algorithms, as often there is a spatial mismatch between optical measurements and histopathology. For instance, during tissue fixation by the pathologist there is tissue shrinkage and therefore the spatial correlations between the specimen and stained slides differ.

2.9 Conclusions

Future work on IMA tools must take into consideration several factors to create a rapid, non-contact device that confers accuracy in discriminating between normal and malignant breast tissue. Firstly, the wavelengths of light to be used in any device must be selected carefully. Spatial resolution and depth resolution will be crucial as identifying microscopic disease for example, is what will make an IMA tool useful to prevent re-excision surgery. Tailoring of these factors is essential to enable future IMA tools to have diagnostic accuracy rates similar or better to those discussed in this chapter. Speed and data processing time will be crucial to a surgical workflow pattern.

Chapter 3: Spatial Resolution of Optical Margin Assessment Tools

3.1 Relevance of Margins to this Thesis

The minimum distance between disease and a resection margin that defines a clear or negative margin is highly relevant to the functionality of technology utilising tissue optics such as our proposed multispectral camera. Firstly, spatial resolution as previously described in chapter one and two, is a measure of the smallest discernible detail an optical imaging system can display, affecting the clarity and detail of the resulting image. The spatial resolution of the imaging system(s) under study in this thesis will impact on the feasibility of the system for detection of disease at different margin widths. To be useful clinically, IMA tools should be able to identify macroscopic and ideally microscopic disease at a spatial depth resolution that parallels the accepted definition of a clear or negative margin (Figure 3.1 A). Chapter one described multiple risk factors for positive margins including lobular type breast cancer or DCIS, and it has been shown that margins in BCS can be deemed positive from regions of microscopic disease, so it is imperative any margin assessment tools used intraoperatively can distinguish small heterogenous areas of breast tissue.

Secondly, visible light can only penetrate tissue up to 2 to 3 mm [194, 195]. This can be considered a limitation of utilising tissue optics. It is valuable therefore to review the evidence to confirm that the current data supports minimum acceptable margin width within this spatial / depth resolution. (Figure 3.2 B),

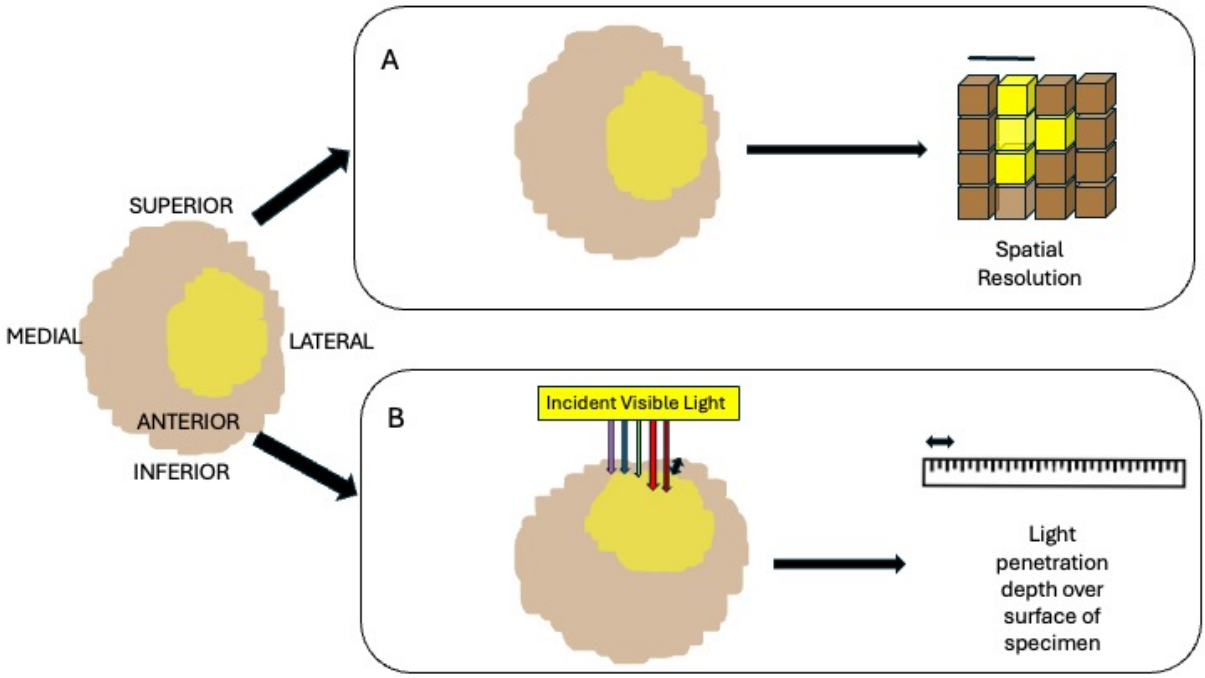


Figure 3.1 Schematic to show orientation of a wide local excision specimen following breast conserving surgery from the left breast of a patient, where the anterior and lateral aspects of the tumour are close to the surface of the specimen. The brown area represents healthy tissue, and yellow represents cancer cells. (A) If an intraoperative margin assessment tool utilising tissue optics is applied to the anterior surface of the specimen it should be able to discriminate between the healthy and tumour border, spatial resolution. A 1 – 2mm spatial resolution is possible between different tissue types. (B) Visible light of the electromagnetic spectrum covers a range of wavelengths from 380 to 750 nm. Incident light separated into different wavelengths represents different colours represented by the vertical arrows. Here if a IMA tool is applied to the lateral surface of the excised specimen, light should be able to penetrate deep enough to identify cancer cells. Any real-time feedback to the surgeon in theatre would be useful to help guide them to know where to take further tissue to prevent re-excision surgery.

3.2 Impact of Margin Width on Oncological Outcome

Breast conserving surgery (BCS) is recommended for patients with early-stage breast cancer [16, 196]. As an oncological procedure, “clear” or “negative” margins is one factor that should be achieved to prevent the risk of local recurrence (LR). Two landmark papers have shaped international guidance regarding the definition of a minimum distance between disease and resection that defined a “clear margin” in invasive and ductal carcinoma in-situ (DCIS) breast cancer [43, 191]. In 2014, Houssami *et al.* published a key paper in which they investigated the association between margin width after BCS for invasive breast cancer and the odds of local recurrence [43]. The authors concluded that negative margins decrease the odds ratio of local recurrence (0mm (OR 1.47 (95% CI 0.67 – 3.2) versus 2 mm (OR 0.95 (95%

CI 0.54 – 1.67)). However, it was evident that increasing distance between disease and the resection margin beyond 2mm was not associated with a further significant reduction in the odds of local recurrence (at 5mm threshold margin distance OR 0.65 (95% CI 0.34 – 1.26)), allowing for follow up time [43]. They also observed that "close" margins increased the risk of LR, but the definition of "close" was not numerically stated as they combined margin threshold distances of 0 mm and less than 1 mm. Similarly, in 2016, Marinovich *et al.* conducted a similar meta-analysis but aimed to investigate the odds of local recurrence following BCS for DCIS and found that margin widths of less than 2 mm were inadequate [191]. In patients who received whole breast radiotherapy, the probability of a positive or close margins leading to local recurrence (tumour on ink (0 mm) or 1 mm) is 30.1% compared to 17.8% with a 2 mm margin threshold distance, or 15.6% with 3 or 5 mm [191]. Marinovich *et al.* found that the odds ratio for negative versus positive/close margin status was 0.53 (95% CI 0.45-0.62; p>0.001) [191]. Radiotherapy, systemic adjuvant therapy and clinicopathological factors are the other risk factors which affect local recurrence and overall survival [197-199], and both studies adjusted for these factors.

Other parameters to assess the impact of margin width distance on patient outcomes are contralateral breast recurrence, distant recurrence and overall survival. Contralateral breast recurrence is defined as a tumour in the opposite breast diagnosed more than 6 months from the detection of the primary breast cancer. In a retrospective study of 56,626 patients who had a positive margin following primary BCS, there was an increased risk of contralateral recurrence (HR 1.06, 95% CI 0.7 – 1.6) [200]. Distant recurrence is defined as a recurrence of breast cancer which has developed beyond the ipsilateral or contralateral breast, chest wall, or regional lymph nodes (ipsilateral axillary nodes, supraclavicular, or internal mammary lymph node). Bundred *et al.* report a pooled overall distant recurrence risk of 25.4% (95% CI 14.5% - 40.6%) if patients had positive margins (defined as "tumour on ink") at the time of primary BCS compared to a pooled overall distant recurrence risk of 8.4% (95% CI 4.4% - 15.5%) if margins were 'close', in their recent meta-analysis of 68 studies investigating the impact of margin width distance where patients were followed up for a minimum of 60 months [201]. The location of distant recurrence is known to impact clinical prognosis, with patients with bony metastases have better overall survival than those with visceral metastases [202]. Overall survival was also assessed by Bundred *et al.* who identified that positive or close margins (tumour on ink or <2 mm) is

associated with an increased mortality (HR 1.32 (CI 1.01 -1.73), p=0.05) compared to wider margins (≥2 mm) [201].

3.3 Global Variation in Margin Guidance

Despite a wealth of research evaluating the relationship between margin width and LR and survival [43, 203, 204], there remains no international consensus on what constitutes a precise “clear” resection margin for either invasive breast cancer or non-invasive breast cancer. A defined numerical value for a negative margin width is imperative to appreciate in this thesis as the spatial resolution and light penetration depth of the optical imaging systems to be explored in chapters four to six utilise visible light which we know penetrates to a depth of 2 mm.

3.3.1 Invasive Breast Cancer Margin Guidance Currently

Internationally, most breast groups agree that disease at the inked resection margin (i.e. margin=0 mm) is inadequate, as it increases the risk of ipsilateral breast LR by 2.4 fold for invasive breast cancer [43], and requires re-excision surgery to achieve clear margins [42, 201]. However, there remains no international consensus on what the precise distance from disease to the resection edge constitutes a minimum clear margin.

In the United Kingdom, the National Institute of Health and Care Excellence (NICE NG101) guidelines recommend re-excision if invasive disease is within one millimetre of a resection margin [205]. However, in the United States of America, the Surgical Society of Oncology (SSO) in collaboration with the American Society of Radiation Oncology (ASTRO) advise that for invasive disease provided there is “no tumour on at the inked resection margin” then re-excision is not required [206]. In Australia, further re-excision surgery is recommended for patients who are found to have invasive cancer present at radial margins (i.e. “tumour on ink”) [207]. Despite national consensus guidelines, within the UK national variation in what an accepted negative margin is varies as discussed in chapter one. Tang *et al.* demonstrated that in some centres “tumour on ink” was accepted [44]. The GIRFT report highlighted the

huge variation within the UK regarding re-excision rates as discussed in chapter one, ranging from 9 to 32%, with a national average of 19% [47]. The variation in what surgeons deem acceptable as a negative margin width may be a contributory factor to such re-excision rates. The most recent meta-analysis assessing the impact of margins on survival outcomes by Bundred *et al.* recommends a minimum clear margin of 1 mm should be achieved, and that international guidelines should be re-evaluated [201].

3.3.2 Current Ductal Carcinoma In Situ Margin Guidance

Despite DCIS being non-invasive disease, it is highly prevalent with The Sloane Project (a Public Health funded prospective cohort study looking at screen detected non-invasive breast neoplasia) identifying that 70% of the 9938 patients with screen detected DCIS required BCS [208]. Therefore, it is imperative that surgeons excise DCIS with a healthy rim of tissue, as clinically an inadequate margin contributes to a risk of local recurrence and can impact overall survival [191, 209]. Again, there is no international consensus on what a “clear” resection margin in patients with DCIS is.

The odds-ratio meta-analysis conducted by Marinovich *et al.* led to the SSO-ASTRO Consensus guidance recommending a minimum of 2 mm margins for BCS for DCIS [206] in the United States. However in the UK, the Association of Breast Surgery (ABS) consensus statement recommends DCIS should be excised with a minimum negative margin of 1 mm [210]. In January 2024, NICE NG101 guidelines further compound the controversy on margin guidelines by recommending that with DCIS re-excision surgery is advised to achieve a minimum clear margin of 2 mm. In Australia, further re-excision surgery is recommended for patients who are found to have DCIS present at radial margins (i.e. “tumour on ink”) [207].

3.4 Systematic Review and Meta-Analysis

3.4.1 Indication for Revised Systematic Review and Meta-Analysis

Prior meta-analyses seeking to guide practice in this area are either outdated [43, 191], with key trials subsequently being published [201], or suffer from methodological limitations that preclude recommendations on minimum margin distance. Each meta-analysis controlled for different clinicopathological factors known to influence oncological outcomes following BCS. With invasive cancer Houssami *et al.* [43] controlled for age, endocrine therapy, and year of recruitment whereas Bundred *et al.* [201] adjusted for age, cancer grade, nodal status and chemotherapy and radiotherapy. Comparatively, Marinovich *et al*. for DCIS adjusted for age, high grade disease, endocrine therapy and median year of recruitment [191]. Radiotherapy following BCS not only reduces the risk of local recurrence to 19%, compared to 35% without, but also improves survival [197]. In addition, boost radiotherapy to the tumour bed has been shown to improve loco-regional control [211, 212].

In the most recent meta-analysis for invasive breast cancer by Bundred *et al*. [201], the authors grouped patients based on quantitative margin width thresholds into “close”, “positive” or “negative” margins, inherently biased by assumptions on numeric categoric definitions [201]. Moreover, the analysis focused solely on hazard ratios (HR), rather than odds ratio (OR) and relative risk (RR) which are clinically more intuitive when counselling patients about risk [213].

This chapter represents an updated systematic review and meta-analysis of margin width on outcomes following BCS for invasive breast cancer and DCIS. The primary aim was to identify the impact of margin widths on the risk of local recurrence, and to justify a few millimetres penetration depth of light through tissue as sufficient for optical imaging. The secondary aim was to provide clinicians with a comprehensive updated evidence synthesis of all metrics for local recurrence. Here, for the first time, we sought to establish local recurrence outcomes for invasive cancer and DCIS, by presenting relative risk (RR), odds ratio (OR) and hazard ratio (HR) data of margin widths 0mm, 0.1-1mm, 0.1-2mm, >1mm and >2mm. Thus, to date, this is the only meta-analysis which concurrently reports on all local recurrence outcome metrics based on precise numeric margin widths. Moreover, this is the only meta-analysis that adequately controls for the effect of boost radiotherapy on local recurrence.

3.4.2 Methodology

3.4.2.1 Search Strategy and Selection Criteria

This systematic review was registered on PROSPERO (CRD42022308524). An electronic search on Medline and Embase was conducted to identify all English-language studies published up to October 1st, 2023. Search terms utilised were “breast cancer”, “ductal”, “invasive”, “local recurrence” and “margins”. A full search strategy adopted for each database is shown in the Appendix B1.

2644 abstracts were generated from the search strategy. Additionally, references cited in the included publications and previous published meta-analyses were investigated to identify additional relevant articles. The Preferred Reporting Items for Systematic Reviews and Meta-Analyses (PRISMA) guidelines were utilised for study selection. Covidence software (Veritas Health Innovation, Melbourne, Australia) allowed two reviewers (myself (DS) and Ahmed Ezzat (AE, Clinical Research Fellow)) to perform initial abstract screening. A further two reviewers were consulted when conflicts arose (Naomi Laskar (NL, Clinical Research Fellow) and Mr Daniel Leff (DRL)). Full text review was performed by these named reviewers, plus a further eight clinicians who are named in Appendix B2. Secondary full text review was performed by DS, AE, NL and DRL.

Inclusion criteria were defined, as follows: a) a clear definition of margin status and specified margin width (mm); b) minimum of 48 months follow up; c) receipt of whole breast adjuvant radiotherapy following BCS. Conference abstracts and case reports were excluded. An exception was made for one abstract recently published which contained data felt to be critical for this meta-analysis relevant to invasive breast cancer, and for which the authors provided us with the original raw data specific to this study’s requirements [214]. Therefore, all studies included were peer-reviewed. Studies in which patients received partial breast irradiation, via various techniques such as multi-catheter or balloon brachytherapy, conformal radiation therapy or intraoperative radiation therapy, were excluded [215]. Where margin width was not clearly defined or raw local recurrence data was not available for individual margin widths, these studies were excluded. We screened additional references by reviewing bibliographies of included articles and previous meta-analyses.

3.4.2.2 Data Analysis

Data was extracted from eligible studies within the following categories: study details, tumour characteristics, neoadjuvant and adjuvant therapies, local recurrence data as reported or computed per margin width. The following data were extracted regarding study details: study name, publication year, first author's name, study design (e.g. prospective or retrospective), median or mean age of patients, median or mean follow up period in months. In terms of tumour characteristics data on the median or mean tumour size, hormone receptor status and tumour grade were gathered. The proportion of patients within each study that received neoadjuvant chemotherapy, adjuvant chemotherapy or endocrine therapy and boost radiotherapy was noted. Local recurrence data extracted or computed included: total number of LR, LR per margin width; survival data where documented; re-excision rates and types of surgical procedures performed to manage recurrence. Data extraction was performed by all reviewers mentioned above and in Appendix B2. Study populations included in more than one article were only included in this meta-analysis once, and when relevant we used data from the most current article. Quality assessment was performed using the ROBINS-2 quality assessment tool by co-authors (DS, AE and NL) (Appendix B3). Where conflicts could not be resolved, final decisions were made by senior author DRL.

The primary outcome of the study was to compare the risk of ipsilateral LR based on subcategories of margin width (mm). The secondary outcome of the study was to report the level of risk using clinically translatable metrics (OR, RR and HR), to enable informed patient counselling in the clinical setting. Therefore, margins widths were numerically categorised based on the precise distance from the inked resection margin to invasive disease, as follows: tumour on ink (0mm), >0.1 mm to 1mm, >0.1 mm to <2mm, ≤1mm and ≥1mm, and ≤2mm and ≥2mm. For each margin width, the number of patients with local recurrence was recorded. Once data extraction was performed, odds ratio and relative risk were computed from the raw data. Where individual studies had reported hazard ratios and associated 95% confidence intervals (CI) these were extracted. Where possible data was extracted for the proportion of patients within each margin width who received neoadjuvant chemotherapy, adjuvant

chemotherapy and boost radiotherapy. Risk of bias was assessed using the ROBINS-I tool (Appendix) B3 [216].

3.4.2.2 Meta-Analysis

Meta-analysis to compute pooled OR, RR and HR was performed using DerSimonian and Laird random effects modelling [217] with support from a study statistician (Dr Hutan Ashrafian). Statistical heterogeneity within each outcome comparison was assessed by calculating the I^2 statistic. A value of less than 30% was considered low heterogeneity; between 30 to 60% moderate; and over 60% as high. Missing data for study-level confidence intervals was accommodated for analysis by single imputation. Here, the assumptions included homogeneity of variances, distribution normality, consistency of effect sizes, and correct specification of covariates. Subgroup and sensitivity analyses were performed to assess the effect of highly variable reporting of margins distances reported and local recurrences by obtaining summary estimates of OR, RR and HR across all reported margins. Statistical packages used were Stata: Release 13 and TX: Stata Corp (StataCorp LP, Texas, USA).

3.5 Results

This results section outlines demographic data and outcome measures in turn for both invasive breast cancer and DCIS.

3.5.1 Studies selected and demographic data

3.5.1.1 Invasive Cancer

This systematic review identified 2689 studies from the search strategy (Figure 3.2). The primary goal was to assess the RR, OR and HR for LR and following full text review 43 studies [218-260] were selected, yielding 72,357 patients. Included studies contained patients with a median age of 55 years (interquartile range 36 – 63.1). The

median follow up time was 76.8 months (interquartile range 47 – 159.6). Table 3.1 depicts characteristics of the studies selected; tumour characteristics; and data related to individual margin width categories. The median tumour size of participants was 1.8 cm (interquartile range 1.3 – 3).

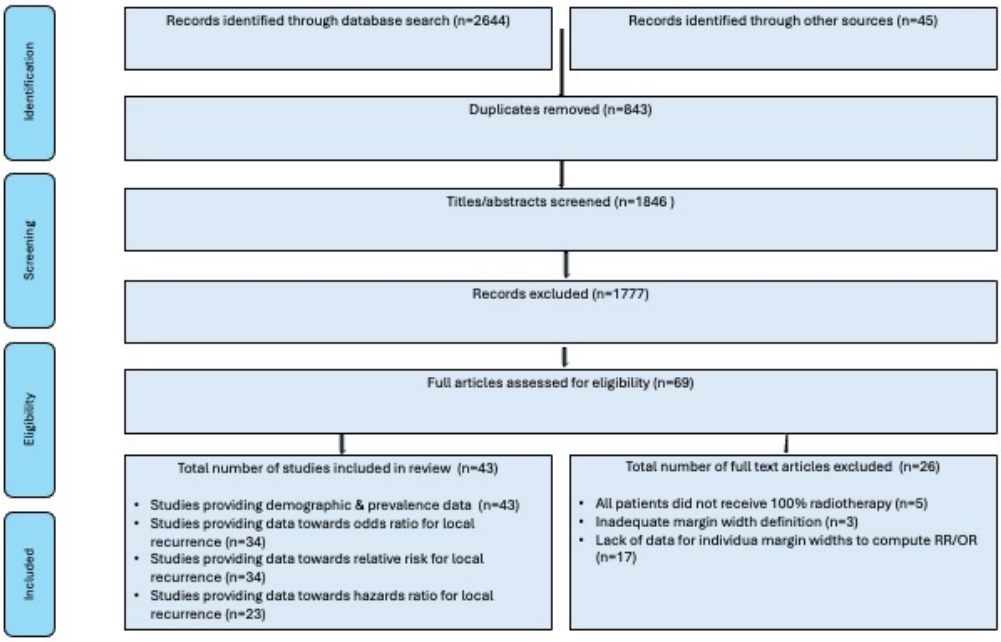


Figure 3.2 PRISMA diagram depicting how final studies for review were selected. Following the described search strategy on Medline and Embase, 2644 studies were identified and a further 45 were found from cross-referencing. Following removal of duplicates, 1846 study abstracts were screened by myself and Ahmed Ezzat. 69 full articles were reviewed, and data demographic data and outcome measures (OR, RR and HR) was extracted from 43 studies.

Table 3.1 Demographic data and tumour characteristics of patients with invasive breast cancer.

Variable		Number of included			
		Studies	Women	Proportion	%
Total no. of patients		43	72357	72357/72357	100
Study design					
	Retrospective	33	48303	48303/72357	66.8
	Prospective	10	24054	24054/72357	33.2
Age in years (Median or mean) **55 (36 – 63.1)**		29	37658	37658/72357	52.0
Follow up in months (Median or mean) **76.8 (47 – 159.6)**		42	68394	68394/72357	94
Tumour size in cm (median or mean) **1.8 (1.3 – 3)**		6	5151	5151/72357	7.1

Systemic treatment					
Neoadjuvant Chemotherapy					
	Yes	15	5668	5668/34798	16.3
	No	15	29130	29130/34798	83.7
	Unknown	28	37559	37559/72357	51.9
Radiotherapy					
	Yes	43	72357	72357/72357	100
	No	0	0	0/0	0
Boost Radiotherapy					
	Yes	27	32601	32601/56709	57.5
	No	27	26267	26267/57392	45.8
	Unknown	15	13489	13489/72357	18.6
Hormone therapy					
	Yes	30	27159	27159/53539	50.4
	No	25	22343	22343/45138	49.5
	Unknown	13	18818	18818/73436	25.6
Receptor status					
	ER positive	30	40300	40300/56880	70.9
	ER unknown	13	15477	15477/72357	21.4
	PR positive	14	16373	16373/33781	48.5
	PR Unknown	29	38576	38576/72357	53.3
Number of re-excision					
	Re-excision BCS	29	7109	7109/46245	15.4
	Re-excision Mastectomy	19	3384	3384/35094	9.6
Margin width					
Negative	All negative	32	35670	35670/46322	77.0
	Negative unknown distance	2	4204	4204/5993	70.1
	Negative >1mm	12	14551	14551/16607	87.6
	Negative >2 mm	17	16294	16294/22311	73.0
	Negative >10mm	4	621	621/2905	21.4
Close					
	Close 0.1-1mm	9	1516	1516/12647	12.0
	Close 0.1-2mm	18	3494	3494/34718	10.1
	>0.1 and <10 mm	5	14056	14056/15885	88.5
Positive (Involved margin)		36	5641	5641/63681	8.9
Unknown		5	7398	7398/72357	10.2
Tumour Grade					

	Grade 1	23	10697	10697/44111	24.3
	Grade 2	23	19013	19013/44111	43.1
	Grade 3	25	17818	17818/59414	30.0
	Unknown	12	1733	733/44759	3.9
Total number of Local recurrence (LR)					
Type of LR					
	DCIS	1	1	1/200	0.5
	Invasive	20	35864	1330/35864	3.7
	Unknown	19	1338	1338/36929	3.6
	Both	3	333	333/8777	3.8
LR per margin width					
	All negative	30	1206	1206/46469	2.6
	Negative >1mm	11	443	443/16426	2.7
	Negative >2 mm	17	556	556/22311	2.5
	Negative >10mm	4	27	27/2905	0.9
	Close 0.1-1mm	7	67	67/11521	0.6
	Close 0.1-2mm	15	165	165/32291	0.5
	>0.1 and <10 mm	3	384	384/13549	2.8
	Positive (Involved margin)	34	341	341/60082	0.6

3.5.1.2 Ductal carcinoma in-situ (DCIS)

For this section of the systematic review, a further 12 studies were included from bibliographic cross-referencing to add to the original 2644 studies screened. Following full text review, 31 [66, 208, 261-287] studies were included for meta-analysis yielding a total of 40,265 patients (Figure 3.3 and Table 3.2). The median (IQR) age of women was 55.5 years (53.1, 57.8), median (IQR) follow up was 86.4 months (69.2-100.2), and median (IQR) tumour size was 1.48 cm (0.8-2.0). Table 3.2 depicts characteristics of the studies selected; tumour characteristics; and data related to individual margin width categories.

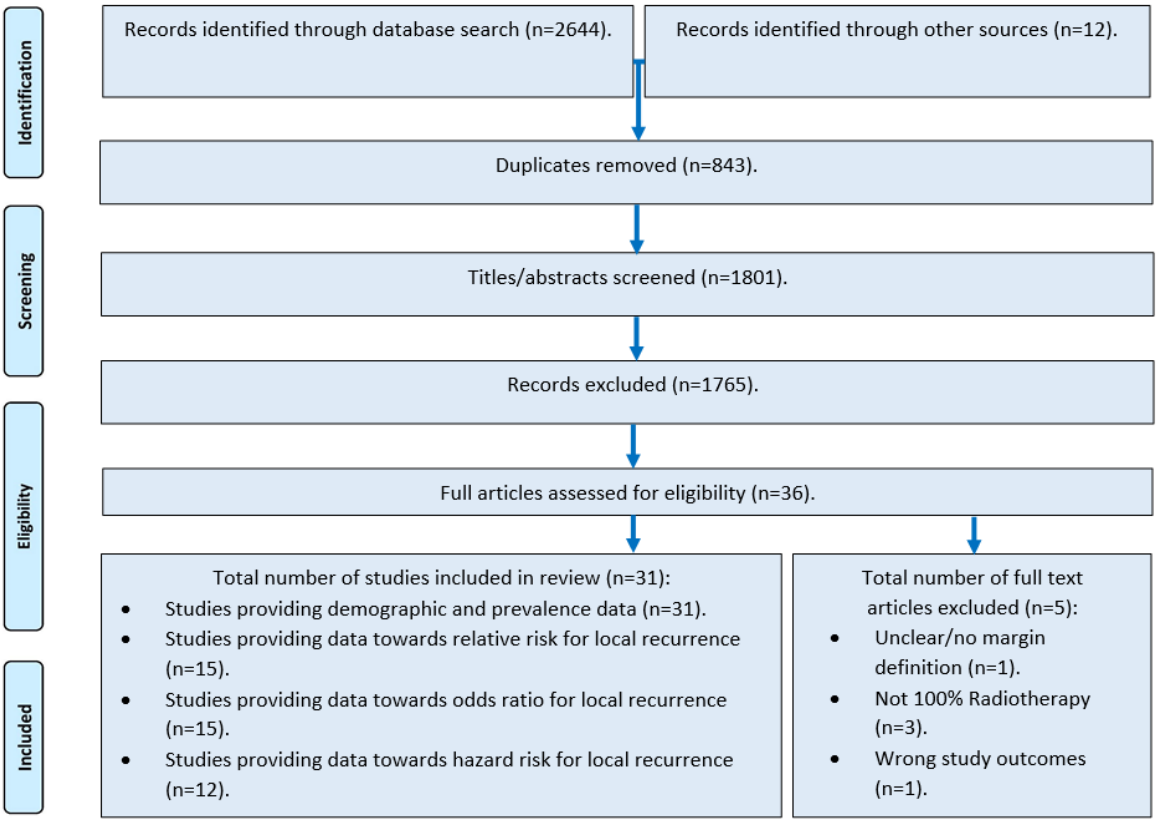


Figure 3.3 PRISMA diagram depicting how final studies for review were selected. Following the described search strategy on Medline and Embase, 2644 studies were identified and a further 12 were found from cross-referencing. Following screening of 1801 of abstracts, 36 studies underwent full text review and five of these were excluded to leave 31 studies where data was extracted for outcome measures (OR, RR and HR) and demographic data.

Table 3.2 Demographic data and tumour characteristics of patients with DCIS included in this study.

Variable		Number of included			
		Studies	Women	Proportion	%
Total no. of patients		31	40265	40265/40265	100
Study design					
	Retrospective	24	38095	38095/40265	94.6
	Prospective	7	2170	2170/40265	5.4
Age in years (Median (IQR)) 55.5 (53.1 – 57.8)		22	37023	37023/40265	91.9
Follow up in months (Median (IQR)) 86.4 (69.2 – 100.2)		28	37807	37807/40265	93.9
Tumour size in cm (Median(IQR)) 1.48 (0.82 – 2.0)		9	3272	3272/40265	8.1
Systemic treatment					

Whole Breast Radiotherapy					
	Yes	31	40265	40265/40265	100
	No	0	0	0	0
Boost Radiotherapy					
	Yes	18	4620	4620/7817	59.1
	No	20	3251	3251/8281	39.3
	Unknown	11	31984	31984/31984	100
Hormone therapy					
	Yes	13	8395	8395/30807	27.3
	No	15	21340	21340/29735	71.8
	Unknown	16	10530	10530/29735	35.4
Receptor status					
	ER positive	8	1983	1983/3527	56.2
	ER unknown	22	36446	36446/36446	100
	PR positive	5	1013	1013/2170	46.7
	PR Unknown	26	38095	38095/38095	100
Number of re-excision					
	Re-excision BCS	8	1214	1214/4607	26.4
	Re-excision Mastectomy	3	39	39/879	94.4
DCIS Grade					
	Low	15	987	987/10636	9.3
	Intermediate	15	3021	3021/10636	28.4
	High	16	6698	6698/12224	54.8
Margin width					
Negative	All negative	24	7412	7412/15149	48.9
	Negative unknown distance	2	68	68/452	15
	Negative >1mm	2	1237	1237/1568	78.9
	Negative >2 mm	11	2824	2824/4289	65.8
	Negative >10mm	11	3283	3283/9292	35.3
Close					
	Close 0.1-1mm	11	657	657/8300	7.9
	Close 0.1-2mm	12	2094	2094/11446	18.3
	>0.1 and <10 mm	11	3853	3853/9001	42.8
Positive (Involved margin)		12	456	456/10309	4.4
Unknown		8	565	565/4877	11.6
Total number of Local recurrence (LR)					
Type of LR					
	DCIS	19	638	638/31780	2

	Invasive	19	738	738/31903	2.3
	Not stated	4	7013	7013/7013	100
	Both	3	23	23/177	1.3
	Unknown	5	69	69/1020	6.8
LR per margin width					
	All negative	14	269	269/5867	4.6
	Negative >1mm	3	80	80/877	9.1
	Negative >2 mm	8	104	104/4451	2.3
	Negative >10mm	4	85	85/2127	4.0
	Close 0.1-1mm	6	41	41/1321	3.1
	Close 0.1-2mm	7	65	65/4628	1.4
	>0.1 and <10 mm	5	40	40/1293	3.1
	Positive (Involved margin)	7	59	59/4115	1.4

3.5.2 Overall pooled results of performance metrics

3.5.2.1 Invasive Breast Cancer

Figure 3.4 and Table 3.3 illustrate performance metrics from the meta-analysis. OR were extracted from 34 studies, however, following statistical analysis OR from only 18 studies were utilised accounting for 24,458 patients. Studies with OR data extracted were excluded if the confidence interval was found to cross the line of no effect as this may skew analysis. Of these patients, 1103 patients experienced LR. On comparing tumour on ink (TOI) vs no TOI, OR was 5.27(IQR 4.63 – 5.99) (Figure 3.4A). TOI vs ≤1mm OR was not able to be computed. For the comparison TOI vs >1mm the OR was 4·09 (3.20 – 5.23) and upon sensitivity analysis the OR was 4.18 (3.20 – 5.44) (Figure 3.4B). Comparing TOI to ≤2mm the OR was 2.51 (1.17 – 5.42) and for TOI vs ≥2mm the OR was 4.95 (3.71 – 6.61) (Fig 14A). OR was 4.32 (IQR 1.57 – 11.89) for 0.1 – 1mm vs ≥1mm, but with sensitivity analysis this group had a OR of 2.55 (1.21 – 5.40) (Figure 3.4 A & B). For 0·1-2mm vs ≥2mm OR was 5 (2.29 – 7.01) (Figure 3.4). Three margin width comparison groups (TOI vs ≥1mm; TOI vs ≤2mm; and 0·1-2mm vs ≥2mm) had low heterogeneity. The other comparison groups showed moderate to high heterogeneity.

RR were extracted from 34 studies, accounting for 57,531 patients. Within this study population, 2188 local recurrences occurred. Upon comparison between TOI vs no TOI, RR was 2.66 (IQR 2.33 – 3.1) (Figure 3.4 C and following sensitivity analysis RR was 2.98 (2.51 – 3.45) (Figure 3.4 D). For TOI vs ≤1mm, the RR was 2.11 (IQR 1.09 – 3.13) (Figure 3.4C), and upon sensitivity analysis the RR was 2.52 (1.37, 3.67) (Figure 3.4 D). RR was 4.02 (IQR 3.12 – 4.92) when TOI vs ≥1mm (Figure 3.4C), with sensitivity analysis highlighting a RR of 4.29 (3.29, 5.29) (Fig.14D). RR of 1.32 (IQR 0.71 – 1.93) when TOI vs ≤2mm and comparatively TOI vs ≥2mm yielded a RR of 3.01 (2.35 – 3.67) (Figure 3.4C). RR was 1.85 (IQR 1.14 – 2.56) for 0·1 – 1mm vs ≥1mm (Figure 3.4C); and RR was 1·44 (IQR 0.67, 2.19) following sensitivity analysis (Figure 3.4D). For 0.1-2mm vs ≥2mm RR was 2.33 (IQR 1.83 – 2.83) (Figure 3.4C). Across all margin width comparisons, heterogeneity ranged from low to moderate.

HR were extracted from 23 studies, accounting for 57621 patients. 6123 local recurrences were identified from the total study population. 18 of these studies were included in the recent Bundred *et al.* analysis [201]. On comparing TOI vs no TOI, HR was 1.42 (IQR 1.07 – 1.77). HR was 3.01 (IQR 1.31 – 4.71) when TOI vs ≥1mm. When TOI vs ≥2mm HR was 2.53 (IQR 1.44 – 3.63). HR was 0.69 (IQR 0.45 – 0.93) on comparing 0.1 – 1mm vs ≥1mm; and HR was 1.41 (IQR 0.93 – 1.90) for comparison of 0.1 – 2mm vs >2mm. TOI vs ≥1mm achieved a higher HR (3.01) compared with TOI vs ≥2mm (2.53). For all margin widths comparisons, depicted in Figure 3.4D, heterogeneity was substantial. The results of ROBINS-Q assessment are provided in Appendix B3.

Table 3.3 Pooled risk scores for ipsilateral locally recurrent invasive breast cancer based on varying threshold of resection margin width. (I2 = sample heterogeneity score, p = probability significance <0·05). ND = unable to compute.

	Local Recurrence				
	OR 95%CI (IQ range)	**OR (sensitivity analysis)** 95%CI (IQ range)	**RR** 95%CI (IQ range)	**RR (sensitivity analysis)** 95%CI (IQ range)	**HR** 95%CI (IQ range)
Tumour on ink vs No tumour on ink	5·27 (4.63, 5.99) p=0·141 I^2 =29.6% 14 studies	5·44 (4.76, 6.23) p=0·146 I^2 =30.7% 12 studies	2·66 (2·33, 3·1) p= 0·000 I^2 =67·5% 21 studies	2.98 (2·51, 3.45) p=0·000 I^2 =62.1% 18 studies	1·42 (1·07, 1.·7) p= <0·005 I^2=59·2% 10 studies
Tumour on ink vs <1mm	ND	ND	2·11 (1·09, 3·13) p= 0·058 I^2 = 59·8% 4 studies	2·52 (1·37, 3·67) p= 0·075 I^2 = 61·4% 3 studies	ND
Tumour on ink vs ≥1mm	4·09 (3·20, 5·23) p= 0·972 I^2 =0% 5 studies	4·18 (3·20, 5·44) p=0·951 I^2 =0% 4 studies	4·02 (3·12, 4·92) p= 0·270 I^2 =22·7% 5 studies	4·29 (3·29, 5·29) p=0·296 I^2 =18·9% 4 studies	3·01 (1·31, 4·71) p=<0·005 I^2 =80·1% 2 studies
Tumour on ink vs <2 mm	2·51 (1·17, 5·42) p= 0·923 I^2 =0% 2 studies	ND	1·32 (0·71, 1·93) p= 0·903 I^2 = 0% 11 studies	ND	ND
Tumour on ink vs ≥2 mm	4·95 (3·71, 6·61) p= 0.·116 I^2 =46% 5 studies	ND	3·01 (2·35, 3·67) p= 0·006 I^2 = 62·6% 9 studies	ND	2·53 (1·44,3·63) p= <0·005 I^2 =80·1% 2 studies

0·1-1mm vs ≥1mm	4·32 (1·57, 11·89) p= 0·007 I^2 =79·9% 3 studies	2·55 (1·21, 5·40) p= 0·932 I^2 =0% 2 studies	1·85 (1·14, 2·56) p= 0·102 I^2 =41.4% 8 studies	1·43 (0·67, 2·19) p= 0·934 I^2 =0% 7 studies	0·69 (0·45, 0·93) p= <0·005 I^2 =94% 3 studies
0·1-2mm vs ≥2 mm	5 (2.99, 7.01) p= 0·816 I^2 =0% 8 studies	ND	2·33 (1·83, 2·83) p= 0·071 I^2 = 36·6% 16 studies	ND	1·41 (0·93,1·90) p= <0·005 I^2 =64·1% 5 studies

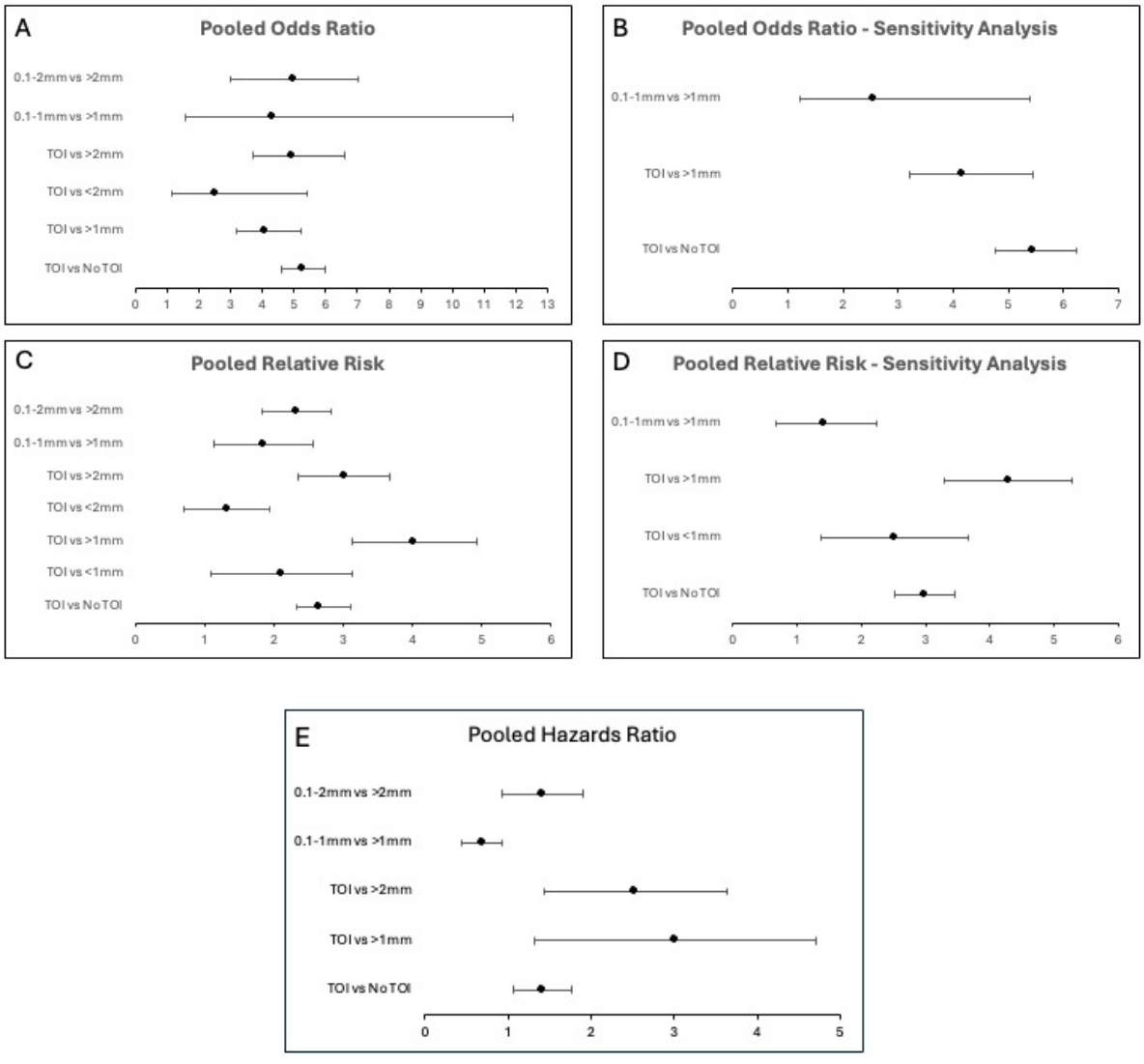


Figure 3.4 Forest Plot showing pooled results for different performance metrics of local recurrence of different margin comparisons for invasive breast cancer (A) Forest plot for pooled odds ratio (B) Forest plot for pooled odds ratio where sensitivity analysis performed (C) Forest plot for pooled relative risk

(D) Forest plot for pooled relative risk where sensitivity analysis performed (E) Forest plot for pooled hazards ratio.

3.5.2.2 Ductal Carcinoma In-Situ (DCIS)

Here, OR and RR was computed or extracted from 20 studies yielding 677 local recurrences from 13,270 patients. With OR the wider the margin width, the lower the risk of local recurrence. When TOI vs ≥2mm OR was 4·43 (95%CI 3·02-6·50; p<0·05) (Figure 3.5A and Table 3.4). In 0·1 – 1mm vs ≥1mm, the OR was 4·82 (95% CI 2·45-9·48; p<0·05 (Figure 3.5A). The odds of local recurrence remained statistically significant when comparing 0·1-2mm vs ≥2mm, the odds ratio was 3·36 (95% CI 2·04-5·56; p<0·05). Heterogeneity for OR range from low to high (Table 3.4).

Similarly, when RR was assessed for TOI vs ≥2mm, the pooled RR was 2·97 (95%CI 2·16-3·78; p<0·05) (Figure 3.5B). In 0·1 – 1mm vs ≥1mm, the RR was 2·88 (95% CI 1·86-3·90; p<0·05), compared with 0·1-2mm vs ≥2mm in which RR was 1·72 (95% CI 1·09-2·35; p<0·05). All between-group comparisons were statistically significant. Sensitivity analyses for the latter two margin width comparisons yielded lower RR. Heterogeneity for RR ranged from moderate to high (Table 3.4).

HR was extracted from 11 studies, yielding 790 local recurrences from 15,797 patients. 0mm vs ≥2mm HR (1·56, 95% CI 0·02-3·11; p<0·05), compared with 0·1-1mm vs ≥ 1mm, HR (1·34, 95% CI 1·01-1·67; p<0·05)(Figure 3.5E and table 3.4. When comparing 0·1-2mm vs ≥2mm, the hazard ratio was (0·76, 95% CI 0·59- 0·93; p<0·05).

Table 3.4 Pooled risk scores for ipsilateral locally recurrent disease in patients with DCIS based on varying threshold of resection margin width. (I2 = sample heterogeneity score, p = probability significance <0·05). ND = unable to compute.

	Local Recurrence			
	OR 95% CI (IQ range)	**RR** 95% CI (IQ range)	**RR** **(Sensitivity Analysis)** 95% CI (IQ range)	**HR** 95% CI (IQ range)
Tumour on ink vs No tumour on ink	3.07 (1.77 – 5.33) p=<0.05 I^2=0 % 2 studies	2.12 (1.13 – 3.12) p= <0.05 I^2 =67.9% 4 studies	ND	2.04 (1.3 – 2.78) p= 0.581 I^2=61% 6 studies
Tumour on ink vs ≥1mm	ND	ND	ND	1.97 (1.07 – 2.87) p= 0.455 I^2=80.1% 2 studies
Tumour on ink vs <2 mm	ND	1.61 (0.61 – 2.6) p= <0.05 I^2 =67.9% 4 studies	ND	1.53 (1.09 – 1.97) p= 0.464 I^2=72.9% 3 studies
Tumour on ink vs ≥2 mm	4.43 (3.02 – 6.5) p=<0.05 I^2=83.3% 4 studies	2.97 (2.16 – 3.78) p= <0.05 I^2=78.8% 6 studies	ND	1.56 (0.02 – 3.11) p= 0.547 I^2=72.9% 3 studies
0·1-1mm vs ≥1mm	4.82 (2.45 – 9.48) p=<0.05 I^2=93% 3 studies	2.88 (1.86 – 3.9) p= <0.05 I^2=85.1% 4 studies	0.51 (-0.65 – 1.68) p=0.31 I^2=72.9 % 3 studies	1.34 (1.01 – 1.67) p= 0.554 I^2=67.9% 4 studies

0·1-2mm vs ≥2 mm	3.36 (2.04 – 5.56) p=<0.05 I^2=42 % 3 studies	1.72 (1.09 – 2.35) p= <0.05 I^2=52.7% 10 studies	0.9 (-0.11 – 1.92) p=0.08 I^2=67.9% 4 studies	0.76 (0.59 – 0.93) p= 0.183 I^2=87.6% 2 studies

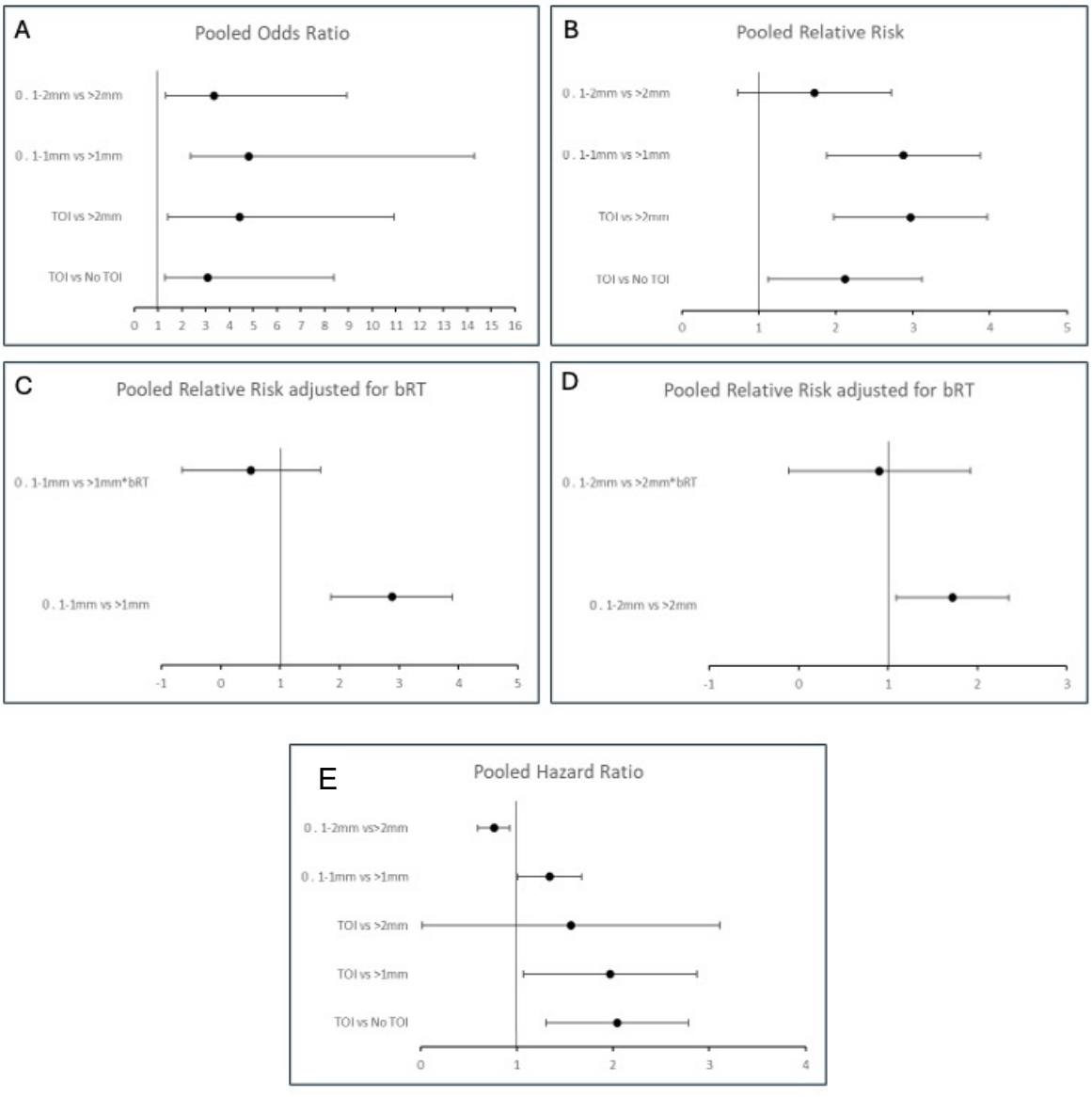


Figure 3.5 Forest Plot showing pooled results for different performance metrics of local recurrence of different margin comparisons in patients who had DCIS. (A) Forest plot for pooled odds ratio (B) Forest plot for pooled relative risk (C & D) Forest plot for pooled relative risk where adjustment has been made for boost radiotherapy (E) Forest plot for pooled hazards ratio.

3.6 Discussion

3.6.1 Justification of Optical Imaging Penetration Depth

The primary goal of this chapter is to appreciate if the limited penetration depth of light through biological tissue suffices for intraoperative breast cancer detection. Few studies document the risk of local recurrence for margin widths 3 mm or more. Regardless of whether invasive disease or DCIS, the majority of studies focus on a margin width range of 0 mm to 2 mm, as this is the common practice in breast surgery. Marinovich *et al.* found no statistical difference when comparing a margin width of ≥2mm to ≥10mm for DCIS following whole breast radiotherapy (OR 0.66, 05% CI 0.35 – 1.23), negating the requirement for a 10mm resection margin [191].

However, from this review it can be appreciated that the current dilemma is deciding whether a negative margin width should be 1mm or 2mm. Therefore, any intraoperative margin assessment tool utilising tissue optics with the ability to assess surface pathology on excised tissue can be justified.

3.6.2 Invasive Ductal Carcinoma

To our knowledge this is the first meta-analysis to report the association between margin width and all outcome metrics for local recurrence following breast conservation for invasive breast cancer. The results affirm what is already understood in the breast surgical field, that trends suggest the wider the negative margin the lower the risk of ipsilateral in breast recurrence. Compared to a resection margin width of more than or equal to 1mm, tumour at the inked margin was found to carry a four-fold risk of recurrence when assessing RR. Similarly, compared with a margin width ≥ 2mm, tumour at ink was associated with a three-fold risk and five-fold odds of in-breast recurrence. Moreover, when compared to tumour at ink, the risk and hazard of local relapse with any wider margin, 1mm, and 2mm were statistically significant. This increased risk of recurrence associated with tumour at the inked resection margin is commensurate with the results of other meta-analyses [43, 201] and supports

international guidelines and recommendations [24, 44] that a minimum clear margin has to be more than no tumour ink.

The main challenge is beyond no tumour on ink, and if the results of this analysis help support recommendations on a specific margin width surgeons should be aiming for. In this regard, the current results are novel as they shed light on the difference between a negative margin of >1mm compared to >2mm. In general, the trends suggest that compared to a close margin, wider margins >1mm and > 2mm lead to a reduction in the odds, risk and hazard of in breast recurrence.

Specifically, compared to a narrow margin defined as more than tumour on ink but less than <1mm and/or <2mm, margins greater than 1mm and greater than 2mm were associated with between four to five-fold reduction in odds and approximately twice the reduction in risk of local recurrence. However, of note, compared to narrower margins neither > 1mm nor >2mm led to a statistically significant decrease in recurrence once adjusted for chemotherapy, endocrine treatment and boost radiotherapy in sensitivity analysis. The current results are in line with the meta-analysis conducted in 2014 by *Houssami et al*. [43] in which the authors found that increasing the definition of a negative margin was not associated with a significant reduction in the odds of recurrence. This highlights the stability of these findings over time given this analysis includes more than double the number of patients as the prior analysis [43], and includes studies treated beyond 2009 with modern chemotherapeutic regimens. Similarly, the consistency in the results transcends different meta-analytical strategies (e.g. meta regression) and subtleties in adjustments in that prior analyses adjusted for age, proportion of oestrogen positivity, endocrine therapy, percentage undergoing re-excision, and type of recurrence [201]. Here certain barriers seen in prior work have been overcome by avoiding assumptions in meta-regressive analysis about the relationship between margin status (i.e. positive, close, negative) and margin distance and instead use exact margin thresholds.

The results of hazard ratio meta-analysis are interesting and support the findings of the recent analysis by *Bundred et al*.[201] in that both analyses show that compared to margins 0.1-2mm, margins >2mm are associated with a statistically significant decrease in the hazard of in breast recurrence. Unlike *Bundred et al*.[201] however, we did not observe an increase in recurrence for 0.1-1mm margins vs >1 mm [HR 0.69, 95%CI 0.45 – 0.93]. A likely cause for this disparity is differences in papers used in the meta-analysis due to differences in exclusion criteria. Specifically,

whilst *Bundred et al*.[201] included papers in whom 95% of patients received radiotherapy, this analysis only included papers in whom all patients received radiotherapy.

Due to a lack of reported data for margin width 1·1 – 2mm, firm conclusions cannot be drawn regarding the additional benefit of wider margins >1mm. Only 12% of patients from the total study population were reported to have margins and related LR data within the 0·1- 1mm, and 10.1% within the 0·1 – 2mm categories. Similarly prior meta-analyses also lack margin level data for these comparison groups [43, 201]. Therefore, there is not enough evidence to state that a clear margin of >2mm is required, because this review for the comparison group (0.1 – 2mm) may be confounded by a high proportion of patients in whom resection margins where in fact much closer to 0.1mm.

3.6.3 Ductal Carcinoma In Situ (DCIS)

This is the first study that concurrently reports RR, OR and HR for the impact of specific margin widths on local recurrence in DCIS, and has the largest number of patients since the landmark study of 2016 [191]. Within the margin width group 0·1-1mm vs ≥1mm, patients had a statistically significant increased risk of LR, by 4.8 fold. Following adjustment for boost radiotherapy within 0·1-1mm vs ≥1mm and 0·1-2mm vs ≥2mm, differences in local recurrence rates were no longer significant. These findings suggest that a negative margin of more than 2mm should be achieved to lower the risk of LR, and correlate with recently published guidance from the Association of Breast Surgery who recommend that it is critical to achieve this negative margin width [288].The findings are also compatible with current NICE NG101 guidelines and SSO/ASTRO [24, 206]. In relation to current practice in the UK, Tang *et al.* identified that 53.2% of breast units accept 1mm compared to 38% of units accepting 2mm as a negative margin width in patients undergoing BCS for DCIS, followed by whole breast radiotherapy [44].

It is universally accepted that DCIS found at the inked margin is inadequate and requires reoperative intervention. The NSABP B-17 trial reported DCIS found at the inked margin posed a two-fold relative risk for LR, compared with no disease found at the inked margin [289]. This meta-analysis compliments these findings, as all

performance metrics from this study showed a two or three-fold risk of LR when tumour on ink was compared to ≥0.1 mm. It also shows that achieving a negative margin of ≥2mm reduced the risk of local recurrence by three-fold.

The effects of boost radiotherapy have uniquely been assessed in relation to margin widths and LR risk here. The data suggests that when boost radiotherapy is applied to margin widths of ≥0mm but less than <2mm, the impact on local recurrence was no longer statistically significant. In 5897 patients of margin width group 0·1-1mm vs ≥1mm who received boost radiotherapy, there was an 82% risk reduction in the RR of LR (p=0.31), favouring boost radiotherapy. Comparatively, 2108 patients of group 0·1-2 mm vs ≥2mm, the relative risk reduction in LR with boost radiotherapy was nearly 48% (p=0.08). Chua *et al.* showed boost radiotherapy reduced local recurrence by 43%, so findings from this meta-analysis are corroborative [290]. Unlike this review, Chua *et al*. failed to evaluate margin widths 0.1 to 1mm, as their inclusion criteria was a margin width of ≥1mm. Similarly, Moran *et al.* observed that boost radiotherapy significantly reduced LR with a HR of 0.68 (95% CI 0.5 -0.91; p<0.05) irrespective of age, margin status and endocrine therapy [291].

As expected, this review identifies that DCIS at the inked margin or narrow margin widths are associated with a higher risk of LR, with the greatest risk TOI vs ≥2mm, followed by 0·1-1mm vs ≥1mm. If surgeons achieve at least 2mm as a negative margin we predict a risk reduction of at least three-fold for LR. This review therefore supports the recently updated recommendations from the ABS in October 2024, which concludes that DCIS should be resected with a 2mm negative margin [288].

This review also highlights that boost radiotherapy can mitigate the effects of DCIS not at the inked margin (i.e. ≥0mm). The novelty of findings of this review shows that if a margin is close (i.e. >0mm to <2mm) there is the potential option of re-excision or boost radiotherapy. However, patients must be counselled appropriately as boost radiotherapy has been reported to affect cosmesis, cause induration and increase the risk of breast fibrosis [290, 292, 293].

3.6.4 Limitations

It is evident that all studies included do not universally report demographic data or data regarding adjuvant therapy in the same manner. Radiotherapy regimes and doses were not clearly stated in all studies, and variation in radiation schedules and dosimetry may have confounded LR. Similarly, adjuvant endocrine therapy was not stated in 13 studies investigating invasive cancer for example. Only 6 studies of DCIS and margin width reported administrating boost radiotherapy [208, 270, 271, 274, 279, 292, 294]. Of these only two reported the actual dose delivered for relevant margin width groups [270, 294, 295].

With patient level data a more robust meta-analysis could have been performed allowing for meta-regression for confounding factors, which we know impacts local recurrence. Therefore, several factors, such as tumour biology, grade and immunophenotype influence the risk of local recurrence that have not been controlled in the meta-analysis for this chapter. For example, evidence suggests that triple negative and HER2 positive cancers increase the risk of local recurrence [296]. There is also a reported association between tumour grade and risk of recurrence, with higher grade tumours leading to increased local relapse (grade 2 HR 0.95; 95% CI 0.72 – 1.26; grade 3 HR 1.05; 95% CI 0.79 – 1.39)[297].

Certain studies have sparse data for given margin widths which may skew the relationship between margin width and local recurrence. Specifically, OR sensitivity analyses were limited by paucity of data within certain margin width groups (see Table 3.3 & 3.4, Figure 3.4 & 3.5). Therefore, the results presented here should be interpreted with a degree of caution, because each comparison group had different number of studies included.

Meta-analysis data for OR and RR had computed confidence intervals which can incur a statistical risk. These include introduction of analytical bias; under or overestimation of effect sizes; mass inconsistency effects across studies and sensitivity to outliers. It is noted that negative values were identified for example in RR for DCIS. Similarly, OR analysis could not be performed in some cases due to negative values resulting from logarithmic computations. This issue is highlighted by the discrepancy between the calculated OR for invasive disease in 37 studies and the OR sensitivity analysis, which included only 18 studies.

A challenge when categorising papers into different groups based on margin width is that for example when a margin was documented as ≥2mm, the margin could be as wide as 10mm or as narrow as 2.1mm. We accept that the lack of precise, exact, quantitative margin width may have influenced the results. Although for example overall adjuvant therapy figures may have been given, there was an inability to account for all confounding factors within this data. This was also noted within the Bundred sub-analyses.

Heterogeneity was observed among the computed metrics (OR, RR, and HR) due to variations in the number of studies included after logarithmic computations. Several OR category analyses could not be performed because of these computations.

3.6.5 Future Work

Future work in this field should aim to gather patient level data for invasive breast cancer and DCIS, to enable meta-analysis to not be affected by confounding factors. The main margin width categories that should be focused on are the 0.1 to 1mm, or 0.1 to 2mm group, as the paucity of data does not enable us to interpret results clearly. This may be in part due to the fact many studies predate when guidelines were set. However, for now, we conclude that the evidence base for the recommendations of clear margins of 1mm for invasive disease are insufficient.

In contrast, our analysis suggests that for DCIS minimum clear margins of 2mm are sufficient. There is also evidence from this work suggesting that for DCIS a radiotherapy boost mitigates the effects of disease within the margin width group 0.1 to <2mm and therefore is a potential alternate management option. A clinical trial can be advocated of invasive disease and DCIS to evaluate the use of boost radiotherapy in margin widths ≥0 - 1 mm, ≥0 - 2 mm and ≥2mm, to establish if the benefits in local recurrence are reproducible.

Chapter 4: Spectroscopy Use on Freshly Frozen Breast Tissue Samples

4.1 Introduction

Spectroscopy was presented in chapter two as a modality to discriminate between malignant and healthy breast tissue rapidly, with the view towards intraoperative margin assessment to improve precision of breast conserving surgery. Spectroscopy is also a fundamental component of any spectral imaging system. Chapter two discerns areas that need to be explored in studies that use spectroscopy to interrogate breast tissue in the intraoperative setting, accounting for the lack of tissue heterogeneity, examination of surface pathology of freshly excised specimens and machine learning for data analysis. The objectives of this chapter are to evaluate the efficacy of a custom-built spectroscopy probe to differentiate between normal and malignant tissue. Secondly, to determine the ability of the probe in differentiating tumour heterogeneity (e.g. ductal, lobular), given the varied nature of breast cancer biology. Lastly, the experimental set up of this probe and spectral data gathered from this first experimental chapter is used to inform the methodology of multispectral imaging experimental work in chapter five.

4.2 History of Optical Spectroscopy

In 1672 Issac Newton's fundamental work with prisms identified that white light could be divided into colours, as what we now identify as a "spectrum". In 1802, William Wollaston built the first spectrometer [298]. He used a lens to focus light from the sun onto a screen identifying an uneven distribution of colours the light was divided into [298]. He also observed dark lines where no light was cast [298]. In 1814, Joseph von Fraunhofer independently discovered these dark lines, "Fraunhofer lines', and was able to explain that these were a result of absorption of light by chemicals in the solar atmosphere [298]. Fraunhofer made significant contributions to spectrometer design

as he added diffraction gratings which allowed the wavelength of the cast coloured light to be determined [299]. In 1820, John Herschel investigated the infrared and ultraviolet regions of the electromagnetic spectrum and also showed that chemical compounds could be distinguished via their spectral signatures. In the mid 19th century Gustav Kirchhoff and Robert Bunsen showed that each element emits light at specific wavelengths, from their work with salts and metals [298].

4.3 Optical Spectroscopy

Optical spectroscopy is a point-based optical diagnosis technique. The interaction of light with a tissue surface culminates in various optical processes namely reflection, absorption, scattering and fluorescence, as previously discussed (see section 2.1). There are a wide range of techniques available for spectroscopic analysis of these processes, namely, diffuse reflectance spectroscopy, elastic scattering spectroscopy, Raman spectroscopy and fluorescence spectroscopy [300]. Depending on the wavelength region used, optical spectroscopy, is sensitive to the electronic structure of ultraviolet and visible wavelength forms (UV-VIS), and responds to the intramolecular bond vibrations of the infrared (IR) wavelength range [301].

4.3.1 Components of Optical Spectroscopy

An optical spectroscopic system incorporates a light source; an optical analyser with a detector (spectrometer); and a light transport conduit which is commonly a fibre optic cable [302].

4.3.1.1 Spectrometer

A spectrometer is defined as an instrument that separates and measures spectral components of a physical characteristic. It is an instrument that measures a continuous variable in which the components of the spectrum are separated from their original mix. Different variations of spectrometers exist including nuclear magnetic

resonance spectrometer, mass spectrometer and the most relevant for this thesis, optical spectrometer.

An optical spectrometer measures the consequences of the interaction of light (or electromagnetic radiation) with molecules [303]. More specifically, it probes the transitions between energy levels associated with either the electronic or vibrational degrees of freedom (associated with the UV-VIS or IR range, respectively) [304].

An optical spectrometer consists of one or several diffraction gratings, an optical path, and a detector array [305]. Figure 4.1 illustrates the components of a typical spectrometer.

4.3.1.2 Light source

Various light sources are found in a spectrometer including tungsten halogen, light emitting diode) LED, lasers or xenon arcs [299].

4.3.1.3 Slit

Light produced from a source enters the entrance slit. The size of the slit determines the amount of light that the instrument measures, but also the optical resolution of the spectrometer [299]. Resolution is improved with a smaller size slit. Slit size varies from 5 to 800 μm, with a height of 1 to 2 mm. The light beam becomes divergent after passing through the slit. This divergent beam is reflected on a collimating mirror, and therefore the beam becomes collimated. The collimated rays are directed towards a diffraction grating.

4.3.1.4 Diffraction Grating

A diffraction grating disperses light into its constituent wavelengths (essentially different colours) [306]. A grating is preferred to a prism as it can disperse colours over a larger angle but also across the UV, VIS and IR spectrum. Each wavelength of light is reflected from a different angle of the diffraction grating. Therefore, diffraction gratings vary in size to accommodate for this. Once light is reflected from the grating it becomes divergent again and hits a second mirror which focuses and directs light towards the detector.

4.3.1.5 Detector

Light spectra are captured by the detector. The detector is a CCD, photodiode array, or photomultiplier tube [301]. The detector measures the intensity of light as a function of wavelength. This spectral data is digitized and plotted onto software as a graph.

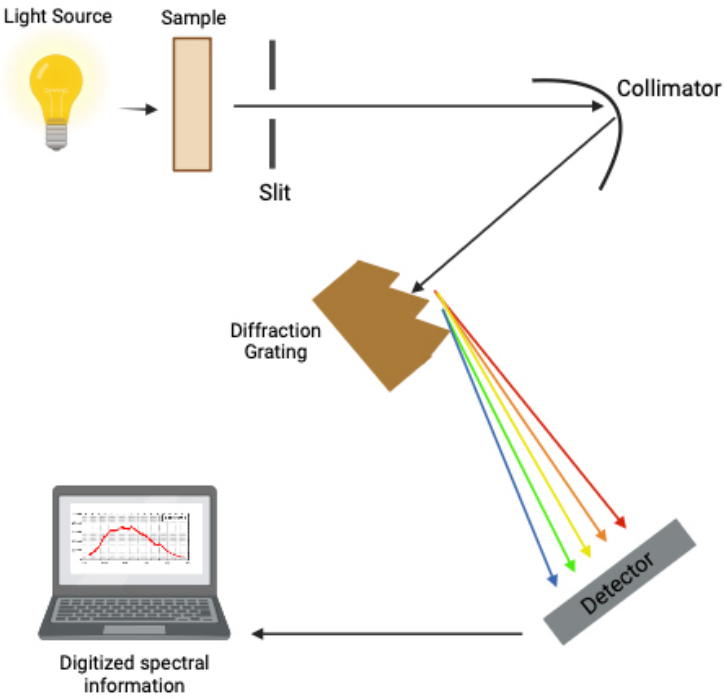


Figure 4.1 Schematic showing principal components of a spectrometer. A light source (commonly a tungsten halogen, laser emitting diode or xenon arc) emits light which passes through a slit, and the size of the slit determines the amount of light the spectrometer measures and influences optical resolution. Once the light hits a collimating mirror. The collimated light rays fall onto a diffraction grating which disperses light into its constituent wavelengths. Light spectra are captured by a detector which measures the intensity of light as a function of wavelength, and the information is digitized into spectral graphs.

4.3.1.6 Fibre

An optical fibre transmits light based on the principle of total internal reflection [302]. Commonly there are separate illumination and collection fibre paths to minimize background signals produced in the illumination fibre. A fibre consists of a core, cladding and a supportive jacket. The core is made from glass or plastic. The cladding is of similar material, however with a lower refractive index.

4.3.1.7 Diffuse reflectance probes

Reflectance is described as the elastically scattered light that escapes a tissue surface [307]. The mean free path (MFP) of a photon in turbid media is defined as:

$$MFP = 1/(\mu a + \mu's)$$

The diffuse reflectance signal is influenced by the absorption coefficient (μa) and scattering coefficient (μ's), and by analysing the reflected light across different wavelengths the optical properties of both of these coefficients can be extracted to reveal tissue composition.

The absorption coefficient (μa) determines how much of incident light is absorbed by chromophores within tissue and does not return to the surface as reflected light. Relevant chromophores in breast tissue are oxygenated and deoxygenated haemoglobin, lipids and water [138]. Chromophore concentration is one factor that influences the absorption coefficient, and it is known that adipose tissue contains more lipids whereas fibroglandular tissue and cancer contains more haemoglobin and water [308]. Each chromophore absorbs at different wavelength ranges producing a unique spectrum (oxy/deoxyhaemoglobin absorbs within 650-850 nm, whereas water and lipid absorb within 900-1000 nm) [309]. The wavelength of light influences the absorption coefficient as each chromophore contributes differently to the total absorption. Tissue type also influences the absorption coefficient, and in relation to breast tissue heterogeneity exist amongst patients in terms of breast density and between normal breast tissue and breast cancer [310].

The reduced scattering coefficient (μ's) quantifies the amount of scattering of light, whilst also considering the directionality (anisotropy) of scattering. The reduced scattering coefficient equates to:

$$\mu's = \mu s\ (1 - g)$$

where μs is the scattering coefficient, representing the probability per unit length a photon is scattered through medium, and g is the average cosine of the scattering angle probability. Here, g represents the anisotropy factor which ranges from minus

one to one. The anisotropy factor identifies how much scattering is forward-directed (if g =1 all scattering is forward, if g = 0, scattering is in all directions, if g = -1 scattering is only backwards). The reduced scattering coefficient is crucial in describing the diffusive reflective nature of light in tissues and influences the spatial distribution of reflected light. Relevant light scatterers in breast tissue are collagen and fibroglandular content.

Absorption and scattering properties are required to be extracted for DRS, and several techniques are used to do this, but with relevance to this thesis “multi-distance measurements” will be discussed. With multi-distance diffuse reflectance spectroscopy reflectance profiles are measured at multiple source detector separation. This technique is enabled by placing multiple detectors at different intensities from the light source, with separation distances range from 2 mm to 20 mm in tissue. By assessing reflectance at different distances, the individual contributions of absorption and scattering are more easily distinguished [311]. Different configurations of fibres within the probe help contribute to these different source detector separation distances. The end of a probe is either bevelled or flat surfaced, to enable optimal coupling [302].

4.3.1.8 Fluorescence spectroscopy probes

The components of a fluorescence spectroscopy probe differ, as here, fluorescence excitation is required. Fluorescence excitation is commonly achieved by lasers, which emit light at a wavelength selected to match the absorption peak of the fluorophore known to be within the tissue being studied, causing them to emit fluorescence [312]. When the laser hits the tissue sample, photons are absorbed by the fluorophores, causing their electrons to alter from a ground to an excited state [312]. Additional mirrors are used to remove infrared light from the main path to prevent excessive radiation [302]. A long pass filter is placed in front of the spectrograph to reduce residual background light from the excitation light source.

4.4 Methodology

4.4.1 Study Setting

Breast tissue samples were prospectively collected from patients undergoing elective breast conserving surgery or mastectomy at either Imperial College London NHS Trust (Charing Cross Campus) or Barts Health NHS Trust. Samples were collected immediately after the patient underwent surgery, and freshly frozen without any use of formalin. Tissue samples acquired from Imperial College London NHS Trust were collected either by myself or via the Imperial College Tissue Bank team. Comparatively, tissue samples from Barts Health NHS Trust were collected by the research team affiliated with Breast Cancer Now.

Imperial College Tissue Bank ethics (R21032-4A) and Breast Cancer Now ethics (REC ref no. 21EE0072) allowed prospective collection of tissues used in this study. The use of diffuse reflectance spectroscopy (DRS) on these tissue samples was approved with Integrated Research Ethics Approval (IRAS) [REC ref no. 08/H0719/37].

4.4.2 Spectroscopy Instrumentation

A custom-built experimental setup was constructed by Dr Vadzim Chaulau, which was used for data acquisition. This six-channel fibre optic probe utilises DRS-IFS. The system includes two broadband light sources (wavelength range 360 – 2400 nm) for DRS, halogen lamps Ocean Optics HL-2000-HP-232R and Ocean Optics HL-2000-FHSA-LL (Ocean Optics Inc., USA); spectrometer Ocean Optics USB4000-UV-NIR (Ocean Optics Inc. USA) with fitted fluorescence excitation rejection long pass 425-1000 nm filter OD=4 (Techspec (R) High Performance filter, Edmund Optics Ltd.), which detect spectra in the range 425 – 850 nm and used for registration of LIFS and DRS spectra, spectrometer Ocean Optics Flame-S-VIS-NIR (Ocean Optics Inc.) which detects light at a range of 400 – 1100 nm and used for detection of DRS spectra only. Fluorescence excitation sources were laser diodes NICHIA NDU1113E, 375 nm (Nichia Inc.,Anan, Japan) and Thorlabs DLS5146-101SP, 405 nm, installed in

Thorlabs laser diode drivers. A schematic of the experimental DRS-IFS system is presented in Figure 4.2.

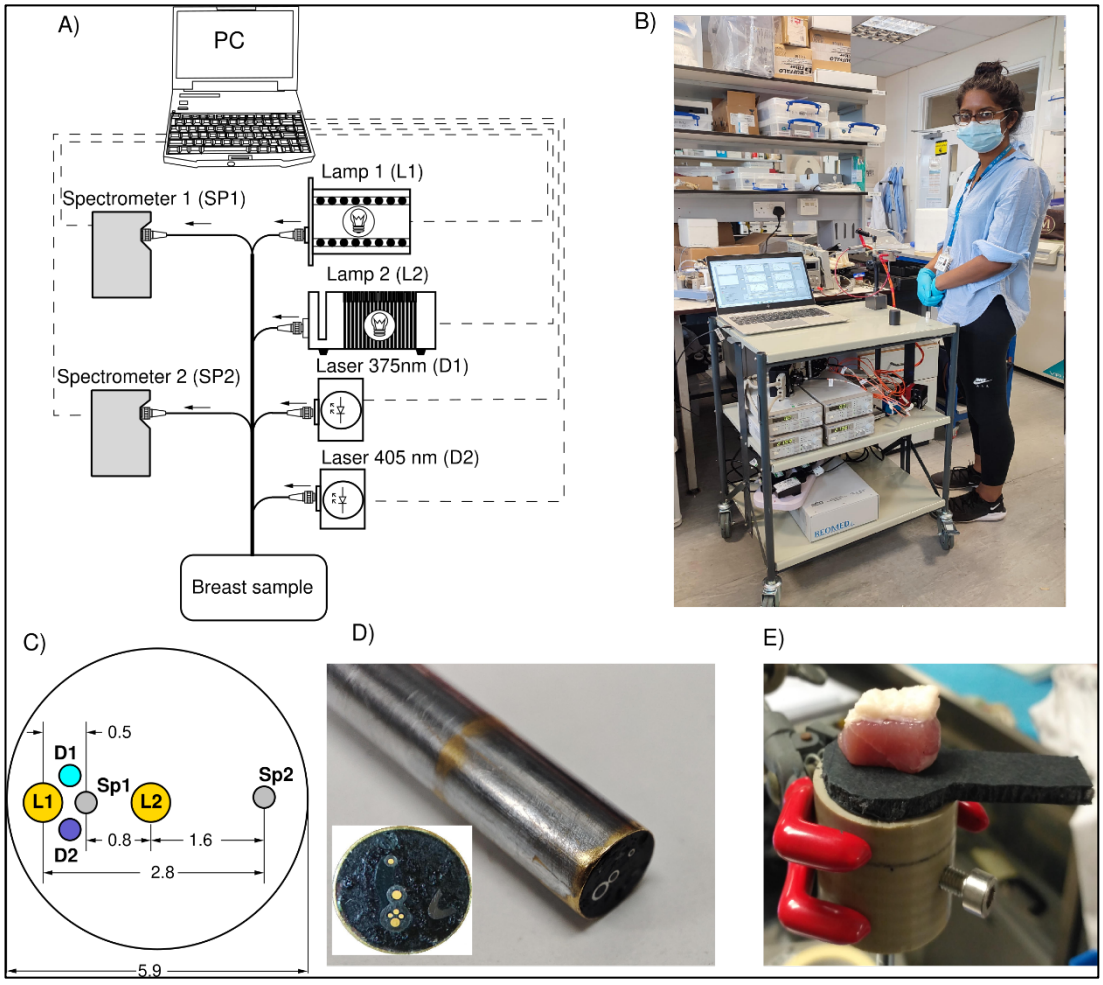


Figure 4.2 DRS-IFS experimental setup: a) Schematic of the components of the custom-built probe system illustrating two lamps (Lamp 1 (L1) and Lamp 2 (L2)) which deliver light in the wavelength range 360 – 2400nm; two laser diodes delivering light at wavelengths 375nm and 405nm for fluorescence excitation; two spectrometers detecting spectra in the wavelength range 400 – 1100nm. (b) Photographic illustration of myself in the laboratory with the spectroscopy probe set up with all components in situ. (c) Diagram of fibre configuration, where L1 and L2 are the fibres connected to the broadband DRS light sources, D1 and D2 are the fibres connected to laser diodes 405 nm and 375 nm, Sp1 and Sp2 are the fibres connected to spectrometer 1 (DRS and IFS) and spectrometer 2 (DRS) (d) DRS-IFS multifiber probe distal tip, inset –photograph of the fibre configuration (e) Sample holder and fibre optic probe with tissue sample.

Advantages of combining two light sources and two spectrometers include reduced acquisition time without loss of efficiency and a broader wavelength range coverage [313]. The acquisition time for the registration of four DRS and two IFS spectra of our custom-built system is 20 seconds. In other spectroscopy setups where there is one spectrometer and multiple light sources, there is a long acquisition time

[313]. Similarly, where there is only one light source, but multiple detectors are required, this incurs additional costs.

The originality of this custom built six channel probe lies within the distances between the different elements, as illustrated in figure 4.3. The probe tip incorporating all fibres was 5.9 mm in diameter. The distance of 0.5 mm between the first lamp and spectrometer enable sensitivity to scattering properties. The pathlength of 1.6 mm between the second lamp and second spectrometer fibres is relatively non sensitive to scattering properties. The distance of 2.8 mm between the first lamp and second spectrometer fibres allows sensitivity to light absorption, in the context of haemoglobin.

When autofluorescence is excited at 375 nm and 405 nm, spectrometers detect simultaneously two spectra at SDD 0.3 mm When DRS lamp one is enabled the spectrometers detect simultaneously two DRS spectra at distances 0.5 mm and 2.8 mm. When DRS lamp two is enabled, the spectrometers record simultaneously two DRS spectra at distances 0.8 mm and 1.6 mm.

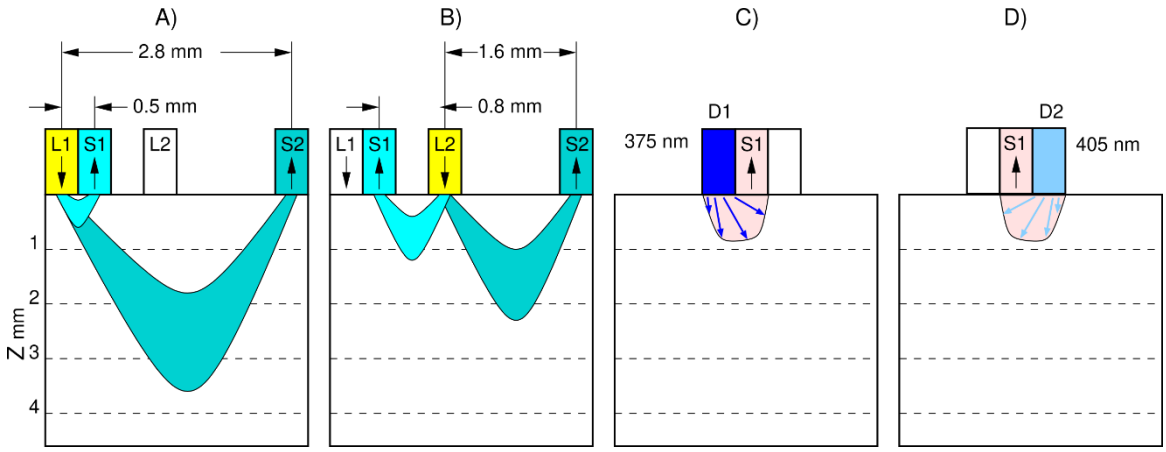


Figure 4.3 Acquisition of DRS and LIFS spectra: a) Lamp 1 is on and SDR spectra with source-detector separations 0.5 mm and 2.8 mm are registered; b) Lamp 2 is on and SDR spectra with source-detector separations 0.8 mm and 1.8 mm are detected; laser diode with wavelength c) 375 nm or d) 405 nm is on and IFS spectrum is recorded. Here, the Z axis represents the 'interrogation' depth in millimetres (i.e. depth in tissue from the surface).

4.4.3 Data Acquisition Protocol

Frozen breast tissue samples were thawed all the way through, and data acquisition occurred within 30 minutes of this. The DRS-IFS setup was calibrated in advance to allow for efficient workflow. A Spectralon® White Diffuse Reflectance Standard target

(Edmund Optics Ltd, UK) was used for DRS calibration, and a custom-built fluorescence reference of white fluorescent film was used for IFS calibration.

Each tissue sample was placed on a specimen holder on top of the multifibre probe (Figure 4.2E). A black plastic cylindrical cover was placed over the tissue sample to minimise contamination of ambient light. Firstly, data was acquired from the anterior surface of the sample by rotating the sample over the probe to capture 8 to 10 data acquisition points, at different orientations over the surface of the tissue. Data acquisition from multiple points was performed to ensure representation of the whole tissue sample. Each data acquisition pointed captured two autofluorescence spectra and four DRS spectra. The sample was then turned over to the posterior aspect and the above protocol was repeated. On average, 32 to 40 autofluorescence or 64 to 80 DRS (overall 96-120) spectra per tissue sample were acquired.

4.4.4 Histopathology Correlation

Macroscopic photographs of the tissue samples were taken sequentially and concomitantly with probe measurements to enable histopathological correlation (Figure 4.4a). Histopathology correlation was acquired via two methods depending on the source of the tissue sample. For 122 samples (from the Imperial College Tissue Bank), following data acquisition, the posterior aspect of the tissue sample was inked with a small yellow dot using tissue dye (Cancer Diagnostics Inc). The tissue samples were sent to histopathology in formalin; set in paraffin and then underwent haematoxylin and eosin (H&E) staining as per standard protocol (Figure 4.4b). Both anterior and posterior aspects of each sample were accounted for in this processing to correlate histological diagnoses with spectral data. H&E slides were interpreted by an experienced consultant pathologist, Dr Anna Silvanto, who was blinded to spectral data.

The remaining 59 samples (acquired from Breast Cancer Now Tissue Bank) had frozen section applied prior to being used for data acquisition. Each tissue sample had several slices taken (micrometre in thickness) and slides were read by a different experienced pathologist. Samples were only given to researchers for use if it was felt the whole sample represented the tissue type. Frozen section was performed on these 59 samples as per protocol of the Breast Cancer Now Tissue Bank.

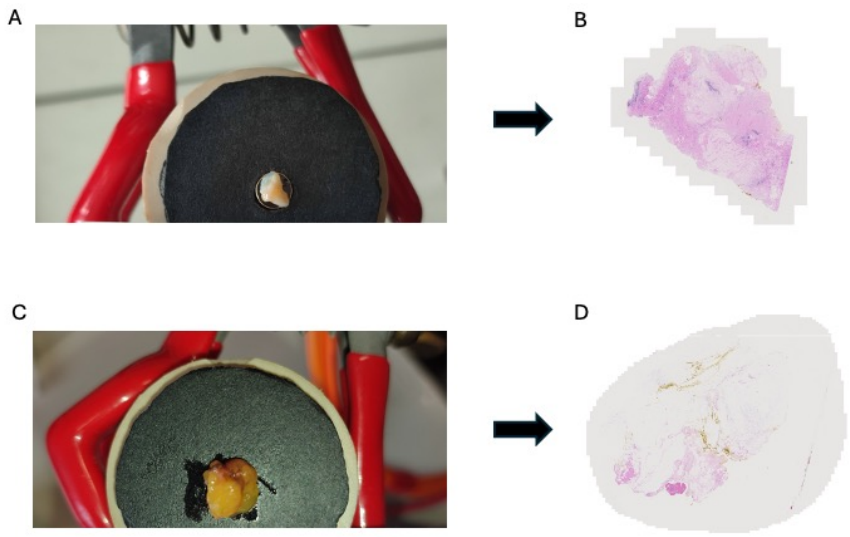


Figure 4.4 (a) Macroscopic photograph of breast tissue sample interrogated with our DRS-IFS system. (b) Corresponding histopathology slide image following review by an experienced consultant pathologist identified invasive lobular cancer. (c) Macroscopic photograph of a further breast tissue sample with normal breast tissue appearances. (d) Corresponding histopathology slide identifying healthy breast tissue.

4.4.5 Data Processing Techniques

Data processing was carried out in two phases and was performed by Yufeng Shi and Ria Ranjiktar (Imperial Masters' students) under the supervision of Professor Daniel Elson and Dr Vadzim Chalau. Firstly, spectral processing, followed by spectral classification. The components of each of these phases is depicted in Figure 4.5.

4.4.5.1 Pre-Processing

Pre-processing of spectral data was performed to account for inter-sample heterogeneity, background light, and signal quality variability. To account for these variabilities' normalization and noise reduction of spectra were performed. The processing technique applied to our acquired spectral data is described below (Figure 4.5).

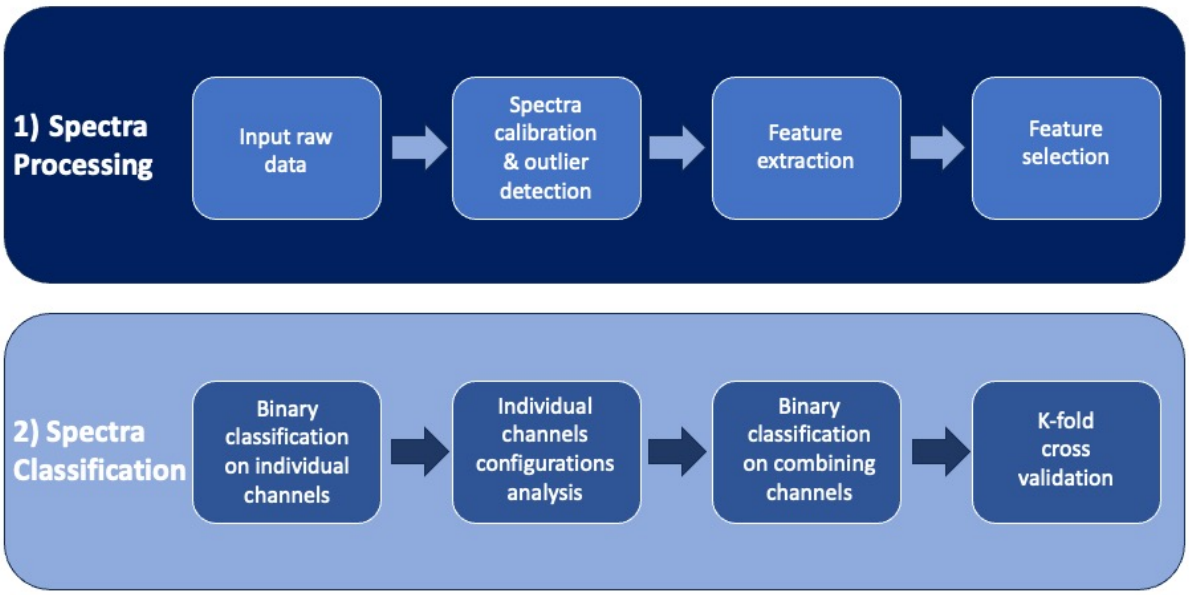


Figure 4.5 Schematic to summarise the processing of spectral data. This was conducted in two phases – pre-processing followed by classification. 1) Pre-processing of spectral data is performed to account for inter-sample, background light, and signal quality variability. DRS spectra integration time was normalised. A Savitzky-Golay filter was used to smooth the data and remove noise. Similar technique was done for fluorescent spectra, but to account for variability in laser power the fluorescent spectrum of normal and malignant tissues was scaled by multiplying the scale ratio. Three types of features were extracted from the raw spectra namely Fixed Window Features, Peak Valley Features and Peak Valley Slope Features. Feature selection using Boruta was performed on DRS and fluorescent spectra to reduce dimensionality of data and improve accuracy. 2) The spectral data was subdivided into six different subsets for binary classification from each of the six channels as follows: healthy vs. invasive ductal cancer (IDC); healthy vs. invasive lobular cancer (ILC); healthy vs. ductal carcinoma in-situ (DCIS); healthy vs. pathological complete response (PCR); healthy vs. invasive cancer (IDC and ILC); healthy vs. all cancer (IDC and ILC and DCIS). Binary classification was carried out on multiple channel combinations. Utilising DRS08, DRS28 and fl405 channels were deemed to produce the best overall results and the channel combinations presented in the results section.

4.4.5.1.1 DRS Calibration and Pre-Processing

Normalisation occurred in two steps. Spectral integration time refers to the duration for which a spectrometer collects light from a sample before signal processing, and here it was set to 1000 milliseconds. Scaling of the integration time is performed to optimize the collection of raw signal data by controlling how long the detector captures light from the tissue sample before delivering a signal. This scaling process involves adjusting the integration time to balance signal intensity and detector saturation, and allows raw spectral data to be collected with improved signal-to-noise ratios [314]. Noise reduction can be performed by using white reflection standard and dark field readings, as summarised below:

$$\lambda DRS = \frac{\lambda RAW - \lambda DN}{\lambda WST - \lambda DN}$$

Where λRAW is the raw signal collected during data acquisition, λDN is the dark-field signal which is the average raw signal between 350 to 380 nm. The white reflectance standard signal λWST, is multiple calibration spectra for each sample collected at the beginning of all spectra acquisition experiments. λDRS is the final reflectance value.

A Savitzky-Golay filter was used to smooth the data and remove noise, while preserving the trend. This is a widely used digital filter, which achieves the desired effect by convolution [315]. A window is slid onto the original data, and the algorithm uses a polynomial function to fit the data points within that window. The smooth output value for the centre point of the window is calculated by the polynomial function. By sliding the window from left to right, a new smooth signal data is generated.

Linear interpolation was then applied. The final DRS spectra contained 401 equally spaced intensity measurements in the 450 to 850 nm spectral range.

4.4.5.1.2 Fluorescence Spectroscopy Calibration and Pre-Processing

Similar calibration and pre-processing techniques were used to treat fluorescence spectra. However, two further steps were applied to compensate for fluorescence collection efficiency and variability in laser power. These steps are performed to allow for wavelength calibration to ensure the spectrometer is correctly assigning wavelengths to the detected fluorescence signal and enable instrument response correction to ensure accurate intensity values are gathered across the spectrum. Here, the spectral integration time was scaled to 26 ms followed by application of noise reduction similarly to the DRS spectra.

To account for variability in laser power, the emission spectrum of the calibrated lamp was gathered, and then compared to measured spectrum and the ratio of the known intensity to the measured intensity at each wavelength gives a correction factor. The fluorescence spectrum of normal and malignant tissues was scaled by the correction factor at each wavelength.

For final processing of fluorescent spectra, the Savitzky-Golay filter was applied, as was linear interpolation. The fluorescence spectra contained 451 equally spaced intensity measurements in the 400 to 850 nm spectral range.

4.4.5.2 Outlier Detection

Two methods were utilised for outlier detection, and once again performed by Yufeng Shi and Yufeng Shi and Ria Ranjiktar under the supervision of Professor Daniel Elson. Firstly, 'zero variance detection' identifies spectral data where there is no variation (i.e., the data points are all identical) which indicates an issue. Secondly, intensity thresholds were used. For data files containing DRS spectra, low intensity values are flagged as outliers. The threshold used for DRS intensity check was 10000, such that if the mean intensity was less than 10000 then this was deemed to be an outlier. Similarly, for fluorescence spectra with low fluorescence values (here if adjusted mean intensity was less than 2500) this was considered an outlier.

4.4.5.3 Feature Extraction

Following pre-processing, three types of features were extracted from the raw spectra before being used for the classifiers. They are named "Fixed Window Features", "Peak Valley Features", and "Peak Valley Slope" features. The configurations of these features were manually selected based on the DRS05 channel and subsequently applied to DRS08, DRS16 and DRS28.

4.4.5.3.1 Fixed Window Features

Fixed Window Features is a feature engineering technique in which data is divided into fixed-size windows or segments, and features are extracted from each window [316]. The following five features were extracted from each window: a) window mean intensity; b) window maximum intensity; c) wavelength corresponding to maximum intensity in this window; d) window minimum intensity; and finally, e) wavelength corresponding to minimum intensity in this window.

The DRS raw spectra, in the range 450 – 850 nm, were divided into 20 windows. Each window length was 20 nm. Thus, 100 features were extracted per DRS spectra. For each fluorescence spectra, the 400 – 840 nm range was divided into 22 windows. Each window length was again 20 nm. Here, 100 features were extracted per fluorescence spectra.

The extracted features from each window are then concatenated into a feature vector. Each window corresponds to a data point, and the feature vector represents that data point in the machine learning model.

4.4.5.3.2 Peak Valley Features

In spectroscopy, a “peak valley feature” describes distinct peaks and valleys seen in graphs of spectral data. These features represent the intensity of light at different wavelengths (Figure 4.6).

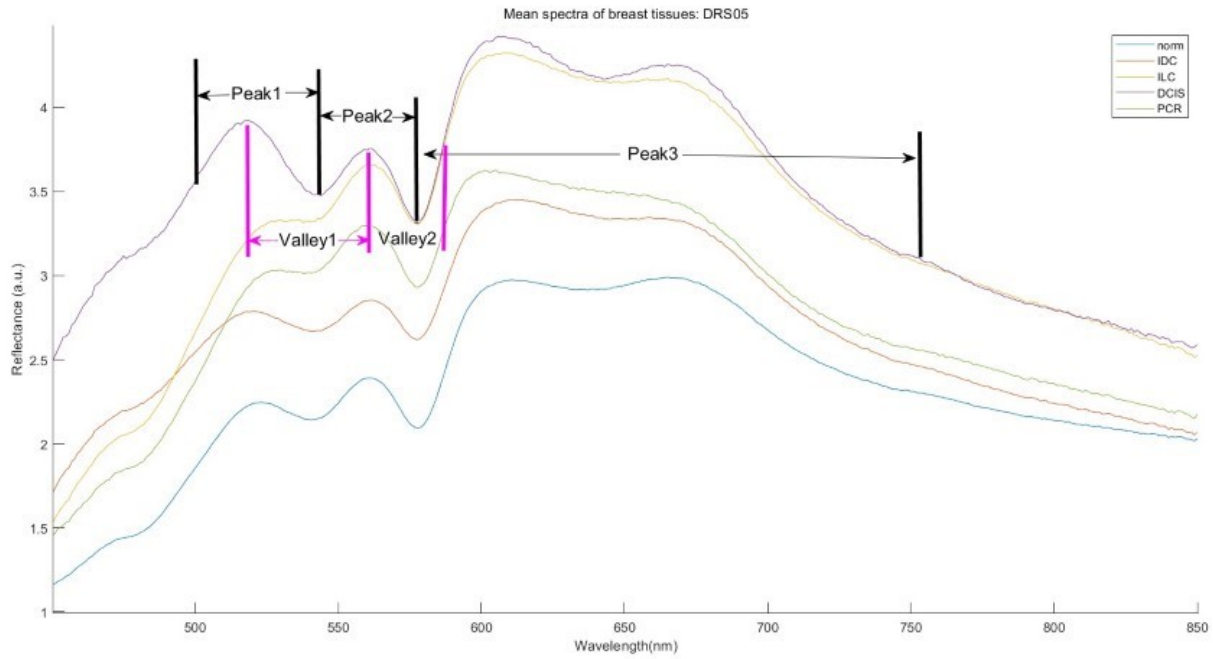


Figure 4.6 Graph depicting “peaks” and “valleys” acquired from spectral data, which represent the intensity of light at different wavelengths. This graph is an example of one diffuse reflectance channel only. A “peak” represents a point where the intensity of reflectance or fluorescence light is at its highest for a particular wavelength. A “valley” depicts a point where the intensity of reflectance of fluorescence is at its lowest between two adjacent peaks. The different colours represent the different tissue types interrogated in this experimental work (blue = healthy breast tissue, red = invasive ductal carcinoma, green = invasive lobular cancer, yellow = ductal carcinoma in-situ, purple = pathological complete response).

A “peak” represents a point where the intensity of reflectance or fluorescence light is at its highest for a particular wavelength. In this study for each peak, the following three features were extracted: window mean intensity; window maximum intensity; wavelength corresponding to maximum intensity in this window. Three peaks were selected from the four DRS channels. These peaks lie within the spectral range: 500 – 543 nm; 543 – 577 nm and 577 – 750 nm (Figure 4.6).

With fluorescence 375 and 405 nm, only two peaks were extracted. The range of the main peak was 435 – 550 nm. Features from within the range 550 – 650 nm were also extracted; however, this was not a real peak (Figure 4.6).

Comparatively, a “valley” depicts a point where the intensity of reflectance or fluorescence is at its lowest between two adjacent peaks. Here, to each valley window mean intensity; Window minimum intensity; And wavelength corresponding to minimum intensity in this window were extracted. Here, the two valleys selected had ranges of 518 – 560 nm, and 560 – 587 nm (Figure 4.6).

4.4.5.3.3 Peak Valley Slopes

The “slope” in a spectral graph refers to the change in intensity or amplitude as a function of wavelength or frequency. Here slope features are referred to the difference in intensity measurements at two specific wavelengths. The slopes were chosen manually based on the mean spectra (Figure 4.6). Here, the slopes were the difference in reflectance of the first and second peak; and the difference of reflectance of the first and second valley. No slope features were extracted from fluorescence spectra.

4.4.5.4 Feature Selection

Feature selection is defined as the process of identifying and removing as many irrelevant and redundant features as possible [317]. Feature selection serves three purposes. Firstly, it allows dimensionality reduction, by reducing the number of features whilst retaining the most relevant ones. This avoids overfitting and increased computational complexity. Secondly, by focusing on the most important features, we

build a more accurate machine learning model. Finally, by removing redundant or irrelevant features, attenuates noise.

"Boruta" is an example of a feature selection technique [318]. It is chosen here as it is unclear which features amongst the spectral data are more relevant for analysis. Boruta first creates a copy of the original dataset with the same features (columns). However, within this "shadow" data set the columns are shuffled or randomized. The original and "shadow" dataset are then merged. A feature selection algorithm, commonly random forest, is used to build a model on this combined dataset. The importance of each feature is ranked. Boruta compares the importance of each real feature with that of the corresponding "shadow" feature. Features with a higher ranking are considered to be relevant features, whereas those with a lower ranking are considered unimportant. Several iterations of these steps occur to ensure feature selection is robust. Confirmed features are then used for training machine learning models.

Feature selection was performed on both the DRS and fluorescent spectra raw spectra, but also on the above three described feature extraction methods described above. The aim of feature selection was to reduce dimensionality of the data and improve accuracy.

4.4.6 Quality Assessment of Samples

During data acquisition it was noted that the quality of the 181 samples interrogated varied. Factors affecting this variability included size; diathermy marks; stains with either blue dye or pathology ink; tissue thickness and homogeneity. To account for variability, and to allow assessment of how accuracy is affected by this, it was decided to rank the samples with a quality score from one to three.

Samples ranked with a quality score of 1 were deemed to be of "poor quality". These samples were less than three millimetres in size in any direction, and it was not possible to fold or combine these samples. They may be contaminated by dye, ink, or diathermy. The thickness of these samples may have also not been consistent, and less than 3 mm.

Samples ranked with a quality score of two were of "average quality". These samples had a minimum size of at least 3 mm in one direction. They may have been

affected by ink, dye, or diathermy however their tissue thickness was still more than 4 mm.

By contrast, samples run with a score of three, were of “superior quality”. Here tissue thickness was more than four millimetres. There was no evidence of ink or dye stains, or diathermy.

4.4.7 Spectra Classification

Once relevant features were extracted from the spectral data, classification was performed. Data classification is defined as learning the structure of a data set which has already been separated into categories or classes [319]. A model is then used to ‘learn’ these categories, and estimates the group class labels of one or more previously unseen data sets with unknown labels [319]. With relevance to this thesis data was categorised with the aim of comparing healthy breast tissue to malignant breast tissue subtypes (B5a/b). The model is then used to estimate the class labels of one of more previously unseen data examples with unknown labels. A training set is an example data set which is inputted into a classification problem, that has already been sub-categorised into different classes (i.e. either healthy or malignant breast tissue). The model learned is defined as the ‘training model’ [319]. The unseen spectral data features that need to be classified are the ‘test data set’. The algorithm that creates the training model for predicting if the tissue sample is healthy or malignant is defined as the ‘learner’.

Supervised machine learning aims to build a concise model of the distribution of class labels in terms of predictor features [317].

4.4.7.1 Binary Classification on Individual channels

The spectral data was subdivided into six different categories to account for comparing healthy breast tissue against malignant breast tissue for binary classification, as follows:

1. Healthy vs. Invasive ductal cancer (IDC)
2. Healthy vs. Invasive lobular cancer (ILC)

3. Healthy vs. Ductal carcinoma in-situ (DCIS)
4. Healthy vs. Pathological complete response (pCR)
5. Healthy vs. Invasive cancer (IDC & ILC)
6. Healthy vs. All cancer (IDC & ILC & DCIS)

4.4.7.2 Combining Channels

The custom-built probe utilised for experiments has six channels. Each channel provides different information and the objective in combining these channels is to improve the accuracy and reliability of spectral measurements. There are a few advantages of combining channels, firstly there is enhanced sensitivity as different breast tissue components absorb or reflect light at specific wavelengths, leading to improved detection where there is low concentration of chromophores/fluorophores. Secondly, there is improved noise reduction as random noise found amongst spectral measurements is averaged out by combining channels. Thirdly, different channels will identify different properties of biological tissue and by combining channels feature extraction is enhanced. Finally, combining channels increases the volume of data available to train classification models and hence more features available to differentiate between healthy and malignant breast tissue.

4.4.8 Classifiers

Data was divided into the training and testing sets using the repeated stratified k-fold cross-validation (CV) method, with five folds and five repeats. When using the CV method, the data set was split into five folds such that each fold contains approximately the same percentage of samples of each target class as the complete set. The model is train and tested on each fold. After the five iterations the performance metrics (in this thesis sensitivity, specificity, area under the curve and accuracy) are averaged across all five test sets [320]. The CV method was chosen for the following key reasons: it's ability for efficient use of data, reduced overfitting, more reliable performance estimates and flexible for different dataset sizes [320]. K-fold cross-validation uses all data points for both training and testing, which is advantageous particularly if a dataset is small which in the case of this experimental work is noted in

some tissue subtypes. Compared to a simple train-test split, K-fold CV reduces overfitting as the model performs over multiple splits. K-fold CV averages the performance across different test sets, and this allows an improved estimate of the ability of a model to be generalizable to unknown data.

Logic based algorithms can be divided into either decision trees or rule based classifiers [321]. A tree-based classification model was used in this study. They are a type of supervised machine learning algorithm that uses a series of conditional statements to partition training data into subsets. Each successive split adds some complexity to the model, which can be used to make predictions. Decision trees are suitable for this small size data set as they are easy to implement.

Here, two tree-based classifiers were used: Gradient Boosting, and Extreme Gradient Boosting (XGBoost). These classifiers lie within a type called boosting. Boosting is a type of ensemble learning that combines weak learners to achieve improved model performance. With gradient boosting (GB), gradient descent algorithm is used for optimization. So, at each iteration of model building, gradient boosting fits subsequent models to the residuals from the previous one. It iteratively boosts the accuracy of individual trees, therefore improving overall model performance. XGBoost, in addition to gradient boosting, enables regularisation which further helps reduce overfitting [322].

All the experiment types (normal vs tumour, or tumour vs tumour) were trained and validated on three tree classifiers. For each experiment type, the highest area under the curve (AUC) achieved among the three classifiers was selected. The corresponding accuracy was also recorded.

4.4.8.1 Evaluation of Performance of Classification Algorithms

A confusion matrix is a table which contains information about actual outcomes and predicted classifications by the same classifier [323]. It is a concept that can be used to evaluate the performance of a classification algorithm. For this thesis, confusion matrices were created to assess how well the GB or XGB classifier can distinguish between the different binary classification subsets outlined in 4.5.7.1. A confusion matrix highlights how well a classifier distinguishes between classes, in this case tissue subtypes [324]. The components of a matrix (Figure 4.7) are outlined below:

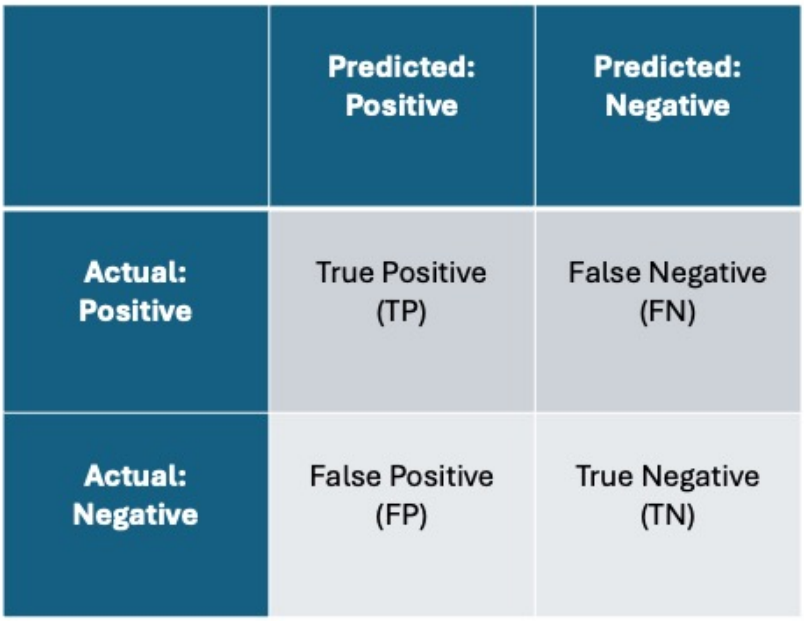


Figure 4.7 Confusion matrix schematic where each row represents the actual class of the tissue histological subtypes in relevance to this thesis, and each column represents the predicted tissue histological subtype [324].

Within the matrix the following: true positive, false negative, false positive and true negative are represented and defined as below:

- True Positive (TP) – The number of correct predictions where the actual class is positive, and the classifier also predicted it as positive.
- False Negative (FN) – The number of incorrect predictions where the actual class is positive, but the classifier predicted it as negative. This represents a type II error.
- False Positive (FP) – The number of incorrect predictions where the actual class is negative, but the classifier predicted it as positive. This represents a type I error.
- True Negative (TN) – The number of correct predictions where the actual class is negative and equally the classifier predicted it as negative.

4.5 Results

4.5.1 Spectral Data Quantity & Spectral graphs

When all tissue samples were utilised (irrespective of quality assessment) 181 samples were available, with a total number of 18,349 spectra. 106 tissue samples were of the best quality, with accumulative spectra count of 11,045.

4.5.2 Demographics

92 of the samples were invasive cancer types, with equal distribution of invasive ductal and lobular subtypes. Unlike other spectroscopy studies in which DCIS was not interrogated, in this thesis, DCIS represented 12% of samples. Table 4.1 presents the full demographics of the dataset.

4.5.3 Performance Metrics

Following analysis of individual channels and then combining all different possibility of channels, it was decided for final analysis to combine DRS08, DRS28 and fl405 channels as this gave the best performance metrics (accuracy, sensitivity, specificity, area under the curve (AUC) and mean average precision (mAP)). Appendix C outlines the performance metrics of individual channels and the results following combining different channels. I have outlined in this chapter the results for the selected channel combination only (DRS08, DRS28 and fl405).

Table 4.1 Tissue samples categorised into histopathological subtype; tumour grade and receptor status. (IDC- invasive ductal carcinoma; ILC-invasive lobular carcinoma; DCIS-ductal carcinoma in situ; pCR-pathological complete response to neoadjuvant chemotherapy.

Tissue Subtype	Number of Samples	Mean Age (Range)	Tumour Grade	Receptor Status
IDC	46	57.3 (34 – 91)	1:1 2:28 3:17	ER+PR+HER2-:29 ER+PR-HER2-:2 Triple -ve:15
ILC	46	65.7 (43 – 94)	1:0 2:35 3:11	ER+PR+HER2-:42 ER+PR-HER2-:4 Triple -ve:0
DCIS	21	51.8 (25 – 76)	Low:1 Intermediate/high:11 High:9	Not applicable
Healthy	62	56.7 (20 – 90)	Not applicable	ER+PR+HER2-:55 ER+PR-HER2-:2 Triple -ve:4 Unknown: 11
PCR	6	54.8 (40 – 88)	Not applicable	ER+PR+HER2-:2 ER+PR-HER2-:0 Triple -ve:4

4.5.3.1 Healthy Breast Tissue versus Malignant Breast Tissue

The DRS-IFS probe was able to differentiate between normal and malignant tissue with an accuracy of 75.26% (SD ± 3.19), a sensitivity of 83.51% (SD ± 13.14) and specificity of 61.13% (SD± 16.40) with the XBG classifier on the best quality samples (quality score 3) as highlighted in table 4.2. When all tissue samples were assessed the XGB classifier distinguished normal and malignant samples with an accuracy of 76.11% (SD ± 2.97), sensitivity 85.60 % (SD± 1.67) and specificity 56.73% (SD ± 8.92).

With the GB classifier on quality three samples was applied, accuracy was 74.92% (SD ± 4.04), sensitivity was 82.43% (SD ± 13.88) and specificity was 62.23% (SD ± 13.03). When all tissue samples were assessed with the GB classifier accuracy was 76.89% (SD ± 3.91), sensitivity 85.61% (SD ± 1.23) and specificity was 59.07% (SD ± 10.71).

Table 4.2 Overall performance metrics of both GB and XGB classifiers on either selected tissue samples (i.e. the best quality score samples) and all tissue samples.

Classifier	Sample Quality	Accuracy (%)	Sensitivity (%)	Specificity (%)	AUC (%)	mAP (%)
GB	All (1 to 3)	76.89 ± 3.91	85.61 ± 1.23	59.07 ± 10.71	81.03 ± 4.87	88.26 ± 5.09
XGB		76.11 ± 2.97	85.60 ± 1.67	56.73 ± 8.92	81.32 ± 3.78	89.30 ± 3.98
GB	3	74.92 ± 4.04	82.43 ± 13.88	62.23 ± 13.03	83.13 ± 3.28	87.84 ± 3.05
XGB		75.26 ± 3.19	83.51 ± 13.14	61.13 ± 16.40	83.95 ± 3.01	88.99 ± 2.72

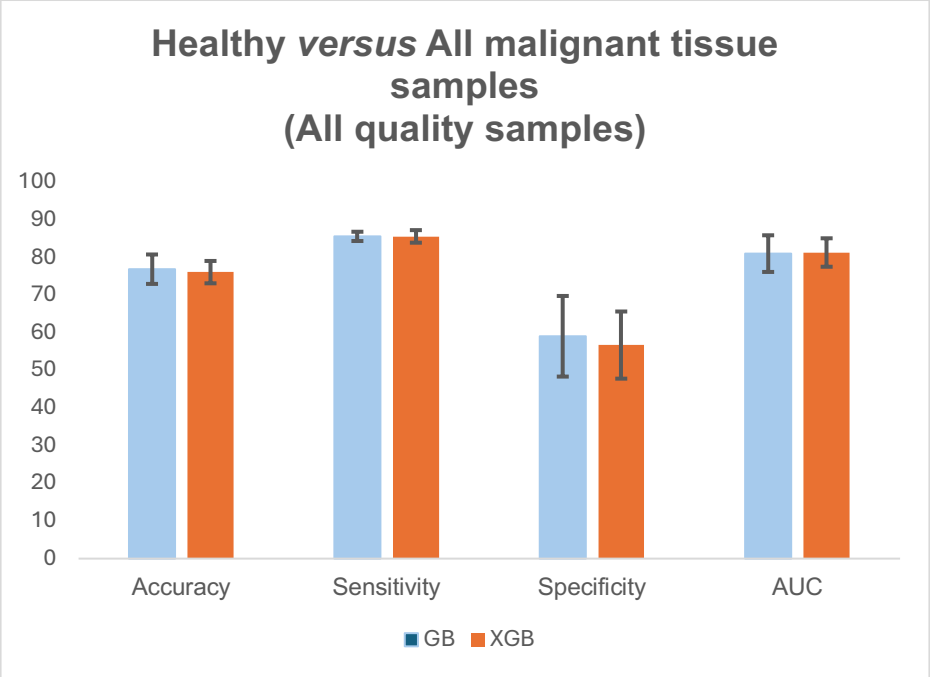


Figure 4.8 Bar chart comparing performance metrics (accuracy, sensitivity, specificity and AUC) for all healthy tissue samples when compared to all malignant tissue samples (IDC & ILC & DCIS). For each performance metric comparison results are represented for GB classifier and XGB classifier with the vertical error bars representing standard deviations.

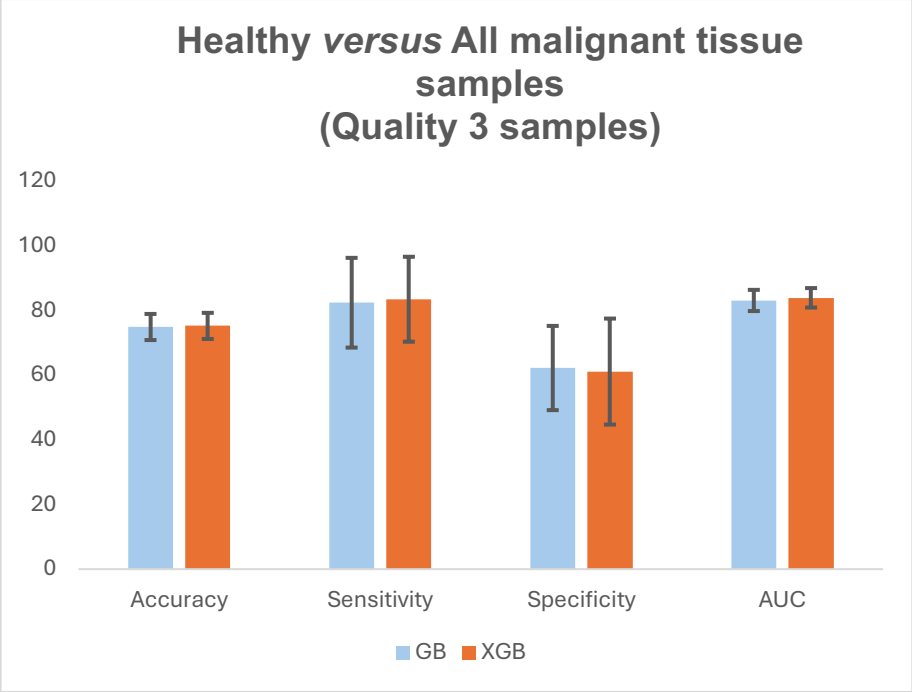


Figure 4.9 Bar chart comparing performance metrics (accuracy, sensitivity, specificity and AUC) for quality three healthy tissue samples when compared to quality three malignant tissue samples (IDC & ILC & DCIS). For each performance metric comparison results are represented for GB classifier and XGB classifier with the vertical error bars representing standard deviations.

4.5.3.2 Healthy Tissue versus Different Histological Subtype Results

Accuracy rates between healthy tissue and distinct tissue subtypes were also compared (Table 4.3 to 4.4). DRS-IFS was able to differentiate between healthy and ILC with XGB [accuracy 80.18% (SD ± 13.91), sensitivity 73.31 % (SD± 19.91) and specificity 61.13% (SD ± 16.40)], better than IDC [accuracy 72.04% (SD ± 11.44), sensitivity 61.06 % (SD± 17.57), specificity 78.74% (SD ± 17.15)].

Table 4.3 Table depicting performance metrics for both classifiers when comparing healthy tissue with invasive lobular cancer.

Classifier	Sample Quality	Accuracy (%)	Sensitivity (%)	Specificity (%)	AUC (%)	mAP (%)
GB	All (1 to 3)	73.36 ± 10.06	73.25 ± 19.03	74.42 ± 16.38	82.61 ± 10.3	81.99 ± 8.86
XGB		74.56 ± 9.67	75.87 ± 17.88	74.14 ± 16.48	82.13 ± 10.28	81.38 ± 9.39
GB	3	80.69 ± 13.97	75.12 ± 20.95	85.76 ± 14.92	86.89 ± 11.74	82.66 ± 15.9
XGB		80.18 ± 13.91	73.31 ± 19.91	86.08 ± 15.55	87.05 ± 12.09	83.85 ± 16.2

Table 4.4 Table depicting performance metrics for both classifiers when comparing healthy tissue with invasive ductal cancer.

Classifier	Sample Quality	Accuracy (%)	Sensitivity (%)	Specificity (%)	AUC (%)	mAP (%)
GB	All (1 to 3)	76.89 ± 3.91	85.61 ± 1.23	59.07 ± 10.71	81.03 ± 4.87	88.26 ± 5.09
XGB		76.11 ± 2.97	85.60 ± 1,67	56.73 ± 8.92	81.32 ± 3.78	89.3 ± 3.98
GB	3	72.96 ± 11.0	61.46 ± 21.04	79.42 ± 13.96	78.91 ± 17.53	76.93 ± 17.1
XGB		72.04 ± 11.44	61.06 ± 17.57	78.74 ± 17.15	78.38 ± 16.37	76.69 ± 16.6

Unique to this study, we interrogated 21 DCIS samples, which accumulated 2520 spectra. As discussed previously (section 1.4.2), DCIS is a common cause for positive margins, and it was prudent to evaluate the effectiveness of DRS-IFS in detecting this pathological entity. The accuracy of the probe to distinguish healthy tissue from DCIS (Table 4.5) in the best quality samples was 83.71% (SD± 10.29), with a sensitivity of 52.93% (SD ± 26.99) and specificity of 92.38% (SD ± 12.15). When all samples were analysed accuracy was 85.42% (SD ± 6.41) sensitivity 72.25% (SD ± 18.87) and specificity was 91.19 % (SD± 6.31).

Table 4.5 Table depicting performance metrics for both classifiers when comparing healthy tissue with ductal carcinoma in-situ.

Classifier	Sample Quality	Accuracy (%)	Sensitivity (%)	Specificity (%)	AUC (%)	mAP (%)
GB	All (1 to 3)	85.42 ± 6.41	72.25 ± 18.87	91.19 ± 6.31	89.01 ± 9.92	82.97 ± 13.6
XGB		83.48 ± 4.73	75.87 ± 17.88	90.54 ± 5.35	89.52 ± 7.44	82.60 ± 12.7
GB	3	83.71 ± 10.29	52.93 ± 26.99	92.38 ± 12.15	86.41 ± 9.89	73.44 ± 16.3
XGB		83.22 ± 10.73	55.72 ± 28.03	91.12 ± 12.52	87.62 ± 9.26	75.76 ± 16.5

Many patients receive neoadjuvant chemotherapy prior to surgery, especially those with HER2 enriched or triple negative disease [325, 326]. This may lead to a complete pathological response (pCR), defined as no residual invasive or non-invasive cancer within the breast or lymph nodes [327]. pCR is clinically important as it is associated with multiple beneficial outcomes, namely event-free survival, disease-free survival and overall survival and therefore has long been a surrogate marker for survival [327-329]. Different breast cancer molecular subtypes related to the receptor status have statistically significant varying responses to NACT, with one trial of 756 patients

identifying pCR rates of 38.2% in triple-negative, 45.4% in HER2-positive, and 11.4% in hormone-receptor-positive, HER2-negative disease [330]. In this thesis, pCR was considered as a separate tissue class, distinct from healthy tissue. From the six samples used for analysis, five yielded good quality and led to an accuracy of 88.71% (SD ± 5.15), with sensitivity of 40.29% (SD ± 40.88) and specificity of 95.14% (SD ± 2.70) when compared to healthy tissue in the context of imbalanced datasets (Table 4.6).

Table 4.6 Table depicting performance metrics for both classifiers when comparing healthy tissue with tissue taken from patients who received NACT and achieved a pathological complete response.

Classifier	Sample Quality	Accuracy (%)	Sensitivity (%)	Specificity (%)	AUC (%)	mAP (%)
GB	All (1 to 3)	89.24 ± 3.39	27.87 ± 34.14	95.69 ± 3.65	71.73 ± 23.38	35 ± 29.46
XGB		88.85 ± 4.51	19.34 ± 21.81	96.26 ± 4.66	75.24 ± 16.32	34.66 ± 26
GB	3	88.71 ± 5.15	40.29 ± 40.88	95.14 ± 2.70	87.81 ± 11.79	59.16 ± 30.9
XGB		90.24 ± 3.85	35.29 ± 43.86	97.53 ± 1.84	88.15 ± 8.89	52.32 ± 29.3

4.5.3.3 Comparison of performance metrics with intertumour heterogeneity

The accuracy of distinguishing between tumour classes was much lower for both classifiers regardless of tissue sample quality. IDC and ILC had balanced datasets, and accuracy of distinguishing between them was 66.37% (SD± 7.99) with XGB.

When IDC was compared to non-invasive disease (DCIS) accuracy was 80.59% (SD ± 5.08), sensitivity 70.74% (SD ± 16.81), and specificity was 86.43% (SD ± 6.89) for all tissue samples utilising GB classifier.

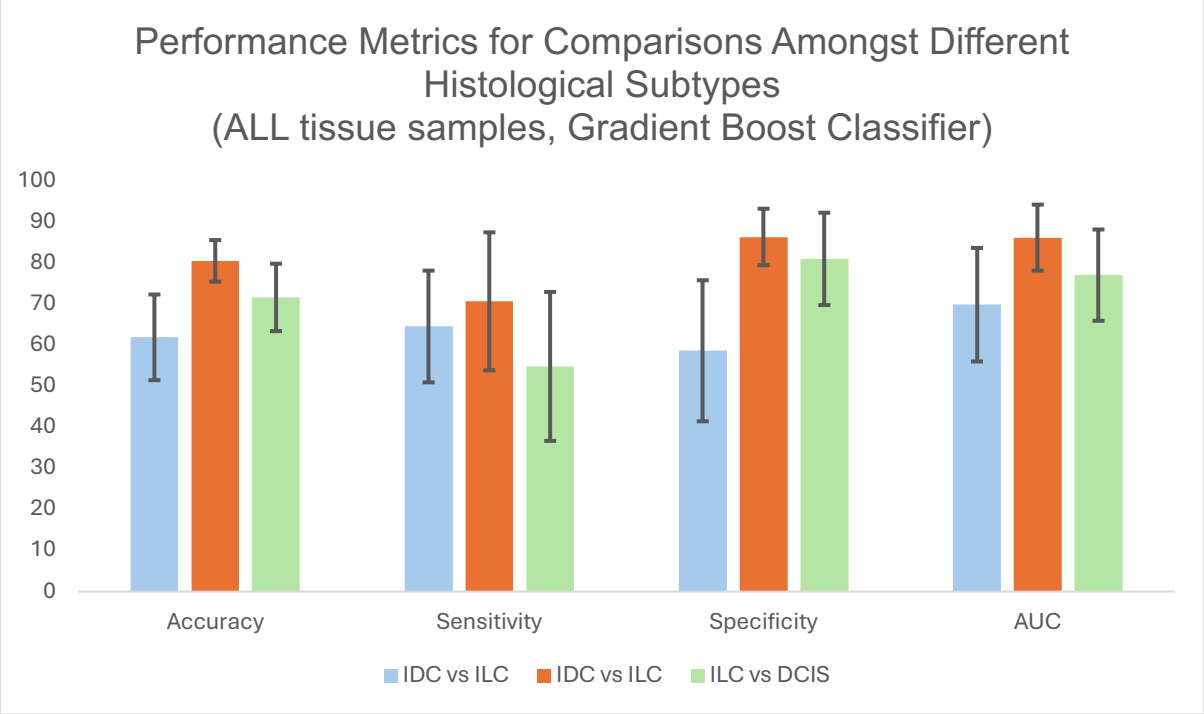


Figure 4.10 Bar chart depicting performance metrics for intertumour comparisons for all tissue samples (quality 1 to 3) when gradient boost classifier was applied. The vertical bars represent standard deviations.

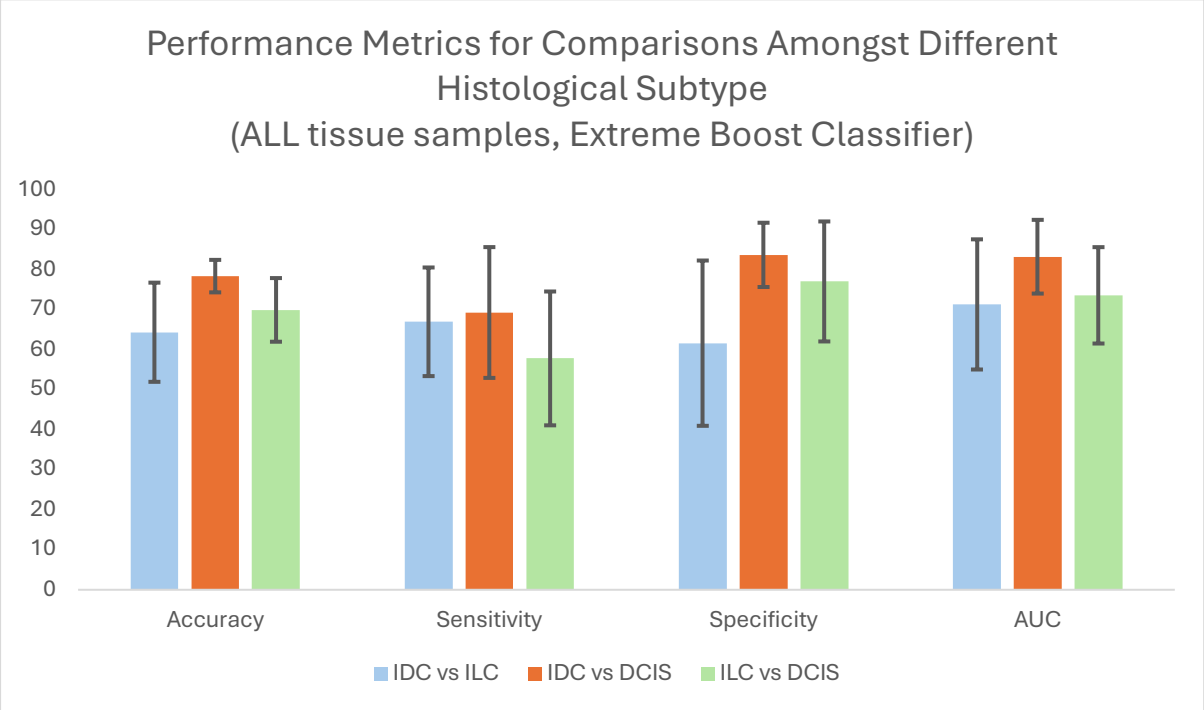


Figure 4.11 Bar chart depicting performance metrics for intertumour comparisons for all tissue samples (quality 1 to 3) when extreme gradient boost classifier was applied. The vertical bars represent standard deviations.

4.5.4 Spectral Graphs

For each tissue subtype at the three different channels selected (DRS 08, DRS28 and fl405) a graph was produced to show mean spectra. The peaks on these graphs represent where tissue samples had the most reflectance at a particular wavelength of light. The troughs represent where the samples absorbed light the best.

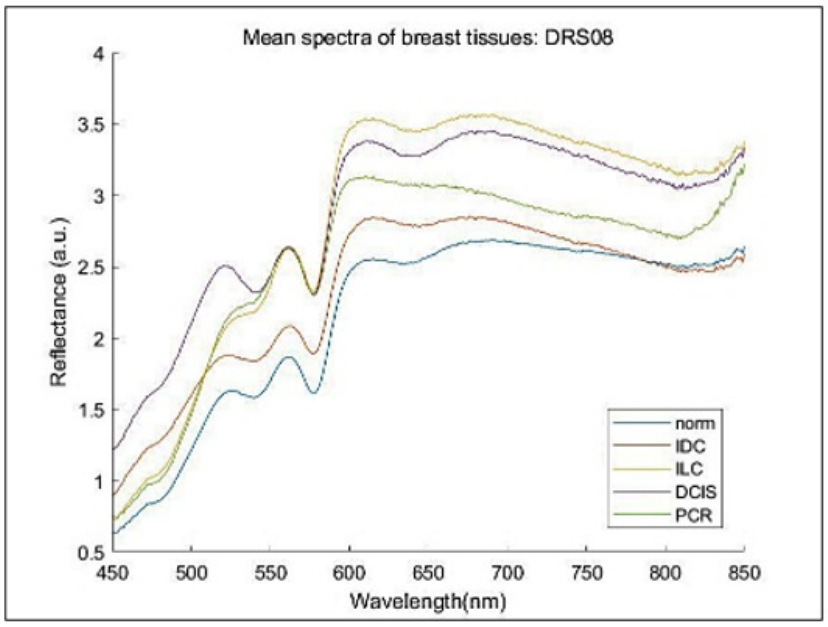


Figure 4.12 Spectral graph for mean spectra of DRS08 channel. With DRS08 channel, the three main peaks identified were at 525, 560 and 625nm respectively. The troughs were identified at 540 and 580nm. (norm - normal breast tissue; IDC – invasive ductal cancer; ILC – invasive lobular cancer; DCIS – ductal carcinoma in situ; PCR – pathological complete response).

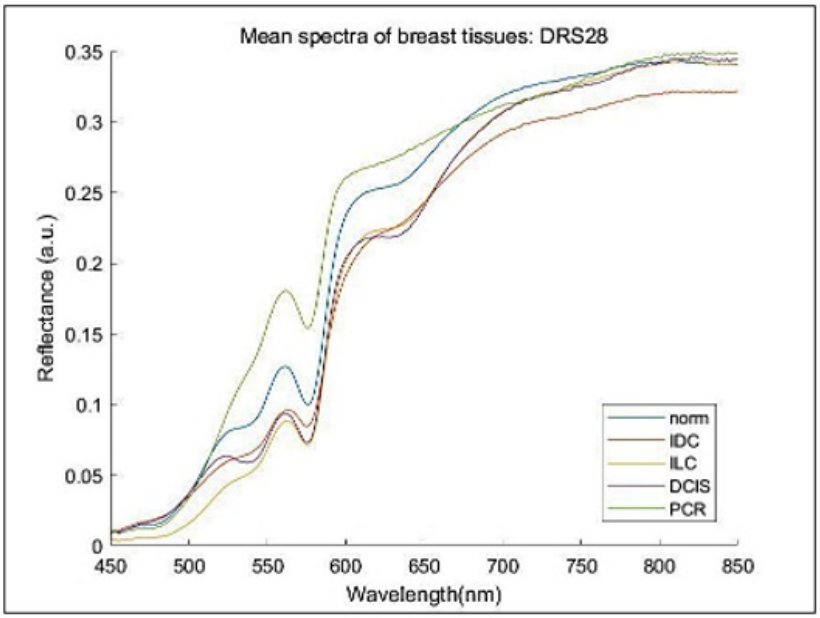


Figure 4.13 Spectral graph for mean spectra of DRS28 channel. With DRS28, the main peak was identified at 560nm and the main trough at 575nm. (norm - normal breast tissue; IDC – invasive ductal cancer; ILC – invasive lobular cancer; DCIS – ductal carcinoma in situ; PCR – pathological complete response).

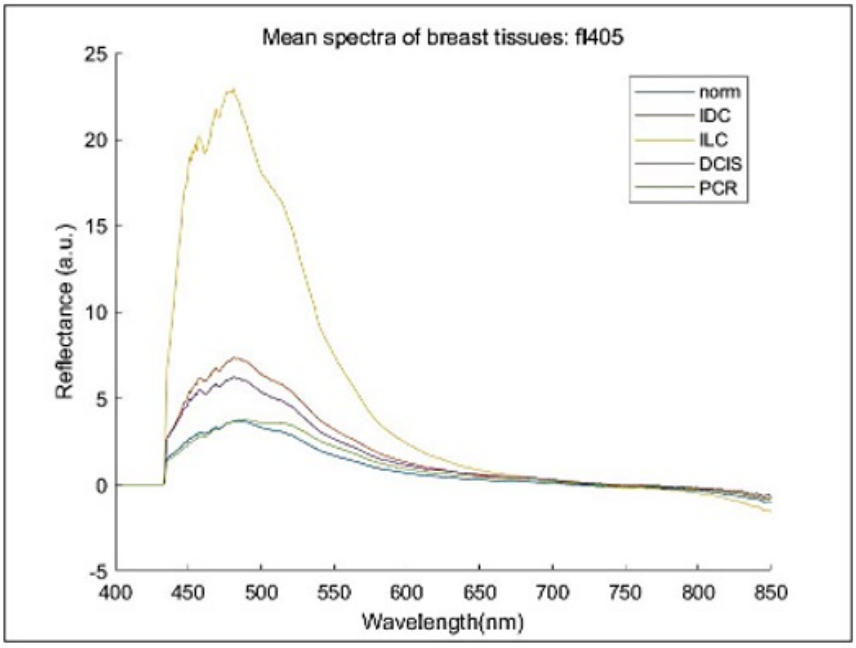


Figure 4.14 Spectral graph for mean spectra of fl405nm channel. The main peak occurred at 475 nm. Mean spectra for the different tissue classes in the three different channels used for analysis a) Diffuse reflectance 08 b) Diffuse reflectance 28 c) Fluorescence at excitation wavelength 405 nm. (norm - normal breast tissue; IDC – invasive ductal cancer; ILC – invasive lobular cancer; DCIS – ductal carcinoma in situ; PCR – pathological complete response).

4.5.5 Confusion Matrices

When comparing healthy tissue samples were to all malignant tissue samples (IDC, ILC and DCIS), it was observed that the models (GB or XGB) exhibited more spectral values within the 'predicted tumour' box.

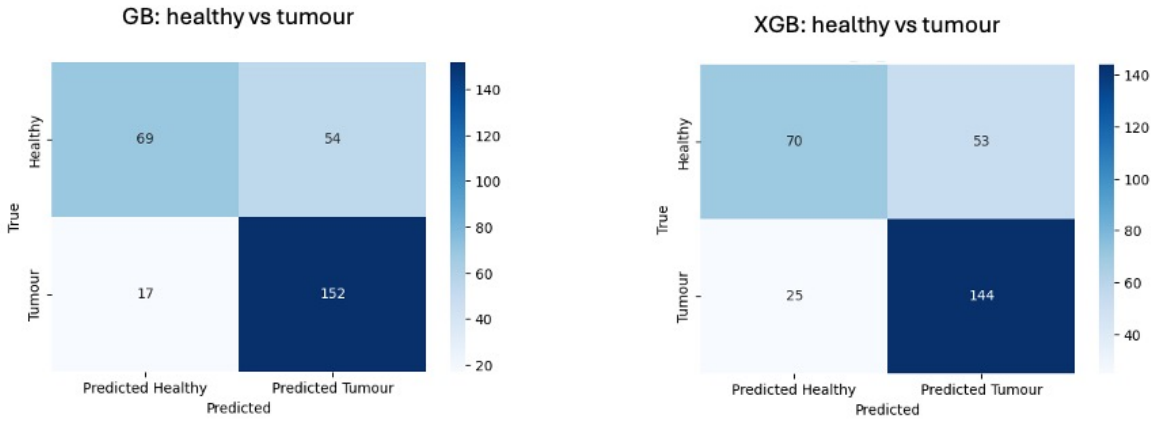


Figure 4.15 Confusion matrix comparing gradient boost classifier and extreme gradient boost classifier on healthy tissue samples versus all tumour samples (IDC & ILC & DCIS) on quality three samples.

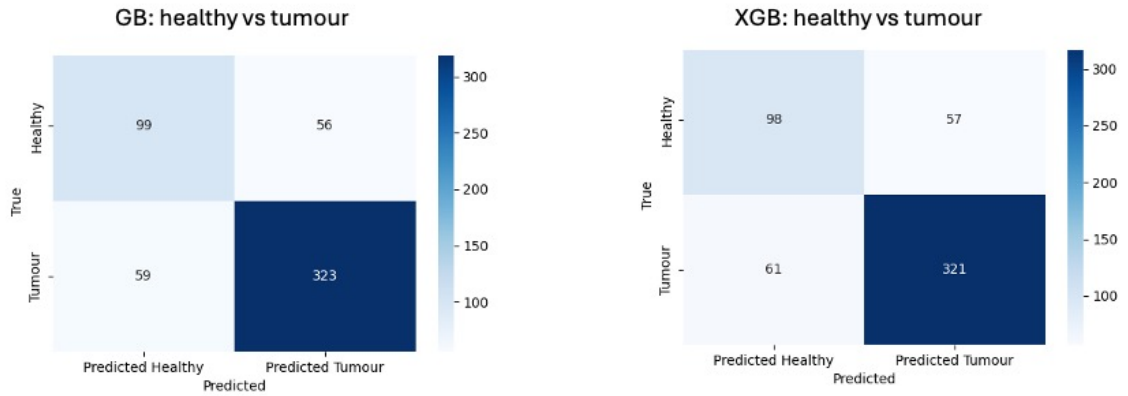


Figure 4.16 Confusion matrix comparing gradient boost classifier and extreme gradient boost classifier on healthy tissue samples versus all tumour samples (IDC & ILC & DCIS) on all tissue samples irrespective of quality score.

The appendix (Appendix C) contains confusion matrices for all other comparisons discussed above.

4.6 Discussion

Experimental results demonstrate that overall this DRS-IFS system was able to differentiate between normal and malignant tissue with good overall accuracy and sensitivity. When considering assessment of all tissue samples, the XGB classifier achieved an accuracy of 76.11% (SD ± 2.97), sensitivity of 85.60 % (SD± 1.67) and specificity of 56.73% (SD± 8.92). Compared to other studies which had interrogated breast tissue samples with DRS or DRS-IFS spectroscopy reviewed in chapter two (section 1.10.3) where the number of spectra acquired ranged from 129 to 1073 [156], this work has a significantly higher number of spectra at 18,439 [156]. Although spectra were acquired from multiple data points from the same sample, this provides more data for machine classifiers.

4.6.1 Assessment of Performance Metrics (Healthy versus Malignant)

Overall, the DRS-IFS probe was able to differentiate between normal and malignant tissue with good overall accuracy and sensitivity when all tissue samples were assessed, as well as when only the best quality samples were interrogated. The meta-analysis presented in chapter two states a pooled sensitivity of 0.84 (0.78 – 0.89), and results achieved here are comparable [156]. The sensitivity is comparable to previous spectroscopy studies [136, 163, 165], due to the ability of DRS-IFS to detect scattering and absorption via enhanced path length. As there are multiple scattering events the optical path length of light is increased within biological tissue allowing more opportunities for the light to interact with absorbing molecules, thus enhancing detection of weak absorption features that simpler reflection or transmission techniques may miss. DRS-IFS is responsive to modest differences in absorption characteristics such as chromophores or blue dye contaminants, affecting sensitivity.

However, lower specificity was noted in these experimental results with a specificity of 56.73% (SD ± 8.92) with XGB classifier when all tissue samples were assessed, and when only the best quality samples were assessed, specificity was 61.13% (SD ± 16.4) so comparatively lower than the pooled specificity of 0.85 (0.79 – 0.91) outlined in chapter two. As per table 2.6 of chapter two the lowest specificity

noted was 66.7% as per Brown *et al*. [161], compared with the highest of 100% as per de Boer *et al.* [170]. There are several reasons for these differing specificity results namely frozen tissue sample utilization, imbalanced datasets in this work, and methodology of previous studies introducing bias which are discussed extensively in section 4.7.3.

As previously discussed, (section 1.4.2), there are known predictors of positive margins, namely large tumour size, DCIS and lobular type cancers [25, 187, 188]. Clinically, any IMA tool that has high diagnostic accuracy rates for discriminating between histological subtypes of breast tissue would be advantageous. Accuracy rates between healthy tissue and distinct tissue subtypes were also compared. DRS-IFS differentiated between healthy and ILC, better than IDC. When the best quality samples were interrogated with GB classifier IDC had an accuracy of 72.96% (SD ± 11) whereas ILC had ac accuracy of 80.69% (SD ± 13.97). Morphological differences between lobular and ductal cancer may explain the disparities. Lobular cancer is composed of small, discohesive cells which infiltrate the stroma in a single-file manner due to [161] the lack of e-cadherin protein [38, 331] possibly contributing to superior detection by DRS-IFS. Here, 46 lobular breast tissue samples were interrogated. Chapter two's meta-analysis identified five spectroscopy studies, which in combination only had spectral data from 14 lobular tissue type samples [160, 162-164, 171]. Regarding histological subtypes, it is not possible to compare the accuracy of detection of specific histological subtypes with other studies, as all previous work focused solely on comparing healthy against malignant breast tissue.

4.6.2 Assessment of Performance Metrics (Malignant versus Malignant)

As previously discussed, (section 1.4.2), there are known predictors of positive margins, namely tumour size, DCIS and lobular phenotype [25, 187, 188]. Clinically, any IMA tool that has high diagnostic accuracy rates for discriminating between histological subtypes of breast tissue would be advantageous. For example, in chapter three it is found that if disease is at the inked margin with either invasive ductal cancer or DCIS there is a fourfold increased odds of local recurrence, so it is imperative for IMA tools to be developed to detect both invasive and non-invasive disease.

Accuracy rates between healthy tissue and distinct tissue subtypes were also compared. DRS-IFS differentiated between healthy and ILC, better than between healthy and IDC. Morphological differences between lobular and ductal cancer may explain the disparities. Lobular cancer is composed of small, discohesive cells which infiltrate the stroma in a single-file manner due to [161] the lack of e-cadherin protein [38, 331] possibly contributing to better detection by DRS-IFS. Here, 46 lobular breast tissue samples were interrogated. Chapter two's meta-analysis identified five spectroscopy studies, which in combination only had spectral data from 14 lobular tissue type samples [160, 162-164, 171]. To date, there is no current literature which looks at comparing accuracy rates amongst different breast cancer subtypes, so we are unable to compare the metrics reported in this experiment.

This experimental work has interrogated the largest set of DCIS samples with DRS-IFS, to date. DCIS compared to healthy tissue was detected with good accuracy and specificity, although sensitivity was not as good (with all samples assessed accuracy was 85.42% (SD ± 6.41), sensitivity 72.25% (SD ± 18.87), specificity 91.19% (SD ± 6.31) with GB classifier. An IMA tool that can distinguish DCIS from IDC would be useful as DCIS is known to increase the odds of a positive margin by eight fold, and current guidelines suggest a wider negative margin is required for DCIS [332]. DRS-IFS here was able to distinguish between IDC and DCIS with reasonable accuracy, but poor sensitivity. Therefore, here when all samples were assessed, DRS-IFS has an accuracy of 80.59% (SD ± 5.08), sensitivity 70.74% (SD ± 16.8) and specificity of 86.43% (± 56.89). Kho *et al.* described that the spectral features of DCIS and IDC are not significantly different [333], which may be a reason for these results. Figures 4.12 to 4.13 depict the mean spectra for all tissue classes in the three different channels used for analysis, and as per Kho *et al.* mean spectra for IDC and DCIS are similar. Similarly, in a recent study of 107 freshly sliced specimens using DRS, it was noted that 75% of spectral features assessed for IDC and DCIS showed the same results (where the p value was statistically significant), which also is evidence that optical characteristics are similar between invasive and non-invasive disease [333].

With the advent of increased neoadjuvant chemotherapy (NACT) use, an ideal IMA tool should not only be able to assess breast tissue which has received treatment but also be able to identify residual disease or DCIS amongst this tissue. NACT alters breast tissue on a cellular level as chemotherapy induces apoptosis and inhibits proliferation [334]. Tissue structure is also altered as NACT induces fibrosis which

results in increased collagen deposition and scarring [326]. Therefore, a more substantial dataset is required as these changes differ from normal healthy breast tissue. There continues to be a lack of consensus within the surgical community if the original or post-NACT footprint should be excised [335]. Therefore an IMA tool that can distinguish the pCR tissue subtype maybe of clinical value in the future.

4.6.3 Critical Analysis of Methodology

Previous spectroscopy work has mainly used fresh breast tissue samples. Due to logistical challenges of obtaining fresh tissue (at Imperial Healthcare NHS Trust samples for research purposes can only be obtained if the lesion is over two centimetres; tissue retrieval does not affect oncological integrity for reporting, etc) freshly frozen breast tissue samples were utilised instead. Overall, our work has identified lower sensitivity/specificity but are still comparable to fresh tissue. The challenges of access to freshly excised breast tissue include interruption to surgical workflow and requires an on-site pathologist. This study has demonstrated that frozen tissues are as informative as fresh tissues.

There is no documented literature on how spectral measurements in human breast tissue are affected by the freezing and thawing process. However, studies investigating various tissue types in animal models have demonstrated optical properties are altered [336, 337]. Tissue structure is altered during freezing due to intra- and extracellular ice crystal formation. This formation creates mechanical stress on cell structures pertaining to cell damage [336]. Cryogenic processing in rat brain, heart and kidney tissues led to a significant decrease in absorption (around 50%) and reduced scattering coefficients (up to 30%), independent of light wavelength [337]. Similarly in hamster cheek pouch there were deviations in diffuse reflectance and intrinsic fluorescence [338]. A decrease in absorption can be attributed to the fact that during the storage process, samples have no access to air and deoxygenation occurs [339].The freeze/thaw process causes haemoglobin reoxygenation that is released from haemolyzed erythrocytes, and partial cell membrane damage [340, 341]. Diffuse reflectance is lower following the freeze/thaw process as cell lysis causes more blood to be on the surface of the sample, which increases the effects of haemoglobin absorption [338].

Some previous studies have acquired spectra from specific locations, where a pathologist has macroscopically pre-identified tissue subtypes, on sliced lumpectomy specimens [163, 169, 171, 333]. This introduces bias and may account for improved specificity. de Boer *et al.* used frozen samples, achieving 100% sensitivity and specificity [170]. In this study after data acquisition, tissue samples were placed in formalin and then blocks were created to assess both the anterior and posterior sides. On certain occasions it was noticed that the tissue sample had more than one tissue subtype, a possible contributory factor to lower overall accuracy. The overall tissue class for each specimen was chosen for machine learning.

Sample quality has been critically analysed here. Spectral measurements are affected by the presence of pigments (surgical patent blue V or pathological dye), therefore a limitation of optical techniques [166, 193]. Approximately 16% of samples here had significant dye contamination, with partial contamination in 40%. Previous studies have failed to document in their methodology about how dyed samples were assessed [166, 171, 333]. Bydlon *et al.* assessed the effects of patent blue dye on optical absorption and scattering in the breast [342], and identified dye up to a particular concentration (80 μm) does not impact the extractions of total haemoglobin; ß carotene and reduced scattering coefficient spectrum from DRS. In the context of modern-day breast surgery, any future IMA tool must consider the effects of emerging tracers used for sentinel lymph node biopsy (SLNB) such as indocyanine green and supermagnetic iron oxide may affect spectral readings, during varied clinical practice.

Imbalanced sample size in datasets may lead to classification performance being biased towards the group with majority of samples [343]. For example, when healthy tissue is compared to PCR (n=6) or DCIS (n=21), sensitivity is poor but overall accuracy is good. de Boer *et al.* have shown that DRS can identify DCIS but they noticed that the optical characteristics of IDC and DCIS were similar [333], so we should expect the same accuracy when comparing normal tissue versus either IDC or DCIS. Future work must employ strategies to overcome imbalanced datasets such as resampling techniques at the data level to either increase the number of samples in the minority class, or decrease the number of samples in the majority class; or assign different weights to classes at the algorithm level [344, 345]. Nachabe *et al.* performed classification on parameters derived from spectra (i.e., blood, water, lipid volume fractions, reduced scattering amplitude, Mie slope, Mie scattering fraction, and

pigment packaging fraction [169]. Other papers perform classification on spectra directly.

A certain type of classifier was used for supervised learning for this data set. However, it is known that decision trees are prone to overfitting. This is challenging because the decision tree model tends to learn the granular details and noise in the training data, to the extent that it impairs the ability to make predictions on new data. Another challenge of decision trees is variance. Of note, a few of the selected classes in this study for example pathological complete response and DCIS had small data sets. This can result in variable results depending on how the training and testing samples are split.

4.6.4 Further Clinical Applications

DRS-IFS could be proposed as a rapid diagnostics tool in the clinic setting pre-operatively. Patients attend breast clinics either via abnormal findings detected during mammographic surveillance [346], or referred due to breast specific symptoms [347]. As part of a “triple assessment” in the breast clinic, a core biopsy of breast tissue is performed [348]. Vacuum-assisted biopsy (VAB) is used for impalpable lesions and acquires ten-fold more tissue volume in comparison to core biopsy [349]. Histological subtype and receptor status is acquired from these samples, but can take up to two weeks for this information to be discussed in a multidisciplinary setting to plan definitive management [350].

The waiting period patients experience until they receive their histology results has significant psychosocial impact, regardless whether the final diagnosis is benign or malignant [351]. Communication with patients can help ameliorate or prevent psychological morbidity [352]. Utilising rapid diagnostic tools in the breast outpatient setting is a potential solution. DRS-IFS applied to the core biopsy sample or VAB (the latter being more promising due to larger volume tissue) taken in clinic, allowing differentiation between healthy and malignant tissue, and even further the histological subtype would be invaluable to alleviate patient uncertainty.

Women have emphasized the importance of minimising delays in the diagnostic process [353]. So, if DRS-IFS could differentiate between IDC and DCIS, the clinician would be able to explain a more definitive management plan. DCIS is a non-invasive

disease, not requiring chemotherapy, which is reassuring to a patient at their initial appointment. Similarly, to discriminate between IDC and ILC in the clinic is crucial to impeding diagnostic waiting times. The true extent of ILC on mammography is difficult to gauge, with false negative mammograms are twice more common than IDC. Therefore, an MRI is ordered to elucidate the full extent of disease. Waiting times for scans delays the treatment pathway and compounds patient anxiety. By utilising DRS-IFS to identify ILC in the first appointment, the clinician could prevent delays by pre-emptively ordering an MRI scan.

Obviously, this custom DRS-IFS would need modifications for rapid diagnostic purposes and be applicable to small core biopsy tissue samples, however such an application is warranted in the field of breast surgery diagnostics.

4.6.5 Limitations

The overall accuracy of this DRS-IFS system is similar to that of previous studies. This allows us to postulate that any spectral library created from this work is transferable to the in-vivo setting, however this has not been directly compared. Ideally DRS-IFS should be utilised on fresh breast tissue from mastectomy or breast conservation specimens, however many pathology units will have a “memorandum of understanding” that excising tissue samples will affect the histopathology process. Alternatively, the DRS-IFS probe could be applied to fresh tissue intraoperatively, however identifying these locations post-operatively for ground truth validation may prove challenging.

Ideally measurements from normal areas and malignant areas from the same patient should have been analysed. This data was available for certain patients but was not comprehensive. It is also important to note that there is heterogeneity amongst the healthy tissue group that has not been addressed here, as proliferative changes might exist. Table 4.1 highlights there were no HER2 positive tumours, which are associated with an increased risk of recurrence, and therefore tumour biology heterogeneity has not been fully represented in this study.

This custom-built probe provides single-point spectral measurements and leaves no marks on the tissue during scanning so in real-time would be difficult to track which areas have been interrogated with the device. This limitation could be overcome

by surgical tool tracking approaches [354]. Surgical tool tracking is something that is used during minimally invasive surgery, whereby the two-dimensional position and orientation (x and y axes, angle) of a probe is marked on tissue using a colour marker. For usability intraoperatively, a surgeon would benefit from having a probe that is able to track where it has been placed on the tissue to allow for real-time assessment of breast margins. This is something that has been explored recently in upper gastrointestinal surgery margin assessment and could be translated into breast surgery [355].

Data analysis could be altered in future work. GB and XGB classifiers produced similar results. Apart from machine learning, other statistical methods such as Principal Component Analysis could be trialled on this dataset.

The issue of imbalanced sample size in datasets can be addressed for future work by gathering more tissue samples from histology subtypes which were underrepresented. In an initial pilot study trialling this DRS-IFS setup, a power calculation was performed. It was estimated that at least 30 samples of each tissue subtype were required to achieve study power 0.8 and a significance level of 0.05. The underrepresented subtypes in this chapter were DCIS, and pCR subtypes.

Lesions of uncertain malignant potential (B3 lesions) have not been investigated here. B3 lesions are heterogenous and account for between 3.3% and 12.6% of lesions or areas of concern from mammography that undergo a core biopsy [356]. B3 lesions encompass the following lesions: atypical intraductal epithelial proliferation (AIDEP); non-pleomorphic or classical lobular carcinoma in-situ; flat epithelial atypia (FEA); radial scar; spindle cell lesions; cellular fibroepithelial lesion and mucocele like lesions. The concern with B3 lesions is that they can be associated with “atypia”, which are abnormal cells which have the risk for transforming into DCIS or invasive cancer, which can cause significant anxiety to patients until appropriately managed. Management of B3 lesions vary depending on the histological diagnosis and includes either radiological vacuum assisted biopsy or surgical excision, with mammographic surveillance. When surgical excision is performed for a B3 lesion it does not need to be resected with a clear margin. For any potential rapid diagnostic tool, this lesion type must be investigated because if a tool differentiates between atypia or DCIS for example, this will influence the volume of tissue excised.

Chapter 5: Multispectral Imaging System – Use in the laboratory and intraoperative setting

In this chapter I aim to appraise the background to multispectral system(s) and describe the instrumentation and set-up of a custom-built MSI system utilised for the original experiments. Secondly, the custom-built MSI system with eight preselected bands is used to interrogate breast tissue samples in the laboratory, to evaluate if MSI can differentiate tissue types in the ex-vivo setting. Data collected from this work was used to compare accuracy of detection of malignant issue compared to spectroscopy alone. This work creates a dataset that informs the use of MSI methodology for in the intraoperative setting.

Furthermore, MSI will be evaluated in the theatre environment to assess if normal and malignant tissue can be differentiated intra-operatively. In the intraoperative setting, current margin assessment techniques preclude full resection surface assessment in real time, in a cost-effective manner. This experimental work aims to identify the advantages of the custom-built MSI system for margin assessment of resected specimens and clarify the further improvements that are required for MSI towards oncological margin control in breast surgery.

5.1 History of Multispectral Imaging

This thesis explores the use of multispectral imaging in the intraoperative setting, however MSI is used in varying fields such as remote sensing, agriculture, and geology. The concept of multispectral imaging can be traced back to the 19th century, when researchers explored the idea of capturing images in different parts of the electromagnetic spectrum. However, due to technological limitations, few practical applications ensued. During World War II, military researchers developed MSI for military purposes, such as identifying camouflage and detecting enemy equipment [357]. At this stage, researchers were using photographic techniques but exploring the visible and infrared light wavelength range.

It was not until the mid-21st century that significant advancements in MSI occurred, with the advent of satellite technology and the development of specialised sensors. The advantage of these sensors was the ability to capture data in multiple spectral bands including visible, infrared and microwave wavelengths. In 1972, the Landsat programme was initiated by National Aeronautics and Space Administration (NASA), and the first earth-observing satellites were created using MSI [358]. Landsat satellites capture images of the Earth's surface in multi-spectral bands, and provide informative data for forestry, agriculture, and urban planning [359-361]. In the past three decades, further advancements in sensor technology have continued, enabling MSI to capture spectral information with the finest resolution. This has been advantageous in mineral exploration and agriculture for example [362]. MSI is widely used in agriculture to help farmers optimise crop health and productivity [363]. It is utilised for crop monitoring, disease detection, and yield prediction. The use of MSI extends to space exploration to study distant planets and celestial bodies, and to collect data about the surface and composition of these unknown areas [358].

MSI has multiple applications in medicine, ranging from the laboratory setting to surgical guidance. MSI can be used in the histopathology laboratory to aid pathologists in characterising tissue samples accurately [364]. MSI has been found to identify skin cancer as it can capture information about melanin and haemoglobin concentrations [365]. Another use of MSI for skin applications is in the acute setting, where it can accurately evaluate burn wounds by assessing tissue depth, viability, and perfusion [366]. In terms of surgical guidance, MSI incorporated with endoscopy can enhance the detection of polyps or lesions in the gastrointestinal tract, by assessing tissue composition and blood flow [367]. In minimally invasive surgery, MSI can help surgeons better visualise tissues, blood vessels and abnormalities [368]. In ophthalmology, MSI can evaluate the optic nerve and retinal vasculature to help diagnose conditions such as macular degeneration and diabetic retinopathy, with Ma *et al.* reporting a sensitivity of 84.21% and specificity of 93.10% for detecting choroidal vasculopathy [369, 370]. Functional brain mapping is required for diagnosing neurological conditions. MSI can assist in this form of diagnostics by providing further information about brain activity and tissue composition [371]. In a recent meta-analysis, Anichini *et al* report a pooled sensitivity of 0.35 (0.28 – 0.42) and specificity of 0.96 (0.84 – 1.08) when MSI was assessed for intraoperative use in neurosurgery [372].

5.2 Multispectral Instrumentation

A multispectral camera integrates spectroscopy and optical imaging (Figure 5.1). Spectroscopy allows sensitivity to the chemical composition of tissue and cellular morphology. Imaging, on the other hand, provides spatial information. The advantage of using imaging as an intraoperative margin assessment tool is the ability to capture the whole region of interest. In theory, this allows real-time feedback to a surgeon, with the aim to provide an image to guide intraoperative dissection and integrate into an efficient surgical workflow.

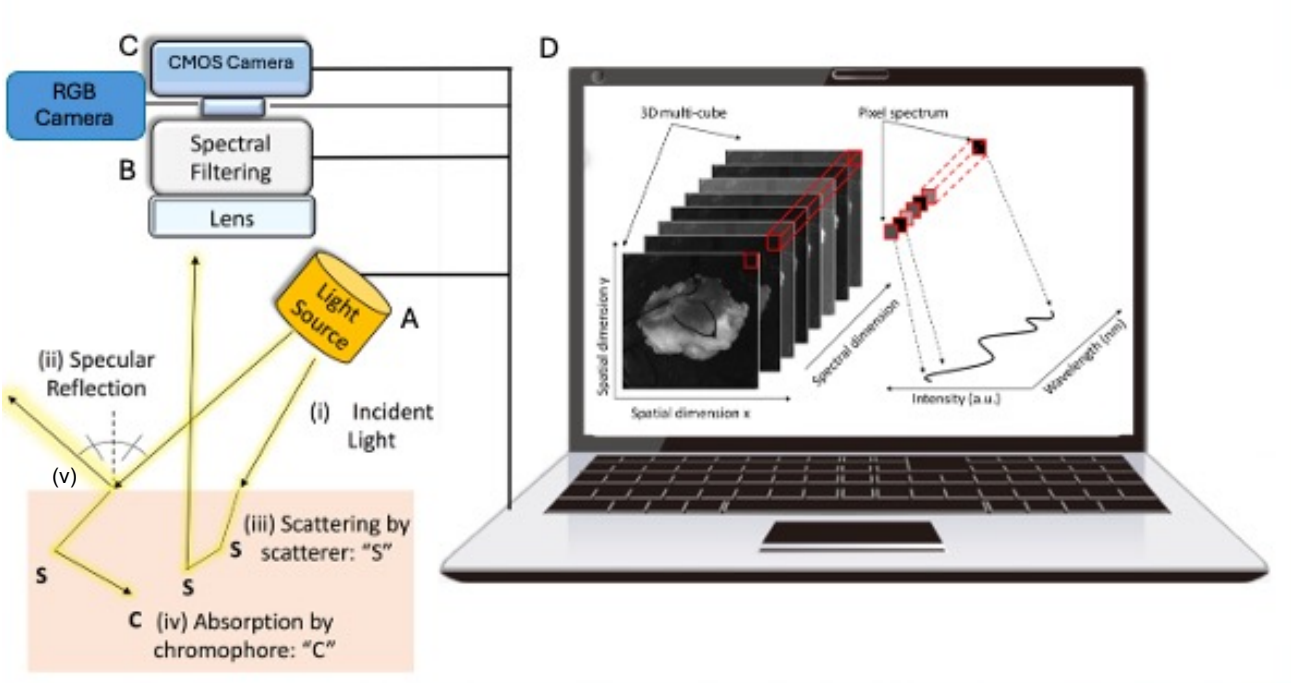


Figure 5.1 Schematic of the MSI imaging principles highlighting how when biological tissue is illuminated by light, the diffusely reflected light is received by the camera system and is converted into an electronic signal for computational analysis. (A) Upon tissue illumination the incident light (i) can be reflected from the surface yielding the specular reflection (ii), or refracted inside the tissue, where it can undergo scattering (iii) from scatterers or absorption (iv) from chromophores and re-emerge from the surface as diffusely reflected light (v) to be captured by the MSI system. (B) Lens has a specific field of view and spectral filtering decomposes the captured light into its spectral components (colours). (C) There are two camera systems (CMOS) and RGB (D) 3D-multicube encompassing spatial and spectral information. The illustration demonstrates the capability of MSI to capture a spectral signature (values at different colour bands) for each pixel in the MSI image.

Light must be filtered or dispersed within such multispectral camera systems to remove unwanted spectral components from the imaged surface before they reach the imaging sensor [369]. Examples of optical filters include filter wheels, a generalized Lyot filter, an electrically tunable filter or multiple-band pass filters [153]. Examples of how light is dispersed in multispectral systems are optic-acoustic crystals or multiple prisms [153].

The custom-built system utilised in this thesis was constructed at the Hamlyn Centre, Institute of Global Health Innovation at Imperial College London. It is comprised of two distinct cameras, performing multispectral and colour imaging, respectively. This is a snapshot system, whereby all spatial and spectral information from a specimen is gathered.

This MSI setup enables the acquisition of images in eight spectral bands. This avoids collection of excessive data volume, permitting a reasonable data acquisition time of several seconds. In our analysis, we have leveraged both the visible and the near infrared parts of the acquired images, including information about the chromophore presence and the scattering properties of the imaged tissue.

5.2.1 Hardware Components of the Multispectral Imaging System

A custom-built multispectral imaging system was used for this work and was built by Dr Vadzim Chalau (Figure 5.2). The imaged scene, collected via a single lens (zoom lens f/3.5-4.5, 28-70 mm for manual SLR 35 mm camera (Sigma Co. Japan), was captured at two distinct camera arms, performing multispectral and colour imaging, respectively. The optical design of the system facilitated the acquisition of the same field of view from both an MSI camera and a (red-green-blue) RGB camera.

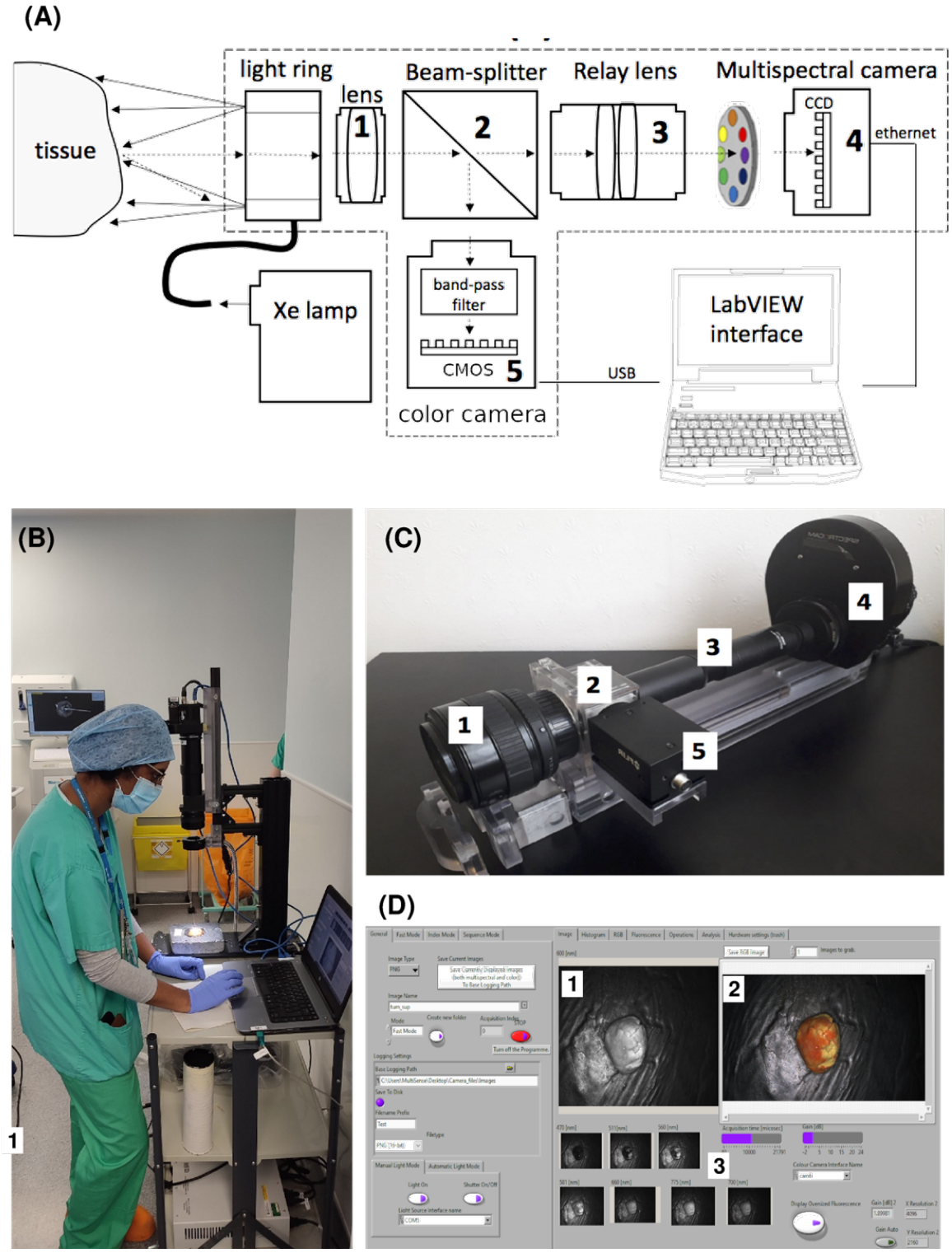


Figure 5.2 Experimental setup for the acquisition of multispectral and colour images. (A) schematic diagram, (B) image acquisition in the operation theatre, (C) MSI camera consists of (1) zoom lens, (2) beamsplitter, (3) relay lens, (4) multispectral camera with spinning filter wheel, (5) colour camera. (D) Screenshot of software interface with monochromatic image at 600 nm band (1), colour image for visualisation and focus control (2) and 7 monochrome images at the rest of the spectral bands (3).

5.2.1.1 Multispectral Camera Components

The multispectral camera branch (Ocean Thin Films SpectroCam™ VIS multispectral 8-channels camera, Ocean Thin Films Ltd., USA) used a filter wheel and monochrome camera to acquire the multispectral image stack. This 'staring' or band sequential approach of MSI acquisition, provided high spatial resolution. Specifically, the camera comprised the Sony ICX285AL image sensor 2/3", with a pixel resolution of 1044 x 1408 pixels. The MSI camera accommodated the acquisition of the MSI stack (8 images) at a rate two MSI images per second. The filter wheel contained eight filters (Ocean Insights, USA), which equated to images being captured at eight spectral bands covering a spectral range of 460 – 825 nm (Table 5.1). This wavelength range was representative of the visible and NIR range of light.

Table 5.1 Specifications of the 8 optical filters installed on the SpectroCam™ filter wheel.

Filter Number	Wavelength (nm)	Full Width at Half Maximum (nm)
1	470	20
2	510	20
3	560	20
4	581	20
5	600	20
6	660	20
7	700	20
8	775	100

The CMOS (complementary metal oxide semiconductor) sensor was used to capture, process and digitize light. The CMOS sensor allows specific pixels to capture different wavelengths of light and converts photons to electrons. Each pixel is converted into an electrical charge whose intensity is related to the intensity of light captured by that pixel.

5.2.1.2 Colour Camera Component

The camera was mounted to a frame with a flange (F) mount system. The colour camera (BFS-U3-89S6C-C USB 3.1 Blackfly S, colour camera) was equipped with the

Sony IMX255 sensor of a sensing area of 14.13 x 7.45 mm, yielding a pixel resolution of 4,096 x 2,160 pixels. The colour camera accommodated a frame rate of up to 42 frames per second. The overall acquisition time for the MSI stack and the corresponding RGB image, including “dark images”, was three to five seconds. It is imperative that both cameras have the same field of view and identical spatial resolution.

5.2.1.3 Light Source

The Xenon light source (Asahi Spectra Max-303, Asahi SpectraCo., Ltd, Tokyo, Japan, configured with the UV and VIS module) was connected to the light ring, and illuminated the tissue through flexible fibre optics light ring (model MA3172, Vision Light Tech B.V., Netherlands). This light source can perform both white excitation and fluorescence excitation using its filter wheel system. The light ring provided a non-collimated illumination of the region of interest. The working distance was measured from the front of the light source to the image and was 30 cm for *in-vivo* work, however, this was adapted to 15 cm for *ex-vivo* work due to the size of the tissue samples.

This light source’s illumination spectrum is presented in Figure 5.3. This spectrum was experimentally acquired with the use of a spectrometer (HR4000CG-UV-NIR, Ocean Optics Inc.) controlled via the SpectraSuite 2.0 software (Ocean Optics Inc.). For the light acquisition, a fibre optic patch cable (FT600EMT, Thorlabs) was positioned after the output of the light ring and through an optical diffuser.

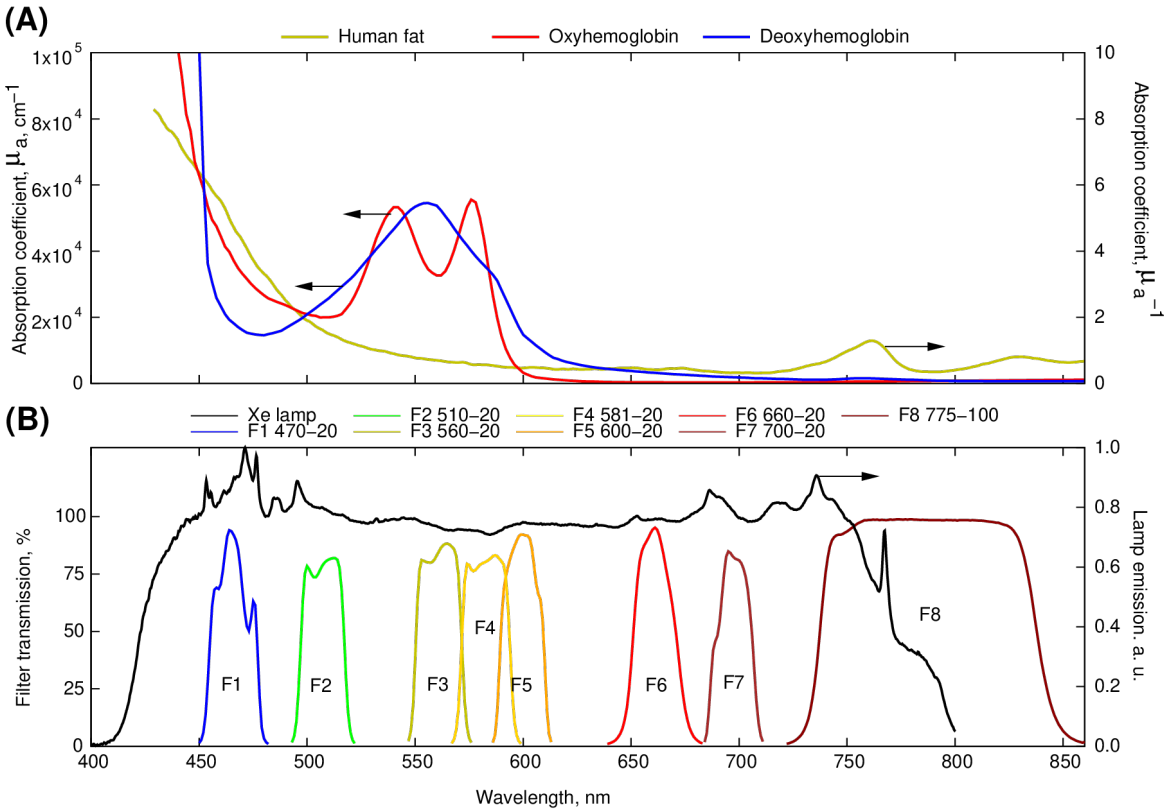


Figure 5.3 (A) Absorption spectra of the typical breast light absorbers: fat **[373]**, oxygenated haemoglobin **[374]**, deoxygenated haemoglobin **[374]**. Tabulated data were obtained from the Oregon Medical Laser Centre site. (B) Emission spectrum of the Asahi Spectra Max-303 Xe lamp (our data) and installed in the bandpass filters (Salvo Coatings, USA **[375]**). In the legend for each filter, the central wavelength is presented with the "Full width half maximum" (FWHM).

5.2.1.4 Beamsplitter

The light beam was split by 50:50 to avoid extra reflections at its limited bandwidth (Figure 5.2A). The experiments performed in this thesis entailed image acquisition from two MSI images: a bright image (light-source on) and a dark image (light source off) within the spectral range 450-850 nm, and one RGB image. Taking into consideration the necessity of acquisition of the "dark frame" (with the illumination light off), for noise and ambient light correction, the overall system's data collection frame rate was around two seconds per dataset

5.2.1.5 Relay Lens

The relay lens allows the field of view across both cameras to be the identical. During system development it was noted the original relay lens component of two doublets

produced poor quality images. Therefore, this was changed to a combination of two good quality photo lenses.

5.2.1.6 Software Interface

Once images are captured by the custom-built MSI system, they need to be displayed so that the user can identify if the image quality is adequate, and the images also need to be stored in folders for data processing.

During initial data acquisition it was noted the interface was not user-friendly as all aspects of images that had been captured were not clearly seen and image settings (e.g. frame rate, acquisition time, gain) had to be manually changed multiple times (Figure 5.4). Therefore, the interface was adapted by Dr Vadzim Chaulau following suggestions by myself, to ensure all information was made to be user-friendly in the limited timeframe required for intraoperative imaging in which integration into the surgical workflow is paramount (Figure 5.5).

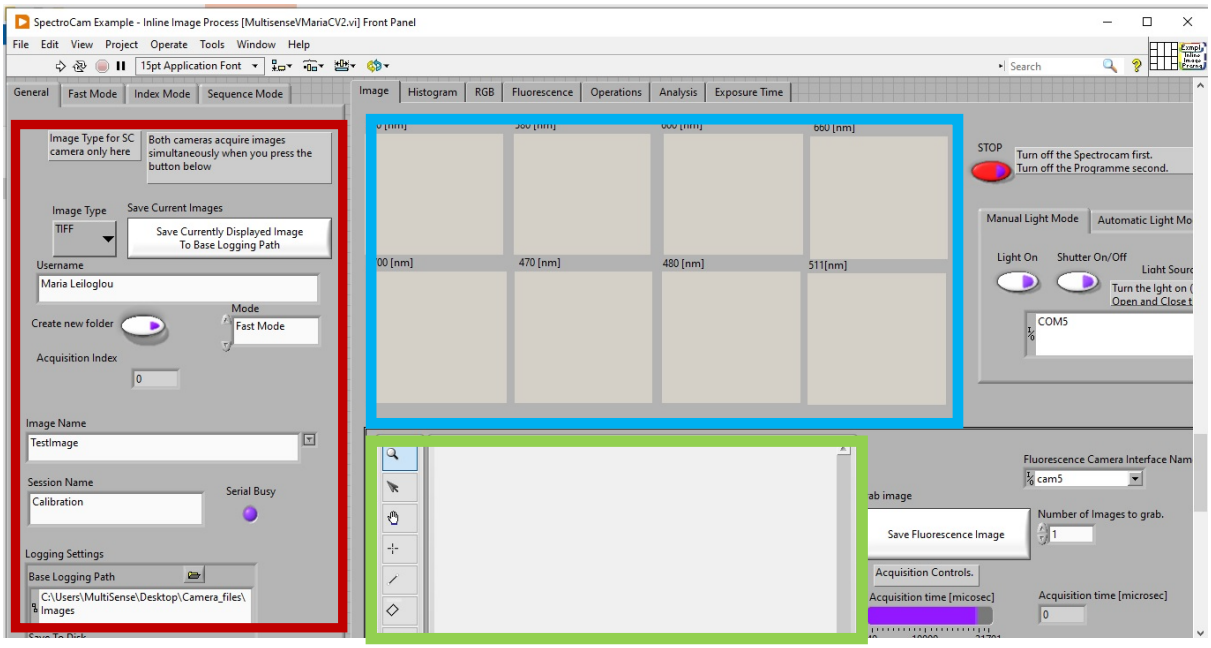


Figure 5.4 Original software interface produced for data collection by the MSI camera. The left hand section (red box) is where information is selected to ensure data is stored in the correct folders. The right upper section (blue box) shows the 8 different MSI images collected for each data acquisition. The bottom right box (green box) was the colour (RGB) image acquired during data acquisition. This was not “user friendly” as all images were not on one page, and the user has to repeatedly scroll down to see the RGB image and adjust acquisition time.

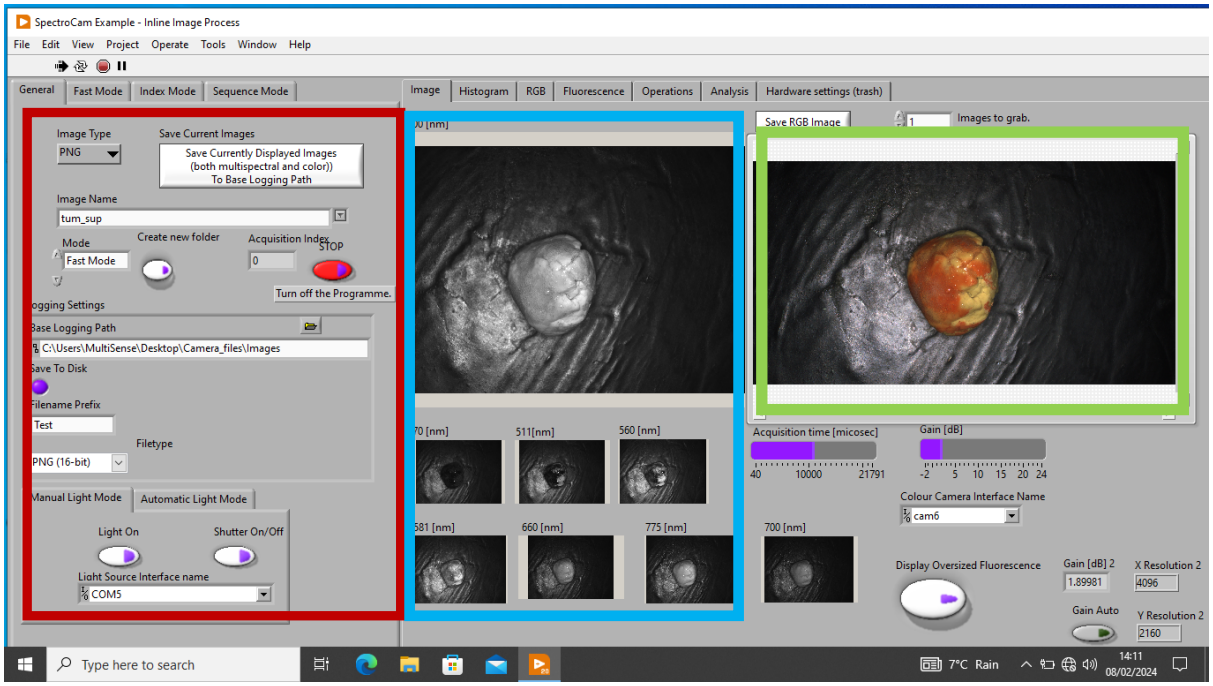


Figure 5.5 Final software interface utilised for data acquisition. All relevant areas that need to be identified or adjusted by the user now all present on the same page without requirement for scrolling down the page. The left-hand section (red box) shows all necessary icons to ensure the correct folders for storage of images are selected. The central section (blue box) shows the eight images captured on image acquisition – the multispectral images. The right-hand section (green box) illustrates the colour (RGB) image captured simultaneously.

5.3 Methodology

5.3.1 Laboratory Study

Breast tissue samples were prospectively collected from patients undergoing elective breast conserving surgery or mastectomy at Imperial College NHS Trust (Charing Cross Campus), London from January 2021 to December 2022 with Imperial College Tissue Bank ethics approval (R21032-4A). Tissue samples were collected intraoperatively immediately after surgical resection. The fresh tissue surgical specimens were delivered to the Charing Cross pathology laboratory where a histopathologist would remove tissue from these specimens, which were then freshly frozen without formalin and banked and archived according to local tissue bank protocol(s).

The “memorandum of understanding” governing tissue collection permitted tissue samples from normal or malignant areas within a surgical specimen only if this

did not affect final histopathological reporting; and malignant tissue sampling was only performed if the tumour size was over two centimetres. As previously discussed in section 4.7.3, it is known that patent V blue dye or histopathology coloured dye can influence spectral readings, which posed a further challenge to avoid tissues stained by such dyes.

To overcome these challenges, improve the sample size and account for breast, further tissue samples were acquired from an external tissue bank, under the remit of Breast Cancer Now charity. Tissue samples were from patients undergoing elective breast conserving surgery or mastectomy at St Bartholomew's Hospital, Barts Health NHS Trust, London under Breast Cancer Now ethics (REC ref no. 21EE0072). A similar protocol was applied as for tissue sample collection at Imperial, in that the samples were not treated with formalin and frozen immediately.

The use of MSI on these tissue samples in the laboratory setting also received REC ethics approval (REC ref no. 08/H0719/37).

5.3.2 Intraoperative Study

Patients undergoing elective surgery at Charing Cross Hospital, London were recruited for this study component. Breast conserving surgery procedures suitable for this work were wide local excision (lumpectomy) or oncoplastic procedures such as therapeutic mammoplasty (e.g. round block, vertical scar, wise pattern, etc). Patients were consented pre-operatively. Data collected for analysis included patient demographics (age, body mass index (BMI), ethnicity); type of BCS procedure performed; tumour characteristics (histological subtype, grade, hormonal receptor status, size); post operative positive margin rate and re-excision status.

5.3.2.1 Inclusion Criteria

Inclusion criteria was any patient undergoing breast conserving surgery or having a diagnostic excision for indeterminate (B3) lesions, who were willing and able to consent for the study. Therefore, these incorporated patients of any age; those who received neoadjuvant chemotherapy; either palpable tumours or non-palpable lesions

with any localisation technique (i.e., wire or MagSeed® guided). Eligible patients were selected from across the Imperial Breast Unit, across all operating lists.

Exclusion Criteria

Exclusion criteria were any patient lacking the capacity to consent, or where English was not their primary language, and therefore they did not understand the study protocol.

5.4 Data Acquisition Protocol

5.4.1 Multispectral Imaging of Freshly Frozen Tissue Samples

Data acquisition occurred within 20 minutes of the frozen breast tissue samples being thawed all the way through to room temperature. Although the pre-operative histology of each tissue sample was known, this was anonymised to avoid introducing measurement/observer bias.

The tissue sample was placed on the black holder of the MSI instrumentation (Figure 5.6A). The working distance between the light ring face and the sample was 15 cm (Figure 5.6B). The anterior surface of the tissue sample was placed upright in preparation for MSI. The tissue sample was placed over a piece of black cloth to absorb excess fluid from the thawing process, as it was noted excess water on the specimen surface causes a lot of reflection. All imaging was achieved with the use of a custom interface, developed in LabVIEW™ (NI Instruments Inc.) software.

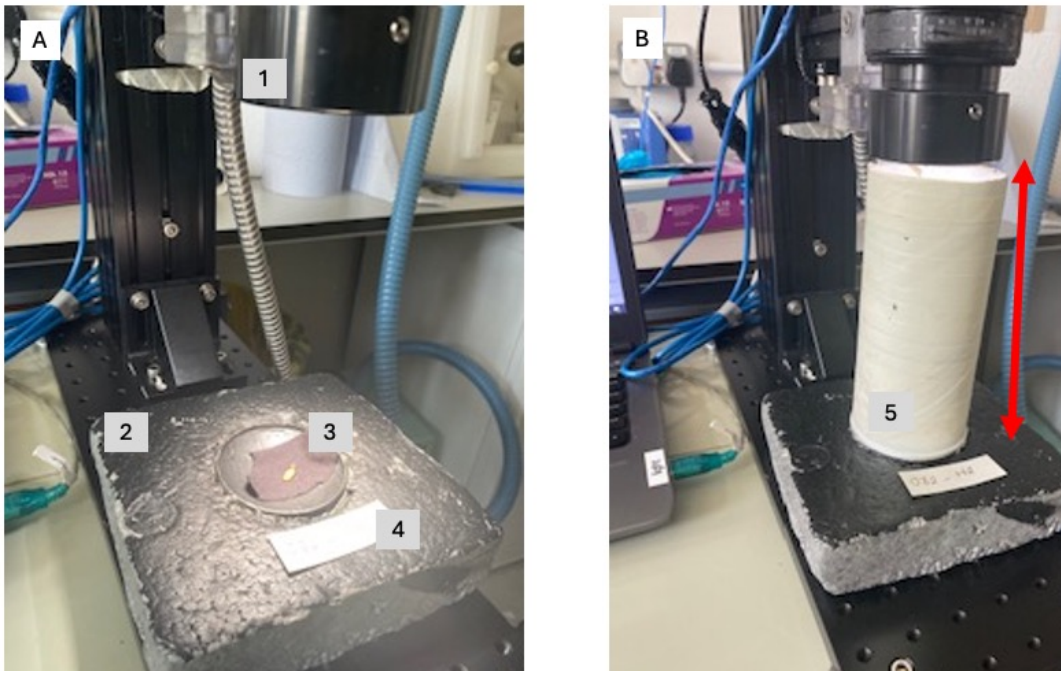


Figure 5.6 (A) Photograph of the experimental set up of the MSI camera in the laboratory imaging the anterior surface of a thawed breast tissue sample. 1-light ring of MSI camera 15 cm away from sample holder; 2-black sample holder; 3-tissue laid onto black cloth to absorb fluid as excess fluid causes increased reflectance; 4-tissue sample reference number (B) A cylindrical cover was place over the sample to allow the MSI light source to illuminate the sample but to prevent ambient room light affecting the images. The distance from light ring to sample holder was 15 cm.

To cope with the limited sensor dynamic range and spectral non-linearity of the detector sensitivity, images were acquired at different exposure settings by manually adjusting the lens aperture. This allowed extension of the image dynamic range up to four times and avoided loss of information in underexposed or saturated overexposed images. Dark reference images ("dark images" of the resection surface acquired with the light source off), to eliminate intrinsic detector noise and ambient light, were automatically acquired in every acquisition.

The tissue sample was then turned over, and an identical imaging protocol was undertaken for the posterior surface. Overall, for each tissue sample, a pair of multispectral and corresponding RGB images was acquired six times to account for the six different aperture settings. In every experiment, a scale image (crosshair target with scale) and a 'bright white reference' image (Spectralon® reflectance standard, Thorlabs Inc.) with its corresponding dark image, namely, 'dark white reference' image, were acquired to be used in the image processing step (Figure 5.7 & 5.8).

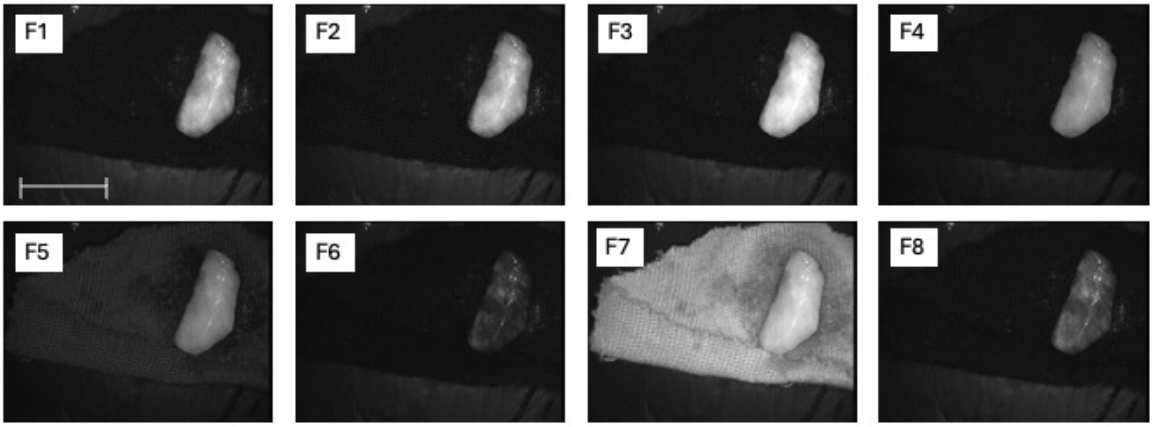


Figure 5.7 Example of the images acquired from data acquisition from the anterior aspect of one freshly frozen tissue sample previously stored in Imperial College London Tissue Bank. The anterior surface imaged here has a separate MSI image from each filter (F1-8) which represents a particular wavelength of light from the visible and NIR spectrum. In the "F1" image in the bottom left hand corned there is a scale which represents 1 cm.

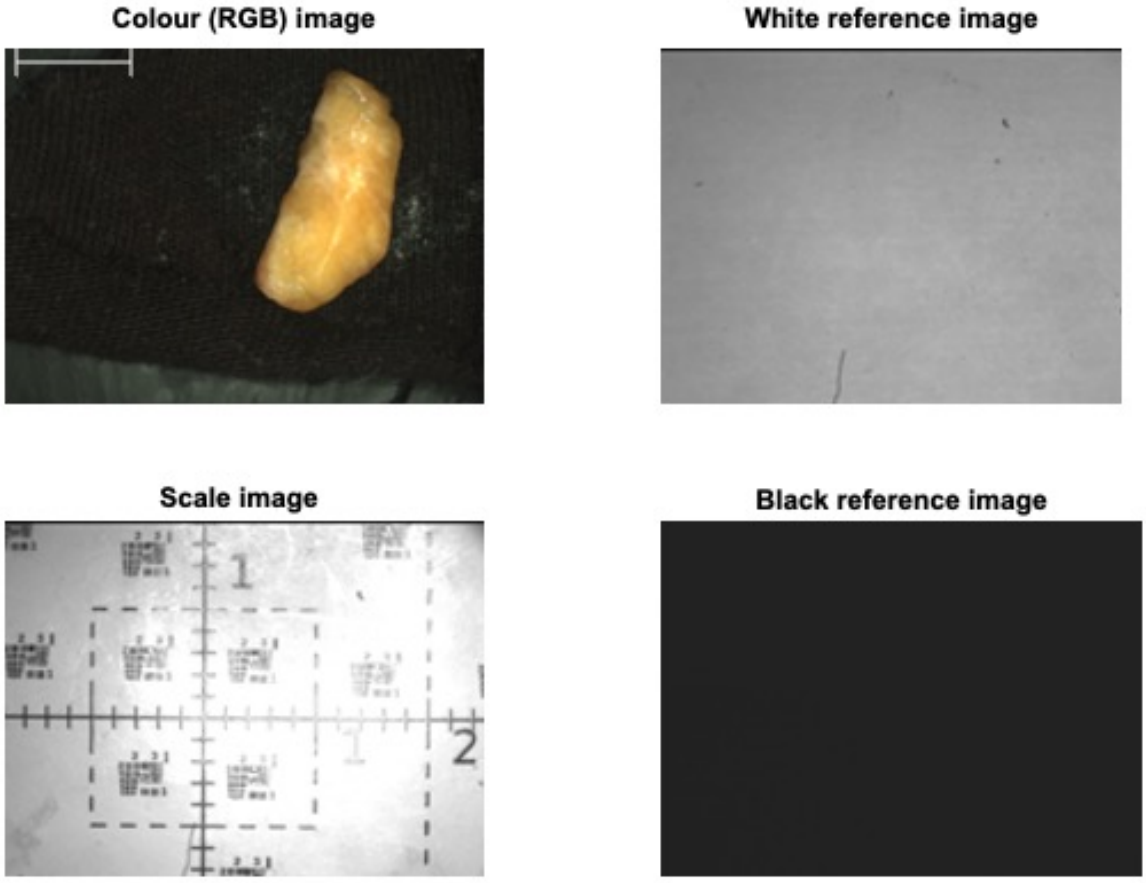


Figure 5.8 For each tissue sample that is imaged, each experiment involved the acquisition of the following further four images (clockwise) colour (red-green-blue) image of the freshly frozen tissue sample with a scale bar shown in the top left hand corner representing 1 cm (here the anterior surface of the same tissue sample from figure 5.7); a white reference image; a black reference image – the light source turned off; and an image of a crosshair target.

5.4.2 Multispectral Imaging of Breast Conserving Surgery Specimens Intraoperatively

Resected specimens were labelled with sutures and/or clips to orientate the wide local excision specimen as per standard care. The conventional labelling technique was a short suture to mark superior resection surface; long suture for the lateral resection surface; and a looped suture to mark the anterior aspect of the specimen. This was often combined with one staple to represent the superior aspect of the specimen and two staples for the lateral aspect. 2D specimen radiographs were obtained using a portable radiography unit (Faxitron®, Hologic, Tuscan Arizona, United States of America) in the operating theatre to attain a specimen radiograph. The surgeon utilised the radiograph to decide if there had been adequate excision of the cancer, and if further margin cavity shaves were required.

Following the above process, the orientated specimen was placed on the black cassette of the MSI instrumentation (Figure 5.9a). Here, the working height of the camera was 30 cm (Figure 5.9b). Data acquisition occurred within 15 minutes of surgical excision from the patient. Multispectral images of each resection surface were acquired (Figure 40). On certain occasions full specimen imaging was not possible due to localizing wires being in-situ, and therefore only anterior and posterior surfaces were imaged. When the excised specimen was large and did not fit into the holder of the black cassette, the specimen was placed onto a black cardboard at the base of the MSI instrumentation to be imaged. A scale image was taken for each specimen to ensure any change in working height had been accounted for later image processing. For every sample, a 'dark image', a 'white reference and a 'dark white reference' image were also acquired.

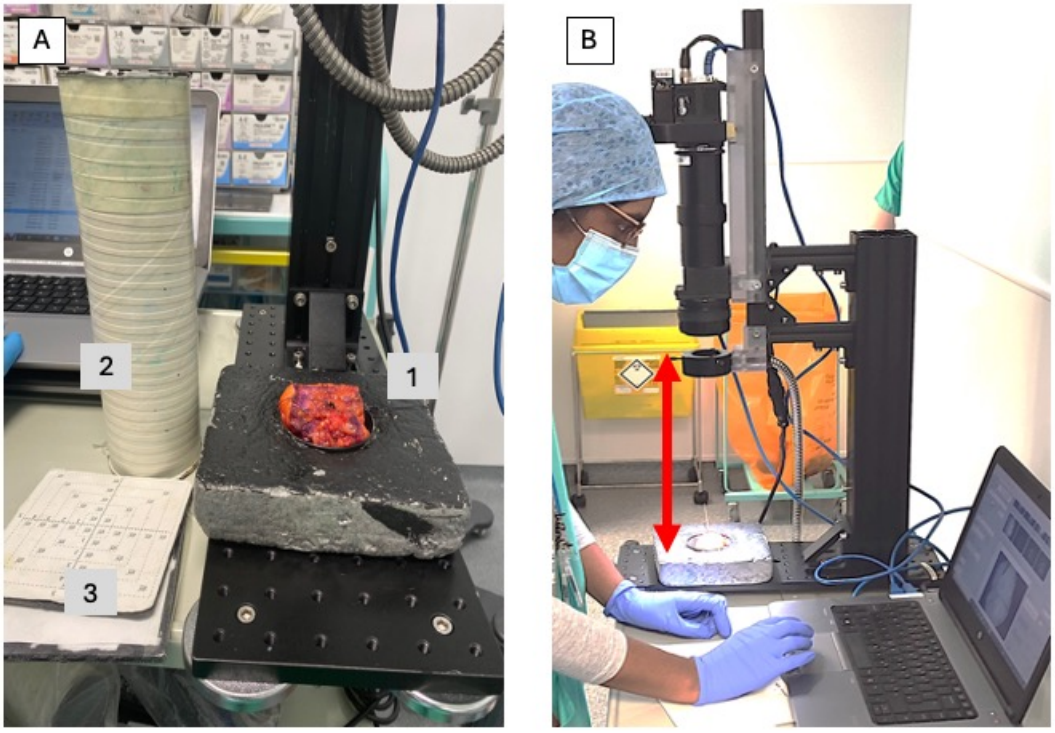


Figure 5.9 (A) Photograph of equipment used for image acquisition of a freshly excised wide local excision in the operating theatre. 1- wide local excision specimen marked with orientation sutures by the surgeon placed onto a black cassette, 2- cylindrical device to block ambient light placed over specimen at time of data acquisition to block out ambient light, 3- crosshair target and 'white' reference tool used for scale and 'white' reference image. (B) Photographic illustration depicting data acquisition in the operating theatre with a working distance of 30 cm from light ring to specimen holder.

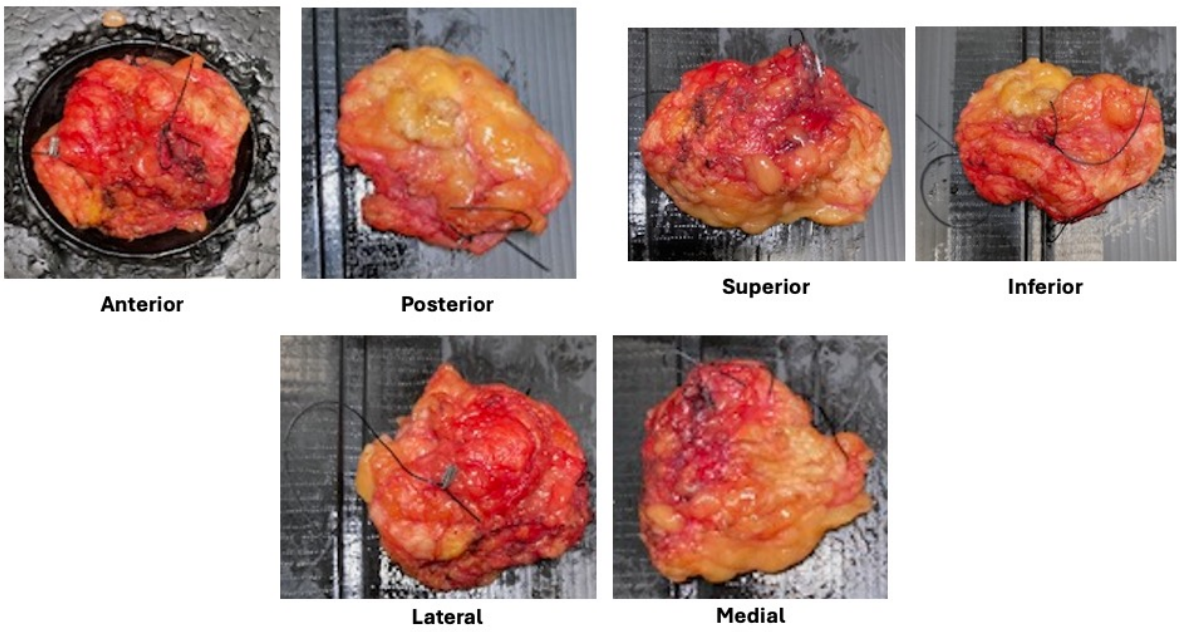


Figure 5.10 Colour (RGB) images of each resection surface of a wide local excision specimen excised from the right breast of a cancer patient. This specimen is marked with a short superior suture with one staple, a long lateral suture with two staples, and one looped suture emphasising the anterior aspect of the specimen. Each resection surface has been imaged in this specimen.

5.4.3 Image Processing

5.4.3.1 Histopathology Correlation

5.4.3.1.1 Freshly Frozen Tissue Samples

Two approaches were taken to obtain histopathological ground truth to correlate and cross-validate MSI data. 53 samples underwent frozen section prior to being allocated to this study by an experienced pathologist (Professor Louise Jones) at St Bartholomew's Hospital, Barts Health NHS Trust, London. These samples were from the Breast Cancer Now tissue bank. 3-4 slices were taken by a pathologist, frozen in a cryostat and then reviewed under the microscope. RNAse free conditions were used. For any tissue sample assessed by frozen section the histological findings were assumed to be representative of the entire sample. The investigators were blinded to avoid introducing measurement/observer bias.

The remaining 88 samples were sent to histopathology following MSI image acquisition. The posterior aspects of these 88 tissue samples were inked with a small yellow dot using tissue dye (Cancer Diagnostics Inc.). The tissue samples were sent to histopathology in formalin; set in paraffin, sectioned and then underwent haematoxylin and eosin (H&E) staining as per standard clinical histopathological processing. Both anterior and posterior aspects of each sample were accounted for in this processing to correlate with data acquisition (yellow dot depicts posterior side). A macroscopic colour image of the tissue samples was taken at the time when MSI images were taken. This enabled orientation to be established for each side.

The H&E slides were interpreted by a Consultant Pathologist Dr Anna Silvanto who was blinded to patient details from whom the tissue sample was acquired. Each H&E slide was marked with regions of interest to allow for classification later (Figure 5.12). Regions of interest within each sample were assigned to the following breast tissue subtypes: fatty breast tissue (benign healthy); fibrous breast tissue (benign healthy); fibroadenoma; ductal carcinoma in-situ (DCIS); invasive ductal carcinoma (IDC) and invasive lobular carcinoma (ILC).

5.4.3.1.2 Intraoperative Freshly Excised Specimens

After each resection surface of an excised breast specimen was imaged with the MSI system intraoperatively, the specimen was placed in formalin for histopathological processing. Whilst in the histopathology lab, the specimen was inked on each resection and serially sectioned into 3-4 mm slices as per standard protocol (Figure 5.11).

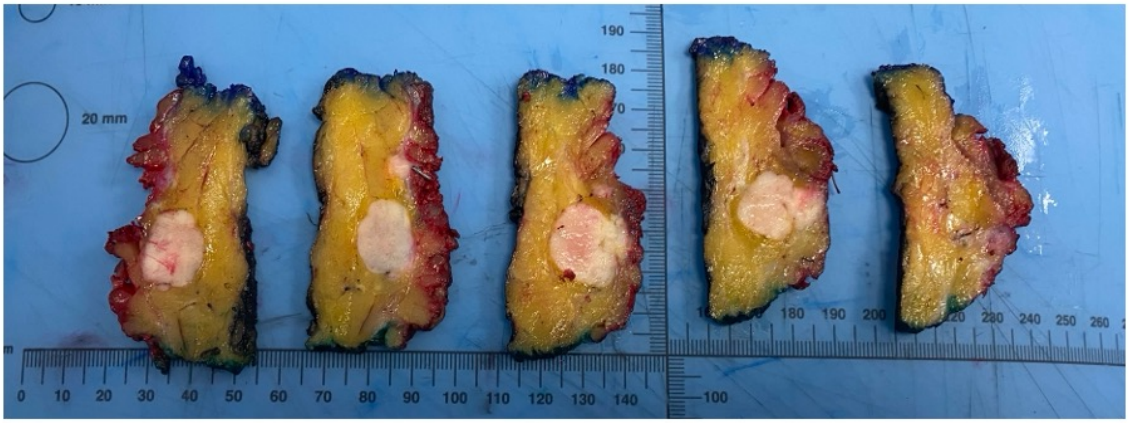


Figure 5.11 Photograph of a sliced wide local excision specimen following being inked on each resection surface with a different colour. The specimen was then "breadloafed" into individual slices. Here a tumour is noted as a white coloured mass within the slices.

Following fixation overnight and paraffin embedding, the tissue was sectioned into slices, then subsequently treated with H&E stain. An experienced histopathologist, blinded to the patient's pre-operative diagnostic biopsy results, prepared a standard pathology report. Within this report margin distance from the identified tumour to the edge of each resection surface was clearly documented, required for image marking. The tissue histological subtype present at each resection surface was also noted for image marking. These labels, acquired from H&E analysis, were the definitive ground truth labels utilised for training of machine learning classifiers.

5.4.3.2 Ground Truth Extraction

5.4.3.2.1 Tissue Samples

Following histopathological validation, the tissue subtypes within each tissue sample were identified. Using this knowledge, a multispectral image from each aspect of the

tissue sample (i.e. anterior or posterior surface) was marked to create masks for use in image processing. GNU Image Manipulation Program (GIMP) software was used to superimpose marked H&E slides onto MSI images of the tissue samples being investigated (Figure 5.12).

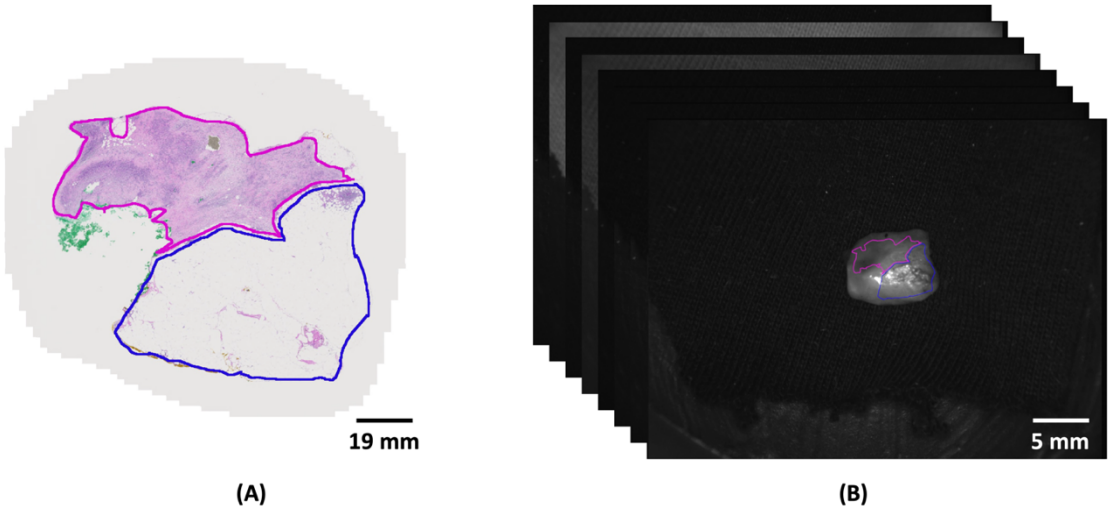


Figure 5.12 Illustration of the ground truth extraction process based on the H&E staining. (A) A scanned H&E slide was marked with the regions of interest (the blue segmentation is adipose tissue, and the pink segmentation is lobular cancer) using GIMP software (B) the corresponding multispectral image was marked for the regions of interest after scaling and alignment with the marked H&E image for mask extraction.

5.4.3.2.2 Freshly excised wide local excision specimens

The formal histological report and the intraoperative specimen radiography image were utilised to mark any MSI image where there was a known tumour within and up to 3 mm from the imaged surface. This threshold was chosen since light comprising visible and near-infrared wavelengths cannot penetrate more than 3mm, and in relation to chapter three of this thesis this distance is justified in terms of our results on minimum clear margin thresholds [376]. Using the acquired scale image per sample case, the real-world dimension of tumour size, and its distance from each resection surface were known. Imaging software (GIMP, GNU, California, United States of America) was used to extract the real-world dimensions from the scale image and mark the MSI image for tumour-free resection surfaces (as per the histopathology report) and for the tumour (Figure 5.13). The tumour was marked using the specimen radiography image as a reference for orientation and the histopathology report as a

guide for the tumour location, as well as distance from edge of tumour to the edge of the specimen.

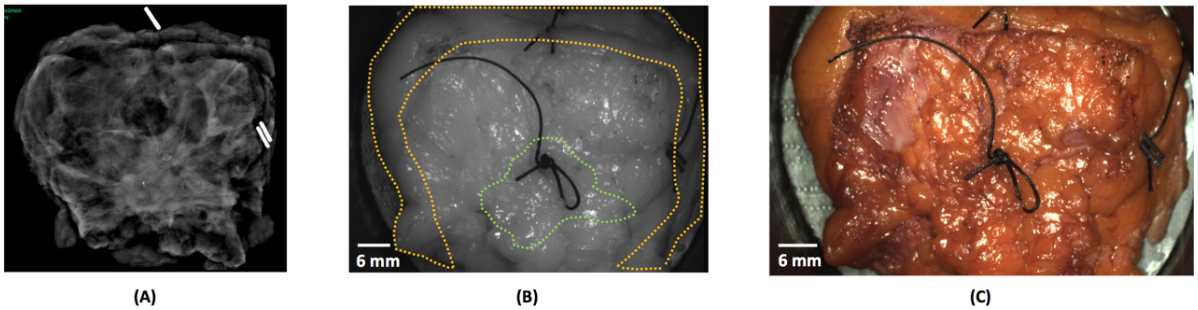


Figure 5.13 Schematic to illustrate how a multispectral image was marked to show areas of healthy tissue and regions of interest (i.e., tumour) to create masks for spectral analysis. This example shows a case where the tumour is less than 1 mm from the anterior surface. (A) X-ray image of a BCS specimen from a patient. The specimen has been orientated by the surgeon intraoperatively, one clip to represent superior aspect of the specimen, two clips to represent lateral aspect of the specimen. (B) MSI image marked for the tumour (green) and healthy margins (orange). (C) RGB image of the specimen for reference.

5.4.3.2.3 Pre-Processing of the MSI Images

For both tissue samples and freshly-excised specimens, pre-processing of the MSI images occurred, involving several steps (Figure 5.14).

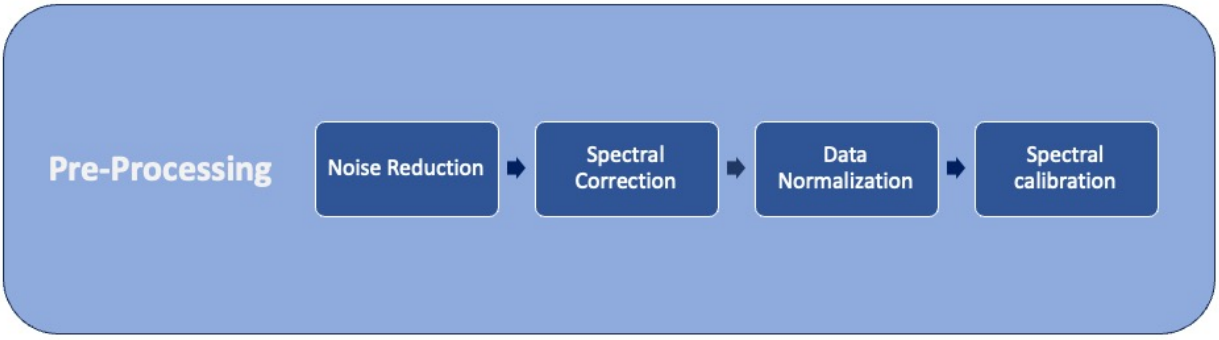


Figure 5.14 Schematic highlighting the sequential steps involved in pre-processing of multispectral images.

5.4.3.2.4 Noise Reduction

Noise reduction identifies and minimizes unwanted variations in the image data that does not represent the true signal captured from the scene imaged by the MSI camera. This "noise' refers to environmental conditions, electronic interference and

imperfections in the sensor (camera) system [377]. To correct for dark noise and ambient light, the dark image (acquired with the light source off) of each sample was subtracted from the corresponding bright (acquired with the light source on) sample image. Subsequently, to correct for the spectral characteristics/response of the optical system, each image (eight bands in total) was divided by a spectral correction factor specific to each band. This factor was extracted by:

1. subtracting the dark white reference from the bright white reference image to correct the white reference image
2. calculating the mean pixel value in each band out of the eight images of the corrected white reference image
3. dividing each band mean value with the maximum out of all eight bands value.

5.4.3.2.5 Spectral Correction

To ensure spectral information captured by the multispectral camera was accurate and consistent, spectral correction involved adjusting for optical imperfections and correcting for spectral band misalignment. We know that diffusely reflected light is absorbed and scattered [134]. The scattering properties of tissue samples are very complex, and during pre-processing spectra dominated by specular reflectance (direct scattering) need to be removed as outliers [378].

5.4.3.2.6 Normalization Techniques

Normalization was performed to adjust the MSI image data so it was consistent and comparable across the different filters used, apertures and operating room lighting conditions. To compensate for the variations in working distance and light intensities, and to avoid the dominance of a specific spectral band in the classification process, the corrected MSI images were normalised. Nine different normalisation techniques were implemented according to similar literature [18-25]. Table 5.2 summarizes the formulas utilised to deploy these techniques.

After the normalisation steps, the pixel values from each tissue type were extracted with the use of the ground truth masks as described above. Lastly, to ensure that the disease prevalence in our dataset was 1, meaning that the number of tumour pixels was the same as the number of healthy pixels, the two pixel classes in each

sample set were randomly equalised. This was possible in the freshly excised sub-set of data because each sample consisted of both healthy and tumour areas. However, this was not the case in the tissue samples. In this case, the size difference between the two classes was monitored for each fold to ensure a balanced dataset.

Table 5.2 Nine normalization techniques were utilised in pre-processing of spectral data acquired from the MSI images. $\boldsymbol{x_{i,j,\lambda,new}}$ is the new normalised pixel value at the spatial image location i,j of the band λ, while the $\boldsymbol{x_{i,j,\lambda,old}}$ is the old non-normalised value of the same pixel. $imagemin/imagemax$ is the minimum or maximum, respectively, pixel value in the whole spatial image. $bandmin/\ bandmax$ is the minimum or maximum, respectively, pixel value in each pixel spectrum. $\sum_{\lambda=470nm}^{\lambda=775nm} x_{i,j,\lambda,old}$ is the sum of all pixel values at the different 8 bands for each pixel, $\sum \lambda$ is the total number of bands, $\sum_{i=1}^{i=1044}\sum_{j=1}^{j=1408} x_{i,j,\lambda,old}$ is the sum of all pixel values in a single image (band) and $\sum i * \sum j$ is the total number of image pixels. $pixel\ value\ rank: \{1,2,3,4,5,6,7,8,\}$ means replacing a pixel value with its rank when compared to the other values across the nine bands of the same pixel.

Number	Name	Formula	Reference
1	Min/Max	$x_{i,j,\lambda,new} = \frac{x_{i,j,\lambda,old} - image\min\,(x_{i,j,\lambda,old})}{image\max\,(x_{i,j,\lambda,old}) - image\min\,(x_{i,j,\lambda,old})}$	[379]
2	Band SNV (Standard Normal Variate)	$x_{i,j,\lambda,new} = \frac{x_{i,j,\lambda,old} - \frac{\sum_{\lambda=470nm}^{\lambda=775nm} x_{i,j,\lambda,old}}{\sum \lambda}}{\sqrt{\frac{\sum_{\lambda=470nm}^{\lambda=775nm}(x_{i,j,\lambda,old} - \frac{\sum_{\lambda=470nm}^{\lambda=775nm} x_{i,j,\lambda,old}}{\sum \lambda})^2}{\sum \lambda}}}$	[173]
3	Norm1/Band Reflectance Division	$x_{i,j,\lambda,new} = \frac{x_{i,j,\lambda,old}}{\sum_{\lambda=470nm}^{\lambda=775nm} x_{i,j,\lambda,old}}$	[380]
4	Band Max Method	$x_{i,j,\lambda,new} = \frac{x_{i,j,\lambda,old}}{bandmax(x_{i,j,\lambda,old})}$	[381]
5	Band Min/Max Method	$x_{i,j,\lambda,new} = \frac{x_{i,j,\lambda,old} - band\min\,(x_{i,j,\lambda,old})}{band\max\,(x_{i,j,\lambda,old}) - band\min\,(x_{i,j,\lambda,old})}$	[382]
6	Norm-2/Square of Band Reflectance Division	$x_{i,j,\lambda,new} = \frac{x_{i,j,\lambda,old}}{\sqrt{\sum_{\lambda=470nm}^{\lambda=775nm} x_{i,j,\lambda,old}}}$	[383]
7	Band Value Ranking	$x_{i,j,\lambda,new} = \frac{pixel\ value\ rank: \{1,2,3,4,5,6,7,8,\}}{\sum \lambda}$	[384]
8	Max Method	$x_{i,j,\lambda,new} = \frac{x_{i,j,\lambda,old}}{bandmax(x_{i,j,\lambda,old})}$	[382]

9	SNV (Standard Normal Variate) Method	$x_{i,j,\lambda,new} = \frac{x_{i,j,\lambda,old} - \frac{\sum_{i=1}^{i=1044}\sum_{j=1}^{j=1408} x_{i,j,\lambda,old}}{\sum i * \sum j}}{\sqrt{\frac{\sum_{i=1}^{i=1044}\sum_{j=1}^{j=1408}(x_{i,j,\lambda,old} - \frac{\sum_{i=1}^{i=1044}\sum_{j=1}^{j=1408} x_{i,j,\lambda}}{\sum i * \sum j}}{\sum i * \sum j}}}$	[385]

5.4.3.2.7 Spectral Calibration

Imperfection in the camera lens or spectrometer grating can cause spectral variations. To ensure data analysis was reliable, spectral calibration was performed to ensure the wavelengths associated with the spectral bands captured by the MSI camera were accurately aligned with the reference wavelengths of the light being measured.

5.5 Tissue Sample Classification

Four classification models were applied, namely Logistic Regression, Support Vector Machines (SVM), Multilayer Perceptron (MLP), and Extreme Gradient Boosting (XGB). All classification routines were tested in a five-fold cross validation manner and separately for the tissue sample and freshly excised sample sub-sets with the support of Dr Maria Leiloglou. The validation metrics used were sensitivity, specificity and accuracy (defined as the area under the Receiver Operating Characteristics (ROC) curve). This yielded in each data sub-set (tissue sample, freshly excised sample) and for each normalisation approach (nine overall), each classification routine (four overall): 36 mean (over five folds) values for each classification metric.

5.5.1 Logistic Regression

Logistic Regression was implemented in Matlab (Matlab®, 2019b version) and consisted of:

1. Linear Discriminant analysis (LDA) for dimensionality reduction
2. Logistic Regression for assigning each pixel with a probability for tumour

3. Receiver Operating Characteristics (ROC) analysis to convert probabilities to a binary classification.

LDA is used in a two staged approach [386]. Firstly, dimensionality reduction to reduce the number of features in a dataset whilst retaining as many features as possible. Secondly, LDA projects data onto a lower-dimensional space and aims to maximize the separation between tissue subtypes.

Here, LDA identifies the optimal spectral dimension (the linear combination of the eight spectral bands) that optimally separates the two classes [172]. The spectral dimension is found when the value: $\frac{D^2}{S}$ is maximised, where D represents the linear combination of differences between the means in each spectral band and S is the sum of the within class variance in values for each spectral band.

After LDA, each MSI pixel is represented by one value, i.e. the optimal linear combination of its eight spectral values. Logistic regression was then used to convert the LDA-derived pixel value into probability for tumour [387]. Logistic regression was applied here, as the binomial distribution dictates the probability for tumour for each LDA-derived pixel value in the dataset [388].

Finally, ROC analysis was used to plot the true positive rate against the false positive rate while the classification threshold was varied [389]. This analysis identified the optimal threshold separation, i.e. the LR-derived probability above which the corresponding pixels would be considered as tumour. This threshold was the optimal ROC curve operating point, yielding the best combination of true positive/true negative rate in the training dataset.

5.5.2 Support Vector Machines

The main aim of SVM is to maximize the generalization ability of a model (Don Quixote) [390]. The three main concepts of SVM are hyperplane, margin and support vectors [390]. A set of n examples is needed for SVM training, and each example comprises of a pair (an input vector x and associated label y). The data are linearly separable by a line if in a two-dimensional space, or a plane in a three-dimensional space “hyperplane” (Figure 5.15) [391]. SVM aims to find the optimal separation hyperplane that maximizes the margin between the two classes. The margin is defined as the distance between the hyperplane and support vectors. “Support vectors” are

the data points that lie closest to the hyperplane, and are crucial in deciding the position and orientation of the hyperplane [391].

In this thesis a linear SVM version was implemented to identify the linear combination of spectra (hyperplane) in the eight spectral dimensions that could optimally classify the data, implemented with Python 3.7.

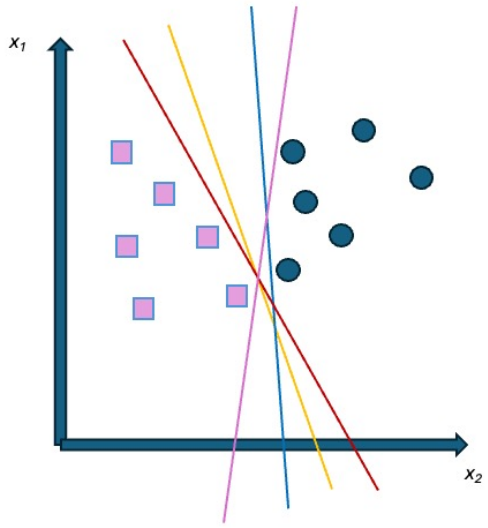


Figure 5.15 Graph showing a 2D representation of several separation hyperplanes that separate the input data set well. There are many potential hyperplanes that could separate the data. (Modified from Cervantes *et al.* 2020 **[391]**).

5.5.3 Multilayer Perceptron

Multilayer Perceptron (MLP) is a common type of artificial neural network, and consists of a network of nodes (processing elements) arranged in layers [392]. Typically there are three or more layers of processing nodes: input, hidden and output layers. The input layer receives external data, and involves no computation [392]. The hidden layers are where computation is performed and allows the network to learn complex representations by transforming the data via non-linear functions. The output later performs the classification task. Each node (or neuron) within a layer is connected to every node in the subsequent layer, allowing a fully connected network. Nodes within the hidden and output layers compute the weighted sum of inputs at the presence of the bias, and this sum is directed through an activation function [393].

The MLP then requires training, commonly done by forward and backpropagation. Forward propagation is where input data is passed through the

network layer by layer, and is influenced by weights, biases and activation functions at each node. Backpropagation adjusts for the errors identified from weight and biases in forward propagation. In this thesis the MLP was based on the 'MLPClassifier' class from the scikit-learn library, version 0.24.0. Default parameters were employed for model training and testing [394].

5.5.4 Extreme Gradient Boosting

This machine classifier system was used in chapter four. XGB constructs an ensemble of decision trees and iteratively adds new models by focusing on the gradient reduction of loss in the previous models. In this thesis XGB was implemented using the 'xgboost' package, version 1.5.2. A random seed of 1234 was set for reproducibility. Default parameters were used for the tree-based model with logistic regression as the objective function [395].

5.6 MSI Classification Overlays

After comparison of the sensitivity, specificity and accuracy between the different normalisation /classification combinations used, the best-performing combination was used for visualisation of the final classification result. This was implemented by overlaying the colour-map representing the tumour location on top of the colour image of the imaged scene for reference. The red, green and blue channels of this colour image were reconstructed from the MSI image, by simulating the signals of each of the three broadband filters. This involved calculating the weighted sum of the spectral bands contributing to each channel. The weights for each spectral band were determined based on their contribution to the corresponding RGB channels (Figure 5.16).

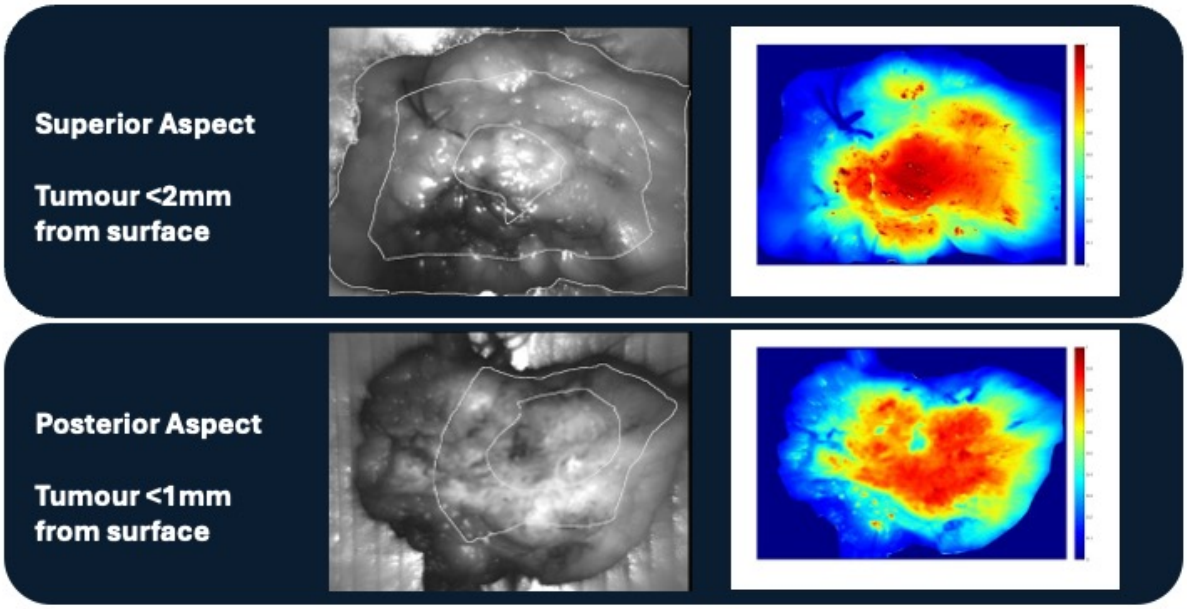


Figure 5.16 Examples of colourmaps produced from two different multispectral images. Colourmaps are classification overlays that depict the probability of tumour within 3mm of the resection surface. As seen in the far right images, the colour gradient represents likelihood of tumour and normal tissue (blue). The corresponding marked multispectral image for ground truth marking is also presented (the area within the centrally marked area depicts known tumour, and area outside the most peripherally marked area represents healthy breast tissue).

5.7 Results

5.6.1 Freshly Frozen Tissue Samples

5.6.1.1 Demographics

In total, 184 freshly frozen tissue samples were interrogated with MSI. Following quality assessment 68 samples were utilised for final analysis. Table 5.3 identifies the patient and tumour characteristics of these samples. All patients included in final analysis were female. The median age of patients where breast tissue samples were taken was 60.4 years (range 25 – 94). The most common ethnicity was Caucasian (62.3%). Healthy tissue comprised 30.9% of tissue samples, followed by invasive ductal carcinoma (IDC) (25%), invasive lobular carcinoma (ILC) (23.5%), ductal carcinoma in-situ (DCIS) (13.2%) and pathological complete response (pCR) (5.9%).

Table 5.3 Patient demographic data and tumour characteristics of all freshly frozen breast tissue samples utilized in final data analysis. (pCR – pathological complete response; DCIS – ductal carcinoma in situ; IDC – invasive ductal carcinoma; ILC – invasive lobular carcinoma; ER+ - oestrogen receptor

positive; ER - - oetrogen receptor negative; PR- - progesterone receptor negative; PR+ - progesterone receptor positive; Her2+ - Herceptin receptor positive; Her2- Herceptin receptor negative); NACT – neoadjuvant chemotherapy).

Patient Demographics	
Age (years):	
Median	60.4
Range	25 - 94
Ethnicity:	
Caucasian	43/68
Afro-Caribbean	4/68
Asian	4/68
Arabic	5/68
Other	4/68
Unknown	8/68
Tumour Characteristics	
Histological subtype:	
Healthy	21/68
PCR	4/68
DCIS	9/68
IDC	17/68
ILC	16/68
Grade of invasive tissue samples:	
1	2/37
2	25/37
3	10/37
Intermediate	4/9
High	5/9
Hormone receptor status (of invasive and PCR subtypes):	
ER+PR-HER2-	17/37
ER+PR+HER2-	10/37
ER+ PR+ HER2+	1/37
ER-PR-HER2+	0/37
ER-PR-HER2-	9/37
Neoadjuvant therapy:	
NACT	8/68

5.6.1.2 Validation Metrics

Each classification model was applied to the data for each normalization approach, and the metrics as tabulated in table 5.4 was produced.

Table 5.4 Table to show results for each classification model (Logistic regression; SVM; MLP and XGB for each normalization approach. (AUC – area under curve).

	Normalization Technique								
	Min/Max	***Band SNV***	***Norm1***	***Band Max***	***Band Min/Max***	***Norm2***	***Ranking***	***Max***	***SNV***
Logistic Regression									
AUC	35 ±15 %	61 ±14 %	47 ±27 %	55 ±26 %	50 ±12 %	60 ±25 %	33 ±18 %	38 ±9 %	50 ±3 %
Sensitivity	80 ±45 %	94 ±11 %	68 ±45 %	77 ±43 %	86 ±31 %	97 ±5 %	99 ±17 %	60 ±55 %	80 ±45 %
Specificity	20 ±20 %	28 ±33 %	44 ±44 %	39 ±53 %	22 ±41 %	25 ±39 %	11 ±14 %	40 ±55 %	20 ±45 %
SVM									
AUC	36 ±15%	34 ±18%	38 ±18%	40 ±22%	36 ±24%	42 ±20%	37 ±20%	30 ±14%	49 ±2%
Sensitivity	94 ±4%	95 ±3%	90 ±4%	87 ±7%	93 ±6%	87 ±8%	88 ±15%	92 ±6%	100 ±0%
Specificity	2 ±1%	2 ±2%	10 ±7%	11 ±6%	1 ±1%	15 ±9%	11 ±16%	2 ±2%	0 ±0%
MLP									
AUC	63 ±13%	64 ±13%	71 ±13%	73 ±12%	71 ±14%	72±0.1%	37 ±12%	63 ±1%	49 ±5%
Sensitivity	80 ±6%	79 ±8%	84 ±3%	81 ±9%	84 ±3%	82 ±5%	82 ±13%	75 ±16%	84 ±2%
Specificity	46 ±18%	45 ±14%	52 ±15%	55 ±14%	53 ±19%	56 ±15%	10 ±15%	47 ±14%	16 ±3%
XGB									
AUC	63 ±16%	66 ±13%	75 ±14%	74 ±14%	71 ±13%	73 ±15%	38 ±11%	64 ±12%	50 ±6%
Sensitivity	85 ±1%	80 ±12%	84 ±4%	83 ±7%	85 ±5%	83 ±5%	83 ±15%	84 ±2%	89 ±2%
Specificity	42 ±16%	44 ±14%	58 ±19%	58 ±18%	46 ±21%	58 ±19%	11 ±15%	42 ±18%	11 ±2%

Table 5.4 displays variation in results not only amongst the classifiers, but also amongst the normalization techniques. However, the MLP and XGB classification methods demonstrated the most favourable scores. MLP and XGB classification outcome metrics are tabulated below for the two best and worst performing normalization techniques (Table 5.5).

Table 5.5 Outcome metrics for the Multilayer Perceptron and Extreme gradient boosting. Grey shaded boxes are the best performance results for each classifier.

MLP				
	Band Min/Max	**Norm2**	**Ranking**	**SNV**
AUC	71 ±14%	72 ±13%	37 ±12%	49 ±5%
Sensitivity	84 ±3%	82 ±5%	82 ±13%	84 ±2%
Specificity	53 ±19%	56 ±15%	10 ±15%	16 ±3%
XGB				
	Norm1	**Norm2**	**Ranking**	**SNV**
AUC	75 ±14%	73 ±15%	38 ±11%	50 ±6%
Sensitivity	84 ±4%	83 ±5%	83 ±15%	89 ±2%
Specificity	58 ±19%	58 ±19%	11 ±15%	11 ±2%

The selection of the data normalisation technique did not yield statistically significant differences in the classification results, except for the 'Ranking' and the 'SNV' techniques, which underperformed, as indicated in Table 5.4. For the MLP approach, the 'Band Min/Max', for example, performed better than the 'Ranking' and 'SNV' normalisation techniques with AUC: 72 ±13% vs 37 ±12 % ($p=0.001$) and 49 ±5 % ($p=0.003$) and specificity: 53 ±19% vs 10 ±15 % ($p=0.002$) and 16 ±3 % ($p=0.001$), respectively.

Similarly, for the XGB approach, the 'Band Norm-1', for example, performed better than the 'Ranking' and 'SNV' normalisation techniques with AUC: 75 ±14% vs 38 ±11% ($p=0.001$) and 50 ±6% ($p=0.003$) and specificity: 58 ±19% vs 11 ±15% ($p=0.001$) and 11 ±2% ($p<0.001$), respectively. All reported p-values above were computed utilizing the t-distribution with eight degrees of freedom.

5.6.2 Intraoperative Freshly Excised Breast Specimens

5.6.2.1 Demographics

Following camera development final recruitment involved 46 patients. However, for final analysis 23 of the recruited patients were used in the 5-fold cross validation. Nine cases were excluded as tumour was deemed too distant from the resection surface (more than 3mm), six because samples were contaminated with blue dye, five could

not be marked for ground truth because of the small size of the tumour and three were excluded due to workflow barriers.

Demographic data, clinicopathological and tumour characteristics are represented in Table 5.6. All 23 patients were female, with a median age of 59.8 years (range 27 – 80) and a median body mass index of 27.3 kg/m^2 (range 19.9 – 39.8). 70% of patients had a breast density of two or three (as per the breast imaging-reporting and data system (BI-RADS), representing scattered or heterogenous fibroglandular density respectively. Over 78% of patients were of British Caucasian descent. In the Imperial Breast Unit, magnetic seed localisation technique was the commonest method to identify tumour location intraoperatively.

Table 5.6 Patient demographic data and tumour characteristics of all freshly excised breast specimens from 23 patients included in analysis.

Patient Demographics	
Age (years):	
Median	59.8
Range	27 – 80
BMI:	
Median	27.3
Range	19.9 – 39.8
Breast Density: (as per BIRADS classification):	
1	4/23
2	8/23
3	8/23
4	2/23
Not recorded (too young for MMG)	1/23
Ethnicity:	
Caucasian – British	18/23
Caucasian – Other	1/23
Afro-Caribbean	1/23
Asian	2/23
Other	2/23
Localisation technique:	
None	3/23
Wire	3/23
Magseed	17/23

Tumour Characteristics	
Size (mm):	
Mean	16.25
Range	6 – 35
Histological subtype:	
DCIS	4/23
IDC	13/23
ILC	1/23
ILC & LCIS	1/23
Adenoid cystic carcinoma	1/23
Papillary carcinoma	1/23
Fibroadenoma with PASH	1/23
Spindle cell	1/23
Grade of invasive type specimens (where grade relevant):	
1	3/15
2	8/15
3	1/15
Grade of DCIS specimen:	
Intermediate	1/4
High	3/4
Hormone receptor status (for invasive lesions):	
ER+PR-HER2-	1/17
ER+PR+HER2-	13/17
ER+ PR+ HER2+	2/17
ER-PR-HER2+	0/17
ER-PR-HER2-	1/17
Neoadjuvant therapy:	
NACT	1/23
Cavity shaves performed:	
All radial margins	7/23
Specific margins	10/23
None	6/23
Re-excision surgery performed:	
Yes	6/23
No	17/23

The mean size of tumours in the patients recruited for this study was 16.25 mm. In accordance with the commonest breast cancer subtype, 56.5% of patients had IDC. 17.4% of specimens utilised for data analysis had pure DCIS. Other less common cancer subtypes were found amongst the specimens and are highlighted in table 5.6. Only one patient included in final analysis had neoadjuvant chemotherapy. From this patient cohort 26% required re-excision surgery following final histopathological reporting. Intraoperatively, nearly half of the patients had immediate margin shaves performed by the operating surgeon.

5.6.3 Validation Metrics

Once again the four different classifiers were applied to multispectral data using nine different normalization techniques, and shown in table 5.7.

Table 5.7 Overall validation metrics for each classifier and each normalization technique.

	Normalization Technique								
	Min/Max	Band SNV	Norm1	Band Max	Band Min/Max	Norm2	Ranking	Max	SNV
	Logistic Regression								
AUC	76 ±4%	56 ±7%	57 ±7%	59 ±8%	59 ±6%	62 ±6%	52 ±9%	76 ±6%	89 ±7%
Sens	82 ±7%	67 ±31%	70 ±25%	58 ±22%	58 ±9%	57 ±9%	64 ±37%	70 ±20%	86 ±12%
Spec	62 ±12%	46 ±27%	44 ±32%	61 ±15%	57 ±13%	63 ±13%	47 ±9%	75 ±18%	80 ±8%
	SVM								
AUC	78 ± 4%	57 ± 4.9%	57 ±5.8%	58 ± 2.7%	60 ± 2.3%	59 ± 4%	56 ± 4.2%	78 ± 6.3%	87 ±9.5%
Sens	62 ± 33.5%	57 ± 6.4%	61 ± 14.8%	59 ± 8.5%	63 ± 12.7%	60 ± 5.9%	69 ± 11.5%	61 ± 32.4%	80 ± 13.3%
Spec	72 ± 15.1%	50 ± 8.6%	49 ± 6.7%	51 ± 9.8%	51 ± 11.5%	50 ± 8.0%	40 ± 11%	76 ± 12.6%	81 ± 8.7%
	MLP								
AUC	64 ± 13%	60 ± 5.6%	66 ± 6%	66 ± 7.8%	64 ± 6.4%	65 ± 7.4%	57 ± 3.3%	65 ± 9%	82 ± 8.1%
Sens	54 ± 18.1%	53 ± 6.4%	57 ± 10.1%	56 ± 14.5%	52 ± 5.8%	55 ± 13%	69 ± 11.0%	52 ± 16.1%	78 ± 11.2%
Spec	67 ± 18.5%	63 ± 7.1%	66 ± 4.5%	66 ± 8%	66 ± 9.3%	66 ± 4.5%	44 ± 12.3%	67 ± 20.1%	76 ± 6.2%
	XGB								
AUC	66 ± 10.7%	61 ± 5.6%	65 ± 7.9%	65 ± 7.8%	63 ± 6.4%	65 ± 8.1%	58 ± 3%	67 ± 13.1%	83 ± 7.9%
Sens	56 ± 15.7%	53 ± 8.4%	54 ± 13.6%	54 ± 13.3%	53 ± 9.7%	54 ± 13.0%	68 ± 9.4%	51 ± 19.9%	79 ± 10.5%
Spec	66 ± 15.4%	63 ± 4.9%	67 ± 8.1%	67 ± 6.9%	65 ± 10.4%	67 ± 6.9%	44 ± 10.0%	70 ± 18.2%	76 ± 6.0%

Table 5.8 Classification results for different combinations of normalisation and classification methodologies in the freshly excised specimens data-set.

Max				
	Logistic Regression	**SVM**	**MLP**	**XGB**
AUC	76 ± 6%	78 ± 6.3%	65 ± 9%	67 ± 13.1%
Sensitivity	70 ± 20%	61 ± 32.4%	52 ± 16.1%	51 ± 19.9%
Specificity	75 ±18%	76 ± 12.6%	67 ± 20.1%	70 ± 18.2%
SNV				
	Logistic Regression	**SVM**	**MLP**	**XGB**
AUC	89 ± 7%	87 ± 9.5%	82 ± 8.1%	83 ± 7.9%
Sensitivity	86 ± 12%	80 ± 13.3%	78 ± 11.2%	79 ± 10.5%
Specificity	80 ± 8%	81 ± 8.7%	76 ± 6.2%	76 ± 6.0%
Ranking				
	Logistic Regression	**SVM**	**MLP**	**XGB**
AUC	52 ± 9%	56 ± 4.2%	57 ± 3.3%	58 ± 3%
Sensitivity	64 ± 37%	69 ± 11.5%	69 ± 11.0%	68 ± 9.4%
Specificity	47 ± 9%	40 ± 11%	44 ± 12.3%	44 ± 10.0%

In the freshly-excised sample data-set, the ‘Max’ and the ‘SNV’ normalisation techniques yielded the best scores. As is evident from Table 5.7 the selection of the classification model did not lead to statistically significant differences in the results. With the exception of the ‘Min/Max’ technique, the majority of the results in the rest of the normalisation techniques were statistically significantly inferior to the ‘Max’ and the ‘SNV’ results. For example, the ‘SNV’ performed better than the ‘Ranking’ normalisation technique with AUC: 89 ±7% vs 52 ±9 % ($p<0.001$) and specificity: 80 ±8% vs 47 ±9 % ($p<0.001$). All reported p-values above were computed utilizing the t-distribution with eight degrees of freedom.

5.7 Discussion

Multispectral imaging has the ability to distinguish between normal and malignant breast tissue. In combination with machine learning in the ex-vivo setting MSI has an AUC of 75%, and in the in-vivo setting an AUC of 89%. This discussion section will assess the novelty of this work in this field and postulate why the results have occurred but will also dissect the limitations of this work and how future studies can be improved.

5.7.1 Spectral Data Quantity

In the in-vivo validation study 6,301,712 spectra were acquired from 23 patients alone. To the best of our knowledge, this is the largest spectral dataset acquired from any study interrogating breast tissue samples when investigating intraoperative margin assessment tools. By comparison, Laughney *et al*., where 265,000 spectra were acquired from 47 patients in total [175]. Laughney *et al.* imaged the surfaces of sliced fresh breast conserving surgery specimens rather than the exterior surface [175]. Due to the MOU at Charing Cross permission was not granted for us to slice freshly excised lumpectomy specimens, therefore we are not able to replicate work carried in other studies for comparison.

5.7.2 Ability to Distinguish Between Normal Versus Malignant Tissue

This thesis has shown MSI has potential to provide useful information regarding the oncologic status of a whole resection surface which can be presented visually to the surgeon. The systematic review and meta-analysis of chapter two highlighted a pooled sensitivity of 90% (with a range of 82-100%) and specificity of 92% (with a range of 78-106%). When freshly-excised tissue was examined with MSI, we demonstrated a maximum of 86 ± 12% for sensitivity and 80 ± 8% for specificity. These findings are comparable when set in context of other work in this field. The majority of previous studies performed gross sectioning of the freshly excised specimens before imaging, whereas, uniquely here, the whole gross specimen was imaged intra-operatively [168,

172, 173]. This methodology may explain the higher diagnostic accuracy rates identified in such studies. For example, Kho *et al.* used hyperspectral imaging on sliced breast specimens to reveal a sensitivity of 98% and specificity of 99% [173]. Similarly, McClatchy *et al*. interrogated sliced specimens with spatial frequency domain imaging to gain a sensitivity of 90% and specificity of 81% [174].

It is important to correlate the accuracy rates of our MSI system to current commercialised IMA tools. MarginProbe® (Dilon Technologies, USA) utilises radiofrequency spectroscopy and in a recent systematic review the mean sensitivity was 69.07% (SD 10.45) and mean specificity was 63.47% (SD 26.50) however this was calculated from only three studies [130]. Individual studies however have reported higher sensitivity rates 70-100% and specificity 70 to 87% [130]. ClearEdge™ (LSBioPath, Saratoga, CA, USA) is another example of a commercially available device which uses bioimpedance spectroscopy. In a study of 58 patients where ClearEdge™ was used to assess the edges of excised wide local excisions the sensitivity was 84.31% and specificity 81.9% [131]. In a recently published abstract where a systematic review identified 18 studies where micro-CT was used as a IMA tool, the pooled sensitivity was 0.67 (95% CI:0.48-0.82) and pooled specificity was 0.75 (95% CI: 0.63-0.84) [396]. However, individual studies using micro-CT have shown higher sensitivity up to 93% but it is noted in this study that the false positive rate was high [118]. Therefore, our MSI system on freshly excised tissue has similar or even superior accuracy rates compared to current commercialised IMA tools.

5.7.3 Comparison of MSI on Frozen Tissue Versus Fresh Tissue

In chapter four, the effects of freezing on tissue was discussed. These effects are likely to contribute to the lower accuracy rates of MSI on frozen tissue compared to fresh. Freshly excised tissue will have different optical properties, specifically the concentration of oxygenated and deoxygenated haemoglobin (absorbers of light) will typically be higher compared to frozen tissue [339-341].

The physical aspects of the tissue imaged by MSI must also be considered. The freshly frozen tissue samples were thawed and were only a few millimetres thick. In comparison the freshly excised lumpectomy specimens were significantly larger in terms of size and volume and had varying surface contours on each aspect.

5.7.4 Translational Ability To Intraoperative Use

Apart from biophotonic modalities that have been investigated, technologies such as bioimpedance spectroscopy, rapid evaporation ionization spectrometry and MRI have also been used to interrogate breast specimens for tissue differentiation. Thus far none of these techniques have been adopted in routine breast surgery practice as they do not fit into the existing surgical workflow; provide inadequate tissue discrimination; lack ability for real-time feedback; are physically not suitable to fit into theatre space or are bench top arrangements only. This multispectral set-up can be translatable into surgical workflow for margin assessment for several reasons as to be outlined below.

Our multispectral system allows the surgeon to receive real-time feedback in seconds. Short data acquisition time is enabled here by utilising a small number of bands (8-bands) and a frame rate of 0.25 – 0.5 fps. Our multispectral camera can facilitate a frame rate of 1 dataset per 2 seconds (bright and dark MSI, and corresponding RGB image of the same scene). The slow frame rate is attributed to our choice of MSI acquisition hardware (a filter-wheel or a band sequential approach), with the colour information collected over time. A snapshot MSI approach, such as a multiaperture filtered camera, could be a better option for the real-time implementation of our proposed 8-band MSI system [397]. Regarding the choice of the spectral range, bands within the visible and NIR spectrum were chosen because it has been shown by Kho *et al*. [172], and Manen *et al.* [398] the combination can yield better classification scores. The near infrared band was added with the aim to acquire information from deeper tissue layers. Future work should focus on comparing classification performance between imaging at different band combinations.

The classification overlays represented in figure 5.16 represent the visual aids a surgeon would expect to see when using this system intraoperatively, which we anticipate would help guide them regarding the need for targeted immediate margin re-excision. Appendix D represents all the colourmaps produced of the 23 patients included in the final analysis.

Other benefits of our multispectral imaging system are the compact size allows utilisation in confined theatre spaces. Cost is another advantage. The estimated cost of this set up is £5000, in comparison to other systems such as MarginProbe® ($50,000) or micro-CT ($250,000 to $1 million). It's non-invasive approach means that

multispectral imaging does not affect the tissue structure and therefore does not disrupt pathologists' workflow. The above described features of multispectral imaging provide a platform for clinical adoption as a useful intraoperative margin assessment tool.

5.8 Limitations

This is the first study to date that has utilised MSI on both frozen tissue samples and freshly excised specimens to assess its use as an IMA tool. Although the results are promising, clearly there is significant more work to be done to improve accuracy and allow efficiency in the operating theatre. Several limiting factors are identified in this experimental work and are outlined systematically below.

5.8.1 Patient Recruitment

An important consideration when it comes to diagnostic accuracy is a study's statistical power. Based on this study's results, 237 patients should be included in a subsequent study to estimate the true specificity with 5% error margin at 0.5 significance level. Due to time constraints of this thesis the final number of patients recruited were insufficient to meet the power calculation. Any future work should aim to recruit patients not only from the Charing Cross site but also other hospitals to enable recruitment in a more timely fashion.

5.8.2 Drop Out Rate of Specimens

Although a high volume of frozen tissue samples was imaged and 46 patients had their wide local excision specimens imaged, not all were utilised for data analysis due to contamination from blue dye or pathology ink, or the samples were of poor quality. Any IMA tool must be robust enough to tackle the variety of environmental circumstances breast tissue is subjected to in the real-world operating environment.

Six patients were not included in the analysis as specimen surfaces were contaminated with blue dye which is utilised for sentinel lymph node biopsy. This is a

significant limitation as many centres internationally use this along with radioisotope for dual mapping when staging the axilla. However, in light of the recent SOUND trial (Sentinel Node vs Observation After Axillary Ultrasound) it can be argued that the use of blue dye in breast surgery could become obsolete or used significantly less [399]. The SOUND trial was a randomized control trial which identified that in patients with small breast cancers who had negative preoperative axillary ultrasound findings, SLNB could be omitted [399]. It has been evidenced in this trial that omission of axillary surgery in such a patient cohort was non-inferior to patients who had SLNB [399]. Studied endpoints included distant disease-free survival; locoregional relapses; distant metastases; and deaths were comparable in both groups [399]. In view of these findings, the need of SLNB can be reduced and therefore arguably blue dye will be less common place in future.

The challenge of laboratory work was the acquisition of high-quality samples. Ideally freshly excised tissue samples from lumpectomy or mastectomy specimens would be the best tissue samples to image. Ideally every malignant tissue sample should be paired with a normal area of tissue from the same patient for comparison. This was available for many of the cases used in this thesis but due to quality of sample issues, data was unfortunately not analysed in this manner.

5.8.3 Heterogeneity of Tissue Samples/Patients

In this chapter, the focus of data analysis was comparing normal with malignant tissue. In chapter four histological subtypes were compared against each other. However, this was not possible in this chapter due to the uneven distribution of samples of patients amongst each histological breast cancer subtype. Future work to develop this technology as an IMA tool would require the machine learning algorithm to train on a variety of breast tissue subtypes to optimize accuracy. Chapter two highlighted that studies using previous imaging systems utilising spectrally resolved light lacked sample heterogeneity.

DCIS is a strong predictor for a positive margin [332]. Therefore, intraoperative DCIS visualisation accuracy rates are crucial to the ideal IMA tool. Despite efforts to include DCIS cases in this thesis, a clear limitation was to the extract the corresponding ground truth in the images. When there were pockets of DCIS, for

example noted from specimen reports, then these were not marked as it is hard to identify these clearly from the specimen radiograph and felt it would not be accurate. Future work must overcome the challenge to mark for ground truth purposes. In terms of the tissue samples, theoretically DCIS samples here could be used to train the learning algorithm for freshly excised tissue for identification of DCIS. The challenge would be acquiring fresh tissue from patients who have got large areas of DCIS. This could potentially be acquired from patients who are undergoing mastectomy for multifocal DCIS, however this would have to involve multi-site patient recruitment.

5.8.4 Ground Truth Marking

A challenge in the methodology was the segmentation of images for ground truth. Despite that the specimen radiography, the colour image and the corresponding histopathology report has been used to inform the segmentation of the freshly-excised specimens, there still remains inter-observer variability amongst interpretation of this information. For the purposes of this thesis, I performed the freshly-excised image segmentation alone. For the freshly excised tissue the anterior and posterior aspects of each specimen were by far the easiest to mark. For data analysis radial aspects of the specimen were included but it should be considered this is interpretation by one clinician. Ideally, another clinician should perform the task on the same images and segmentation compared.

This challenge was mitigated in the frozen tissue sample dataset by directly overlapping the H&E histopathology images of the samples onto the corresponding MSI images to segment the ground truth regions. The H&E slides visualise the malignancy and considered by definition the ground truth. However, this approach also comes with its limitations. Due to tissue fixation process by the pathologist, there is tissue shrinkage, which, in turn, can lead to alteration of the specimen and the stained slides' spatial correlations [400].

5.8.5 Machine Learning

Several machine learning algorithms were trialled here, but imbalanced datasets clearly affect overall results, and this problem needs to be addressed. GB and XGB are examples of 'bagging and boosting' sampling techniques which can improve the performance of the minority class, in this instance where sample numbers are low [401]. The problem of imbalanced datasets can be tackled at either the data level or algorithmic level [402], and should be considered for future work with larger datasets.

At the data level, re-sampling techniques can be used in the form of over-sampling or undersampling to balance the training data amongst classes [401]. Over-sampling aims to increase the size of the minority class to achieve balanced classes. With random oversampling, samples in the minority class are duplicated having been randomly selected. A more commonly used oversampling method is Synthetic Minority Over-Sampling (SMOTE), where synthetic samples are produced from the minority class [401]. Alternatively, random undersampling can be used whereby during pre-processing of data random sets of sample data from the majority class are removed to balance the classes [401]. The disadvantage of this is that crucial information can be lost. Tomek Links or Edited nearest neighbours are a method in undersampling that removes samples from the majority class which have similar features to samples in the minority class to define the decision boundary better and thus improving overall classification. Hybrid sampling combines sampling methods and reduces the limitations of such methods [401].

At the algorithmic level, cost sensitive learning is a method that can be used to tackle imbalanced datasets [401]. Here the algorithm is modified to account for the imbalance by assigning a higher misclassification cost to the minority class. Another alternative is the use of neural networks which can be trained for iterative weight adjustment to minimize error [401].

5.9 Conclusion

In section 1.6.3 of this thesis functions of an ideal IMA tool were discussed, and MSI has several favourable features for intraoperative use including the ability to image a whole resection surface to a depth of 3 mm, without the requirement for a pathologist to be present. With development of the best machine learning algorithms, real-time feedback would be possible with MSI to augment a surgeon's vision to guide knowledge about margin disease. The ability to discriminate between malignant and healthy breast tissue is far superior to the traditional method of specimen radiography, and similar to current technologies available. However, for MSI to be a technology that is widely accepted in the field of breast surgery further work must entail recruiting further patients, to encompass breast heterogeneity and to allow assessment of MSI to distinguish between different breast cancer subtypes in a clinical trial.

Chapter 6: Comparison of Multispectral Imaging *Versus* Fluorescence Guided Imaging

The use of multispectral imaging is advantageous in the clinical setting of breast surgery as it is non-invasive to the patient and does not require the use of exogenous agents. Chapter five presents the results of how multispectral imaging can distinguish between healthy and malignant breast tissue, but further work is required to enable this potential IMA tool to augment a surgeon's vision intraoperatively to lower re-excision rates. One possible method to improve diagnostic accuracy is to combine several imaging modalities [403]. Section 1.6.2 of this thesis discussed optical and imaging based technologies that have been investigated in breast conserving surgery, with each modality type drawing upon different features of breast tissue

Fluorescence guided imaging is another optical imaging method within biophotonic technologies that is a suitable modality to combine multispectral imaging with. Fluorescence guided imaging relies on understanding how fluorophores work, and section 2.1.4 of this thesis has described intrinsic fluorophores. The objectives of this chapter are to explain the mechanism by which fluorophores function, which are the basis of some exogenous agents that could be used in breast surgical patients for fluorescence guided surgery. A secondary aim was to investigate how performance metrics compared between our custom-built multispectral imaging system and a fluorescence imaging system.

6.1 Fluorescence Imaging

Fluorescence guided surgery (FGS) is an optical technique that identifies targeted tissue. FGS achieves this by specific imaging systems which are sensitive to fluorescent molecules called fluorophores [404, 405]. Once fluorophores are excited with non-ionizing light, their fluorescence is captured by specially built camera systems [406]. The signal in the region of interest (cancerous area) is calculated by the difference in signal between healthy breast tissue and cancer [404].

For clinical use, utilising the near-infrared range of light is advantageous. NIR fluorescence permits improved depth penetration, and the use of a NIR filter set

reduces background autofluorescence [407]. Autofluorescence describes the phenomena whereby when tissue absorbs light, it can also emit fluorescent light [408].

6.2 Fluorophores

As previously discussed (section 2.1.4) key endogenous fluorophores in breast tissue are NADH and FAD, which are key metabolic cofactors involved in cellular metabolism [409]. Solid tumours have unique anatomical and pathophysiological traits. Understanding these traits is crucial to developing suitable exogenous fluorophores to give patients for FGS, and examples of exogenous fluorophores are discussed in section 6.3 below.

Fluorophores can target tumours via two strategies, either passively or actively, dependent on which tumour traits are exploited [403]. Passive targeting relies on the selective accumulation of exogenous contrast agents within the tumour [403]. One particular trait of solid tumours increased vasculature can be exploited by exogenous fluorophores using passive targeting. Increased angiogenesis, a hallmark of cancer, is needed to fuel a growing tumour with nutrition and oxygen [177]. Features of this neovasculature include irregular, dilated and leaky blood vessels [410]. The basement membrane of these new vessels are also altered, and lymphatic drainage of malignant is poor. In combination, these features cause leakage of plasma components into the malignant tissue called the enhanced permeability and retention (EPR) effect [410]. A challenge of passive targeting is that its efficacy is dependent on the EPR effect, which is influenced by [403]. Variations in neovasculature may impede the EPR effect.

Active targeting, in comparison, is where fluorophores are designed to precisely target known receptors [403]. This allows accumulation of fluorophores within particular tissues or cells. Antibodies, nanoparticles, proteins and aptamers are examples of ligands to which a fluorescent contrast agent is bound to, to actively target chosen target receptors. Ligands must have high binding specificity and low toxicity, with selected receptors chosen to reflect knowledge of the tumour microenvironment. Limitations of active targeting include non-specific binding and background ongoing fluorescence from the given agent can occur due to pharmacokinetics [403].

6.3 Current Use of Fluorophores in Medicine

Fluorophores with excitation and emission spectra within the wavelength range 700 to 900 nm, have become the focus of much research. With the advent of improved hardware systems, and drug development of targeted fluorophores, FGS has the potential to transform intraoperative tumour detection. Table 6.1 highlights fluorophores that have been investigated in the clinical setting, of both passive and active targeting methods.

Table 6.1 Table showing examples of fluorophores that have been investigated for passive and active targeting. For each fluorophore, the wavelength of light they have been associated with is noted with their mechanism of action (if known) and the solid tumours the have been investigated with. Finally, it is documented if the fluorophore has been approved for clinical use.

	Fluorophore	**Excitation/ Emission (nm)**	**Mechanism**	**Currently Used in or being investigated in**	**Approval Phase**
Passive	Methylene Blue [411]	665/686	Affinity to bind to intracellular structures with high nucleic acid content	Sentinel lymph node mapping (breast and melanoma) Tumour detection (neuroendocrine, thyroid/parathyroid), Vital structure detection (e.g ureters)	Approved
	ICG [412]	800/822	EPR effect	Sentinel lymph node mapping (breast, skin) Hepatobiliary tumours Endometrial tumours Angiography in reconstructive surgery	Approved
Active	5-ALA [413]	405/635	Intracellular enzymes	Brain tumours	Approved
	Cyanine dyes [414]	Variable (e.g Cy 5 658/666)	Enzymes or receptors	Colorectal, pancreas, oesophageal cancer	Trials
	Fluorescein [415]	460/540	Receptors	Brain tumours	Approved

6.3.1 Indocyanine as a Fluorophore

Indocyanine green (ICG) was the first clinically approved fluorophore for tumour detection. ICG is a heptamethine cyanine fluorophore, with hydrophobic properties which renders it suitable to bind to plasma proteins and therefore stays within the intravascular space [407]. When ICG binds to plasma proteins it does not alter structure, which explains ICG's non-toxicity [416]. The rapid excretion of ICG is due to no metabolite production and its fast excretion into bile (transportation via a protein called glutathione S-transferase) [416]. ICG is a passive fluorophore functioning via the EPR effect. ICG fluoresces within the near infrared range, with a peak absorption of 800 nm and emission peak at 830 nm in-vivo.

ICG has been investigated and is used across numerous specialities. Historically, it has been used to measure cardiac output, hepatic function, and retinal angiography [404]. It can be used for assessing lymphatic vessel drainage and sentinel lymph node mapping in breast cancer and melanoma. In terms of intraoperative tumour detection, ICG's clearance by the liver means its use is conducive in hepatobiliary surgery for primary and secondary liver carcinoma [407].

6.3.2 ALA as a Fluorophore

5-aminolevulinic acid (5-ALA) is a hydrophilic nonproteinogenic amino acid. In cells with high metabolic activity, 5-ALA acts as a substrate in the haem synthesis pathway. 5-ALA is processed via this pathway to produce abundant protoporphyrin IX (PpIX). PpIX is the immediate precursor to haem and is an endogenous fluorophore. Haem is one part of haemoglobin essential to the function of red blood cells (erythrocytes). In early erythrocyte development, haem is needed for the binding and release of oxygen molecules. In other cells of the body synthesizing haem, haem mediates the electron transfer in the mitochondrial respiratory chain.

Within mitochondria, 5-ALA is formed from succinyl coenzyme A and glycin, by ALA-synthase (ALA-S) (Figure 6.1). Haem regulates this step, so ongoing synthesis of ALA-S is inhibited. Following 5-ALA formation, it is released into the cell cytosol.

Several molecules of 5-ALA form one molecule of PpIX, and is chelated with a ferrous iron to haem (Figure 6.1) [417].

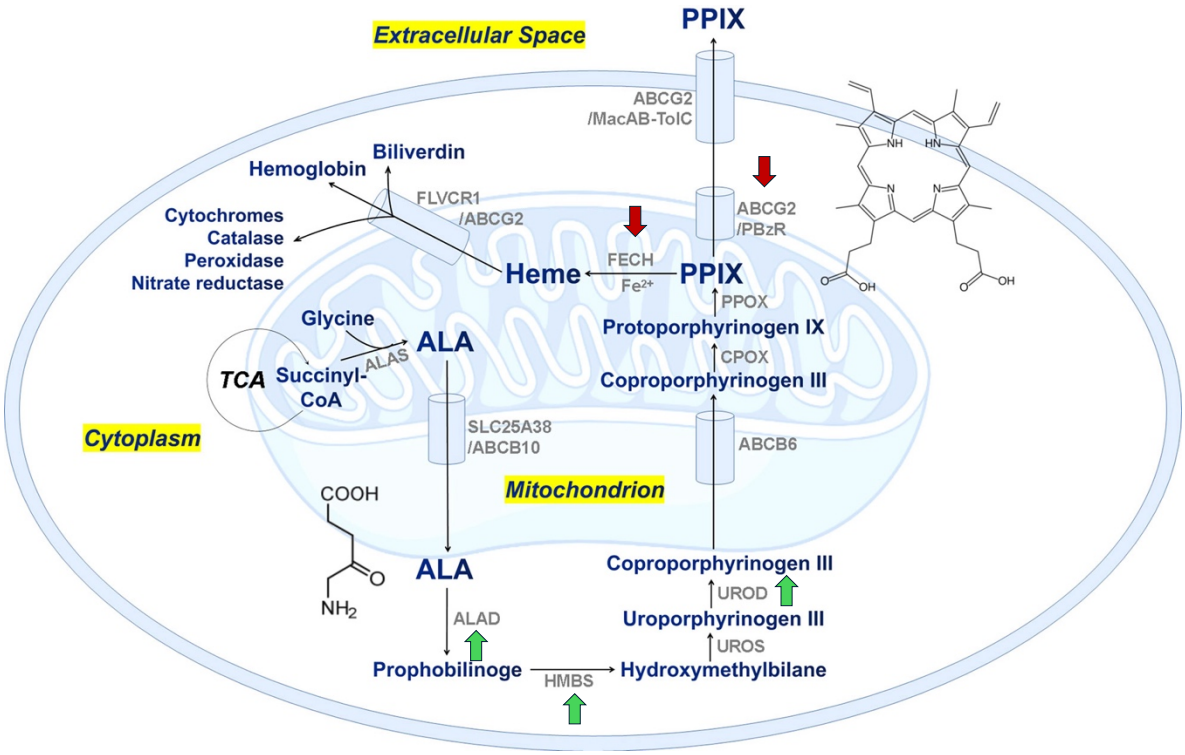


Figure 6.1 Illustration of metabolic pathways of 5-aminolevulinic acid (5-ALA) and mechanism of protoporphyrin IX (PpIX) accumulation in a cancer cell, which relies on multiple enzymatic reactions. Production of PpIX increases with increased activity of the following enzymes as represented by the green arrows: ATP-binding cassette subfamily B member (ALAD), hydroxymethylbilane synthase (HMBS) and uroporphyrinogen decarboxylase (UROD). Decreased activity of ferrochelatase (FECH) and ATP-binding cassette subfamily G member 2 (ABCG2) as represented by the red arrows, causes PpIX to accumulate by limiting conversion to haem. This image was reproduced and modified with permission of the author [418].

Protoporphyrin IX exhibits fluorescence absorption peaks at 405 nm and 635 nm, and consequently two emission peaks at 635 nm [407, 419]. Excitation within the highest peak, known as the Soret band, lies within the violet spectrum at 405 nm, a wavelength at which light is highly absorbed by blood. Of note there is minimal autofluorescence in breast tissue, as it is composed of fat and connective tissues [420]. Porphyrins also have photodynamic properties and can generate triplet oxygen species when excited by light of an appropriate wavelength, namely 405 nm [407].

With exogenous administration of ALA, PpIX accumulates due to the rate limiting step which is the conversion of PpIX to haem. In malignant cells, the accumulation of PpIX is higher [421, 422]. Such a difference enables differentiation between healthy and malignant tissue via fluorescence. It has been evidenced that

multiple enzymes, either via increased PpIX production or the decreased conversion to haem, allow the pathological accumulation of PpIX in breast cancer [421]. Increased production of PpIX leading to its accumulation, has been correlated to the overexpression of ALA dehydratase, porphobilinogen deaminase and uroporphyrinogen decarboxylase [423]. Conversely, PpIX accumulation can occur when there is decreased activity of ferrochelatase, and also the ABCG2 transporter which is specific to ER and HER2 positive cancer cell lines) [424].

ALA is approved for use in glioblastoma surgery in Europe, Canada and Japan [407]. It is also licensed for use in bladder surgery and for photodynamic treatment of skin cancers [422]. It can be administered topically or systemically (i.e oral, intravenous or intradermal). The by-products undergo hepatic or renal clearance. As with any drug, side effects are associated, however the risks with ALA are uncommon. Uncommon side effects (1 in 100 to 1 in 1000 patients) are documented as hypotension, nausea, photosensitivity reaction and photodermatosis [425]. Neurological disorders (such as aphasia, hemiparesis, convulsions, hemianopsia); deranged liver function tests and thrombocytopenia are other associated risks [426].

6.4 Challenges of Fluorescent Guided Surgery

There are some challenges to integrate FGS into the surgical workflow. Firstly, a contrast agent must be administered to patients pre-operatively, often two to three hours before. Patients require counselling on the side effects of any agents given. For the in-vivo use of ICG and ALA, operating room lights need to be switched off to prevent ambient light affecting tumour detection. Regulatory conditions are clearly one of the biggest challenges of FGS [407]. Only a few agents are approved for clinical us, and it is imperative that toxicity to the patient must be avoided. Drug-development pathways can be very time consuming and financially require extensive funding.

6.5 Methodology

An objective of this chapter was to assess the diagnostic accuracy of the multispectral camera, compared to a custom-made modifiable dual-colour and fluorescence camera

system for protoporphyrin IX imaging and ICG imaging. This fluorescence camera has been evaluated in the “GLOW” study at Imperial [427, 428]. Dr Maria Leiloglou and Dr Vadzim Chaulau were involved in construction of the fluorescence camera.

6.5.1 Patient Recruitment

From the 7th of July, 2022 to 28th October, 2022 patients who were undergoing BCS from Charing Cross Hospital, London were recruited to this feasibility study after Integrated Research Ethics Approval (IRAS) (19/LO/0927) approval. During this time 29 consecutive patients were contacted for participation for either MSI imaging; and simultaneously asked if they would be willing to take 5-ALA (an oral solution). Patients for this experimental work were identified pre-operatively via multidisciplinary team meetings, and their health records thoroughly interrogated to understand their past medical history to ensure there was no contraindication for giving 5-ALA. Patients were telephoned seven to ten days prior to surgery and given the context of this study, and an understanding of how 5-ALA works. There were also emailed patient information leaflets and given the opportunity to ask any questions. A further follow up phone call was made to ask if there were willing to participate. Patients were consented for participation on the day of surgery.

I was not involved in patient recruitment for the first section of the “GLOW” study where ICG was being investigated using the fluorescent camera. Dr Martha Kedryzycki recruited patients for her thesis and has granted permission of usage of the results of this work for the purpose of this chapter. Patients who received ICG were recruited at Charing Cross Hospital similarly as above from July 2020 to February 2021.

6.5.1.1 Inclusion Criteria

All participants had to be women over the age of 18. Women with a diagnosis of invasive breast cancer or DCIS and undergoing BCS only were included. Any intraoperative localisation techniques could be utilised.

6.5.1.2 Exclusion Criteria

Any pregnant or lactating patients were excluded. Patients with a history of liver failure or history of porphyria could not be involved in this study. Any patient with a history of photosensitivity was excluded. As written communications were in the English language, patients who were unable to read the patient information leaflets were excluded, as they were not able to give informed consent.

6.5.2 Fluorescence Camera Set Up

In this experiment, once ALA was administered to the patient, PpIX accumulated within the breast tumour being investigated. The fluorescent imaging system then captures the fluorescence induced by PpIX accumulation. A custom-built fluorescence imaging system built at The Hamlyn Centre was utilised, comprised of two cameras; a filtered light source; a display monitor; and controlling software (Figure 6.1). A colour camera was used for visible colour imaging (FLIR Grasshoper3 GS3-US-28S5C-C, FLIR systems, Inc., Wilsonville, OR, USA).

A monochrome camera (FLIR Grasshoper3 GS3-U3-28S5M-C, FLIR Systems, Inc., Wilsonville, OR, USA) for fluorescence imaging was used to capture PpIX fluorescence emission from breast tissue. This monochrome camera had two bandpass emission filters fitted. Firstly, a filter including the Soret band (425 – 625 nm) to capture PpIX fluorescence. Secondly, a filter to exclude the Soret band (<625 nm). The purpose of this latter filter is to enable white light imaging, and to eliminate overlap between excitation, and emission spectra and autofluorescence.

A Xenon light source was used. The light source optical power at the light ring was around 0.8 W (measured via Coherent Field Max power meter with thermopile detector) with a light spot diameter of around 8 cm, and average power density 4 $mWcm^{-2}$. For each image acquired with this FGS system a colour, fluorescent and a dark frame (where light source is turned off) image were captured.

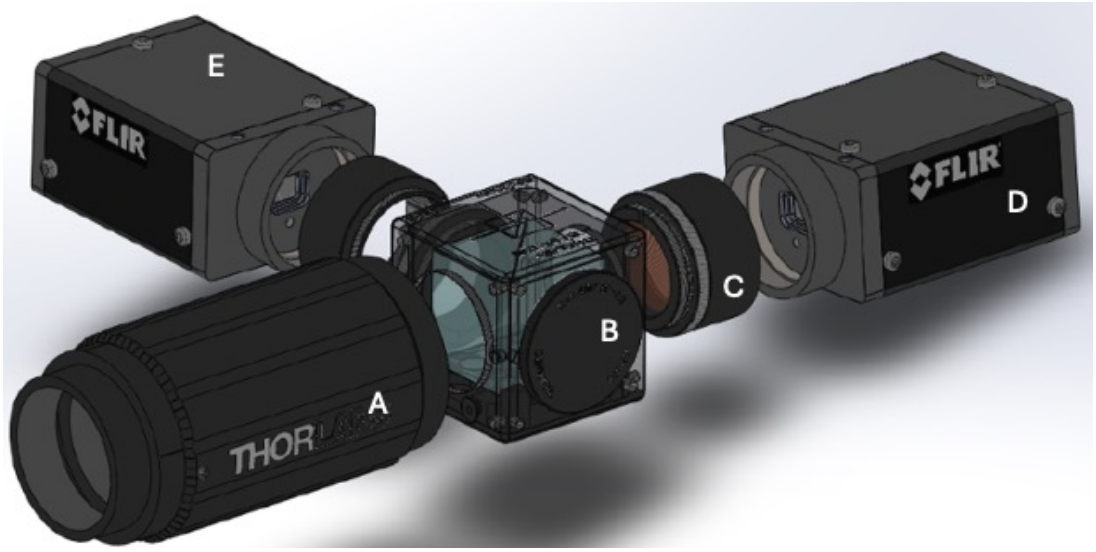


Figure 6.2 GLOW camera (fluorescence imaging camera) set up. (A) Lens system which collects visible and fluorescence (B) A beamsplitter which splits light into two beams. (C) Fluorescence is transmitted through a bandpass filter to (D) monochrome camera and (E) colour images are captured in a RBG camera. Reproduced with permission from Dr M Kedzycki **[429]**.

6.5.3 Multispectral Camera Set Up

The same system used in chapter five was used for data acquisition.

6.5.4 Data Acquisition Protocol

6.5.4.1 ALA administration

Two to four hours before surgery, patients were administered 20 mg/kg 5 - aminolevulinic acid to drink. This dosage was in keeping with current data and guidance.

6.5.4.2 ICG administration

Dr Martha Kedrzycki administered ICG to patients via two different methods to reflect two different cohorts of patients. The first cohort was the angiography cohort, and the second was the EPR cohort. The angiography cohort were given 0.25 mg/kg intravenously (IV) during the operation, only once the skin flaps had been raised by

the surgeon (images acquired 5 minutes after). The EPR cohort were administered 0.25 mg/kg IV preoperatively once they had been anaesthetised (images acquired 25 minutes after).

6.5.4.3 Image Acquisition

Following BCS, the freshly excised specimen was orientated with sutures and clips as previously described (section 5.4.2). Routine specimen radiography using a Faxitron ® (Hologic, Tuscan Arizona, United States of America) machine in theatre was performed. The operating surgeon used the radiographic image to assess if adequate radial margins had been taken, and this would guide them to do any further cavity shaves.

Freshly excised BCS specimens were then imaged on their anterior and posterior resection surfaces only, with both the multispectral camera and then the fluorescence imaging camera. Operating surgeons were blinded to the images collected, to ensure surgical outcomes were reflective of conventional techniques rather than being influenced by experimental data.

Patients received routine post operative care. Outcome data was collected encompassing patient demographic data (age, weight, height, body mass index, ethnicity); tumour characteristics (type, grade, hormonal status, size, location); procedure details (time of ALA administration and imaging, operation performed); and outcomes (margins, positive margin rate, reoperation rates and significant events).

The specimen was sent to histopathology in formalin, for fixation as per chapter five.

6.5.5 Image Processing

Following fixation and H&E staining, and the specimen being breadloafed into slices, an experienced histopathologist (blinded to study participant's details) assessed the slices under a microscope. This produced a final histological report. Specimen radiography and the formal histopathological report were used to mark the fluorescence and multispectral camera images respectively. Specimen radiography identified the location of the tumour on the anterior and posterior ex-vivo images

acquired from each camera system. The histopathological report, which contains margin status of each radial margin, was utilised to identify where healthy tissue is within each image. GIMP software was used for marking. Images excluded from marking were those where resection surfaces were stained with significant blue dye and where there were technical difficulties.

The scale used for marking FGS images differed to MSI. With the FGS camera, the laser provided two points the distance between being a measurement of 3.2 cm. Using GIMP, the distance between the two laser points is measured in pixel values (Figure 6.2). Of note, MSI images were marked by me, and FGS images marked by Dr Martha Kedryzycki.

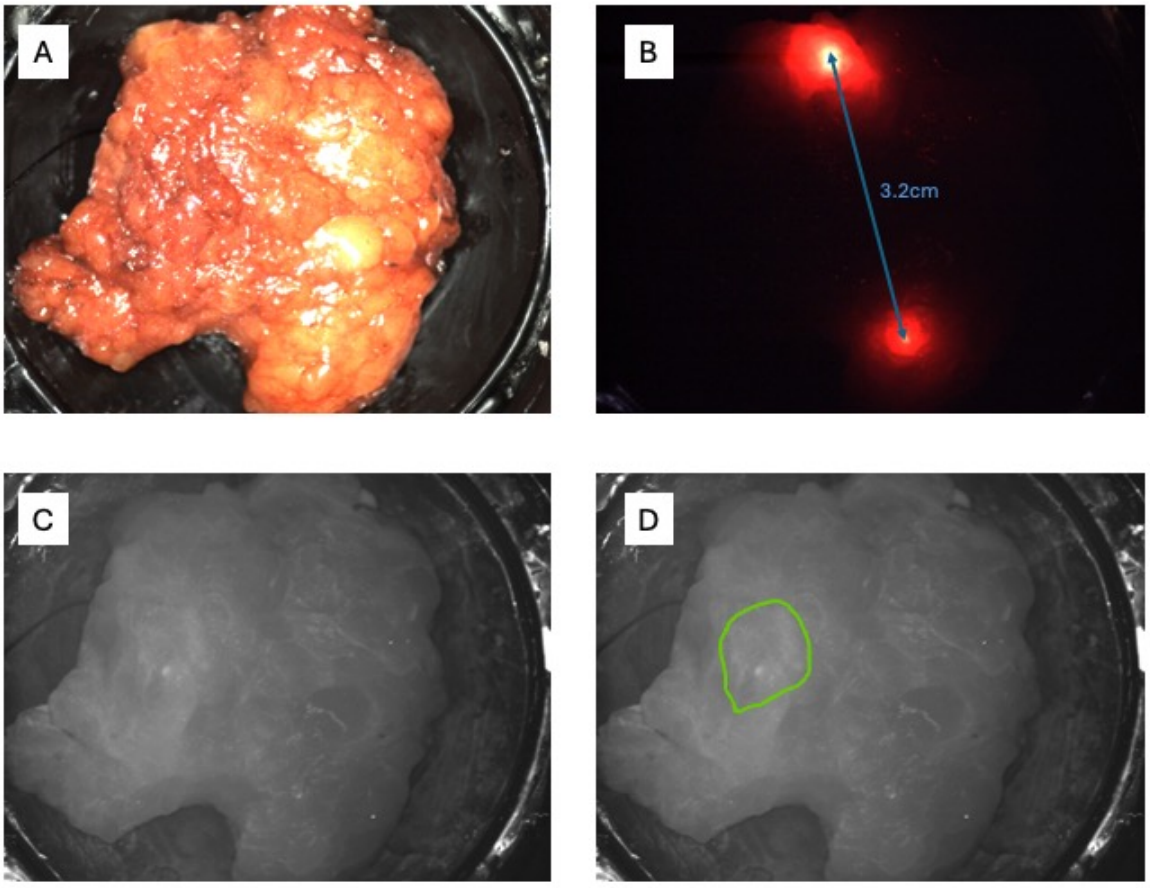


Figure 6.3 Series of images highlighting what the fluorescence guided camera produces for the posterior aspect of the same specimen, and how images are marked. (A) Colour image produced by FGS (B) Laser produces two points, distance between these two points measures a fixed distance of 3.2cm. With GIMP, the distance between these two points is measured in pixels and divided by 3.2cm and is correlated with margins distances given on the histology report (C) The monochrome camera of the FGS system produces an image. (D) The green circle represents the final marked image highlighting disease.

6.5.5.1 Multispectral Image Processing

MSI images were processed as previously discussed in chapter five. Here, pixel features per case were used for training of the logistic training model using method 3 (Norm1/Band Reflectance Division) normalization techniques. Eleven patients were utilised for training the logistic regression model, and two were used for testing.

6.5.5.2 Fluorescent Image Processing

Fluorescence images were processed slightly differently. Pixel values from the tumour and healthy regions for every image were used to calculate the tumour-to-background ratio (TBR) using the formula below:

$$\text{TBR} = \frac{mean\ pixel\ intensity\ in\ the\ tumour\ region}{mean\ pixel\ intensity\ in\ the\ healthy\ region}$$

A logistic regression model (LRM) extracted the pixel-dense tumour probability and results were 5-fold cross validated with receiver operating characteristic (ROC) analysis.

6.5.6 Comparison of MSI versus different fluorophores

The Kruskal-Wallis ANOVA table was used to compare MSI images to images acquired from patients who received:

- 5-ALA (filter 7 used)
- 5-ALA (filter 8 used)
- ICG (angiography cohort)
- ICG (EPR cohort)

This statistical test is a non-parametric test which is suitable to compare multiple groups which are unpaired [295]. In this test chi-squared is calculated and the corresponding p-value is then calculated from the chi-squared distribution. Dr Maria Leiloglou analyzed images from both imaging systems and compared them with the above test.

6.6 Results

Although 29 patients were asked to participate to take 5-ALA, only 11 patients agreed to be involved in this feasibility study. 40 patients were willing to have ICG administered to them (20 for angiography cohort, 20 for EPR cohort) and were recruited by Dr Martha Kedryzcki. There were no adverse events following administration of exogenous agents.

6.6.1 Demographics

Eleven women (median age of 59 years (range 38-79), median body mass index 29.1 kg/m^2 (19.2 – 42.0) were enrolled.

Table 6.2 Demographic data and tumour characteristics of all participants of this study.

Patient Demographics	
Age (years):	
Median	59
Range	38 - 79
BMI:	
Median	29.1
Range	19.2 - 42
Ethnicity:	
Caucasian	11/11
Localisation technique:	
Wire	2/11
Magseed	9/11
Tumour Characteristics	
Size (mm):	
Mean	13.95
Range	7 - 25
Histological subtype:	
IDC	8/11
ILC	3/11

Grade of invasive type specimens:	
1	4/11
2	6/11
3	1/11
Hormone receptor status:	
ER+PR-HER2-	9/11
ER-PR-HER2-	2/11
Neoadjuvant therapy:	
NACT	1/11
Cavity shaves performed:	
All radial margins	3/11
Specific margins	5/11
None	3/11
Re-excision surgery performed:	
Yes	3/11
No	8/11

Of the 40 patients who had ICG, the median age of the angiography cohort was 56.5 years (range 33 - 81); whereas the EPR cohort had a median age of 57.9 (range 34 – 78). The commonest histological subtype for both cohorts was IDC combined with DCIS. 10% of all patients had NACT. The re-excision rate for the whole patient group who received ICG was 30%. Further breakdown of both ICG cohorts are represented in Kedryzkci *et al*. [428].

6.6.2 Comparison of Precision Metrics of MSI versus FGS

When logistic regression was used as a classifier following image processing of FGS and MSI images respectively, MSI validation reached an accuracy of 0.80 (SD±0.2); sensitivity of 0.47 (SD±0.27) and specificity of 0.93 (SD±0.08).

The box and whisker plots depicted (Figure 6.3 to 6.5) are representation of how respective fluorophores 5-ALA and ICG performed against MSI. In terms of

sensitivity MSI underperformed compared to FGS, apart from the ICG EPR cohort. MSI had good comparative specificity with FGS.

MSI had superior accuracy compared with patients who had ICG and ALA (filter 8) and this was statistically significant (p = 0.0014).

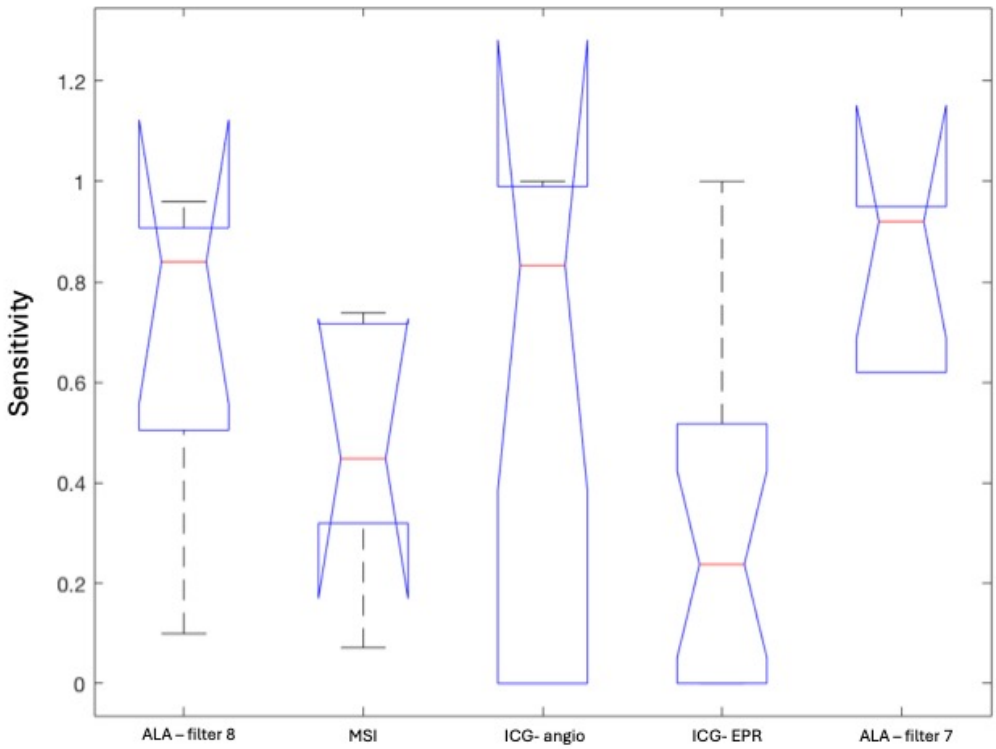


Figure 6.4 Box and whisker plots depicting comparative sensitivity (p = 0.049) results for ALA (filter 8) vs MSI vs ICG (angiography cohort) vs ICG (EPR cohort) vs ALA (filter 7).

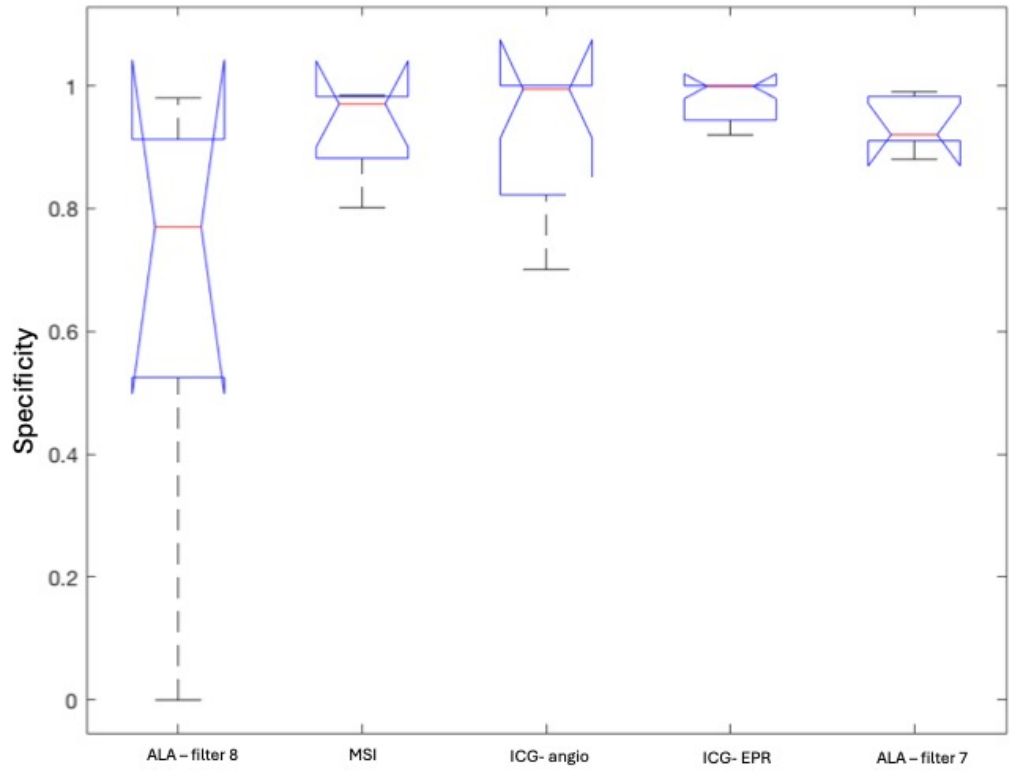


Figure 6.5 Box and whisker plots depicting comparative specificity (p = 0.0278) results for ALA (filter 8) vs MSI vs ICG (angiography cohort) vs ICG (EPR cohort) vs ALA (filter 7).

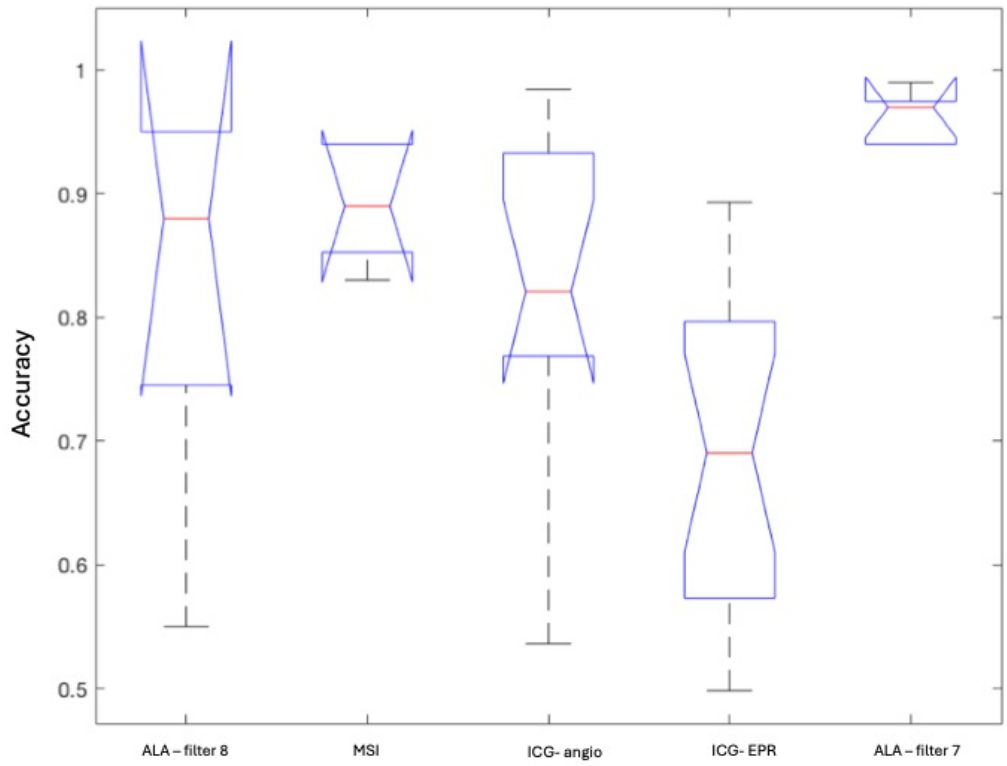


Figure 6.6 Box and whisker plots depicting comparative accuracy (p = 0.0014) results for ALA (filter 8) vs MSI vs ICG (angiography cohort) vs ICG (EPR cohort) vs ALA (filter 7).

6.7 Discussion

This feasibility study is novel, as no other research group has compared the use of MSI and FGS. In this very small pilot study where FGS imaging was compared with MSI, FGS had a better detection of breast cancer intraoperatively than MSI in terms of sensitivity, but MSI had better accuracy and similar specificity. Possible reasons for MSI having improved accuracy is that ICG for example is a passive fluorophore and binds to plasma proteins and distributes throughout the vasculature, and therefore cannot discriminate between healthy and malignant tissue boundaries well as the contrast agent diffuses into surrounding tissues [430]. Furthermore, ICG does not target breast cancer specific molecules or biomarkers and hence does not monopolize on the specific biological traits of tumours [430]. Particularly with ALA, as signals are identified in the visible spectrum of light, background interference from endogenous fluorophores can contribute to poorer accuracy of cancer detection. For both ALA and ICG, the timing of when agents are given can influence accuracy rates as if given early there can be accumulation within healthy tissue too reducing accuracy rates.

There are two main criticisms of this work. Firstly, the study number of patients was small, particularly the patients who had MSI imaging and received ALA. The patients recruited to the ICG cohort were of a larger population but were not imaged with the MSI system. Secondly, there were different clinicians marking images for the MSI and FGS groups.

There are several disadvantages of using an FGS system compared with a MSI system. Firstly, for FGS a contrast agent needs to be given to the patient. This means the patient must attend early prior to their operation as they need to ingest the contrast agent in some cases, and due to restrictions for safety of anaesthesia there needs to be a period of no fluid ingestion. An operating list must therefore account for administration of an agent, and this is a limiting factor for use of an FGS system in terms of surgical workflow. There is a risk of photosensitivity too for example if ALA is given [431]. At an anxious time for a patient, it may be deemed inappropriate to burden them with more potential risks. Also related to timing, agents with fluorescent properties can lose their effectiveness during longer procedures due to photobleaching [432]. Photobleaching describes the process by which each fluorescent dye molecule

in a contrast agent is degraded after excitation-emission cycles [433]. This leads to irreversible loss of optical properties. Similarly, once an agent is cleared by the body there will be no useful fluorescence signal. This was evident as the ICG angiography cohort had better overall results than the ICG EPR cohort, as it takes at least two to three minutes for ICG to begin to be cleared.

Comparatively, MSI does not confer any risk to the patient as it is a non-invasive technique that does not require any exogenous agents. Secondly, a FGS system incurs more cost to the healthcare system as the vials of contrast agent are expensive [432]. Training to administer the agents are also required, in an already resource-limited healthcare system this proves an additional challenge [432].

As with MSI, there is limited depth penetration of light with FGS of a few millimetres [428]. 5-ALA acts within the visible spectrum, and therefore interactions with chromophores can affect results. Although in this feasibility study FGS had better accuracy, it is crucial to note that not all exogenous agents target tissue specifically and this can lead to non-specific fluorescence and therefore yield poor specificity. There is also an issue of autofluorescence, as some biological tissue has natural fluorescent properties, with the presence of NADH, FAD, flavins and lipo-pigments causing fluorescence [434].

There is an argument that combining a FGS with MSI could help improve specificity and accuracy. However, there are some disadvantages of combining two imaging systems that must be considered. Firstly, it could incur a financial cost from maintenance of equipment plus the requirement of training [432]. Secondly, surgical workflow could be delayed due to image acquisition and data processing times. Lastly, it must be noted that both FGS and MSI have limited depth penetration, so combining the two systems does not overcome this [156, 428].

6.8 Conclusion

This chapter highlights that combining MSI with a FGS system has the potential to augment a surgeon's visualisation intraoperatively to help reduce re-excision rates. However significant work would have to be done to combine camera systems and data processing of captured images to allow for integration of such a novel system into an efficient surgical workflow. The biggest challenge would be the willingness of patients

to have contrast agent given to them preoperatively. Combining IMA tools with different modalities is something that has yet to been explored in this field but could be a potential solution to improve intraoperative detection of cancer to help guide tumour resection.

Chapter 7: Conclusions and Future Work

7.1 Conclusions

7.1.1 Clinical problem in breast conserving surgery and methods to tackle this

This thesis advocates the use of optical techniques as a suitable intraoperative margin assessment tool (IMA) to tackle the ongoing clinical problem of positive margins following breast conserving surgery (BCS). Re-excision surgery due to positive margins impacts not only the patient, but also our healthcare system which is already under tremendous strain as reported in the latest Darzi NHS review [50, 61, 65, 74, 435].

Conventional techniques to detect the boundary zone between breast cancer and normal breast or to control oncological margins intraoperatively either have poor sensitivity/specificity or else interrupt surgical workflow and hence have failed to penetrate clinical practice. Therefore, there is an urgent clinical need to develop novel intraoperative margin assessment techniques to provide a solution to this problem and reduce rates of surgical re-excision. Emerging technologies range from imaging, optical, bioimpedance and mass spectroscopy techniques [123, 133, 156]. Some technologies are disadvantaged however by their cost and lack of ease of use. This thesis champions the use of optical techniques as a potential IMA tool as it involves a rapid, non-invasive and non-ionizing technique, that can be easily adoptable into the operating room.

7.1.2 Light-Tissue Interactions

Understanding the interactions that occur when light interacts with breast tissue is imperative to creating an ideal IMA tool. The processes of reflection, refraction, absorption, scattering and intrinsic fluorescence were discussed in chapter two [135].

A systematic review and meta-analysis was conducted to appraise all known literature studying technologies utilising diffusely reflected light [156]. Findings from this review and meta-analysis identified weaknesses in work in this field and helped shaped experimental work found in chapters four to six. Parameters of imaging systems (e.g. modality type, spatial and spectral resolution, field of view and acquisition time) were reviewed, to inform how any potential IMA tool would influence surgical workflow. Breast cancer heterogeneity was discussed in chapter one, and this review identified that previous studies showed a paucity of data for particular histological subtypes (i.e. lobular carcinoma and DCIS) which are known predictors contributing to a positive margin [25], but also patients who had received neoadjuvant chemotherapy (NACT).

Chapter two was instructive in terms of methodology, image processing and performance metrics (i.e. sensitivity, specificity and accuracy) of previously investigated technologies. This review identified the amount of spectral data acquired thus far by technologies related to this thesis. A critical analysis of methodology was made possible by this chapter. Image processing techniques utilised in the literature was used to inform methods used in chapter five. Most importantly, by meta-analysing performance metrics in previous studies, experimental data from this thesis was compared. Probe based studies were found to have a pooled sensitivity of 0.84 (0.78 (lower limit), 0.89 (upper limit)) and pooled specificity of 0.85 (0.79 (lower limit), 0.91(upper limit)). Comparatively, image-based studies had a pooled sensitivity 0.90 (0.76 (lower limit), 1.03 (upper limit)), and pooled specificity 0.92 (0.78 (lower limit), 1.06 (upper limit)). With these results, comparison of optical techniques utilised in this thesis could be compared to previous technologies but crucially add novelty to this field.

7.1.3 Influence of Margin Width on Local Recurrence

Margin width in BCS is relevant to any technology utilising tissue optics for two reasons. Firstly, spatial resolution is paramount in identifying disease intraoperatively. Secondly, it is well known that light can penetrate biological tissue by a few millimetres, therefore any IMA tool which can identify surface pathology to this depth is justified for intraoperative use. A systematic review and meta-analysis were performed. In this

original review, the outcome metrics of OR, RR and HR were concurrently reported to assess the impact of precise margin widths on the impact of local recurrence in both invasive breast cancer and DCIS.

For DCIS within the margin width group 0·1-1 mm vs ≥1 mm, patients had a statistically significant increased risk of ipsilateral recurrence, by 4.8-fold. Following adjustment for boost radiotherapy within 0·1-1 mm vs ≥1 mm and 0·1-2 mm vs ≥2 mm, differences in local recurrence rates were no longer significant. This meta-analysis has identified therefore that boost radiotherapy can mitigate the effects of disease which is not at the inked margin, which is a novel finding and offers an alternative to clinical management.

However, with invasive disease the results were not so well defined. As expected, the general trend of wider negative margin widths leads to a lower risk of local recurrence. The evidence for 0·1- <1 mm vs ≥1 mm and 0·1-2 mm vs 0·1- <2 mm vs ≥2 mm varied amongst different outcome metrics and hence the best negative margin width to aim for is less clear due to a paucity of patient level data amongst these groups.

Despite this, if any IMA tool can detect surface pathology to a depth of 2 mm this justified the use of this technology in theatre as a method to reduce re-excision rates.

7.1.4 Spectroscopy use on Freshly Frozen Breast Tissue Samples

Spectroscopy is a point-based technique, that can potentially be used intraoperatively to distinguish between normal and malignant breast tissue. Chapter four is the first experimental chapter in this thesis, where a custom-built spectroscopy probe was used to interrogate freshly frozen breast tissue samples acquired from two different tissue banks. Data and methodology from this chapter was useful to inform work for chapter five, as the multispectral camera has a spectroscopy component.

Previous spectroscopy studies utilising diffusely reflected light and/or intrinsic fluorescence were analysed in chapter two. The work from this chapter has some novel aspects, namely it was the first study to utilise freshly frozen tissue including procurement of tissue subtypes underrepresented or not used in previous studies (i.e. DCIS, lobular cancer, patients who received NACT) [156]. It also accounted for the

influence of surgical or pathological dyes on tissue on spectral measurements, comparisons amongst inter-tumour heterogeneity, and the use of machine learning for data processing.

Overall, 181 tissue samples were interrogated with our custom-built spectroscopy device (DRS-IFS) with 18,349 spectra accumulated, the largest to date. With gradient boost classifier, accuracy of 76.11% (SD ± 2.97), sensitivity of 85.60 % (SD ± 1.67) and specificity of 56.73% (SD ± 8.92) was achieved. Comparing these results to those of the meta-analysis in chapter two, sensitivity was comparable however specificity was lower than expected. The reason for a lower specificity was critically assessed, with causation attributed to use of frozen tissue samples altering intrinsic tissue structure, methodology from previous studies introducing bias as spectral measurements were taken from pre-selected points, and imbalanced datasets affecting machine classifiers.

Despite the use of freshly frozen samples, this chapter provides insight into how a spectral data library can be created in the *ex-vivo* setting and potentially be used to train machine classifiers in the *in-vivo* setting.

7.1.5 Multispectral Camera Use in the ex-vivo and in-vivo Setting

This thesis represents the first multispectral imaging camera used to investigate whether such a system can differentiate between normal and malignant breast tissue in both the *ex-vivo* and *in-vivo* setting. Previous literature documenting imaging systems have always been hyperspectral [156]. Multispectral cameras have the advantage of quicker image processing time due to fewer pre-selected wavelengths. Multispectral systems also have better spatial resolution and are more cost effective.

Chapter two highlighted the characteristics of an ideal IMA tool. These characteristics were considered in construction and adaptation of a custom-built system. Furthermore, capturing images in an efficient manner in order not to hinder surgical workflow was noted, and therefore the software interface was adjusted accordingly.

Chapter five evaluated the use of the custom-built multispectral camera in two sections. Firstly, freshly frozen breast tissue samples were imaged in a laboratory based *ex-vivo* validation study. Secondly, the MSI camera was used in the

intraoperative environment on freshly excised BCS specimens, an *in-vivo* component aimed to emulate the potential use of MSI as an IMA tool. In the *ex-vivo* study, following pre-processing and classification 68 freshly frozen samples interrogated with MSI yielded a sensitivity of 84%, specificity 58% and AUC 75% with extreme gradient boost classifier with “normalization 1” technique. Poor specificity may be attributed to the freezing process affecting tissue components, in particular haemoglobin. With the *in-vivo* study, where specimens from 23 patients were image processed, 6,301,712 spectra were acquired. Here, MSI had the ability to distinguish between normal and malignant tissue using logistic regression with AUC at 89% (SD ± 7), sensitivity 86% (SD ± 12), and specificity 80% (SD ± 8). As expected, *in-vivo* results had better precision metric results.

Importantly, this MSI system has sensitivity/specificity which is comparable to the pooled sensitivity and specificity identified in chapter two. Further work is required to establish if a spectral library database created from frozen tissue samples can be translated into the *in-vivo* setting. This would enable more spectral data to be acquired for classification. This would enable spectral signatures for tumour biology specific factors (such as tumour grade, receptor status, or histological subtype) to be established, which in the clinical setting would be invaluable. For the *in-vivo* studies, this work was underpowered, and for translation into surgical workflow a large clinical study would need to be carried out.

7.1.6 Multispectral Imaging *Versus* Fluorescence Guided Surgery

Thus far in this thesis, multispectral imaging has relied on the inherent properties of biological tissue interacting with light to create an optical fingerprint. Fluorescence guided surgery takes advantage of endogenous or exogenous fluorescent molecules within a targeted lesion for information [404]. In chapter six MSI imaging performance was compared to the performance of FGS imaging whereby patients were given exogenous agents (either ICG or 5-ALA).

When logistic regression was used as a classifier following image processing of FGS and MSI images respectively, MSI validation reached an accuracy of 0.80 (SD ± 0.2); sensitivity of 0.47 (SD ± 0.27) and specificity of 0.93 (SD ± 0.08). In terms of specificity MSI underperformed compared to FGS, apart from the ICG EPR cohort.

However, MSI had superior accuracy compared with patients who had ICG and ALA (filter 8) and this was statistically significant ($p = 0.0014$).

Although the sample size was small, the study population was representative, and the work identified the potential of enhancing any future IMA tool by using a MSI system with a FGS system, to augment the different features of tissue optics (i.e. MSI capitalizes on chromophores, whereas FGS augments inherent fluorescence). It is imperative to note MSI and FGS were not combined into one system for these experiments, but future work could investigate this.

7.1.7 Concluding Remarks

Compared to current commercial devices, MSI offers several advantageous features that allow it to be a technique that is integrated into surgical workflow. It is cost-effective; non-invasive and non-ionizing; rapid; minimal learning curve; no requirement for endogenous agents; and preserves specimen margin orientation for final pathology. To allow for uptake by the breast surgical community further optimisation is required to improve overall performance metrics for intraoperative detection.

7.2 Future Work

The findings from this thesis have identified strengths and weaknesses in the field of tissue optics as a IMA tool for BCS. This work has identified additional avenues of research to further this field.

7.2.1 Growth of *ex-vivo* and *in-vivo* Database

A major limitation of this thesis was the number and quality of tissue samples for the *ex-vivo* experimental work. Although, breast tissue samples were acquired from two different tissue banks, there was a time and cost restriction to acquiring further samples. Ideally, for a thorough investigation of any IMA tool we must develop a spectral database which explores the heterogeneity of breast tissue and cancer,

including all aspects of tumour biology which influence our breast cancer management. To allow for translation from the *ex-vivo* to *in-vivo* environment the breast tissue samples should be fresh, rather than frozen. Fresh samples from either breast conserving specimens or mastectomy specimens, with a paired normal sample would be the best method for laboratory work. However, due to restrictions at the Imperial Breast Unit this was not possible. Another aspect of breast disease that needs to be accounted for are benign and B3 (indeterminate lesions). It is therefore crucial any IMA tool should be able to detect low levels of atypia associated with B3 lesions and differentiate from DCIS, as otherwise the surgeon will remove excess breast tissue as B3 lesion excision does not require a clear margin.

In the *in-vivo* setting, not all patients had their specimens imaged, therefore results were limited. Again, to enhance accuracy rates and allow training of classifiers, informed by a priori sample size calculation. To gain an appreciation of how heterogeneity of breast disease affects performance metrics, data from MSI systems should be assessed in different breast units. More data is required to allow for multivariate analysis on several tumour biology and patient factors (i.e. DCIS; tumour grade; receptor status; breast density; NACT use) to determine the overall ability of MSI to detect cancer intraoperatively.

7.2.2 Improvements to Data Analysis Methods

For the scope of this thesis, certain machine learning classification systems and software have been used for data analysis. Future work will need to assess if better algorithms can be used. It has also been noted that imbalanced datasets have contributed to poorer results in some aspects of this thesis. With improvements in acquiring data from an *ex-vivo* or *in-vivo* database, it will be possible to perform more complex data analysis to account for other factors that can affect spectral signatures from breast cancer patients.

7.2.3 Overcoming Challenges with Image Marking and Processing

One methodological weakness identified was marking freshly excised BCS specimens. It could be argued that images marked from radial margins were not accurate. The other limitation was that DCIS is a common cause of positive margins; however, it was not always possible to represent this during marking images. This was for two reasons. Firstly, pathology reports will state DCIS was found at a margin but does not report the exact distance along a margin where this non-invasive disease is located. Secondly, DCIS is often seen as calcifications on radiography and has a microscopic nature on a sub-millimetre scale. These make marking DCIS almost impossible.

The specimens were imaged over each resection surface, in a two-dimensional view. However, the surface of a specimen has contours and is uneven, and marking of MSI images does not account for this. For ground truth extraction, specimens are sliced. To improve methodology in the future it could be attempted to stack all slices and use this to create a three-dimensional model to gain more accuracy where disease is [436].

7.2.4 Multimodal Approach for an IMA Tool

It could be argued that combining MSI with another IMA tool of a different modality would be beneficial. In chapter six FGS was explored, which could enhance accuracy of intraoperative cancer detection, but has similar issues of detection of microscopic disease such as DCIS due to limited submillimetre resolution. Therefore, future work must investigate the benefits of combining MSI with alternative modalities such as iKnife. This would allow MSI to detect surface pathology by creating an image identifying macroscopic features, but a combined method using information from excisional techniques to detect smaller pockets of disease. Of course, for integration into surgical workflow significant work would be required for miniaturization of such systems.

7.2.5 Adaptation of Hardware

This thesis has focused on the use of MSI to image the resection surface of a freshly excised BCS specimen. It was noted that some specimens were large, and the field of view may not fully capture a specimen surface. Hardware could be adapted to cater for this with a larger field of view. Also interestingly, there may be scope to image the surgical cavity instead. For this, there will be of course hindrances such as tight breast cavities and blood from the surgical site affecting results.

Although multispectral imaging is in its infancy, there is a scope for its use in the operating room to help reduce re-excision rates in breast conserving surgery. The camera system can be used in the operating room with minimal interruption to surgical workflow. There is a minimal learning curve to use this multispectral system, and once the specimen is excised by a surgeon, a member of the surgical team could image each resection surface in real-time. Following optimisation of data and image processing, the MSI system should be able to provide a visual aid in the form of a heatmap to guide the operating surgeon to identify presence of cancer at each resection surface. With this knowledge, the surgeon can take further breast tissue at the time of primary surgery.

Chapter 8: References

1. Observatory GC. Breast Cancer Statistics 2022 [Available from: https://www.wcrf.org/cancer-trends/breast-cancer-statistics/.
2. Organization WH. Breast Cancer Fact Sheet 2023 [Available from: https://www.who.int/news-room/fact-sheets/detail/breast-cancer.
3. UK CR. Breast Cancer Statistics 2023 [Available from: https://www.cancerresearchuk.org/health-professional/cancer-statistics/statistics-by-cancer-type/breast-cancer.
4. Cancer AB. Breast Cancer Statistics 2020 [Available from: https://www.againstbreastcancer.org.uk/about-us/about-breast-cancer/breast-cancer-facts-statistics.
5. England ND. Cancer Registration Statistics, England 2020. 2020.
6. Sakorafas GH, Safioleas M. Breast cancer surgery: an historical narrative. Part I. From prehistoric times to Renaissance. Eur J Cancer Care (Engl). 2009;18(6):530-44.
7. Moore W. Extreme measures: the history of breast cancer surgery. BMJ. 2012;344:e834.
8. WSI H. The Results of Radical Operations for the Cure of Carcinoma of the Breast. Ann Surg. 1907;46:1-19.
9. Cotlar AM, Dubose JJ, Rose DM. History of surgery for breast cancer: radical to the sublime. Curr Surg. 2003;60(3):329-37.
10. Patey DH, Dyson WH. The prognosis of carcinoma of the breast in relation to the type of operation performed. Br J Cancer. 1948;2(1):7-13.
11. Fisher B, Anderson S, Bryant J, Margolese RG, Deutsch M, Fisher ER, et al. Twenty-year follow-up of a randomized trial comparing total mastectomy, lumpectomy, and lumpectomy plus irradiation for the treatment of invasive breast cancer. N Engl J Med. 2002;347(16):1233-41.
12. Arriagada R, Le MG, Rochard F, Contesso G. Conservative treatment versus mastectomy in early breast cancer: patterns of failure with 15 years of follow-up data. Institut Gustave-Roussy Breast Cancer Group. J Clin Oncol. 1996;14(5):1558-64.
13. Blichert-Toft M, Nielsen M, During M, Moller S, Rank F, Overgaard M, et al. Long-term results of breast conserving surgery vs. mastectomy for early stage invasive breast cancer: 20-year follow-up of the Danish randomized DBCG-82TM protocol. Acta Oncol. 2008;47(4):672-81.
14. Poggi MM, Danforth DN, Sciuto LC, Smith SL, Steinberg SM, Liewehr DJ, et al. Eighteen-year results in the treatment of early breast carcinoma with mastectomy versus breast conservation therapy: the National Cancer Institute Randomized Trial. Cancer. 2003;98(4):697-702.
15. van Dongen JA, Voogd AC, Fentiman IS, Legrand C, Sylvester RJ, Tong D, et al. Long-term results of a randomized trial comparing breast-conserving therapy with mastectomy: European Organization for Research and Treatment of Cancer 10801 trial. J Natl Cancer Inst. 2000;92(14):1143-50.
16. Veronesi U, Cascinelli N, Mariani L, Greco M, Saccozzi R, Luini A, et al. Twenty-year follow-up of a randomized study comparing breast-conserving surgery with radical mastectomy for early breast cancer. N Engl J Med. 2002;347(16):1227-32.
17. de Boniface J, Szulkin R, Johansson ALV. Survival After Breast Conservation vs Mastectomy Adjusted for Comorbidity and Socioeconomic Status: A Swedish National 6-Year Follow-up of 48 986 Women. JAMA Surg. 2021;156(7):628-37.

18. Waks AG, Winer EP. Breast Cancer Treatment: A Review. JAMA. 2019;321(3):288-300.
19. Runowicz CD, Leach CR, Henry NL, Henry KS, Mackey HT, Cowens-Alvarado RL, et al. American Cancer Society/American Society of Clinical Oncology Breast Cancer Survivorship Care Guideline. J Clin Oncol. 2016;34(6):611-35.
20. Mauri D, Pavlidis N, Ioannidis JP. Neoadjuvant versus adjuvant systemic treatment in breast cancer: a meta-analysis. J Natl Cancer Inst. 2005;97(3):188-94.
21. Shien T, Iwata H. Adjuvant and neoadjuvant therapy for breast cancer. Jpn J Clin Oncol. 2020;50(3):225-9.
22. Eroles P, Bosch A, Perez-Fidalgo JA, Lluch A. Molecular biology in breast cancer: intrinsic subtypes and signaling pathways. Cancer Treat Rev. 2012;38(6):698-707.
23. Oakman C, Santarpia L, Di Leo A. Breast cancer assessment tools and optimizing adjuvant therapy. Nat Rev Clin Oncol. 2010;7(12):725-32.
24. Excellence NIfHaC. Early and locally advanced breast cancer: diagnosis and management. NICE guidelines NG1012023. p. 9.
25. van Deurzen CH. Predictors of Surgical Margin Following Breast-Conserving Surgery: A Large Population-Based Cohort Study. Ann Surg Oncol. 2016;23(Suppl 5):627-33.
26. Harvey JA, Bovbjerg VE. Quantitative assessment of mammographic breast density: relationship with breast cancer risk. Radiology. 2004;230(1):29-41.
27. Bani MR, Lux MP, Heusinger K, Wenkel E, Magener A, Schulz-Wendtland R, et al. Factors correlating with reexcision after breast-conserving therapy. Eur J Surg Oncol. 2009;35(1):32-7.
28. Barentsz MW, Postma EL, van Dalen T, van den Bosch MA, Miao H, Gobardhan PD, et al. Prediction of positive resection margins in patients with non-palpable breast cancer. Eur J Surg Oncol. 2015;41(1):106-12.
29. Kedrzycki MS, Elson DS, Leff DR. Guidance in breast-conserving surgery: tumour localization versus identification. Br J Surg. 2023;110(8):920-2.
30. Shirazi S, Hajiesmaeili H, Khosla M, Taj S, Sircar T, Vidya R. Comparison of Wire and Non-Wire Localisation Techniques in Breast Cancer Surgery: A Review of the Literature with Pooled Analysis. Medicina (Kaunas). 2023;59(7).
31. Dua SM, Gray RJ, Keshtgar M. Strategies for localisation of impalpable breast lesions. Breast. 2011;20(3):246-53.
32. Gennari R, Galimberti V, De Cicco C, Zurrida S, Zerwes F, Pigatto F, et al. Use of technetium-99m-labeled colloid albumin for preoperative and intraoperative localization of nonpalpable breast lesions. J Am Coll Surg. 2000;190(6):692-8; discussion 8-9.
33. Ahmed M, Douek M. Radioactive seed localisation (RSL) in the treatment of non-palpable breast cancers: systematic review and meta-analysis. Breast. 2013;22(4):383-8.
34. Moreira IC, Ventura SR, Ramos I, Fougo JL, Rodrigues PP. Preoperative localisation techniques in breast conservative surgery: A systematic review and meta-analysis. Surg Oncol. 2020;35:351-73.
35. Singh P, Scoggins ME, Sahin AA, Hwang RF, Kuerer HM, Caudle AS, et al. Effectiveness and Safety of Magseed-localization for Excision of Breast Lesions: A Prospective, Phase IV Trial. Ann Surg Open. 2020;1(2):e008.
36. Vijayaraghavan GR, Ge C, Lee A, Roubil JG, Kandil DH, Dinh KH, et al. Savi-Scout Radar Localization: Transitioning From the Traditional Wire Localization to

Wireless Technology for Surgical Guidance at Lumpectomies. Semin Ultrasound CT MR. 2023;44(1):12-7.
37. Burstein H, Polyak K, Wong J, Lester S, Kaelin C. Ductal Carcinoma in Situ of the Breast. The New England Journal of Medicine. 2004;350.
38. Christgen M, Steinemann D, Kuhnle E, Langer F, Gluz O, Harbeck N, et al. Lobular breast cancer: Clinical, molecular and morphological characteristics. Pathol Res Pract. 2016;212(7):583-97.
39. Elston CW, Ellis IO. Pathological prognostic factors in breast cancer. I. The value of histological grade in breast cancer: experience from a large study with long-term follow-up. Histopathology. 1991;19(5):403-10.
40. Lee SJ, Go J, Ahn BS, Ahn JH, Kim JY, Park HS, et al. Lymphovascular invasion is an independent prognostic factor in breast cancer irrespective of axillary node metastasis and molecular subtypes. Front Oncol. 2023;13:1269971.
41. Obedian E, Haffty BG. Negative margin status improves local control in conservatively managed breast cancer patients. Cancer J Sci Am. 2000;6(1):28-33.
42. Singletary SE. Surgical margins in patients with early-stage breast cancer treated with breast conservation therapy. Am J Surg. 2002;184(5):383-93.
43. Houssami N, Macaskill P, Marinovich ML, Morrow M. The association of surgical margins and local recurrence in women with early-stage invasive breast cancer treated with breast-conserving therapy: a meta-analysis. Ann Surg Oncol. 2014;21(3):717-30.
44. Tang SS, Kaptanis S, Haddow JB, Mondani G, Elsberger B, Tasoulis MK, et al. Current margin practice and effect on re-excision rates following the publication of the SSO-ASTRO consensus and ABS consensus guidelines: a national prospective study of 2858 women undergoing breast-conserving therapy in the UK and Ireland. Eur J Cancer. 2017;84:315-24.
45. Francesca Tamburelli FM, Caterina Marchiò, Davide Balmativola, Alessandra Magistris,Franziska Kubatzki, Paola Sgandurra, Maria Rosaria Di Virgilio Daniele Regge, Filippo Montemurro, Marco Gatti, Anna Sapino, Riccardo Ponzone a. Reoperation rate after breast conserving surgery as quality indicator in breast cancer treatment: A reappraisal. The Breast. 2020;53:181-8.
46. M Piper JW, K Fahrner-Scott, C Ewing, M Alvarado, L Esserman, R Mukhtar. Success rates of re-excision after positive margins for invasive lobular carcinoma of the breast. npk Breast Cancer. 2019.
47. Fiona MacNeill TI. Breast Surgery
GIRFT Programme National Specialty Report. Getting It Right First Time; 2021.
48. Jeevan R, Cromwell DA, Trivella M, Lawrence G, Kearins O, Pereira J, et al. Reoperation rates after breast conserving surgery for breast cancer among women in England: retrospective study of hospital episode statistics. BMJ. 2012;345:e4505.
49. Jeffe DB, Perez M, Cole EF, Liu Y, Schootman M. The Effects of Surgery Type and Chemotherapy on Early-Stage Breast Cancer Patients' Quality of Life Over 2-Year Follow-up. Ann Surg Oncol. 2016;23(3):735-43.
50. Gagliato Dde M, Gonzalez-Angulo AM, Lei X, Theriault RL, Giordano SH, Valero V, et al. Clinical impact of delaying initiation of adjuvant chemotherapy in patients with breast cancer. J Clin Oncol. 2014;32(8):735-44.
51. Hershman DL, Wang X, McBride R, Jacobson JS, Grann VR, Neugut AI. Delay in initiating adjuvant radiotherapy following breast conservation surgery and its impact on survival. Int J Radiat Oncol Biol Phys. 2006;65(5):1353-60.
52. Fuzesi S, Becetti K, Klassen AF, Gemignani ML, Pusic AL. Expectations of breast-conserving therapy: a qualitative study. J Patient Rep Outcomes. 2019;3(1):73.

53. Al-Ghazal SK, Blamey RW, Stewart J, Morgan AA. The cosmetic outcome in early breast cancer treated with breast conservation. Eur J Surg Oncol. 1999;25(6):566-70.
54. Matar-Ujvary R, Haglich K, Flanagan MR, Fuzesi S, Sevilimedu V, Nelson JA, et al. The Impact of Breast-Conserving Surgery Re-excision on Patient-Reported Outcomes Using the BREAST-Q. Ann Surg Oncol. 2023;30(9):5341-9.
55. Cochrane RA, Valasiadou P, Wilson AR, Al-Ghazal SK, Macmillan RD. Cosmesis and satisfaction after breast-conserving surgery correlates with the percentage of breast volume excised. Br J Surg. 2003;90(12):1505-9.
56. Lim CC, Devi MK, Ang E. Anxiety in women with breast cancer undergoing treatment: a systematic review. Int J Evid Based Healthc. 2011;9(3):215-35.
57. Rustoen T, Moum T, Wiklund I, Hanestad BR. Quality of life in newly diagnosed cancer patients. J Adv Nurs. 1999;29(2):490-8.
58. Omne-Ponten M, Holmberg L, Sjoden PO. Psychosocial adjustment among women with breast cancer stages I and II: six-year follow-up of consecutive patients. J Clin Oncol. 1994;12(9):1778-82.
59. Shimozuma K, Ganz PA, Petersen L, Hirji K. Quality of life in the first year after breast cancer surgery: rehabilitation needs and patterns of recovery. Breast Cancer Res Treat. 1999;56(1):45-57.
60. Palmer SC, Kagee A, Coyne JC, DeMichele A. Experience of trauma, distress, and posttraumatic stress disorder among breast cancer patients. Psychosom Med. 2004;66(2):258-64.
61. Gordon L, Scuffham P, Hayes S, Newman B. Exploring the economic impact of breast cancers during the 18 months following diagnosis. Psychooncology. 2007;16(12):1130-9.
62. Blinder VS, Gany FM. Impact of Cancer on Employment. J Clin Oncol. 2020;38(4):302-9.
63. Dumas A, Vaz Luis I, Bovagnet T, El Mouhebb M, Di Meglio A, Pinto S, et al. Impact of Breast Cancer Treatment on Employment: Results of a Multicenter Prospective Cohort Study (CANTO). J Clin Oncol. 2020;38(7):734-43.
64. Metcalfe LN, Zysk AM, Yemul KS, Jacobs LK, Oker EE, Underwood HR, et al. Beyond the Margins-Economic Costs and Complications Associated With Repeated Breast-Conserving Surgeries. JAMA Surg. 2017;152(11):1084-6.
65. Grant Y, Al-Khudairi R, St John E, Barschkett M, Cunningham D, Al-Mufti R, et al. Patient-level costs in margin re-excision for breast-conserving surgery. Br J Surg. 2019;106(4):384-94.
66. Census TRCoP-HW.
67. Olsen A NK, Margenthaler J, Wallace A, Mines D, Miller J, Fraser V, Warren D. Increased Risk of Surgical Site Infection Among Breast-Conserving Surgery Re-Excisions. Ann Surg Oncol. 2015;22:2003-9.
68. Olsen MA, Chu-Ongsakul S, Brandt KE, Dietz JR, Mayfield J, Fraser VJ. Hospital-associated costs due to surgical site infection after breast surgery. Arch Surg. 2008;143(1):53-60; discussion 1.
69. Czajika MPC. StatPearls. 2023.
70. Glanz K LC. Psychosocial Impact of Breast Cancer: A Critical Review. Annals of Behavioral Medicine. 1992;14(3).
71. Chen W, Lv X, Xu X, Gao X, Wang B. Meta-analysis for psychological impact of breast reconstruction in patients with breast cancer. Breast Cancer. 2018;25(4):464-9.

72. Schmauss D, Machens HG, Harder Y. Breast Reconstruction after Mastectomy. Front Surg. 2015;2:71.
73. Matar DY, Wu M, Haug V, Orgill DP, Panayi AC. Surgical complications in immediate and delayed breast reconstruction: A systematic review and meta-analysis. J Plast Reconstr Aesthet Surg. 2022;75(11):4085-95.
74. Vanni G, Materazzo M, Pellicciaro M, Marino D, Buonomo OC. From Patient Reported Outcome Measure (PROM) to Environment Related Outcome Measure (EROM): Towards "Green Breast Surgery". In Vivo. 2023;37(4):1867-72.
75. Lodhia S, Pegna V, Abrams R, Jackson D, Rockall TA, Rizan C. Improving Environmental Sustainability of Operating Theatres: A Systematic Review of Staff Attitudes, Barriers, and Enablers. Ann Surg. 2024.
76. MacNeill AJ, Rizan C, Sherman JD. Improving sustainability and mitigating the environmental impacts of anaesthesia and surgery: a narrative review. Br J Anaesth. 2024.
77. Chagpar AB. Techniques to reduce positive margins in breast-conserving surgery. In: Burstein HJ, editor. UpToDate.
78. Clough KB, Kaufman GJ, Nos C, Buccimazza I, Sarfati IM. Improving breast cancer surgery: a classification and quadrant per quadrant atlas for oncoplastic surgery. Ann Surg Oncol. 2010;17(5):1375-91.
79. Andre C, Holsti C, Svenner A, Sackey H, Oikonomou I, Appelgren M, et al. Recurrence and survival after standard versus oncoplastic breast-conserving surgery for breast cancer. BJS Open. 2021;5(1).
80. Gulcelik MA, Dogan L, Yuksel M, Camlibel M, Ozaslan C, Reis E. Comparison of outcomes of standard and oncoplastic breast-conserving surgery. J Breast Cancer. 2013;16(2):193-7.
81. Chakravorty A SA, Sanmugalingam N, Rapisarda F, Roche N, Querci Della Rovere G, Macneill FA. How safe is oncoplastic breast conservation? Comparative analysis with standard breast conserving surgery. Eur J Surg Oncol. 2012;25:395-8.
82. De La Cruz L, Blankenship SA, Chatterjee A, Geha R, Nocera N, Czerniecki BJ, et al. Outcomes After Oncoplastic Breast-Conserving Surgery in Breast Cancer Patients: A Systematic Literature Review. Ann Surg Oncol. 2016;23(10):3247-58.
83. Chen JY, Huang YJ, Zhang LL, Yang CQ, Wang K. Comparison of Oncoplastic Breast-Conserving Surgery and Breast-Conserving Surgery Alone: A Meta-Analysis. J Breast Cancer. 2018;21(3):321-9.
84. Kosasih S, Tayeh S, Mokbel K, Kasem A. Is oncoplastic breast conserving surgery oncologically safe? A meta-analysis of 18,103 patients. Am J Surg. 2020;220(2):385-92.
85. Nanda A, Hu J, Hodgkinson S, Ali S, Rainsbury R, Roy PG. Oncoplastic breast-conserving surgery for women with primary breast cancer. Cochrane Database Syst Rev. 2021;10(10):CD013658.
86. Urban C, Lima R, Schunemann E, Spautz C, Rabinovich I, Anselmi K. Oncoplastic principles in breast conserving surgery. Breast. 2011;20 Suppl 3:S92-5.
87. Tenofsky PL, Dowell P, Topalovski T, Helmer SD. Surgical, oncologic, and cosmetic differences between oncoplastic and nononcoplastic breast conserving surgery in breast cancer patients. Am J Surg. 2014;207(3):398-402; discussion
88. Chagpar AB, Killelea BK, Tsangaris TN, Butler M, Stavris K, Li F, et al. A Randomized, Controlled Trial of Cavity Shave Margins in Breast Cancer. N Engl J Med. 2015;373(6):503-10.

89. Kobbermann A, Unzeitig A, Xie XJ, Yan J, Euhus D, Peng Y, et al. Impact of routine cavity shave margins on breast cancer re-excision rates. Ann Surg Oncol. 2011;18(5):1349-55.
90. Janes SE, Stankhe M, Singh S, Isgar B. Systematic cavity shaves reduces close margins and re-excision rates in breast conserving surgery. Breast. 2006;15(3):326-30.
91. Unzeitig A, Kobbermann A, Xie XJ, Yan J, Euhus D, Peng Y, et al. Influence of surgical technique on mastectomy and reexcision rates in breast-conserving therapy for cancer. Int J Surg Oncol. 2012;2012:725121.
92. Jones V, Linebarger J, Perez S, Gabram S, Okoli J, Bumpers H, et al. Excising Additional Margins at Initial Breast-Conserving Surgery (BCS) Reduces the Need for Re-excision in a Predominantly African American Population: A Report of a Randomized Prospective Study in a Public Hospital. Ann Surg Oncol. 2016;23(2):456-64.
93. Dupont E, Tsangaris T, Garcia-Cantu C, Howard-McNatt M, Chiba A, Berger AC, et al. Resection of Cavity Shave Margins in Stage 0-III Breast Cancer Patients Undergoing Breast Conserving Surgery: A Prospective Multicenter Randomized Controlled Trial. Ann Surg. 2021;273(5):876-81.
94. Chen K, Zhu L, Chen L, Li Q, Li S, Qiu N, et al. Circumferential Shaving of the Cavity in Breast-Conserving Surgery: A Randomized Controlled Trial. Ann Surg Oncol. 2019;26(13):4256-63.
95. Mohamedahmed AYY, Zaman S, Srinivasan A, Peterknecht E, Saeed SMS, AlBendary M, et al. Do we need to routinely perform cavity shaving with breast-conserving surgery for breast cancer? A systematic review and meta-analysis. Surg Oncol. 2021;36:7-14.
96. Huston TL, Pigalarga R, Osborne MP, Tousimis E. The influence of additional surgical margins on the total specimen volume excised and the reoperative rate after breast-conserving surgery. Am J Surg. 2006;192(4):509-12.
97. Kim SH, Cornacchi SD, Heller B, Farrokhyar F, Babra M, Lovrics PJ. An evaluation of intraoperative digital specimen mammography versus conventional specimen radiography for the excision of nonpalpable breast lesions. Am J Surg. 2013;205(6):703-10.
98. St John ER, Al-Khudairi R, Ashrafian H, Athanasiou T, Takats Z, Hadjiminas DJ, et al. Diagnostic Accuracy of Intraoperative Techniques for Margin Assessment in Breast Cancer Surgery: A Meta-analysis. Ann Surg. 2017;265(2):300-10.
99. Park KU, Kuerer HM, Rauch GM, Leung JWT, Sahin AA, Wei W, et al. Digital Breast Tomosynthesis for Intraoperative Margin Assessment during Breast-Conserving Surgery. Ann Surg Oncol. 2019;26(6):1720-8.
100. Svahn TM, Chakraborty DP, Ikeda D, Zackrisson S, Do Y, Mattsson S, et al. Breast tomosynthesis and digital mammography: a comparison of diagnostic accuracy. Br J Radiol. 2012;85(1019):e1074-82.
101. Kaufman CS, Jacobson L, Bachman BA, Kaufman LB, Mahon C, Gambrell LJ, et al. Intraoperative digital specimen mammography: rapid, accurate results expedite surgery. Ann Surg Oncol. 2007;14(4):1478-85.
102. Manhoobi IP, Bodilsen A, Nijkamp J, Pareek A, Tramm T, Redsted S, et al. Diagnostic accuracy of radiography, digital breast tomosynthesis, micro-CT and ultrasound for margin assessment during breast surgery: A systematic review and meta-analysis. Acad Radiol. 2022;29(10):1560-72.

103. Chand JT, Sharma MM, Dharmarajan JP, Nambiar A. Digital Breast Tomosynthesis as a Tool in Confirming Negative Surgical Margins in Non-palpable Breast Lesions. Indian J Surg Oncol. 2019;10(4):624-8.
104. Kim JY, Jung YS, Han SH, Sung JH, Hur MH. Indications and methods of intraoperative specimen radiography in breast-conserving surgery. Transl Cancer Res. 2020;9(11):6625-8.
105. Graham RA, Homer MJ, Katz J, Rothschild J, Safaii H, Supran S. The pancake phenomenon contributes to the inaccuracy of margin assessment in patients with breast cancer. Am J Surg. 2002;184(2):89-93.
106. Bianchi S, Palli D, Ciatto S, Galli M, Giorgi D, Vezzosi V, et al. Accuracy and reliability of frozen section diagnosis in a series of 672 nonpalpable breast lesions. Am J Clin Pathol. 1995;103(2):199-205.
107. Garcia MT, Mota BS, Cardoso N, Martimbianco ALC, Ricci MD, Carvalho FM, et al. Accuracy of frozen section in intraoperative margin assessment for breast-conserving surgery: A systematic review and meta-analysis. PLoS One. 2021;16(3):e0248768.
108. Nowikiewicz T, Srutek E, Glowacka-Mrotek I, Tarkowska M, Zyromska A, Zegarski W. Clinical outcomes of an intraoperative surgical margin assessment using the fresh frozen section method in patients with invasive breast cancer undergoing breast-conserving surgery - a single center analysis. Sci Rep. 2019;9(1):13441.
109. Boughey JC, Keeney GL, Radensky P, Song CP, Habermann EB. Economic Implications of Widespread Expansion of Frozen Section Margin Analysis to Guide Surgical Resection in Women With Breast Cancer Undergoing Breast-Conserving Surgery. J Oncol Pract. 2016;12(4):e413-22.
110. Esbona K, Li Z, Wilke LG. Intraoperative imprint cytology and frozen section pathology for margin assessment in breast conservation surgery: a systematic review. Ann Surg Oncol. 2012;19(10):3236-45.
111. Maloney BW, McClatchy DM, Pogue BW, Paulsen KD, Wells WA, Barth RJ. Review of methods for intraoperative margin detection for breast conserving surgery. J Biomed Opt. 2018;23(10):1-19.
112. Osako T, Nishimura R, Nishiyama Y, Okumura Y, Tashima R, Nakano M, et al. Efficacy of intraoperative entire-circumferential frozen section analysis of lumpectomy margins during breast-conserving surgery for breast cancer. Int J Clin Oncol. 2015;20(6):1093-101.
113. Pallialil N AV, Sharmila P, Maheswari P. Evaluation of Intraoperative Imprint Cytology and Frozen Section in
Determination of Tumor and Tumor Margins. Saudi Journal of Pathology and Microbiology. 2023.
114. Tamanuki T, Namura M, Aoyagi T, Shimizu S, Suwa T, Matsuzaki H. Effect of Intraoperative Imprint Cytology Followed by Frozen Section on Margin Assessment in Breast-Conserving Surgery. Ann Surg Oncol. 2021;28(3):1338-46.
115. Weinberg E, Cox C, Dupont E, White L, Ebert M, Greenberg H, et al. Local recurrence in lumpectomy patients after imprint cytology margin evaluation. Am J Surg. 2004;188(4):349-54.
116. Bakhshandeh M, Tutuncuoglu SO, Fischer G, Masood S. Use of imprint cytology for assessment of surgical margins in lumpectomy specimens of breast cancer patients. Diagn Cytopathol. 2007;35(10):656-9.
117. Schwarz J, Schmidt H. Technology for Intraoperative Margin Assessment in Breast Cancer. Ann Surg Oncol. 2020;27(7):2278-87.

118. DiCorpo D, Tiwari A, Tang R, Griffin M, Aftreth O, Bautista P, et al. The role of Micro-CT in imaging breast cancer specimens. Breast Cancer Res Treat. 2020;180(2):343-57.
119. McClatchy DM, 3rd, Zuurbier RA, Wells WA, Paulsen KD, Pogue BW. Micro-computed tomography enables rapid surgical margin assessment during breast conserving surgery (BCS): correlation of whole BCS micro-CT readings to final histopathology. Breast Cancer Res Treat. 2018;172(3):587-95.
120. Papa M, Allweis T, Karni T, Sandbank J, Konichezky M, Diment J, et al. An intraoperative MRI system for margin assessment in breast conserving surgery: Initial results from a novel technique. J Surg Oncol. 2016;114(1):22-6.
121. Krammer J, Price ER, Jochelson MS, Watson E, Murray MP, Schoenberg SO, et al. Breast MR imaging for the assessment of residual disease following initial surgery for breast cancer with positive margins. Eur Radiol. 2017;27(11):4812-8.
122. Abe H, Shimauchi A, Fan X, River JN, Sattar H, Mueller J, et al. Comparing post-operative human breast specimen radiograph and MRI in lesion margin and volume assessment. J Appl Clin Med Phys. 2012;13(6):3802.
123. Balasundaram G, Krafft C, Zhang R, Dev K, Bi R, Moothanchery M, et al. Biophotonic technologies for assessment of breast tumor surgical margins-A review. J Biophotonics. 2021;14(1):e202000280.
124. Goh Y, Balasundaram G, Moothanchery M, Attia A, Li X, Lim HQ, et al. Ultrasound Guided Optoacoustic Tomography in Assessment of Tumor Margins for Lumpectomies. Transl Oncol. 2020;13(2):254-61.
125. Majumder SK, Keller MD, Boulos FI, Kelley MC, Mahadevan-Jansen A. Comparison of autofluorescence, diffuse reflectance, and Raman spectroscopy for breast tissue discrimination. J Biomed Opt. 2008;13(5):054009.
126. Hubbard TJE, Shore A, Stone N. Raman spectroscopy for rapid intra-operative margin analysis of surgically excised tumour specimens. Analyst. 2019;144(22):6479-96.
127. Schnabel F, Boolbol SK, Gittleman M, Karni T, Tafra L, Feldman S, et al. A randomized prospective study of lumpectomy margin assessment with use of MarginProbe in patients with nonpalpable breast malignancies. Ann Surg Oncol. 2014;21(5):1589-95.
128. Thill M. MarginProbe: intraoperative margin assessment during breast conserving surgery by using radiofrequency spectroscopy. Expert Rev Med Devices. 2013;10(3):301-15.
129. Bundred N DM, Achuthan R, Barrett E, Benson J, Courtney C, Skene A, Hoar F, Bhaskar P, Watterson D, Barnes N. Does the use of an intraoperative device to assess margins reduce need for re-excison after breast conserving surgery: Multicentre randomised controlled trial2022; 48(5).
130. Rossou C, Alampritis G, Patel B. Reducing re-excision rates in breast conserving surgery with Margin Probe: systematic review. Br J Surg. 2024;111(1).
131. Dixon JM, Renshaw L, Young O, Kulkarni D, Saleem T, Sarfaty M, et al. Intra-operative assessment of excised breast tumour margins using ClearEdge imaging device. Eur J Surg Oncol. 2016;42(12):1834-40.
132. Balog J, Sasi-Szabo L, Kinross J, Lewis MR, Muirhead LJ, Veselkov K, et al. Intraoperative tissue identification using rapid evaporative ionization mass spectrometry. Sci Transl Med. 2013;5(194):194ra93.
133. St John ER, Balog J, McKenzie JS, Rossi M, Covington A, Muirhead L, et al. Rapid evaporative ionisation mass spectrometry of electrosurgical vapours for the

identification of breast pathology: towards an intelligent knife for breast cancer surgery. Breast Cancer Res. 2017;19(1):59.
134. Jacques SL. Optical properties of biological tissues: a review. Phys Med Biol. 2013;58(11):R37-61.
135. V VT. Tissue Optics and Photonics: Light-Tissue Interaction. J of Biomedical Photonics & Eng 2015.
136. Brown JQ, Bydlon TM, Kennedy SA, Caldwell ML, Gallagher JE, Junker M, et al. Optical spectral surveillance of breast tissue landscapes for detection of residual disease in breast tumor margins. PLoS One. 2013;8(7):e69906.
137. Shalaby N, Al-Ebraheem A, Le D, Cornacchi S, Fang Q, Farrell T, et al. Time-resolved fluorescence (TRF) and diffuse reflectance spectroscopy (DRS) for margin analysis in breast cancer. Lasers Surg Med. 2018;50(3):236-45.
138. O'Sullivan TD, Cerussi AE, Cuccia DJ, Tromberg BJ. Diffuse optical imaging using spatially and temporally modulated light. J Biomed Opt. 2012;17(7):071311.
139. Mabley J V-DT, Tuchin V.V. Optical Properties of Tissue. In: Vo-Dinh T, editor. Biomedical Photonics Handbook2014.
140. Tuchin V. Light-Tissue Interactions. In: Vo-Dinh T, editor. Biomedical Photonics Handbook. Boca Raton2014.
141. Kolenc O QK. Evaluating Cell Metabolism Through Autofluorescence Imaging of NAD(P)H and FAD. Antioxidants & Redox Signaling. 2019;30.
142. Cairns RA, Harris IS, Mak TW. Regulation of cancer cell metabolism. Nat Rev Cancer. 2011;11(2):85-95.
143. Moreno-Sanchez R, Rodriguez-Enriquez S, Marin-Hernandez A, Saavedra E. Energy metabolism in tumor cells. FEBS J. 2007;274(6):1393-418.
144. Richards-Kortum R, Sevick-Muraca E. Quantitative optical spectroscopy for tissue diagnosis. Annu Rev Phys Chem. 1996;47:555-606.
145. Evers D, Hendriks B, Lucassen G, Ruers T. Optical spectroscopy: current advances and future applications in cancer diagnostics and therapy. Future Oncol. 2012;8(3):307-20.
146. Garini Y, Young IT, McNamara G. Spectral imaging: principles and applications. Cytometry A. 2006;69(8):735-47.
147. Volynskaya Z, Haka AS, Bechtel KL, Fitzmaurice M, Shenk R, Wang N, et al. Diagnosing breast cancer using diffuse reflectance spectroscopy and intrinsic fluorescence spectroscopy. J Biomed Opt. 2008;13(2):024012.
148. Zonios G, Perelman LT, Backman V, Manoharan R, Fitzmaurice M, Van Dam J, et al. Diffuse reflectance spectroscopy of human adenomatous colon polyps in vivo. Appl Opt. 1999;38(31):6628-37.
149. Farrell TJ, Patterson MS, Wilson B. A diffusion theory model of spatially resolved, steady-state diffuse reflectance for the noninvasive determination of tissue optical properties in vivo. Med Phys. 1992;19(4):879-88.
150. Zhu C, Liu Q. Review of Monte Carlo modeling of light transport in tissues. J Biomed Opt. 2013;18(5):50902.
151. A.J.Moy JWT. Diffuse Reflectance Spectroscopy and Imaging. Imaging in Dermatology: Academic Press; 2016.
152. Wagnieres GA, Star WM, Wilson BC. In vivo fluorescence spectroscopy and imaging for oncological applications. Photochem Photobiol. 1998;68(5):603-32.
153. Li Q, He X, Wang Y, Liu H, Xu D, Guo F. Review of spectral imaging technology in biomedical engineering: achievements and challenges. J Biomed Opt. 2013;18(10):100901.

154. Lu G, Fei B. Medical hyperspectral imaging: a review. J Biomed Opt. 2014;19(1):10901.
155. Dang X, Bardhan NM, Qi J, Gu L, Eze NA, Lin CW, et al. Deep-tissue optical imaging of near cellular-sized features. Sci Rep. 2019;9(1):3873.
156. Shanthakumar D, Leiloglou M, Kelliher C, Darzi A, Elson DS, Leff DR. A Comparison of Spectroscopy and Imaging Techniques Utilizing Spectrally Resolved Diffusely Reflected Light for Intraoperative Margin Assessment in Breast-Conserving Surgery: A Systematic Review and Meta-Analysis. Cancers (Basel). 2023;15(11).
157. Gioux S, Mazhar A, Lee BT, Lin SJ, Tobias AM, Cuccia DJ, et al. First-in-human pilot study of a spatial frequency domain oxygenation imaging system. J Biomed Opt. 2011;16(8):086015.
158. Pereira TV, Patsopoulos NA, Salanti G, Ioannidis JP. Critical interpretation of Cochran's Q test depends on power and prior assumptions about heterogeneity. Res Synth Methods. 2010;1(2):149-61.
159. Jackson D. The power of the standard test for the presence of heterogeneity in meta-analysis. Stat Med. 2006;25(15):2688-99.
160. Zhu C, Palmer GM, Breslin TM, Harter J, Ramanujam N. Diagnosis of breast cancer using diffuse reflectance spectroscopy: Comparison of a Monte Carlo versus partial least squares analysis based feature extraction technique. Lasers Surg Med. 2006;38(7):714-24.
161. Brown JQ, Bydlon TM, Richards LM, Yu B, Kennedy SA, Geradts J, et al. Optical assessment of tumor resection margins in the breast. IEEE J Sel Top Quantum Electron. 2010;16(3):530-44.
162. Zhu C, Palmer GM, Breslin TM, Xu F, Ramanujam N. Use of a multiseparation fiber optic probe for the optical diagnosis of breast cancer. J Biomed Opt. 2005;10(2):024032.
163. Breslin TM, Xu F, Palmer GM, Zhu C, Gilchrist KW, Ramanujam N. Autofluorescence and diffuse reflectance properties of malignant and benign breast tissues. Ann Surg Oncol. 2004;11(1):65-70.
164. Palmer GM, Zhu C, Breslin TM, Xu F, Gilchrist KW, Ramanujam N. Comparison of multiexcitation fluorescence and diffuse reflectance spectroscopy for the diagnosis of breast cancer (March 2003). IEEE Trans Biomed Eng. 2003;50(11):1233-42.
165. Ramanujam N, Brown J, Bydlon TM, Kennedy SA, Richards LM, Junker MK, et al. Quantitative spectral reflectance imaging device for intraoperative breast tumor margin assessment. Annu Int Conf IEEE Eng Med Biol Soc. 2009;2009:6554-6.
166. Keller MD, Majumder SK, Kelley MC, Meszoely IM, Boulos FI, Olivares GM, et al. Autofluorescence and diffuse reflectance spectroscopy and spectral imaging for breast surgical margin analysis. Lasers Surg Med. 2010;42(1):15-23.
167. H.Liu RP-SFSNKPL. Classification of ex-vivo breast cancer positive margins measured by hyperspectral imaging. IEEE International Conference; 15-18 September 2013; Melbourne, VIC, Australia: IEEE; 2013.
168. Aboughaleb IH, Aref MH, El-Sharkawy YH. Hyperspectral imaging for diagnosis and detection of ex-vivo breast cancer. Photodiagnosis Photodyn Ther. 2020;31:101922.
169. Nachabe R, Evers DJ, Hendriks BH, Lucassen GW, van der Voort M, Rutgers EJ, et al. Diagnosis of breast cancer using diffuse optical spectroscopy from 500 to 1600 nm: comparison of classification methods. J Biomed Opt. 2011;16(8):087010.
170. de Boer LL, Molenkamp BG, Bydlon TM, Hendriks BH, Wesseling J, Sterenborg HJ, et al. Fat/water ratios measured with diffuse reflectance spectroscopy to detect breast tumor boundaries. Breast Cancer Res Treat. 2015;152(3):509-18.

171. Evers DJ, Nachabe R, Vranken Peeters MJ, van der Hage JA, Oldenburg HS, Rutgers EJ, et al. Diffuse reflectance spectroscopy: towards clinical application in breast cancer. Breast Cancer Res Treat. 2013;137(1):155-65.
172. Kho E, Dashtbozorg B, de Boer LL, Van de Vijver KK, Sterenborg H, Ruers TJM. Broadband hyperspectral imaging for breast tumor detection using spectral and spatial information. Biomed Opt Express. 2019;10(9):4496-515.
173. Kho E, de Boer LL, Van de Vijver KK, van Duijnhoven F, Vrancken Peeters M, Sterenborg H, et al. Hyperspectral Imaging for Resection Margin Assessment during Cancer Surgery. Clin Cancer Res. 2019;25(12):3572-80.
174. McClatchy DM, Rizzo EJ, Wells WA, Black CC, Paulsen KD, Kanick SC, et al. Light scattering measured with spatial frequency domain imaging can predict stromal versus epithelial proportions in surgically resected breast tissue. J Biomed Opt. 2018;24(7):1-11.
175. Laughney AM, Krishnaswamy V, Rizzo EJ, Schwab MC, Barth RJ, Jr., Cuccia DJ, et al. Spectral discrimination of breast pathologies in situ using spatial frequency domain imaging. Breast Cancer Res. 2013;15(4):R61.
176. Matthew D.Keller SKM, Mark C.Kelley, Ingrid Meszoely, Fouad I. Boulos & Anita Mahadevan-Jansen, editor Optical spectroscopy for therapeutic guidance in breast conserving therapy. European Conference on Biomedical Optics; 2007; Munich Germany: Optica Publishing Group, 2007.
177. Hanahan D, Weinberg RA. The hallmarks of cancer. Cell. 2000;100(1):57-70.
178. Turashvili G, Brogi E. Tumor Heterogeneity in Breast Cancer. Front Med (Lausanne). 2017;4:227.
179. Rivenbark AG, O'Connor SM, Coleman WB. Molecular and cellular heterogeneity in breast cancer: challenges for personalized medicine. Am J Pathol. 2013;183(4):1113-24.
180. Luond F, Tiede S, Christofori G. Breast cancer as an example of tumour heterogeneity and tumour cell plasticity during malignant progression. Br J Cancer. 2021;125(2):164-75.
181. Sinn HP, Kreipe H. A Brief Overview of the WHO Classification of Breast Tumors, 4th Edition, Focusing on Issues and Updates from the 3rd Edition. Breast Care (Basel). 2013;8(2):149-54.
182. Donegan WL. Prognostic factors. Stage and receptor status in breast cancer. Cancer. 1992;70(6 Suppl):1755-64.
183. Anderson E. The role of oestrogen and progesterone receptors in human mammary development and tumorigenesis. Breast Cancer Res. 2002;4(5):197-201.
184. Mitri Z, Constantine T, O'Regan R. The HER2 Receptor in Breast Cancer: Pathophysiology, Clinical Use, and New Advances in Therapy. Chemother Res Pract. 2012;2012:743193.
185. Rakha EA, Pinder SE, Bartlett JM, Ibrahim M, Starczynski J, Carder PJ, et al. Updated UK Recommendations for HER2 assessment in breast cancer. J Clin Pathol. 2015;68(2):93-9.
186. Prat A, Pineda E, Adamo B, Galvan P, Fernandez A, Gaba L, et al. Clinical implications of the intrinsic molecular subtypes of breast cancer. Breast. 2015;24 Suppl 2:S26-35.
187. Vos EL, Gaal J, Verhoef C, Brouwer K, van Deurzen CHM, Koppert LB. Focally positive margins in breast conserving surgery: Predictors, residual disease, and local recurrence. Eur J Surg Oncol. 2017;43(10):1846-54.

188. Rath MG, Uhlmann L, Heil J, Domschke C, Roth Z, Sinn HP, et al. Predictors of Residual Tumor in Breast-Conserving Therapy. Ann Surg Oncol. 2015;22 Suppl 3:S451-8.
189. Moran MS, Schnitt SJ, Giuliano AE, Harris JR, Khan SA, Horton J, et al. Society of Surgical Oncology-American Society for Radiation Oncology consensus guideline on margins for breast-conserving surgery with whole-breast irradiation in stages I and II invasive breast cancer. Int J Radiat Oncol Biol Phys. 2014;88(3):553-64.
190. Kho E, de Boer LL, Post AL, Van de Vijver KK, Jozwiak K, Sterenborg H, et al. Imaging depth variations in hyperspectral imaging: Development of a method to detect tumor up to the required tumor-free margin width. J Biophotonics. 2019;12(11):e201900086.
191. Marinovich ML, Azizi L, Macaskill P, Irwig L, Morrow M, Solin LJ, et al. The Association of Surgical Margins and Local Recurrence in Women with Ductal Carcinoma In Situ Treated with Breast-Conserving Therapy: A Meta-Analysis. Ann Surg Oncol. 2016;23(12):3811-21.
192. Laughney AM, Krishnaswamy V, Rice TB, Cuccia DJ, Barth RJ, Tromberg BJ, et al. System analysis of spatial frequency domain imaging for quantitative mapping of surgically resected breast tissues. J Biomed Opt. 2013;18(3):036012.
193. Kennedy S, Geradts J, Bydlon T, Brown JQ, Gallagher J, Junker M, et al. Optical breast cancer margin assessment: an observational study of the effects of tissue heterogeneity on optical contrast. Breast Cancer Res. 2010;12(6):R91.
194. Tuchin V. Tissue OpticsL Light Scattering Methods and Instruments for Medical Diagnosis: SPIE; 2007.
195. Douplik A SG, Schelkanavoa I, Tuchin V. The response of tissue to laser light. Lasers for Medical Applications2013. p. 47-109.
196. Fisher B, Redmond C, Poisson R, Margolese R, Wolmark N, Wickerham L, et al. Eight-year results of a randomized clinical trial comparing total mastectomy and lumpectomy with or without irradiation in the treatment of breast cancer. N Engl J Med. 1989;320(13):822-8.
197. Early Breast Cancer Trialists' Collaborative G, Darby S, McGale P, Correa C, Taylor C, Arriagada R, et al. Effect of radiotherapy after breast-conserving surgery on 10-year recurrence and 15-year breast cancer death: meta-analysis of individual patient data for 10,801 women in 17 randomised trials. Lancet. 2011;378(9804):1707-16.
198. Early Breast Cancer Trialists' Collaborative G. Effects of chemotherapy and hormonal therapy for early breast cancer on recurrence and 15-year survival: an overview of the randomised trials. Lancet. 2005;365(9472):1687-717.
199. Touboul E, Buffat L, Belkacemi Y, Lefranc JP, Uzan S, Lhuillier P, et al. Local recurrences and distant metastases after breast-conserving surgery and radiation therapy for early breast cancer. Int J Radiat Oncol Biol Phys. 1999;43(1):25-38.
200. Aalders KC, van Bommel AC, van Dalen T, Sonke GS, van Diest PJ, Boersma LJ, et al. Contemporary risks of local and regional recurrence and contralateral breast cancer in patients treated for primary breast cancer. Eur J Cancer. 2016;63:118-26.
201. Bundred JR, Michael S, Stuart B, Cutress RI, Beckmann K, Holleczek B, et al. Margin status and survival outcomes after breast cancer conservation surgery: prospectively registered systematic review and meta-analysis. BMJ. 2022;378:e070346.
202. Solomayer EF, Diel IJ, Meyberg GC, Gollan C, Bastert G. Metastatic breast cancer: clinical course, prognosis and therapy related to the first site of metastasis. Breast Cancer Res Treat. 2000;59(3):271-8.

203. Meric F, Mirza NQ, Vlastos G, Buchholz TA, Kuerer HM, Babiera GV, et al. Positive surgical margins and ipsilateral breast tumor recurrence predict disease-specific survival after breast-conserving therapy. Cancer. 2003;97(4):926-33.
204. Pilewskie M, Morrow M. Margins in breast cancer: How much is enough? Cancer. 2018;124(7):1335-41.
205. NICE. Early and locally advance breast cancer: diagnosis and management. In: Health, editor. 2018.
206. Morrow M, Van Zee KJ, Solin LJ, Houssami N, Chavez-MacGregor M, Harris JR, et al. Society of Surgical Oncology-American Society for Radiation Oncology-American Society of Clinical Oncology Consensus Guideline on Margins for Breast-Conserving Surgery With Whole-Breast Irradiation in Ductal Carcinoma in Situ. Pract Radiat Oncol. 2016;6(5):287-95.
207. Australia C. Guidance for the managament of early breast cancer: Recommendations and practice points, Cancer Australia. Cancer Australia, Surry Hills, NSW2020.
208. Thompson AM, Clements K, Cheung S, Pinder SE, Lawrence G, Sawyer E, et al. Management and 5-year outcomes in 9938 women with screen-detected ductal carcinoma in situ: the UK Sloane Project. Eur J Cancer. 2018;101:210-9.
209. Giannakeas V, Sopik V, Narod SA. Association of a Diagnosis of Ductal Carcinoma In Situ With Death From Breast Cancer. JAMA Netw Open. 2020;3(9):e2017124.
210. Statement AoBSC. Margin Width in Breast Conserving Surgery. 2015.
211. Bartelink H, Horiot JC, Poortmans P, Struikmans H, Van den Bogaert W, Barillot I, et al. Recurrence rates after treatment of breast cancer with standard radiotherapy with or without additional radiation. N Engl J Med. 2001;345(19):1378-87.
212. Romestaing P, Lehingue Y, Carrie C, Coquard R, Montbarbon X, Ardiet JM, et al. Role of a 10-Gy boost in the conservative treatment of early breast cancer: results of a randomized clinical trial in Lyon, France. J Clin Oncol. 1997;15(3):963-8.
213. George A, Stead TS, Ganti L. What's the Risk: Differentiating Risk Ratios, Odds Ratios, and Hazard Ratios? Cureus. 2020;12(8):e10047.
214. Wang LYYP, E; Forouhi, P; Kleidi, E. Recurrence rates following breast conserving surgery - A single center observational study. European Journal of Surgical Oncology. 2023;49(5).
215. Njeh CF, Saunders MW, Langton CM. Accelerated Partial Breast Irradiation (APBI): A review of available techniques. Radiat Oncol. 2010;5:90.
216. Sterne JA, Hernan MA, Reeves BC, Savovic J, Berkman ND, Viswanathan M, et al. ROBINS-I: a tool for assessing risk of bias in non-randomised studies of interventions. BMJ. 2016;355:i4919.
217. DerSimonian R, Kacker R. Random-effects model for meta-analysis of clinical trials: an update. Contemp Clin Trials. 2007;28(2):105-14.
218. Atzori G, Gipponi M, Cornacchia C, Diaz R, Sparavigna M, Gallo M, et al. "No Ink on Tumor" in Breast-Conserving Surgery after Neoadjuvant Chemotherapy. J Pers Med. 2022;12(7).
219. Bhatti AB, Khan A, Muzaffar N, Siddiqui N, Syed A, Shah M, et al. Safe negative margin width in breast conservative therapy: results from a population with a high percentage of negative prognostic factors. World J Surg. 2014;38(11):2863-70.
220. Biglia N, Ponzone R, Bounous VE, Mariani LL, Maggiorotto F, Benevelli C, et al. Role of re-excision for positive and close resection margins in patients treated with breast-conserving surgery. Breast. 2014;23(6):870-5.

221. Bodilsen A, Bjerre K, Offersen BV, Vahl P, Amby N, Dixon JM, et al. Importance of margin width in breast-conserving treatment of early breast cancer. J Surg Oncol. 2016;113(6):609-15.
222. Bouvet M, Ollila DW, Hunt KK, Babiera GV, Spitz FR, Giuliano AE, et al. Role of conservation therapy for invasive lobular carcinoma of the breast. Ann Surg Oncol. 1997;4(8):650-4.
223. Cho WK, Choi DH, Park W, Kim H, Cha H. Is higher dose radiation necessary for positive resection margin after breast-conserving surgery for breast cancer? Breast. 2019;47:16-21.
224. Choi J, Laws A, Hu J, Barry W, Golshan M, King T. Margins in Breast-Conserving Surgery After Neoadjuvant Therapy. Ann Surg Oncol. 2018;25(12):3541-7.
225. Clement Z, McLeay W, Hoffmann C, Shin P, Kiu A, Eaton M. Role of radiotherapy in women over the age of 65 after breast conserving surgery for breast cancer: A 5-year retrospective study. Breast Dis. 2018;37(4):197-205.
226. DiBiase SJ, Komarnicky LT, Heron DE, Schwartz GF, Mansfield CM. Influence of radiation dose on positive surgical margins in women undergoing breast conservation therapy. Int J Radiat Oncol Biol Phys. 2002;53(3):680-6.
227. Dixon JM, Thomas J, Kerr GR, Williams LJ, Dodds C, Kunkler IH, et al. A study of margin width and local recurrence in breast conserving therapy for invasive breast cancer. Eur J Surg Oncol. 2016;42(5):657-64.
228. Francis M, Cakir B, Bilous M, Ung O, Boyages J. Conservative surgery and radiation therapy for invasive lobular carcinoma of the breast. Aust N Z J Surg. 1999;69(6):450-4.
229. Gage I, Schnitt SJ, Nixon AJ, Silver B, Recht A, Troyan SL, et al. Pathologic margin involvement and the risk of recurrence in patients treated with breast-conserving therapy. Cancer. 1996;78(9):1921-8.
230. Goldstein NS, Kestin L, Vicini F. Factors associated with ipsilateral breast failure and distant metastases in patients with invasive breast carcinoma treated with breast-conserving therapy. A clinicopathologic study of 607 neoplasms from 583 patients. Am J Clin Pathol. 2003;120(4):500-27.
231. Groot G, Rees H, Pahwa P, Kanagaratnam S, Kinloch M. Predicting local recurrence following breast-conserving therapy for early stage breast cancer: the significance of a narrow (</= 2 mm) surgical resection margin. J Surg Oncol. 2011;103(3):212-6.
232. Jobsen J, van der Palen J, Riemersma S, Heijmans H, Ong F, Struikmans H. Pattern of ipsilateral breast tumor recurrence after breast-conserving therapy. Int J Radiat Oncol Biol Phys. 2014;89(5):1006-14.
233. Jobsen JJ, Riemersma S, van der Palen J, Ong F, Jonkman A, Struikmans H. The impact of margin status in breast-conserving therapy for lobular carcinoma is age related. Eur J Surg Oncol. 2010;36(2):176-81.
234. Karasawa K, Obara T, Shimizu T, Haga S, Okamoto T, Ito Y, et al. Outcome of breast-conserving therapy in the Tokyo Women's Medical University Breast Cancer Society experience. Breast Cancer. 2003;10(4):341-8.
235. Kahlert S, Kolben TM, Schmoeckel E, Czogalla B, Hester A, Degenhardt T, et al. Prognostic impact of residual disease in simultaneous additional excision specimens after one-step breast conserving therapy with negative final margin status in primary breast cancer. Eur J Surg Oncol. 2018;44(9):1318-23.

236. Kreike B, Hart AA, van de Velde T, Borger J, Peterse H, Rutgers E, et al. Continuing risk of ipsilateral breast relapse after breast-conserving therapy at long-term follow-up. Int J Radiat Oncol Biol Phys. 2008;71(4):1014-21.
237. Kunos C, Latson L, Overmoyer B, Silverman P, Shenk R, Kinsella T, et al. Breast conservation surgery achieving>or=2 mm tumor-free margins results in decreased local-regional recurrence rates. Breast J. 2006;12(1):28-36.
238. Leong C, Boyages J, Jayasinghe UW, Bilous M, Ung O, Chua B, et al. Effect of margins on ipsilateral breast tumor recurrence after breast conservation therapy for lymph node-negative breast carcinoma. Cancer. 2004;100(9):1823-32.
239. Lin J, Lin KJ, Wang YF, Huang LH, Chen SL, Chen DR. Association of surgical margins with local recurrence in patients undergoing breast-conserving surgery after neoadjuvant chemotherapy. BMC Cancer. 2020;20(1):451.
240. Lupe K, Truong PT, Alexander C, Lesperance M, Speers C, Tyldesley S. Subsets of women with close or positive margins after breast-conserving surgery with high local recurrence risk despite breast plus boost radiotherapy. Int J Radiat Oncol Biol Phys. 2011;81(4):e561-8.
241. Neuschatz AC, DiPetrillo T, Safaii H, Price LL, Schmidt-Ullrich RK, Wazer DE. Long-term follow-up of a prospective policy of margin-directed radiation dose escalation in breast-conserving therapy. Cancer. 2003;97(1):30-9.
242. Braunstein LZ, Brock JE, Chen YH, Truong L, Russo AL, Arvold ND, et al. Invasive lobular carcinoma of the breast: local recurrence after breast-conserving therapy by subtype approximation and surgical margin. Breast Cancer Res Treat. 2015;149(2):555-64.
243. Hennigs A, Fuchs V, Sinn HP, Riedel F, Rauch G, Smetanay K, et al. Do Patients After Reexcision Due to Involved or Close Margins Have the Same Risk of Local Recurrence as Those After One-Step Breast-Conserving Surgery? Ann Surg Oncol. 2016;23(6):1831-7.
244. Livi L, Meattini I, Franceschini D, Saieva C, Meacci F, Marrazzo L, et al. Radiotherapy boost dose-escalation for invasive breast cancer after breast-conserving surgery: 2093 patients treated with a prospective margin-directed policy. Radiother Oncol. 2013;108(2):273-8.
245. Maishman T, Cutress RI, Hernandez A, Gerty S, Copson ER, Durcan L, et al. Local Recurrence and Breast Oncological Surgery in Young Women With Breast Cancer: The POSH Observational Cohort Study. Ann Surg. 2017;266(1):165-72.
246. McBain CA, Young EA, Swindell R, Magee B, Stewart AL. Local recurrence of breast cancer following surgery and radiotherapy: incidence and outcome. Clin Oncol (R Coll Radiol). 2003;15(1):25-31.
247. Peterson ME, Schultz DJ, Reynolds C, Solin LJ. Outcomes in breast cancer patients relative to margin status after treatment with breast-conserving surgery and radiation therapy: the University of Pennsylvania experience. Int J Radiat Oncol Biol Phys. 1999;43(5):1029-35.
248. Rouzier R, Extra JM, Carton M, Falcou MC, Vincent-Salomon A, Fourquet A, et al. Primary chemotherapy for operable breast cancer: incidence and prognostic significance of ipsilateral breast tumor recurrence after breast-conserving surgery. J Clin Oncol. 2001;19(18):3828-35.
249. Sadek BT, Homayounfar G, Abi Raad RF, Niemierko A, Shenouda MN, Keruakous AR, et al. Is a higher boost dose of radiation necessary after breast-conserving therapy for patients with breast cancer with final close or positive margins? Breast Cancer Res Treat. 2015;154(1):71-9.

250. Schnitt SJ, Abner A, Gelman R, Connolly JL, Recht A, Duda RB, et al. The relationship between microscopic margins of resection and the risk of local recurrence in patients with breast cancer treated with breast-conserving surgery and radiation therapy. Cancer. 1994;74(6):1746-51.
251. Solin LJ, Fowble BL, Schultz DJ, Goodman RL. The significance of the pathology margins of the tumor excision on the outcome of patients treated with definitive irradiation for early stage breast cancer. Int J Radiat Oncol Biol Phys. 1991;21(2):279-87.
252. Sorrentino L, Agozzino M, Albasini S, Bossi D, Mazzucchelli S, Vanna R, et al. Involved margins after lumpectomy for breast cancer: Always to be re-excised? Surg Oncol. 2019;30:141-6.
253. Tang SSK, Rapisarda F, Nerurkar A, Osin P, MacNeill F, Smith I, et al. Complete excision with narrow margins provides equivalent local control to wider excision in breast conservation for invasive cancer. BJS Open. 2019;3(2):161-8.
254. Tyler S, Truong PT, Lesperance M, Nichol A, Baliski C, Warburton R, et al. Close Margins Less Than 2 mm Are Not Associated With Higher Risks of 10-Year Local Recurrence and Breast Cancer Mortality Compared With Negative Margins in Women Treated With Breast-Conserving Therapy. Int J Radiat Oncol Biol Phys. 2018;101(3):661-70.
255. Voogd AC, Nielsen M, Peterse JL, Blichert-Toft M, Bartelink H, Overgaard M, et al. Differences in risk factors for local and distant recurrence after breast-conserving therapy or mastectomy for stage I and II breast cancer: pooled results of two large European randomized trials. J Clin Oncol. 2001;19(6):1688-97.
256. Vos EL, Siesling S, Baaijens MHA, Verhoef C, Jager A, Voogd AC, et al. Omitting re-excision for focally positive margins after breast-conserving surgery does not impair disease-free and overall survival. Breast Cancer Res Treat. 2017;164(1):157-67.
257. Wang L YY, Provenzano E, Forouhi P, Kleidi E. Recurrence rates following breast conserving surgery - A single center observational study. European Journal of Surgical Oncology. 2023;49(5).
258. Yoon TI, Lee JW, Lee SB, Sohn G, Kim J, Chung IY, et al. No Association of Positive Superficial and/or Deep Margins with Local Recurrence in Invasive Breast Cancer Treated with Breast-Conserving Surgery. Cancer Res Treat. 2018;50(1):275-82.
259. Freedman G, Fowble B, Hanlon A, Nicolaou N, Fein D, Hoffman J, et al. Patients with early stage invasive cancer with close or positive margins treated with conservative surgery and radiation have an increased risk of breast recurrence that is delayed by adjuvant systemic therapy. Int J Radiat Oncol Biol Phys. 1999;44(5):1005-15.
260. McIntosh A, Freedman G, Eisenberg D, Anderson P. Recurrence rates and analysis of close or positive margins in patients treated without re-excision before radiation for breast cancer. Am J Clin Oncol. 2007;30(2):146-51.
261. Ben-David MA, Sturtz DE, Griffith KA, Douglas KR, Hayman JA, Lichter AS, et al. Long-term results of conservative surgery and radiotherapy for ductal carcinoma in situ using lung density correction: the University of Michigan experience. Breast J. 2007;13(4):392-400.
262. Cutuli B, Cohen-Solal-Le Nir C, De Lafontan B, Mignotte H, Fichet V, Fay R, et al. Ductal carcinoma in situ of the breast results of conservative and radical treatments in 716 patients. Eur J Cancer. 2001;37(18):2365-72.

263. Dick AW, Sorbero MS, Ahrendt GM, Hayman JA, Gold HT, Schiffhauer L, et al. Comparative effectiveness of ductal carcinoma in situ management and the roles of margins and surgeons. J Natl Cancer Inst. 2011;103(2):92-104.
264. Ekatah GE, Turnbull AK, Arthur LM, Thomas J, Dodds C, Dixon JM. Margin width and local recurrence after breast conserving surgery for ductal carcinoma in situ. Eur J Surg Oncol. 2017;43(11):2029-35.
265. Fowble B, Hanlon AL, Fein DA, Hoffman JP, Sigurdson ER, Patchefsky A, et al. Results of conservative surgery and radiation for mammographically detected ductal carcinoma in situ (DCIS). Int J Radiat Oncol Biol Phys. 1997;38(5):949-57.
266. Group EBCC, Group ER, Bijker N, Meijnen P, Peterse JL, Bogaerts J, et al. Breast-conserving treatment with or without radiotherapy in ductal carcinoma-in-situ: ten-year results of European Organisation for Research and Treatment of Cancer randomized phase III trial 10853--a study by the EORTC Breast Cancer Cooperative Group and EORTC Radiotherapy Group. J Clin Oncol. 2006;24(21):3381-7.
267. Halasz LM, Sreedhara M, Chen YH, Bellon JR, Punglia RS, Wong JS, et al. Improved outcomes of breast-conserving therapy for patients with ductal carcinoma in situ. Int J Radiat Oncol Biol Phys. 2012;82(4):e581-6.
268. Hathout L, Hijal T, Theberge V, Fortin B, Vulpe H, Hogue JC, et al. Hypofractionated radiation therapy for breast ductal carcinoma in situ. Int J Radiat Oncol Biol Phys. 2013;87(5):1058-63.
269. Hennigs A, Riedel F, Gondos A, Sinn P, Schirmacher P, Marme F, et al. Prognosis of breast cancer molecular subtypes in routine clinical care: A large prospective cohort study. BMC Cancer. 2016;16(1):734.
270. Jobsen JJ, Scheijmans L, Smit W, Stenfert Kroese MC, Struikmans H, van der Palen J. Breast-conserving therapy for primary Ductal Carcinoma in Situ in The Netherlands: A multi-center study and population-based analysis. Breast. 2018;42:3-9.
271. Kim K, Kim JH, Kim YB, Suh CO, Shin KH, Kim JH, et al. Selective Radiation Therapy for Ductal Carcinoma In Situ Following Breast-Conserving Surgery According to Age and Margin Width: Korean Radiation Oncology Group 11-04 and 16-02 Studies. J Breast Cancer. 2017;20(4):327-32.
272. Kuru B, Yuruker S, Sullu Y, Gursel B, Ozen N. Does a Close Surgical Margin for Ductal Carcinoma In Situ Associated with Invasive Breast Carcinoma Affect Breast Cancer Recurrence? J Invest Surg. 2020;33(7):627-33.
273. Livingston-Rosanoff D, Trentham-Dietz A, Hampton JM, Newcomb PA, Wilke LG. Does margin width impact breast cancer recurrence rates in women with breast conserving surgery for ductal carcinoma in situ? Breast Cancer Res Treat. 2021;189(2):463-70.
274. Macdonald HR, Silverstein MJ, Lee LA, Ye W, Sanghavi P, Holmes DR, et al. Margin width as the sole determinant of local recurrence after breast conservation in patients with ductal carcinoma in situ of the breast. Am J Surg. 2006;192(4):420-2.
275. Mannu GS, Wang Z, Dodwell D, Broggio J, Charman J, Darby SC. Invasive breast cancer and breast cancer death after non-screen detected ductal carcinoma in situ from 1990 to 2018 in England: population based cohort study. BMJ. 2024;384:e075498.
276. Mathew J, Karia R, Morgan DAL, Lee AHS, Ellis IO, Robertson JFR, et al. Factors influencing local control in patients undergoing breast conservation surgery for ductal carcinoma in situ. Breast. 2017;31:181-5.

277. Meattini I, Livi L, Franceschini D, Saieva C, Meacci F, Marrazzo L, et al. Role of radiotherapy boost in women with ductal carcinoma in situ: a single-center experience in a series of 389 patients. Eur J Surg Oncol. 2013;39(6):613-8.
278. Monteau A, Sigal-Zafrani B, Kirova YM, Fourchotte V, Bollet MA, Vincent-Salomon A, et al. Ductal carcinoma in situ of the breast with close or focally involved margins following breast-conserving surgery: treatment with reexcision or radiotherapy with increased dosage. Int J Radiat Oncol Biol Phys. 2009;75(4):1021-8.
279. Schmitz R, van den Belt-Dusebout AW, Clements K, Ren Y, Cresta C, Timbres J, et al. Association of DCIS size and margin status with risk of developing breast cancer post-treatment: multinational, pooled cohort study. BMJ. 2023;383:e076022.
280. Shaikh T, Li T, Murphy CT, Zaorsky NG, Bleicher RJ, Sigurdson ER, et al. Importance of Surgical Margin Status in Ductal Carcinoma In Situ. Clin Breast Cancer. 2016;16(4):312-8.
281. Shikama N, Sekiguchi K, Nakamura N, Sekine H, Nakayama Y, Imanaka K, et al. Final results from a multicenter prospective study (JROSG 05-5) on postoperative radiotherapy for patients with ductal carcinoma in situ with an involved surgical margin or close margin widths of 1 mm or less. J Radiat Res. 2015;56(5):830-4.
282. Solin LJ, Fourquet A, Vicini FA, Taylor M, Olivotto IA, Haffty B, et al. Long-term outcome after breast-conservation treatment with radiation for mammographically detected ductal carcinoma in situ of the breast. Cancer. 2005;103(6):1137-46.
283. Sweldens C, Peeters S, van Limbergen E, Janssen H, Laenen A, Patil S, et al. Local relapse after breast-conserving therapy for ductal carcinoma in situ: a European single-center experience and external validation of the Memorial Sloan-Kettering Cancer Center DCIS nomogram. Cancer J. 2014;20(1):1-7.
284. Vicini FA, Recht A. Age at diagnosis and outcome for women with ductal carcinoma-in-situ of the breast: a critical review of the literature. J Clin Oncol. 2002;20(11):2736-44.
285. Cambra MJ, Farrus B, Moreno F, Anglada L, Arenas M, Ballester R, et al. Management of breast ductal carcinoma in situ in Catalonia, Spain: Results from the Grup Oncologic Calala-Occita-Catalonia survey with 9-year follow up. Breast. 2017;35:196-202.
286. Co M, Kwong A. Ductal carcinoma in situ of the breast - Long term results from a twenty-year cohort. Cancer Treat Res Commun. 2018;14:17-20.
287. Van Zee KJ, Subhedar P, Olcese C, Patil S, Morrow M. Relationship Between Margin Width and Recurrence of Ductal Carcinoma In Situ: Analysis of 2996 Women Treated With Breast-conserving Surgery for 30 Years. Ann Surg. 2015;262(4):623-31.
288. Surgery AoB. ASSOCIATION OF BREAST SURGERY RECOMMENDATIONS FOR THE MANAGEMENT OF RADIAL SURGICAL MARGINS IN PATIENTS UNDERGOING BREAST CONSERVING SURGERY FOR DUCTAL CARCINOMA IN SITU (DCIS)2024. Available from: https://associationofbreastsurgery.org.uk/media/3z5bk0nj/dcis-margins-guidance-2024-v2.pdf.
289. Fisher ER, Costantino J, Fisher B, Palekar AS, Redmond C, Mamounas E. Pathologic findings from the National Surgical Adjuvant Breast Project (NSABP) Protocol B-17. Intraductal carcinoma (ductal carcinoma in situ). The National Surgical Adjuvant Breast and Bowel Project Collaborating Investigators. Cancer. 1995;75(6):1310-9.
290. Chua BH, Link EK, Kunkler IH, Whelan TJ, Westenberg AH, Gruber G, et al. Radiation doses and fractionation schedules in non-low-risk ductal carcinoma in situ

in the breast (BIG 3-07/TROG 07.01): a randomised, factorial, multicentre, open-label, phase 3 study. Lancet. 2022;400(10350):431-40.
291. Moran MS, Zhao Y, Ma S, Kirova Y, Fourquet A, Chen P, et al. Association of Radiotherapy Boost for Ductal Carcinoma In Situ With Local Control After Whole-Breast Radiotherapy. JAMA Oncol. 2017;3(8):1060-8.
292. Collette S, Collette L, Budiharto T, Horiot JC, Poortmans PM, Struikmans H, et al. Predictors of the risk of fibrosis at 10 years after breast conserving therapy for early breast cancer: a study based on the EORTC Trial 22881-10882 'boost versus no boost'. Eur J Cancer. 2008;44(17):2587-99.
293. Solin LJ, Fourquet A, Vicini FA, Haffty B, Taylor M, McCormick B, et al. Mammographically detected ductal carcinoma in situ of the breast treated with breast-conserving surgery and definitive breast irradiation: long-term outcome and prognostic significance of patient age and margin status. Int J Radiat Oncol Biol Phys. 2001;50(4):991-1002.
294. Turaka A, Freedman GM, Li T, Anderson PR, Swaby R, Nicolaou N, et al. Young age is not associated with increased local recurrence for DCIS treated by breast-conserving surgery and radiation. J Surg Oncol. 2009;100(1):25-31.
295. Cleophas TZ, A. Clinical Data Analysis on a Pocket Calculator
Understanding the Scientific Methods of Statistical Reasoning and Hypothesis Testing: Springer; 2016.
296. Lowery AJ, Kell MR, Glynn RW, Kerin MJ, Sweeney KJ. Locoregional recurrence after breast cancer surgery: a systematic review by receptor phenotype. Breast Cancer Res Treat. 2012;133(3):831-41.
297. Geurts YM, Witteveen A, Bretveld R, Poortmans PM, Sonke GS, Strobbe LJA, et al. Patterns and predictors of first and subsequent recurrence in women with early breast cancer. Breast Cancer Res Treat. 2017;165(3):709-20.
298. N TC. The Early History of Spectroscopy. Journal of Chemical Education. 1991.
299. D W. Methods of Experimental Physics1976.
300. Jang Kim DW, Guang-ZhongYang. Optical spectroscopy for in vivo medical diagnosis—a review of the state of the art and future perspectives. Progress in Biomedical Engineering. 2020.
301. Nikolai T. Optical Spectroscopy - Methods and Instrumentations: Elsevier; 2006.
302. Utzinger U, Richards-Kortum RR. Fiber optic probes for biomedical optical spectroscopy. J Biomed Opt. 2003;8(1):121-47.
303. C Jones BM, A H.Thomas. Microscopy, Optical Spectroscopy, and Macroscopic Techniques. M.Walker J, editor: Humana Press; 1994.
304. Schmidt FM, Metsala,M, Apolonski, A, Cristescu, S. Breathborne Biomarkers and the Human Volatilome (Second Edition)2020. p. 221-38.
305. Yang Z, Albrow-Owen T, Cai W, Hasan T. Miniaturization of optical spectrometers. Science. 2021;371(6528).
306. Palmer C. DIFFRACTION GRATING HANDBOOK. E L, editor: Newport Corporation; 2005.
307. Welch AJ, Martin J.C. van Gemert, Star.W, Wilson, B. Definitions and Overview of Tissue Optics. Optical-Thermal Response of Laser-Irradiated Tissue. Lasersm Photonics, and Electro-Optics. p. 15 - 46.
308. Dehghani H, Pogue BW, Poplack SP, Paulsen KD. Multiwavelength three-dimensional near-infrared tomography of the breast: initial simulation, phantom, and clinical results. Appl Opt. 2003;42(1):135-45.

309. Ruiz J NF, Cho J, Zheng J, Li Y, Chen J-H, Su, M-Y, Gulsen G. Breast density quantification using structured-light-based diffuse optical tomography simulations. Appl Opt. 2017;56:7146-57.
310. Boyd NF, Lockwood GA, Martin LJ, Knight JA, Byng JW, Yaffe MJ, et al. Mammographic densities and breast cancer risk. Breast Dis. 1998;10(3-4):113-26.
311. Feng Z XG, Zhang L, Li Y, Shi W, Gao L, Lu R. Advantages of multiple field of view spectrometer. Optics and Laser Engineering. 2023;160.
312. JR L. Instrumentation for Fluorescence Spectroscopy. Springer Nature; 1999. p. 25-61.
313. Coddington I, Newbury N, Swann W. Dual-comb spectroscopy. Optica. 2016;3(4).
314. Dobson PD, Doig AJ, Blanch EW. A simple approach to normalization for spectroscopic data mining. Appl Spectrosc. 2005;59(4):542-4.
315. S PWT. Savitzky‐Golay Smoothing Filters Computers in Physics and IEEE Computational Science & Engineering 1990;4(6):669 - 72.
316. Kuhn M JK. Feature Engineering and Selection. Boca Raton2019.
317. S.B K. Emerging Artificial Intelligence Applications in Computer Engineering. Maglogiannis I KK, Wallace M, Soldatos J, editor: IOS Press; 2007.
318. Chen RC DC, Huang S, Caraka R. Selecting critical features for data classification based on machine learning methods. Journal of Big Data. 2020;7.
319. Aggarwal C. Data Classification. Data Mining: Springer; 2015.
320. Bro R KK, Smilde AK, Kiers HAL. Cross-validation of component models: A critical look at current methods. In: A B, editor. Analytical and Bioanalytical Chemistry2008. p. 1241-51.
321. Kotsiantis SB ZI, Pintelas PE. Machine learning: a review of classification and combining techniques. Artifical Intelligence Review. 2007;26:159 - 90.
322. Bentejac C CA, Martinez-Munoz G. A comparative analysis of gradient boosting algorithms. Artifical Intelligence Review. 2021;54:1937-67.
323. Deng X LQ, Deng Y, Mahadevan S. An improved method to construct basic probability
assignment based on the confusion matrix for classification
problem. Information Sciences. 2016;340-341:250-61.
324. O C. A Bayesian interpretation of the confusion matrix. Annals of Mathematics and Artifical Intelligence. 812017. p. 429 - 50.
325. Mieog JS, van der Hage JA, van de Velde CJ. Neoadjuvant chemotherapy for operable breast cancer. Br J Surg. 2007;94(10):1189-200.
326. Sahoo S, Lester SC. Pathology of breast carcinomas after neoadjuvant chemotherapy: an overview with recommendations on specimen processing and reporting. Arch Pathol Lab Med. 2009;133(4):633-42.
327. von Minckwitz G, Untch M, Blohmer JU, Costa SD, Eidtmann H, Fasching PA, et al. Definition and impact of pathologic complete response on prognosis after neoadjuvant chemotherapy in various intrinsic breast cancer subtypes. J Clin Oncol. 2012;30(15):1796-804.
328. Cortazar P, Zhang L, Untch M, Mehta K, Costantino JP, Wolmark N, et al. Pathological complete response and long-term clinical benefit in breast cancer: the CTNeoBC pooled analysis. Lancet. 2014;384(9938):164-72.
329. Kuerer HM, Newman LA, Smith TL, Ames FC, Hunt KK, Dhingra K, et al. Clinical course of breast cancer patients with complete pathologic primary tumor and axillary lymph node response to doxorubicin-based neoadjuvant chemotherapy. J Clin Oncol. 1999;17(2):460-9.

330. Boughey JC, McCall LM, Ballman KV, Mittendorf EA, Ahrendt GM, Wilke LG, et al. Tumor biology correlates with rates of breast-conserving surgery and pathologic complete response after neoadjuvant chemotherapy for breast cancer: findings from the ACOSOG Z1071 (Alliance) Prospective Multicenter Clinical Trial. Ann Surg. 2014;260(4):608-14; discussion 14-6.
331. Barroso-Sousa R M-F. Differences between invasive lobular and invasive ductal carcinoma of the breast: results and therapeutic implications. Ther Adv Med Oncol. 2016;8:261 - 6.
332. Chauhan H, Jiwa N, Nagarajan VR, Thiruchelvam P, Hogben K, Al-Mufti R, et al. Clinicopathological Predictors of Positive Resection Margins in Breast-Conserving Surgery. Ann Surg Oncol. 2024;31(6):3939-47.
333. de Boer LL, Kho E, Van de Vijver KK, Vranken Peeters M, van Duijnhoven F, Hendriks BHW, et al. Optical tissue measurements of invasive carcinoma and ductal carcinoma in situ for surgical guidance. Breast Cancer Res. 2021;23(1):59.
334. Cleator S, Parton M, Dowsett M. The biology of neoadjuvant chemotherapy for breast cancer. Endocr Relat Cancer. 2002;9(3):183-95.
335. Whitehead I, Irwin GW, Bannon F, Coles CE, Copson E, Cutress RI, et al. The NeST (Neoadjuvant systemic therapy in breast cancer) study: National Practice Questionnaire of United Kingdom multi-disciplinary decision making. BMC Cancer. 2021;21(1):90.
336. Lanka P, Bianchi L, Farina A, De Landro M, Pifferi A, Saccomandi P. Estimation of porcine pancreas optical properties in the 600-1100 nm wavelength range for light-based therapies. Sci Rep. 2022;12(1):14300.
337. Mesradi M, Genoux A, Cuplov V, Abi Haidar D, Jan S, Buvat I, et al. Experimental and analytical comparative study of optical coefficient of fresh and frozen rat tissues. J Biomed Opt. 2013;18(11):117010.
338. Palmer GM, Marshek CL, Vrotsos KM, Ramanujam N. Optimal methods for fluorescence and diffuse reflectance measurements of tissue biopsy samples. Lasers Surg Med. 2002;30(3):191-200.
339. Genina EAB, A. N; Kochubey V. I; Tuchin V.V. Effect of Storage Conditions of Skin Samples on Their Optical Characteristics. Optics and Spectroscopy in Biomedical Investigations. 2009;107(6):943-38.
340. Salomatina E, Yaroslavsky AN. Evaluation of the in vivo and ex vivo optical properties in a mouse ear model. Phys Med Biol. 2008;53(11):2797-807.
341. Roggan AS, D; Netz. U; Ritx.J-P; Germer, C_T; Muller. G. The effect of preparation technique on the optical parameters of biological tissue. Appl Phys. 1999;69:445 53.
342. Bydlon TM, Barry WT, Kennedy SA, Brown JQ, Gallagher JE, Wilke LG, et al. Advancing optical imaging for breast margin assessment: an analysis of excisional time, cautery, and patent blue dye on underlying sources of contrast. PLoS One. 2012;7(12):e51418.
343. Krawczyk B. Learning from imbalanced data: open challenges and future directions. Prog Artif Intell. 2016:221-32.
344. Mazurowski MA, Habas PA, Zurada JM, Lo JY, Baker JA, Tourassi GD. Training neural network classifiers for medical decision making: the effects of imbalanced datasets on classification performance. Neural Netw. 2008;21(2-3):427-36.
345. Victoria López AF, Salvador García, Vasile Palade, Francisco Herrera An insight into classification with imbalanced data: Empirical results and current trends on using data intrinsic characteristics. Information Sciences. 2013;250:113-41.

346. Blanks RG, Moss SM, McGahan CE, Quinn MJ, Babb PJ. Effect of NHS breast screening programme on mortality from breast cancer in England and Wales, 1990-8: comparison of observed with predicted mortality. BMJ. 2000;321(7262):665-9.
347. Perry NM, Party EW. Quality assurance in the diagnosis of breast disease. EUSOMA Working Party. Eur J Cancer. 2001;37(2):159-72.
348. Britton P, Sinnatamby R. Investigation of suspected breast cancer. BMJ. 2007;335(7615):347-8.
349. Heywang-Kobrunner SH, Schaumloffel U, Viehweg P, Hofer H, Buchmann J, Lampe D. Minimally invasive stereotaxic vacuum core breast biopsy. Eur Radiol. 1998;8(3):377-85.
350. Caplan L. Delay in breast cancer: implications for stage at diagnosis and survival. Front Public Health. 2014;2:87.
351. Hughson AV, Cooper AF, McArdle CS, Smith DC. Psychosocial morbidity in patients awaiting breast biopsy. J Psychosom Res. 1988;32(2):173-80.
352. Fallowfield L, Ratcliffe D, Jenkins V, Saul J. Psychiatric morbidity and its recognition by doctors in patients with cancer. Br J Cancer. 2001;84(8):1011-5.
353. Fallowfield LH, A; Maguire, P; Baum M; A'Hern RP. Psychological effects of being offered choice of surgery for breast cancer. BMJ. 1994;309:448.
354. Bouget D, Allan M, Stoyanov D, Jannin P. Vision-based and marker-less surgical tool detection and tracking: a review of the literature. Med Image Anal. 2017;35:633-54.
355. Gkouzionis I, Nazarian S, Kawka M, Darzi A, Patel N, Peters CJ, et al. Real-time tracking of a diffuse reflectance spectroscopy probe used to aid histological validation of margin assessment in upper gastrointestinal cancer resection surgery. J Biomed Opt. 2022;27(2).
356. Pinder SE, Shaaban A, Deb R, Desai A, Gandhi A, Lee AHS, et al. NHS Breast Screening multidisciplinary working group guidelines for the diagnosis and management of breast lesions of uncertain malignant potential on core biopsy (B3 lesions). Clin Radiol. 2018;73(8):682-92.
357. R.A.Schowengerdt. Reconstrcution of Multispatial, Multispectral Image Data Using Spatial Frequency Content. Photogrammetric Engineering and Remote Sensing. 1980;46:1325-34.
358. Ustin SL, Middleton EM. Current and near-term advances in Earth observation for ecological applications. Ecol Process. 2021;10(1):1.
359. Candiago S RF, Giglio Michaela, Dubbini M, Gattelli M. Evaluating Multispectral Images and Vegetation Indices for Precision Farming Applications from UAV Images. Remote Sensing. 2015;7(4):4026-47.
360. Wuest B ZY. Region based segmentation of QuickBird multispectral imagery through band ratios and fuzzy comparison. ISPRS Journal of Photogrammetry and Remote Sensing. 2009;64(1):55-64.
361. Dash J PG, Watt M. UAV Multispectral Imagery Can Complement Satellite Data for Monitoring Forest Health. Remote Sensing. 2018;10(8).
362. F S. Remote sensing for mineral exploration. Ore Geology Reviews. 1999;14(3-4):157-83.
363. ElMasry G, Mandour N, Al-Rejaie S, Belin E, Rousseau D. Recent Applications of Multispectral Imaging in Seed Phenotyping and Quality Monitoring-An Overview. Sensors (Basel). 2019;19(5).
364. Ortega S, Halicek M, Fabelo H, Callico GM, Fei B. Hyperspectral and multispectral imaging in digital and computational pathology: a systematic review [Invited]. Biomed Opt Express. 2020;11(6):3195-233.

365. Ilisanu MA, Moldoveanu F, Moldoveanu A. Multispectral Imaging for Skin Diseases Assessment-State of the Art and Perspectives. Sensors (Basel). 2023;23(8).
366. Eisenbeiss W, Marotz J, Schrade JP. Reflection-optical multispectral imaging method for objective determination of burn depth. Burns. 1999;25(8):697-704.
367. Joshi BP, Miller SJ, Lee CM, Seibel EJ, Wang TD. Multispectral endoscopic imaging of colorectal dysplasia in vivo. Gastroenterology. 2012;143(6):1435-7.
368. Clancy NT, Stoyanov D, James DR, Di Marco A, Sauvage V, Clark J, et al. Multispectral image alignment using a three channel endoscope in vivo during minimally invasive surgery. Biomed Opt Express. 2012;3(10):2567-78.
369. Ma F, Yuan M, Kozak I. Multispectral imaging: Review of current applications. Surv Ophthalmol. 2023;68(5):889-904.
370. Ma F, Yuan M, Kozak I, Zhang Q, Chen Y. Sensitivity and Specificity of Multispectral Imaging for Polypoidal Choroidal Vasculopathy. Retina. 2021;41(9):1921-9.
371. Andersen AH, Zhang Z, Avison MJ, Gash DM. Automated segmentation of multispectral brain MR images. J Neurosci Methods. 2002;122(1):13-23.
372. Anichini G, Leiloglou M, Hu Z, O'Neill K, Daniel E. Hyperspectral and multispectral imaging in neurosurgery: a systematic literature review and meta-analysis. Eur J Surg Oncol. 2024:108293.
373. van Veen RL, Sterenborg HJ, Pifferi A, Torricelli A, Chikoidze E, Cubeddu R. Determination of visible near-IR absorption coefficients of mammalian fat using time- and spatially resolved diffuse reflectance and transmission spectroscopy. J Biomed Opt. 2005;10(5):054004.
374. Prahl S. Optical Absorption of Hemoglobin [Available from: https://omlc.org/spectra/hemoglobin/.
375. Coatings S. SpectroCam multispectral wheel cameras [Available from: https://salvocoatings.com/products/spectrocam/.
376. S Stolik JD, A Perez, L Anasagasti. Measurement of the penetration depths of red and near infrared light in human “ex vivo” tissues. Journal of Photochemistry and Photobiology B: Biology. 2000;57(2-3):90-3.
377. Amigo JM, Babamoradi H, Elcoroaristizabal S. Hyperspectral image analysis. A tutorial. Anal Chim Acta. 2015;896:34-51.
378. RInnan A BF, Engelsen S. Review of the most common pre-processing techniques for near-infrared spectra. Trends in Analytical Chemistry. 2009;28.
379. Aref MH, Aboughaleb IH, El-Sharkawy YH. Custom optical imaging system for ex-vivo breast cancer detection based on spectral signature. Surg Oncol. 2020;35:547-55.
380. Lu G, Wang D, Qin X, Halig L, Muller S, Zhang H, et al. Framework for hyperspectral image processing and quantification for cancer detection during animal tumor surgery. J Biomed Opt. 2015;20(12):126012.
381. Y Li WX, H Li. Hyperspectral image reconstruction by deep convolutional neural network for classification. Pattern Recognition 2017;63:371-83.
382. Cao FY, Z; Ren J; Jiang M; Ling WK. Does Normalization Methods Play a Role for Hyperspectral Image Classification?2017. Available from: https://arxiv.org/abs/1710.02939.
383. L. Sun ZW, J. Liu, L. Xiao and Z. Wei. Supervised Spectral–Spatial Hyperspectral Image Classification With Weighted Markov Random Fields. IEEE Transactions on Geoscience and Remote Sensing. 2015;53:1490 - 503.
384. Aksoy SH, RM. Feature normalization and likelihood-based similarity measures for image retrieval. Pattern Recognition Letters. 2001;22(5):563-82.

385. Feature normalization (scaling) for Hyperspectral images: Geographic Information Systems; [Available from: https://gis.stackexchange.com/questions/310359/feature-normalization-scaling-for-hyperspectral-images.
386. M M. Logistic regression in data analysis: an overview2011:[281 - 99 pp.].
387. MathWorks. Create generalized linear regression model 2021 [Available from: Create generalized linear regression model-MATLAB fitglm. .
388. A G. Introduction to Machine Learning course, 3rd lecture notes. Department of Electrical and Electronic Engineering, Imperial College London; 2018.
389. Fawcett T. ROC Graphs: Notes and Practical Considerations for Data Mining Researchers. Intelligent Enterprise Technologies Laboratory: HP Laboratories Palo Alto; 2003.
390. W N. What is a support vector machine? Nature Biotechnology. 2006;24:1565 - 7.
391. Cervantes J G-LF, Rodriguez-Mazahua L, Lopez A. A comprehensive survey on support vector machine classification: Applications, challenges and trends. Neurocomputing. 202;408:189-215.
392. Rana ARABABH. Application of Multi Layer (Perceptron) Artificial Neural Network in the Diagnosis System: A Systematic Review: IEEE Xplore; 2018 [
393. Yan H JY, Zheng J, Peng C, Li Q. A multilayer perceptron-based medical decision support system for heart disease diagnosis. Expert systems with Applications 2006;30:272-81.
394. Fabian Pedregosa GV, Alexandre Gramfort, Vincent Michel, Bertrand Thirion, Olivier Grisel, Mathieu Blondel, Peter Prettenhofer, Ron Weiss, Vincent Dubourg, Jake Vanderplas, Alexandre Passos, David Cournapeau, Matthieu Brucher, Matthieu Perrot, Édouard Duchesnay. Scikit-learn: Machine Learning in Python. Scikit-learn: Machine Learning in Python. 2011;12:2825 - 30.
395. Chen TG, C., editor XGBoost: A Scalable Tree Boosting System. 22nd ACM SIGKDD International Conference on Knowledge Discovery and Data Mining 2016; San Francisco California USA: Association for Computing MachineryNew YorkNYUnited States.
396. Vaisgh M YS, Papazoglou A, Liatsos A, Ranjibar K, Bleicher R, Williams A, Pico C, Pierotti M, Michaelson J, editor The role of micro-CT for intraoperative margin assessment of breast cancer. ASCO Annual Meeting; 2023: Journal of Clinical Oncology.
397. Hagen NK, MW. Review of snapshot spectral imaging technologies. Optical Engineering. 2013;52.
398. L. van Manen JE, O. Dzyubachyk, A. Fariña- Sarasqueta, A. Vahrmeijer, et al., editor Snapshot hyperspectral imaging for detection of breast tumors in resected specimens. SPIE; 2019; San Francisco, California, United States: spiedigitallibrary.
399. Gentilini OD, Botteri E, Sangalli C, Galimberti V, Porpiglia M, Agresti R, et al. Sentinel Lymph Node Biopsy vs No Axillary Surgery in Patients With Small Breast Cancer and Negative Results on Ultrasonography of Axillary Lymph Nodes: The SOUND Randomized Clinical Trial. JAMA Oncol. 2023;9(11):1557-64.
400. Zaidi M, Khan S, Farooqi NB, Abbas K, Idrees R. Effect of formalin fixation on surgical margins in breast cancer surgical specimen. Int J Breast Cancer. 2014;2014:121838.
401. Kaur H, Pannu H, Malhi A. A Systematic Review on Imbalanced Data Challenges
in Machine Learning: Applications and Solutions. ACM Comuting Surveys. 2019;52.

402. Chawla N, Japkowicz N, Kotcz A. Editorial: special issue on learning from imbalanced data sets2004; 6(1):[1-6 pp.].
403. Olson MT, Ly QP, Mohs AM. Fluorescence Guidance in Surgical Oncology: Challenges, Opportunities, and Translation. Mol Imaging Biol. 2019;21(2):200-18.
404. Nagaya T, Nakamura YA, Choyke PL, Kobayashi H. Fluorescence-Guided Surgery. Front Oncol. 2017;7:314.
405. Mieog JSD, Achterberg FB, Zlitni A, Hutteman M, Burggraaf J, Swijnenburg RJ, et al. Fundamentals and developments in fluorescence-guided cancer surgery. Nat Rev Clin Oncol. 2022;19(1):9-22.
406. Gioux S, Choi HS, Frangioni JV. Image-guided surgery using invisible near-infrared light: fundamentals of clinical translation. Mol Imaging. 2010;9(5):237-55.
407. Zhang RR, Schroeder AB, Grudzinski JJ, Rosenthal EL, Warram JM, Pinchuk AN, et al. Beyond the margins: real-time detection of cancer using targeted fluorophores. Nat Rev Clin Oncol. 2017;14(6):347-64.
408. Frangioni JV. In vivo near-infrared fluorescence imaging. Curr Opin Chem Biol. 2003;7(5):626-34.
409. Chance B, Cohen P, Jobsis F, Schoener B. Intracellular oxidation-reduction states in vivo. Science. 1962;137(3529):499-508.
410. Iyer AK, Khaled G, Fang J, Maeda H. Exploiting the enhanced permeability and retention effect for tumor targeting. Drug Discov Today. 2006;11(17-18):812-8.
411. Cwalinski T, Polom W, Marano L, Roviello G, D'Angelo A, Cwalina N, et al. Methylene Blue-Current Knowledge, Fluorescent Properties, and Its Future Use. J Clin Med. 2020;9(11).
412. Schaafsma B MJ, Hutteman M, Vorst J, Kuppen P, Lowik C, Frangioni J, Velde C, Vahrmeijer A. The clinical use of indocyanine green as a near-infrared fluorescent contrast agent for image-guided oncologic surgery. J Surg Oncol. 2011:323-32.
413. Stummer W, Pichlmeier U, Meinel T, Wiestler OD, Zanella F, Reulen HJ, et al. Fluorescence-guided surgery with 5-aminolevulinic acid for resection of malignant glioma: a randomised controlled multicentre phase III trial. Lancet Oncol. 2006;7(5):392-401.
414. Wang C, Wang Z, Zhao T, Li Y, Huang G, Sumer BD, et al. Optical molecular imaging for tumor detection and image-guided surgery. Biomaterials. 2018;157:62-75.
415. Acerbi F, Cavallo C, Broggi M, Cordella R, Anghileri E, Eoli M, et al. Fluorescein-guided surgery for malignant gliomas: a review. Neurosurg Rev. 2014;37(4):547-57.
416. Alander JT, Kaartinen I, Laakso A, Patila T, Spillmann T, Tuchin VV, et al. A review of indocyanine green fluorescent imaging in surgery. Int J Biomed Imaging. 2012;2012:940585.
417. Stepp H, Stummer W. 5-ALA in the management of malignant glioma. Lasers Surg Med. 2018;50(5):399-419.
418. Gu L YX, Zhong H, Mei K, Wang D. A new technique of quantifying protoporphyrin IX in microbial cells in seawater. Frontiers in Marine Science. 2022;9.
419. Rollakanti KR, Kanick SC, Davis SC, Pogue BW, Maytin EV. Techniques for fluorescence detection of protoporphyrin IX in skin cancers associated with photodynamic therapy. Photonics Lasers Med. 2013;2(4):287-303.
420. Ladner D SR, Allemann J, Halller U, Walt H. Photodynamic diagnosis of breast tumors after oral application of aminolevulinic acid. Br J Cancer. 2001;84.
421. Millon SR, Ostrander JH, Yazdanfar S, Brown JQ, Bender JE, Rajeha A, et al. Preferential accumulation of 5-aminolevulinic acid-induced protoporphyrin IX in breast

cancer: a comprehensive study on six breast cell lines with varying phenotypes. J Biomed Opt. 2010;15(1):018002.
422. Casas A. Clinical uses of 5-aminolaevulinic acid in photodynamic treatment and photodetection of cancer: A review. Cancer Lett. 2020;490:165-73.
423. Yang X, Li W, Palasuberniam P, Myers KA, Wang C, Chen B. Effects of Silencing Heme Biosynthesis Enzymes on 5-Aminolevulinic Acid-mediated Protoporphyrin IX Fluorescence and Photodynamic Therapy. Photochem Photobiol. 2015;91(4):923-30.
424. Palasuberniam P, Yang X, Kraus D, Jones P, Myers KA, Chen B. ABCG2 transporter inhibitor restores the sensitivity of triple negative breast cancer cells to aminolevulinic acid-mediated photodynamic therapy. Sci Rep. 2015;5:13298.
425. Compendeum EM. Gliolan 30mg/ml powder for oral solution [Available from: https://www.medicines.org.uk/emc/product/4638/smpc.
426. Agency EM. Summary of Product Characteristics - Gliolan: European Medicines Agency (EMA); [Available from: https://www.ema.europa.eu/en/documents/product-information/gliolan-epar-product-information_en.pdf.
427. Leiloglou M, Kedrzycki MS, Chalau V, Chiarini N, Thiruchelvam PTR, Hadjiminas DJ, et al. Indocyanine green fluorescence image processing techniques for breast cancer macroscopic demarcation. Sci Rep. 2022;12(1):8607.
428. Kedrzycki MS, Leiloglou M, Chalau V, Chiarini N, Thiruchelvam PTR, Hadjiminas DJ, et al. The Impact of Temporal Variation in Indocyanine Green Administration on Tumor Identification During Fluorescence Guided Breast Surgery. Ann Surg Oncol. 2021;28(10):5617-25.
429. Kedrzycki M. The Use of Fluorophores for Intraoperative Tumour Detection in Breast Cancer: Imperial College London; 2023.
430. Jansen BAM, Bargon CA, Huibers AE, Postma EL, Young-Afat DA, Verkooijen HM, et al. Efficacy of indocyanine green fluorescence for the identification of non-palpable breast tumours: systematic review. BJS Open. 2023;7(5).
431. Honorato-Cia CM-S, A; Cacho-Asenjo, E; Guillen-Grima, F; Tejada-Solis, S; Diez-Valle, R. Safety Profile of 5-Aminolevulinic Acid as a Surgical Adjunct in Clinical Practice.A Review of 207 Cases From 2008 to 2013. Journal of Neurosurgical Anesthesiology. 2015;27:304-9.
432. Nguyen CL, Zhou M, Easwaralingam N, Seah JL, Azimi F, Mak C, et al. Novel Dual Tracer Indocyanine Green and Radioisotope Versus Gold Standard Sentinel Lymph Node Biopsy in Breast Cancer: The GREENORBLUE Trial. Ann Surg Oncol. 2023;30(11):6520-7.
433. Demchenko AP. Photobleaching of organic fluorophores: quantitative characterization, mechanisms, protection. Methods Appl Fluoresc. 2020;8(2):022001.
434. Croce AC, Bottiroli G. Autofluorescence spectroscopy and imaging: a tool for biomedical research and diagnosis. Eur J Histochem. 2014;58(4):2461.
435. Darzi A. Investigation of the National Health Service in England. In: Health Do, editor. 2024.
436. Gatenbee CD, Baker AM, Prabhakaran S, Swinyard O, Slebos RJC, Mandal G, et al. Virtual alignment of pathology image series for multi-gigapixel whole slide images. Nat Commun. 2023;14(1):4502.

Chapter 9: Appendices

Appendix A

A1. Search Strategy used for Systematic Review. Medline, Embase and Scopus databases were used.

SCOPUS
"diffuse optical spectroscopy imaging"
"diffuse reflection spectroscopy"
"diffuse reflectance spectroscopy"
"diffuse optical spectroscopic imaging"
"multi-spectral imaging"
"multispectral imaging"
"hyperspectral imaging"
"hyper-spectral imaging"
"optical imaging"
"spatial frequency domain imaging"
multispectral W/2 imaging
hyperspectral W/2 imaging
hyperspectral W/2 imag*
multispectral W/2 imag*
AND
"breast cancer"
breast tumo?r
"breast carcinoma"
"breast neoplasm"
breast W/2 cancer
"lumpectomy"
breast AND lesion*
"breast W/2 surg*"
"breast W/1 operation

MEDLINE
Breast cancer.mp or exp Breast Neoplasms/
Breast tumo?r.mp
Breast adj2 carcinoma.mp
Breast lesion*.mp
Lumpectomy.mp or exp Mastectomy, segmental/
Breast adj2 surgery
Breast adj2 operation
AND
Optical imaging.mp or exp Optical Imaging/
Multispectral adj2 imaging
Hyperspectral adj3 imag*
Exp Hyperspectral Imaging/
Diffuse optical spectroscopy imaging.mp
Diffuse optical spectroscopic imaging.mp
Diffuse reflectance spectroscopy.mp
Diffuse reflection spectroscopy.mp
Spatial frequency domain imaging.mp

EMBASE
Breast cancer.mp or exp breast cancer/

Exp breast tumor/ or breast neoplasm*.mp
Breast tumo?r.mp
Breast adj2 carcinoma.mp
Exp breast lesion/ or breast lesion*.mp
Lumpectomy.mp or exp lumpectomy/
Breast adj2 surgery.mp
Breast adj2 operation.mp
AND
Optical imaging.mp
Multispectral adj2 imag*
Hyperspectral adj3 imag*
Diffuse optical spectroscopy imaging.mp
Diffuse optical spectroscopic imaging.mp
Diffuse reflectance spectroscopy.mp or exp diffuse reflectance spectroscopy/
Diffuse reflection spectroscopy.mp
Spatial frequency domain imaging.mp

Figure A2. Forest plots for pooled sensitivity and specificity applied to the subdivisions within probe based studies. Forest plots for pooled sensitivity (left) and specificity (right) where a fixed-model analysis was applied to the DRS studies only (top) and to the DRS with IFS studies only (bottom).

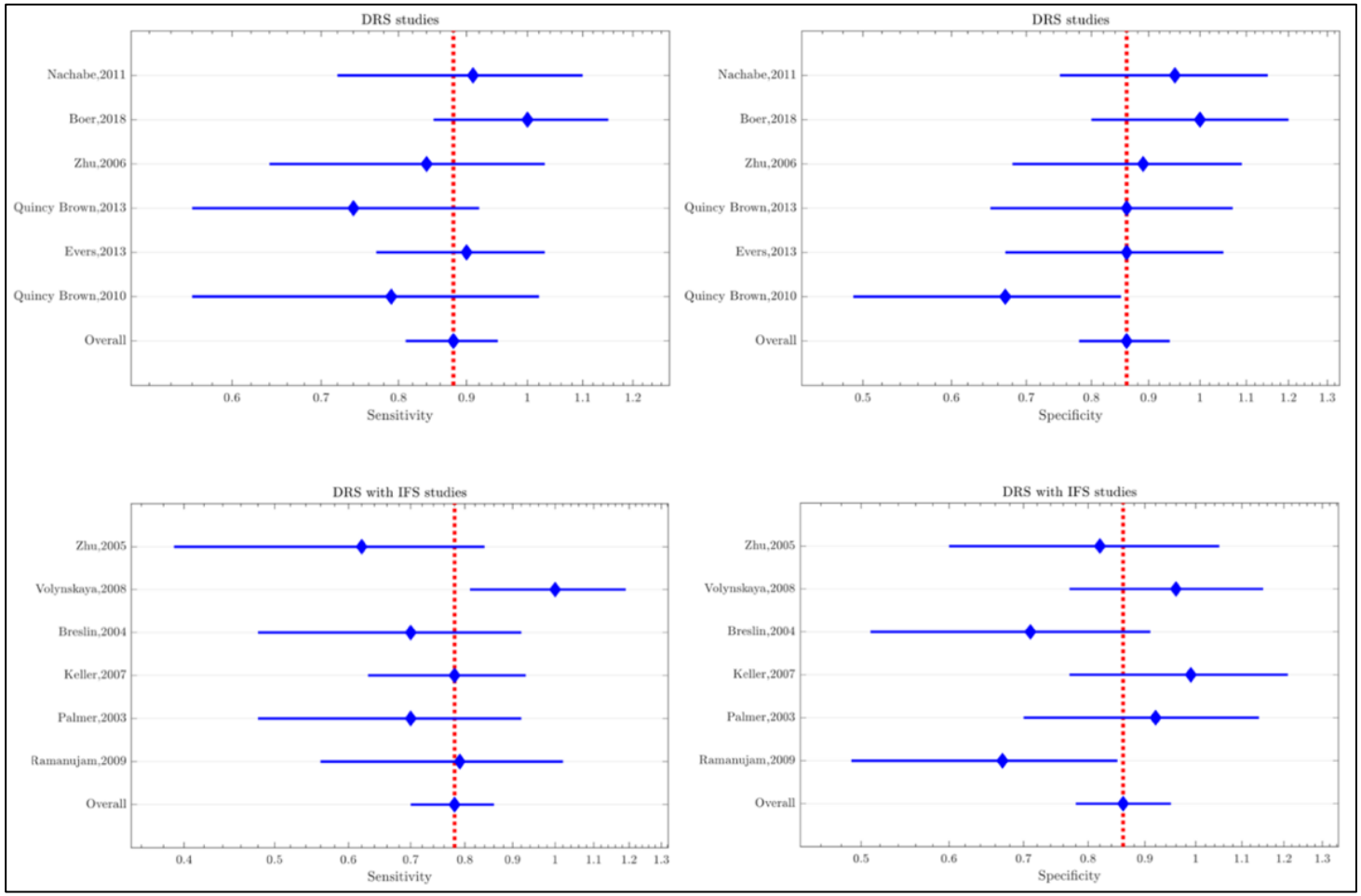


Figure A3 Forest plots for pooled sensitivity and specificity applied to the subdivisions within image based studies. Forest plots for pooled sensitivity (left) and specificity (right) where a fixed model analysis was applied to the HSI studies only (top) and to the SFDI studies only (bottom).

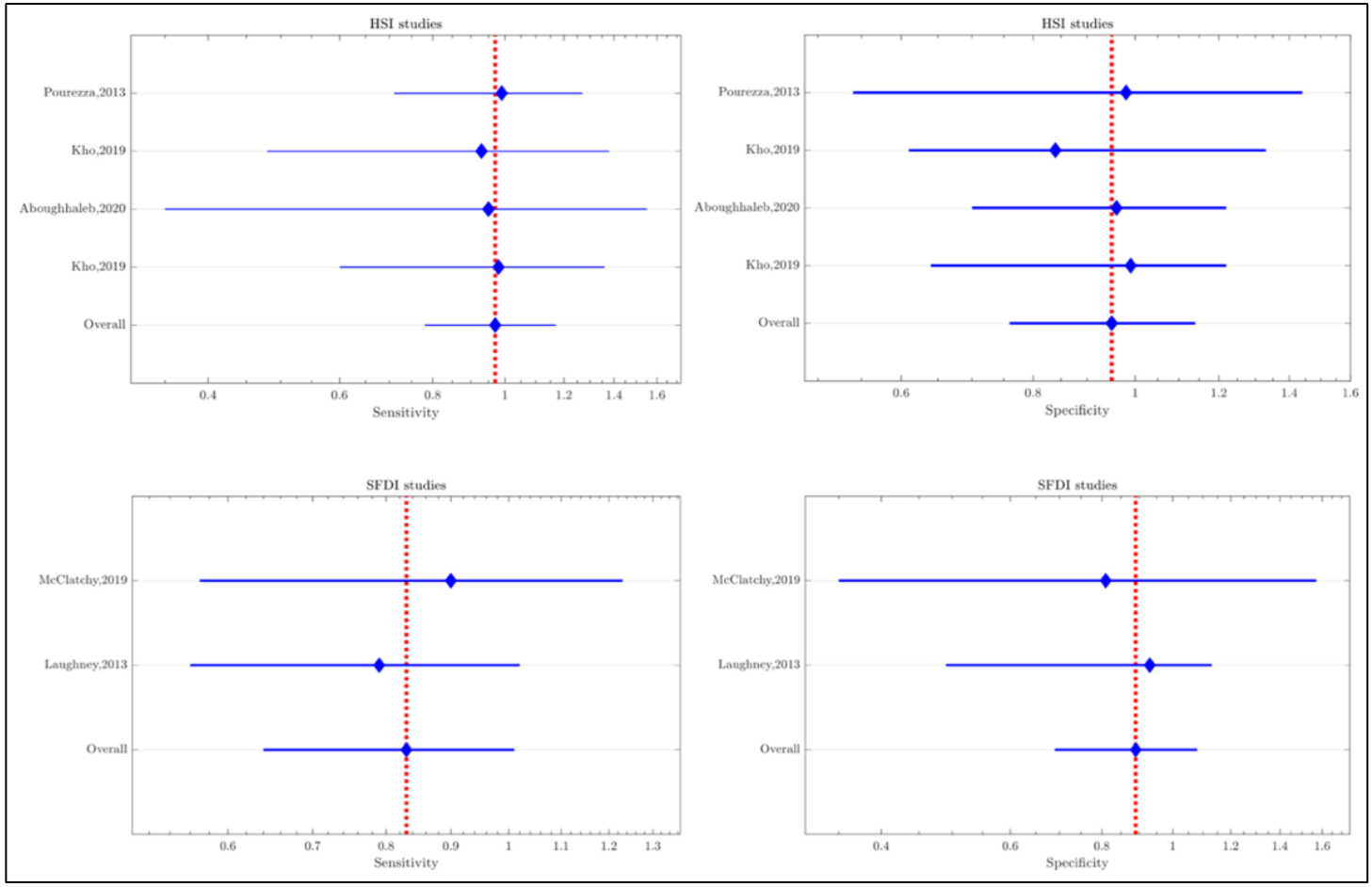


Table A4. Comparison of pooled sensitivity/specificity results with the use of the Q-statistic. P-values are less than 0.05 showing that the differences are not statistically significant at 5% significance level.

Pooled Sensitivity Comparisons		
Studies being compared	**Q statistic (p-value) fixed-model**	**Q statistic (p-value) random-model**
Probe-based vs image-based	0.64 (0.42)	1.85 (0.17)
DRS vs DRS with IFS	3.66 (0.06)	3.22 (0.07)
HSI vs SFDI	1.16(0.28)	1.16 (0.28)
Pooled Specificity Comparisons		
Studies being compared	**Q statistic (p-value) fixed-model**	**Q statistic (p-value) random-model**
Probe-based vs image-based	0.86 (0.35)	0.75 (0.39)
DRS vs DRS with IFS	10^{-6} (~1)	0.01 (0.91)
HSI vs SFDI	0.24(0.63)	0.24(0.63)

Table A5. Various Image Processing Techniques Used in Studies

Study	Feature extraction method used	Classification Method
de Boer[170]	Diffusion theory model to extract quantitative clinical & physical parameters	Fat to water content ratio (F/W) value threshold: F/W=1.
Zhu[162]	Inverse Monte Carlo model to extract quantitative optical parameters or partial least squares (PLS) to extract principal components in the measured DRS.	Wilcoxon rank-sum test for feature selection and support vector machine (SVM) for classification.
Brown[161]	Inverse Monte Carlo model to extract 5 quantitative physical parameters and 3 image descriptive variables (optimum threshold, median, Kolmogorov-Smirnov statistic) for each of the extracted physical parameters.	Conditional inference tree (CIT) model for feature selection and classification.
Evers[171]	Diffusion theory model.	CART algorithm.
Brown[136]	Inverse Monte Carlo model to extract β-carotene and total haemoglobin values.	Receiver Operator Characteristic (ROC) analysis & Youden index to identify β-carotene and total haemoglobin threshold values. Decision tree-based two parameter model for classification.
Volynskaya[147]	Principal Component Analysis (PCA) on the DRS and IFS spectra for principal components.	Wilcoxon rank-sum test for principal components selection and support vector machine (SVM) for classification.
Keller[166]	Diffusion theory model to extract scattering, oxyhaemoglobin, β-carotene parameters. IFS with multivariate curve resolution (MCR) to extract NADH and collagen-like parameters.	3-step binary classification algorithm using logistic regression.
Palmer[164]	Principal component analysis on the DRS and IFS spectra for principal components.	Wilcoxon rank-sum test for principal components selection and support vector machine (SVM) for classification
Ramanujam[165]	Maximum representation and discrimination feature (MRDF)	Sparse multinomial logistic regression (SMLR)
Keller[176]	Principal component analysis on the DRS and IFS spectra for principal components.	Wilcoxon rank-sum test for principal components selection and support vector machine (SVM) for classification
Nachabe[169]	Inverse Monte Carlo model to extract β-carotene and total haemoglobin values.	Wilcoxon rank-sum test for parameter selection. Decision tree-based two parameter model for classification.

Pourezza-Shahri	Fourier coefficient selection features (FCS) for feature extraction.	Minimum Redundancy Maximum Relevance (MRMR) method for feature selection. SVM with Radial Basis Function (RBF) kernel for classification.
Kho[173]	Processed spectral band values were used as features.	Linear, weighted support vector machine (SVM).
Aboughhaleb[168]	-	Contour Mapping with the K-means image clustering up to 8-clusters with variable threshold value from 0.2 up to 0.9 and statistical analysis to identify best threshold.
Kho[172]	Fisher's linear discriminant analysis (LDA) for feature extraction.	1) Pairwise coupling for classification for the LDA-derived features. 2) U-Net for image segmentation/ classification based on spatial-spectral image features.
McClatchy[174]	Minimization of sum of squares residual error between measured and diffusion theory model simulated reflectance to extract optical properties.	Fitted curves between histological fractions and each scattering parameter for optical properties selection. Use of optical properties to extract adipose volume fraction and epithelium to stroma ratio values for classification.
Laughney[175]	Minimization of sum of squares residual error between measured and Monte Carlo simulated modulation amplitude to extract optical parameters.	K-dimensional decision tree-based model for classification of a parameter set based on the known classification of the k nearest neighbours (from training set).

Appendix B

B1.

Search Strategy for Chapter 3: Systematic review and Meta-Analysis regarding the impact of margin width on local recurrence in both DCIS and invasive breast cancer (This search strategy was review by the Royal College of Surgeons library service)

MEDLINE

1 exp Breast Neoplasms/

2 ((cancer* or tumo?r * or carcinoma* or neoplasm*) adj3 (breast* or lobular or ductal)).ti,ab,kw,kf.

3 1 or 2

4 exp Neoplasm Recurrence, Local/

5 ((cancer* or tumo?r* or carcinoma* or neoplasm*) adj3 (relaps* or recur*)).ti,ab,kw,kf.

6 "Margins of Excision"/

7 (margin* adj3 (excision* or surgical or positive or negative or close or wide or distance)).ti,ab,kw,kf.

8 4 or 5 189662

9 6 or 7 31220

10 3 and 8 and 9

11 limit 10 to english language

Embase

1 exp breast cancer/ or breast tumor/

2 ((cancer* or tumo?r * or carcinoma* or neoplasm*) adj3 (breast* or lobular or ductal)).ti,ab,kw,kf.

3 1 or 2

4 cancer recurrence/ or tumor recurrence/

5 ((cancer* or tumo?r* or carcinoma* or neoplasm*) adj3 (relaps* or recur*)).ti,ab,kw,kf.

6 surgical margin/

7 (margin* adj3 (excision* or surgical or positive or negative or close or wide or distance)).ti,ab,kw,kf.

8 4 or 5

9 6 or 7

10 3 and 8 and 9

11 limit 10 to english language

B2.

Names and positions of reviewers involved in reviewing full papers:

Mr Michael Boland (Consultant Oncoplastic Breast Surgeon, Imperial College London)

Miss Meera Joshi (Consultant Oncoplastic Breast Surgeon, Imperial College London)

Mr Ronak Patel (Surgical Registrar, Imperial College London)

Mr Ravi Naik (Surgical Registrar, Imperial College London)

Miss Yasmin Grant (Clinical Research Fellow, Imperial College London)

Dr Josephine Holt (GP trainee, Royal Free NHS Trust)

Dr Saur Hajev (Surgical trainee, Imperial College London)

Dr Hussein Elghazaly (Surgical trainee, Imperial College London)

B3.

Table depicting overall bias grade given to each individual study for both DCIS and invasive papers

Study	Overall bias grade
Atzori et al. 2022	Serious
Behm et al. 2013	Low
Ben-David et al. 2007	Moderate
Bhatti et al. 2014	Serious
Biglia et al. 2014	Moderate
Bodilsen et al. 2016	Low
Bouvet et al. 1997	Moderate

Study	Overall bias grade
Livingsston-Rosanoff et al. 2021	Low
Lupe et al. 2011	Moderate
Maishman et al. 2017	Low
Mannu et al. 2020	Low
McBain et al 2003	Low
McIntosh et al. 2007	Moderate
Meatinni et al. 2013	Low

Braunstein et al. 2016	Moderate
Chasle et al. 2003	Serious
Choi et al. 2018	Moderate
Clement et al. 2018	Critical
Cutuli et al. 2001	Low
DiBiase et al. 2002	Moderate
Dick et al. 2001	Critical
Dixon et al. 2016	Moderate
Ekatah et al. 2018	Moderate
Fisher et al. 1999	Low
Francis et al. 1999	Serious
Freedman et al. 1999	Serious
Goldstein et al. 2003	Moderate
Groot et al. 2011	Low
Hennigs et al. 2016	Moderate
Hennigs et al. 2016	Moderate
Jobsen et al. 2010	Moderate
Jobsen et al. 2018	Moderate
Jobsen et al.2014	Moderate
Kahlert et al. 2018	Low
Karasawa et al. 2005	Moderate
Kreike et al. 2008	Moderate
Kunos et al. 2006	Low
Kuru et al. 2020	Low
Leong et al. 2004	Moderate
Lin et al. 2020	Low
Livi 2013	Low
Neuschtaz et al. 2003	Moderate
Peterson et al.1999	Serious
Pilewskie et al 2014	Serious
Rouzier et al. 2001	Low
Rudolff et al. 2010	Low
Sadek et al. 2015	Moderate
Schnitt et al. 1994	Moderate
Scmitz et al.2023	Moderate
Shaikh et al. 2016	Moderate
Smitt et al. 2003	Moderate
Solin et al. 1991	Moderate
Solin et al. 2005	Moderate
Swelden et al. 2014	Moderate
Tang et al. 2019	Moderate
Thompson et al. 2018	Low
Turaka et al. 2009	Moderate
Tyler et al. 2018	Low
VanZee et al.2015	Low
Vicini et al. 2001	Serious
Voogd 2001	Low
Vos et al. 2017	Low
Wang et al. 2023	Low
Yoon et al.2018	Low

Appendix C

Area under the curve (AUC) of combining different channels with Extreme gradient boost classifier (XBG) – ALL tissue samples

Type of Exp	D8	D28	f3	f4	D8_f3	D8_f4	D28_f3	D28_f4	D8_28_f3	D8_28_f4	D8_f3_4	D28_f3_4	D8_28_f3_4
Healthy vs IDC	74.85%	71.90%	70.16%	61.50%	75.62%	75.72%	73.14%	71.18%	76.70%	74.75%	76.10%	71.66%	76.27%
Healthy vs ILC	80.68%	84.36%	73.06%	74.05%	79.72%	79.51%	82.90%	83.87%	82.30%	81.78%	78.01%	81.67%	82.11%
Healthy vs DCIS	91.21%	83.98%	77.39%	80.09%	88.03%	89.68%	84.11%	84.79%	87.68%	88.14%	89.97%	84.47%	87.94%
Healthy vs PCR	78.02%	60.95%	53.76%	50.37%	82.49%	79.68%	63.95%	54.67%	82.29%	74.93%	81.18%	55.77%	82.73%
Healthy vs IDC+ILC	77.30%	77.64%	71.63%	67.67%	76.00%	77.40%	76.94%	76.14%	80.59%	79.79%	77.74%	78.68%	79.63%
Healthy vs IDC+ILC+DCIS	79.95%	79.74%	71.75%	69.72%	78.93%	81.67%	78.53%	78.13%	81.01%	81.44%	81.21%	78.33%	80.95%
Mean AUC - All exps	80.33%	76.43%	69.62%	67.23%	80.13%	80.61%	76.59%	74.80%	81.76%	80.14%	80.70%	75.10%	81.61%

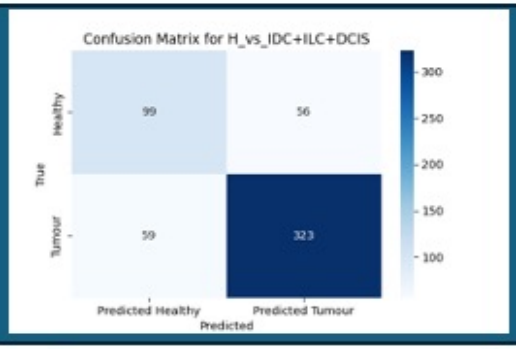
Area under the curve (AUC) of combining different channels with Extreme gradient boost classifier (XBG) – Quality 3 tissue samples

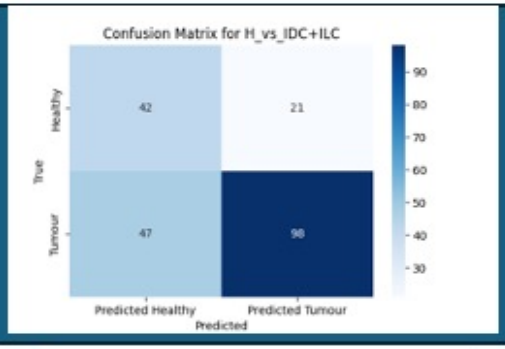
Type of Exp	D8	D28	f3	f4	D8_f3	D8_f4	D28_f3	D28_f4	D8_28_f3	D8_28_f4	D8_f3_4	D28_f3_4	D8_28_f3_4
Healthy vs IDC	69.59%	73.24%	67.31%	59.52%	69.95%	70.06%	74.27%	75.43%	74.50%	77.41%	71.08%	77.52%	77.35%
Healthy vs ILC	80.94%	90.86%	74.83%	76.22%	80.89%	83.94%	88.48%	86.05%	86.99%	86.53%	83.68%	85.98%	83.84%
Healthy vs DCIS	81.53%	77.07%	80.49%	76.20%	82.42%	86.78%	77.35%	77.44%	82.85%	84.29%	88.83%	74.94%	85.73%

Healthy vs PCR	89.41%	55.45%	58.20%	54.00%	88.68%	92.18%	61.46%	61.84%	84.32%	87.32%	86.98%	56.99%	84.67%
Healthy vs IDC+ILC	77.12%	80.18%	70.51%	68.56%	77.51%	77.61%	82.57%	80.13%	82.94%	82.42%	78.01%	78.02%	82.81%
Healthy vs IDC+ILC+DCIS	77.08%	79.33%	72.02%	67.18%	75.99%	78.96%	80.16%	80.27%	81.33%	82.93%	79.21%	79.37%	83.93%
Mean AUC - All exps	79.28%	76.02%	70.56%	66.95%	79.24%	81.59%	77.38%	76.86%	82.15%	83.48%	81.30%	75.47%	83.06%

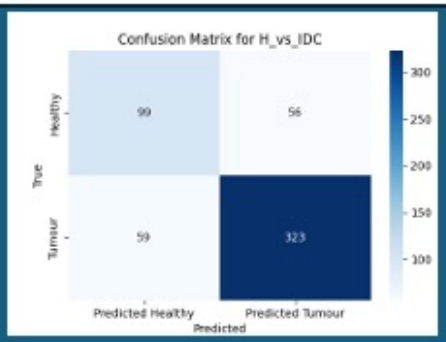
Confusion Matrices for GB classifier (for all tissue samples)

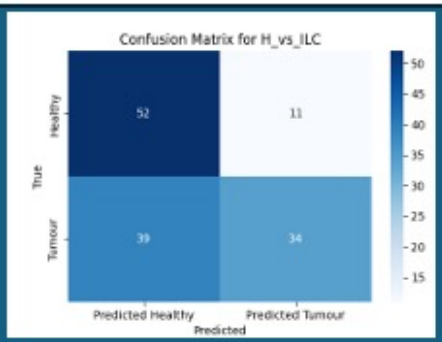
Normal *versus* All Malignant Tissue Samples

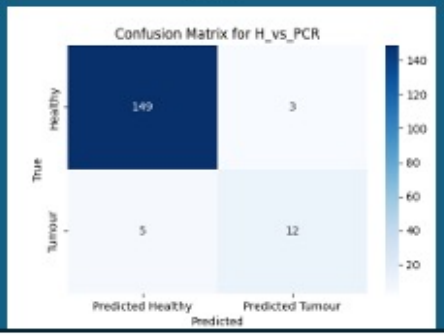


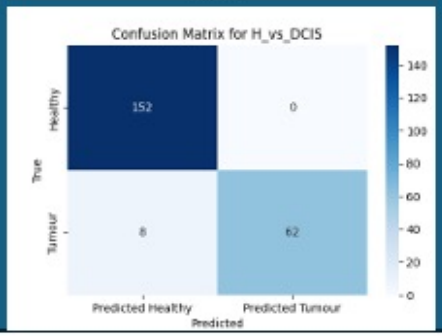


Normal *versus* Specific Histological subtypes

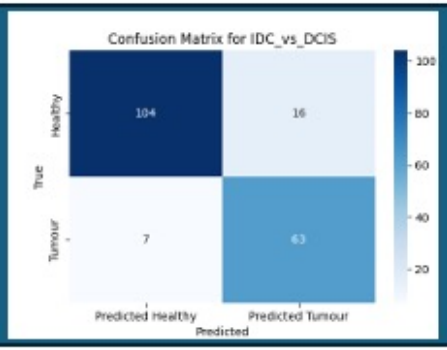


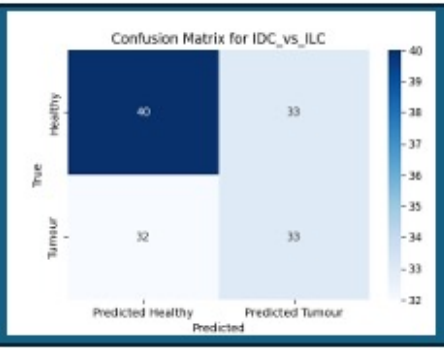


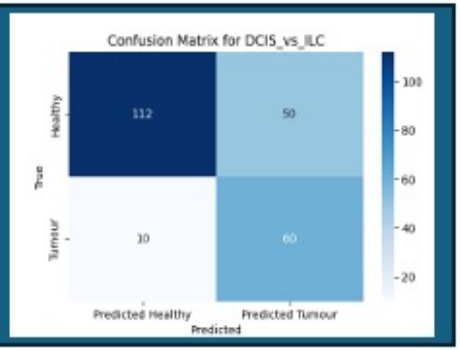




Specific Histological subtypes
versus
Specific Histological subtypes

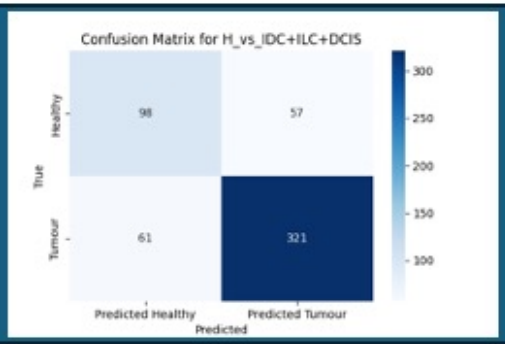


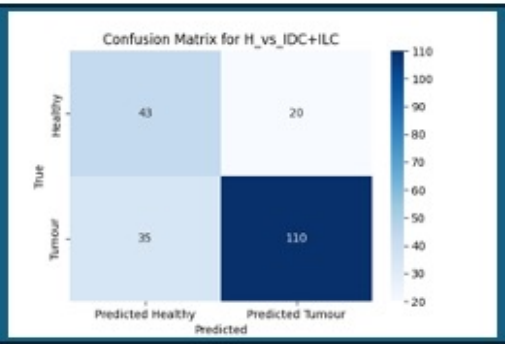




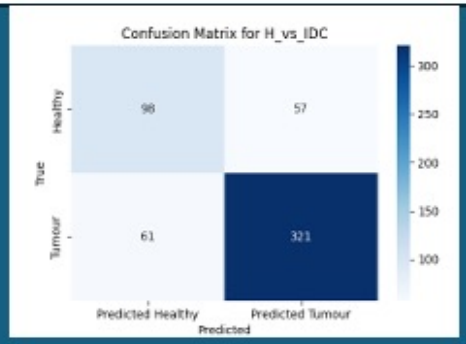
Confusion Matrices for XGB (all tissue samples)

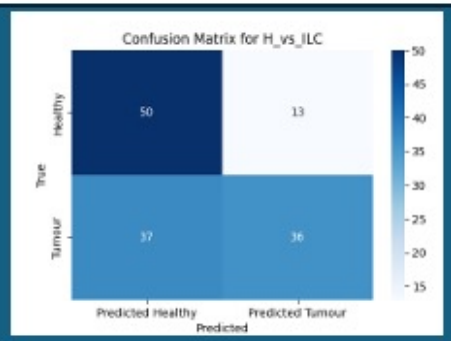
Normal
versus
All Malignant Tissue Samples

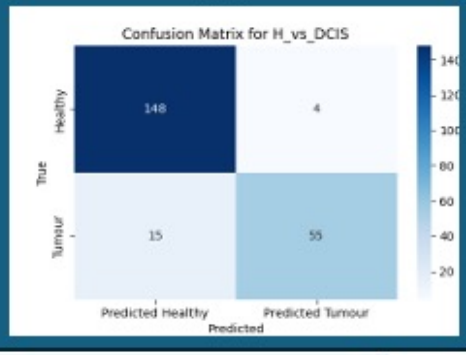


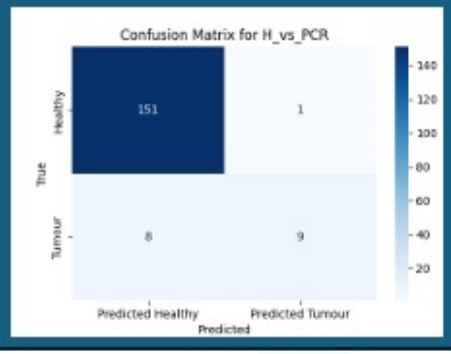


Normal
versus
Specific Histological subtypes

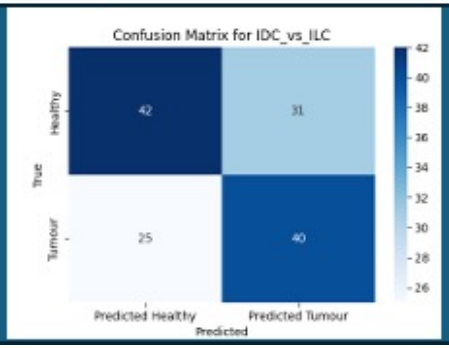


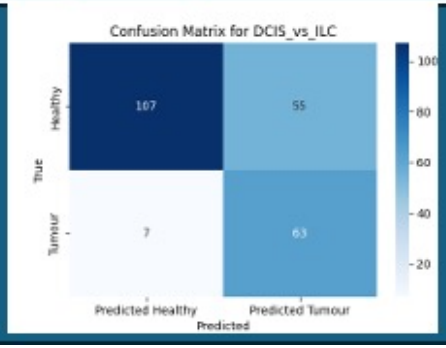


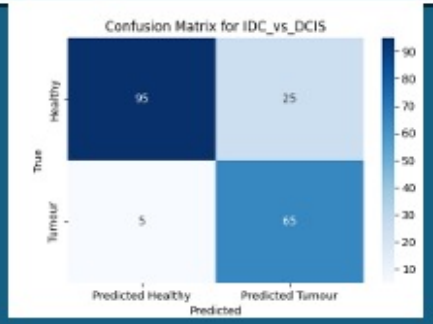




Specific Histological subtypes
versus
Specific Histological subtypes

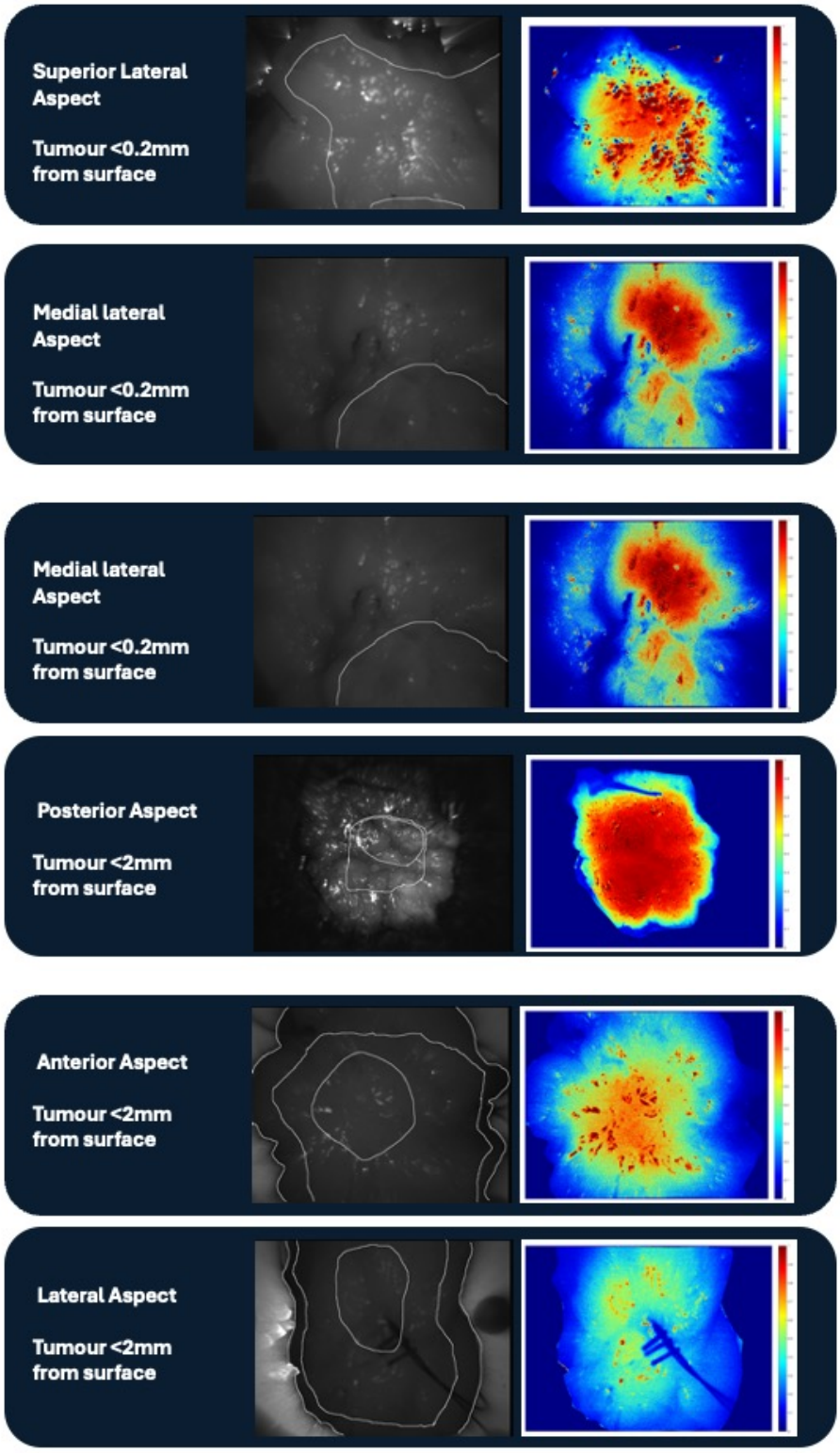


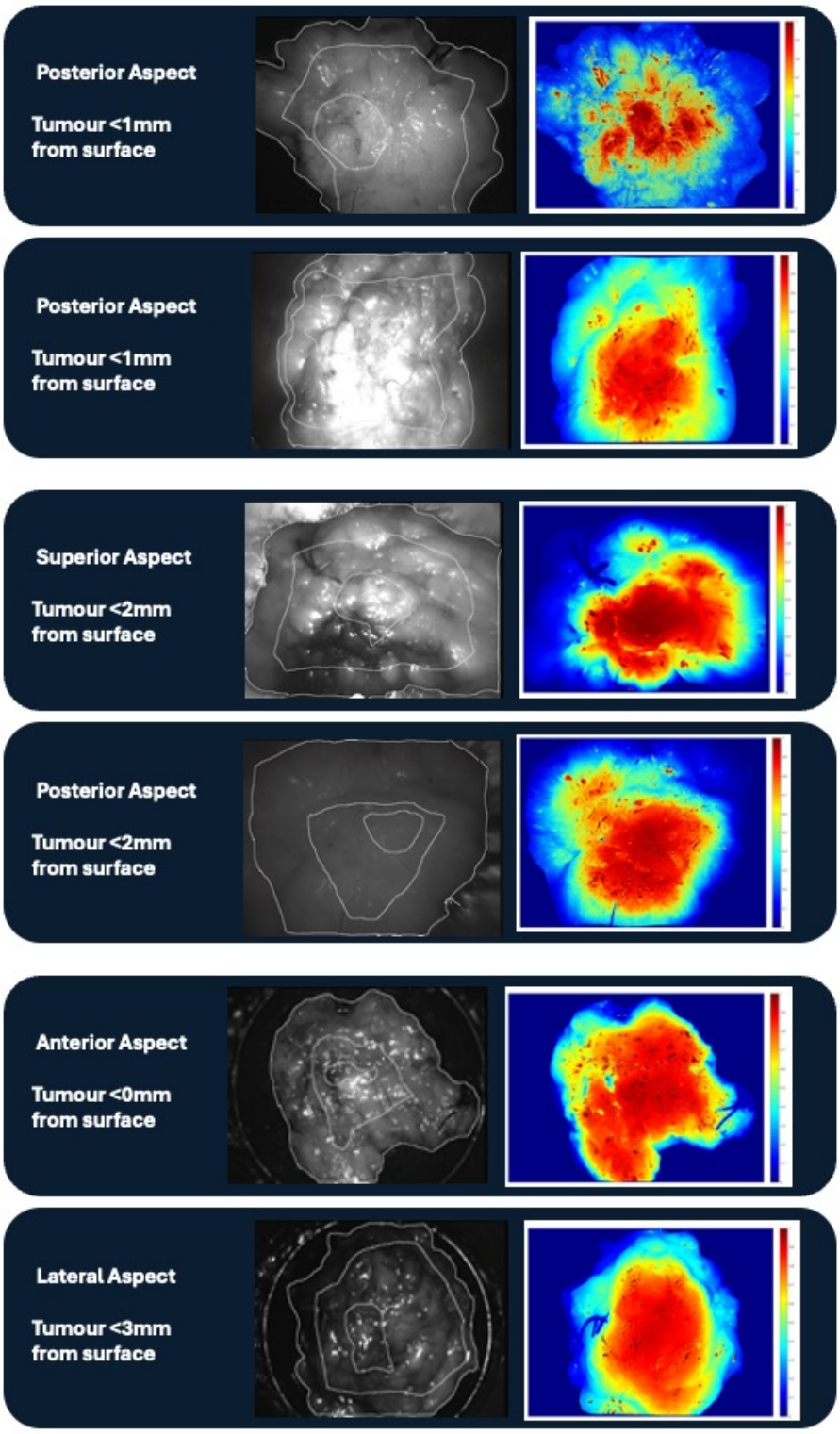


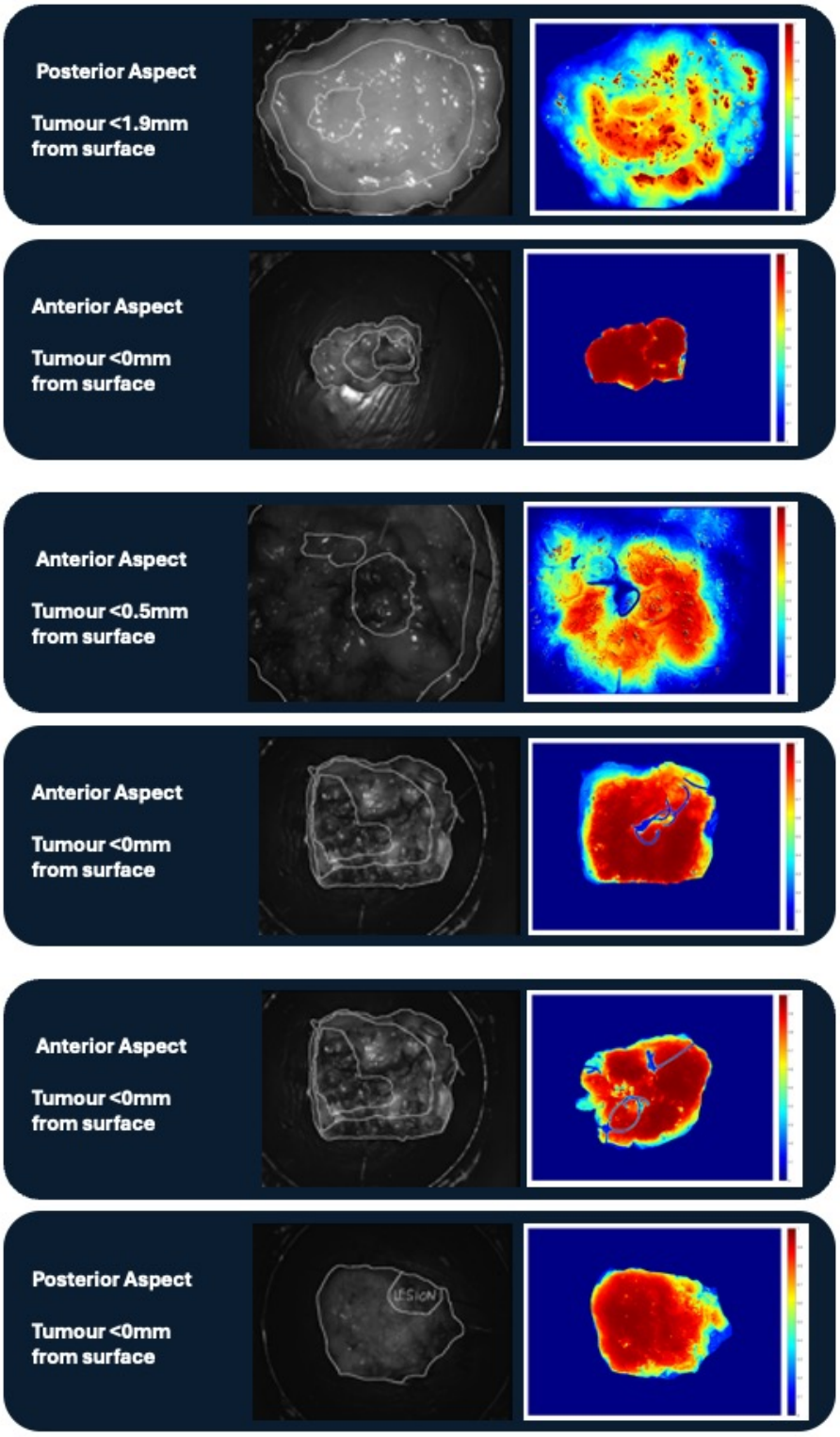


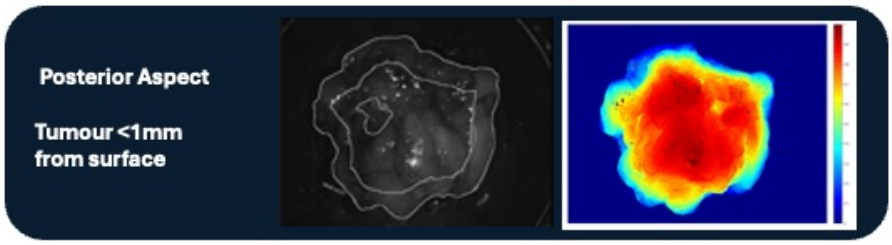
Appendix D

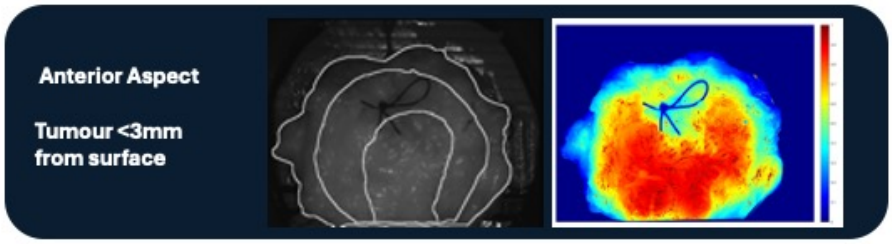
Colourmaps of all freshly excised specimens utilised for data analysis.

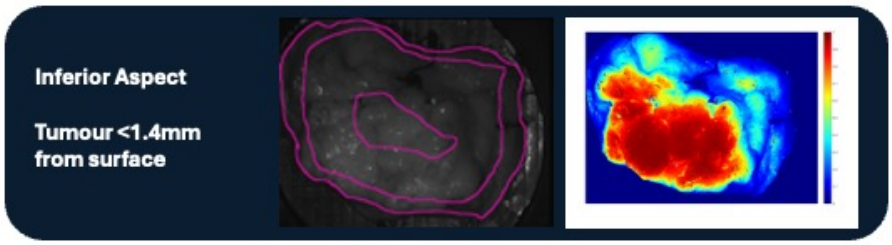


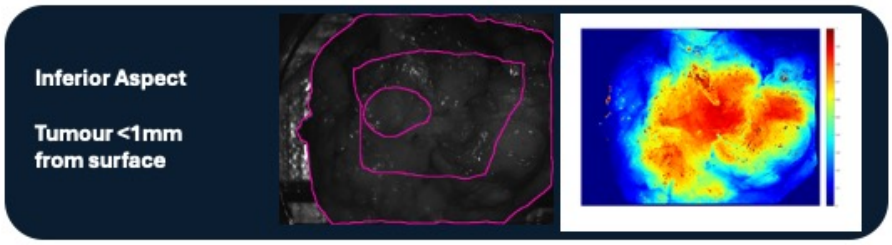

Posterior Aspect
Tumour <1mm
from surface
Posterior Aspect
Tumour <1mm
from surface
Superior Aspect
Tumour <2mm
from surface
Posterior Aspect
Tumour <2mm
from surface
Anterior Aspect
Tumour <0mm
from surface
Lateral Aspect
Tumour <3mm
from surface

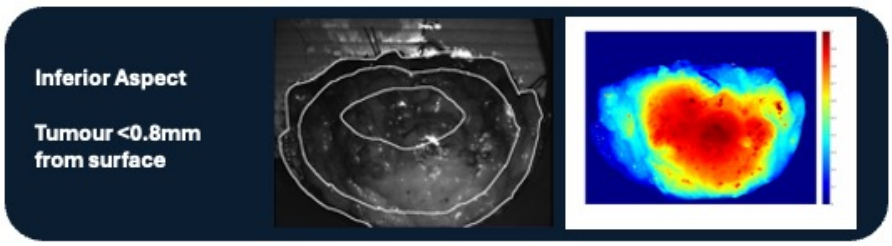

Posterior Aspect
Tumour <1.9mm
from surface
Anterior Aspect
Tumour <0mm
from surface
Anterior Aspect
Tumour <0.5mm
from surface
Anterior Aspect
Tumour <0mm
from surface
Anterior Aspect
Tumour <0mm
from surface
Posterior Aspect
Tumour <0mm
from surface
LESION

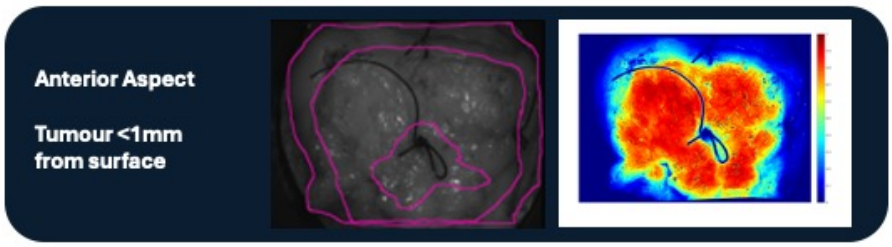

Posterior Aspect
Tumour <1mm
from surface

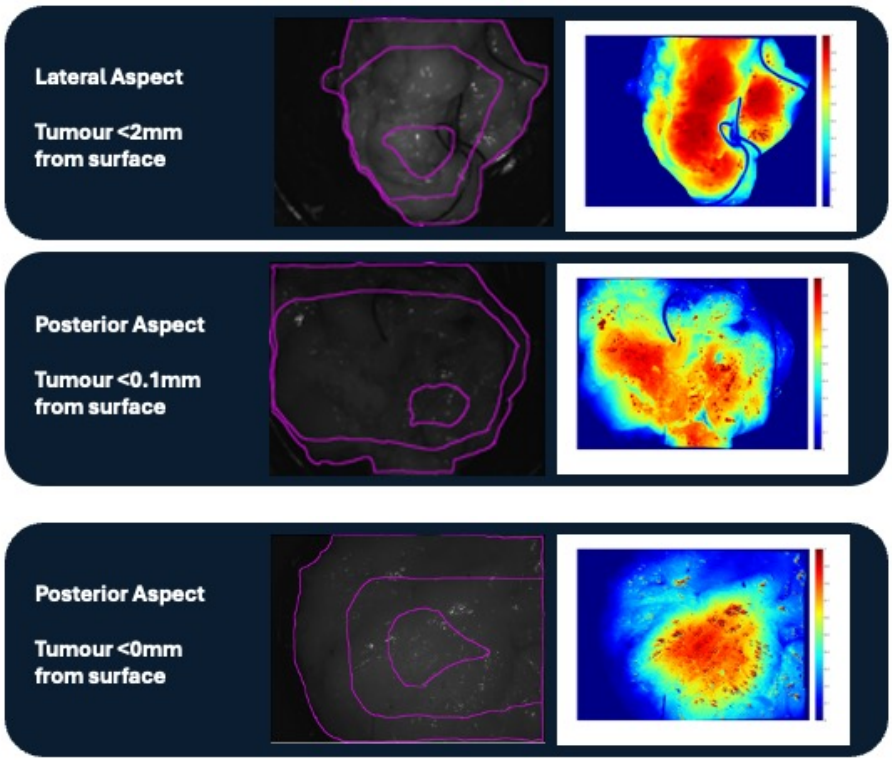

Anterior Aspect
Tumour <3mm
from surface


Inferior Aspect
Tumour <1.4mm
from surface


Inferior Aspect
Tumour <1mm
from surface


Inferior Aspect
Tumour <0.8mm
from surface


Anterior Aspect
Tumour <1mm
from surface


Lateral Aspect
Tumour <2mm
from surface
Posterior Aspect
Tumour <0.1mm
from surface
Posterior Aspect
Tumour <0mm
from surface